UNIVERSITY OF CALIFORNIA
RIVERSIDE

Methods Development for Toxicants Detection and Their Cellular Impacts

A Dissertation submitted in partial satisfaction
of the requirements for the degree of

Doctor of Philosophy

in

Environmental Toxicology

by

Yang Liu

September 2017

Dissertation Committee:
Dr. Wenwan Zhong, Chairperson
Dr. Jay Gan
Dr. Yinsheng Wang

The Dissertation of Yang Liu is approved:

_____

_____

_____

Committee Chairperson

University of California, Riverside

ACKNOWLEDGEMENTS

As I am graduating from UCR, I would like to acknowledge all the great people around me. Without the help and kindness from you, I would not enjoy this five years of Ph.D. life this much.

Thank you, Dr. Zhong! I really appreciate the time and efforts you put on my Ph.D. studies. Your valuable suggestions are always keeping me in the right trail. It is always easy to lose patience during this five years' study, and it is your understanding make me always feel supported. Your hard-working attitude and full dedication on research will keep influence me in the future.

I would also like to acknowledge Dr. Richard Hooley and all the Hooley group members. Without your help in the cavitand projects, I would not get my research projects working out efficiently in my last two years. And you guys are really kind and willing to help whenever I go upstairs.

I would also like to thank Dr. Yinsheng Wang and Dr. Jay Gan for serving as my guidance committee during the past five years. I would like to thank also group members in Dr. Wang's group and Dr. Gan's group for helping me with my research projects. You are awesome and generous people.

I would like to thank all colleges in Zhong group. You guys are really good people. I truly believe we are having a good and warm group, even we are so diverse in ethnicities and culture.

Lastly, I would like to thank my wife Chunying. You are always supportive to my research, and working the best to make my life happier. You have done the most to take care of our son Cary (Yaowen) and my parents. I am indebted to you and will do my best to make you a happy wife.

COPYRIGHT ACKNOWLEDGEMENTS

The text and figures in Chapter 3, in part or full, are an adaptation of the material as it appears in *J. Am. Chem. Soc.*, **2016**, 138 (34), 10746-10749. The coauthor, Dr. Wenwan Zhong, directed and supervised the research that formatted the basis of this chapter.

The text and figures in Chapter 4, in part or full, are an adaptation of the material as it appears in *Chem. Sci.*, **2017**,8, 3960-3970. The coauthor, Dr. Wenwan Zhong, directed and supervised the research that formatted the basis of this chapter.

The text and figures in Chapter 5, in part or full, are an adaptation of the material as it appears in *J. Am. Chem. Soc.*, **2017**, 139 (32), 10964-10967. The coauthor, Dr. Wenwan Zhong, directed and supervised the research that formatted the basis of this chapter.

ABSTRACT OF THE DISSERTATION

Methods Development for Toxicants Detection and Their Cellular Impacts

by

Yang Liu

Doctor of Philosophy, Graduate Program in Environmental Toxicology
University of California, Riverside, September 2017
Dr. Wenwan Zhong, Chairperson

Reactive oxygen species (ROS) are a class of reactive molecules that are continuously generated as a byproduct of aerobic metabolism in animals and plants. ROS were reported to play important roles in both signal transduction and homeostasis. In normal conditions, cells could maintain a delicate balance between oxidants and antioxidants. However, when ROS level go beyond its normal range, various negative effects could be induced including cytotoxicity, mutagenicity and carcinogenicity. Developing ROS detection tools and methods are of pivotal importance here to help understand their functions better.

Heavy metals are another class of molecules that occur naturally with a high atomic weight. Some of them are essential nutrients that are necessary for different biological and physiological functions. Nevertheless, concerns on their health effects were raised along with their increasing usage in industry, agriculture and modern technology. Exposure to heavy metals were reported to cause carcinogen, organ damage and genotoxicity.

Regarding the molecule level mechanism of above toxicants, proteins were reported to be one of the major targets. Protein covalent modifications occur frequently in all kinds of proteins and one of the most important class is the histone protein. Post-transitional modifications (PTM) to histone, including acetylation, methylation, phosphorylation, ubiquitination etc. Other than modification types, histone modification studies are further complexed by possibilities of different modification sites. In this dissertation, Chapter 1 is an introduction on ROS, heavy metal and PTMs, as well as current analytical techniques. Chapter 2 describes a novel microgel based amplification technique aiming to study ROS. Glucose and cholesterol are also measured based on the sample technique. Chapter 3 is reporting a deep cavitand based sensing method used for histone methylation study. Chapter 4 and 5 are more in-depth studies on sensing of different PTMs with deep cavitand based sensor array. Chapter 6 describes a further application of cavitand sensor array in metal detection. In Chapter 7, future directions and some preliminary studies are described.

TABLE OF CONTENTS

LIST OF FIGURES

LIST OF TABLES

Chapter 1 General Introduction

Reactive oxygen species (ROS)

Reactive oxygen species are a class of chemically reactive molecules containing oxygen. They may either be unpaired radicals like superoxide radical ($O_2^{-\bullet}$), hydroxyl radical ($OH^{\bullet}$), or reactive non-radical species such as hydrogen peroxide (H_2O_2).[1] In eukaryotes, the endogenous ROS occur mainly as byproducts of mitochondrial respiratory chain as well as by distinct enzyme systems, e.g. NADPH-oxidase, cytoplasmic xanthine oxidase and organellar sources, e.g., cytochrome P-450 oxidases.[2] ROS are capable of acting as signaling molecules at lower concentration; however, when ROS level exceed the capacity of endogenous antioxidants, damages to the cellular components including DNA, proteins and lipids will occur, and eventually cause apoptosis. Cellular defense mechanism of ROS can be assigned into two categories: antioxidants (such as ascorbic acid, vitamin E, and glutathione) and antioxidant enzymes (such as thioredoxins, superoxide dismutase, catalase and glutathione peroxidase). Among ROS, superoxide radicals are generally considered to be the precursor of most ROS. Superoxide dismutase can convert superoxide radicals into hydrogen peroxide which will be the source of the more potent hydroxyl radicals.[3] Hydrogen peroxide is a fairly stable member of ROS family and can migrate freely through cellular and organellar membranes[4].

ROS overproduction has been proposed to be a common mechanism in many diseases, such as ischemia-reperfusion injury,[5] hypoxia-reoxygenation[6] and cancer[7,8]. Besides, ROS

level can be greatly elevated by exogenous stimuli and stressors, including toxicant exposure[9], drug[10] and radiation[11,12]. Other than biotic stresses, abiotic strategies such as drought, low temperature, high temperature and mechanical stress could also affect the balance between ROS production and scavenging.[13,14] Cellular ROS have been reported to be varying from nano molar to micro molar among different cell types, like cancer cells, stem cells and scavenger cells.[15] Thus, study of the physiological behaviors of ROS in these systems and also the monitoring of therapeutic performance (e.g. cancer drugs) will need advanced detection technique for ROS.

The most commonly used method for ROS detection is based on fluorescent probe, which was regarded to be low cost, highly sensitive, cell permeable and easy to use. Examples of these dyes are hydroethidium (HE), used for $O_2^{-\bullet}$, and dichlorodihydrofluorescein diacetate (DCFH-DA), used for H_2O_2 sensing.[16] New ROS detection fluorescent probes are continuing to be fabricated to substitute these traditional probes partly due to the controversy of their reliability. [17,18] One example of the newly developed probe is the aromatic boronates based probes, which is reported to be able to selectively detect hydrogen peroxide over other competing ROS, and can sensitively detect sub-micromolar of hydrogen peroxide.[19] Other than fluorescent probes, the genetically encoded fluorescent proteins based sensing is a new field to enable transient live-cell imaging. Comparing with fluorescent probes, proteins are more stable upon excitation and also reversible depending on cellular thiol and antioxidants.[20,21]

Nanoparticles (NPs) based sensing systems builds another popular area for ROS sensing due to their unique physiochemical properties. The advantages of using NPs

include their high photo stability and also ease of delivery into cells.[22] The surface modification of NPs also makes it easy to be conjugated with cellular or sub cellular targeting ligands, tumor targeting ligands. NPs used for ROS measurement can be divided into two types, one is NPs with bare intrinsic fluorescence and become ROS sensitive after modification; the other is NPs that serve as carriers to enclose ROS responsive fluorescent probes. Metallic and semiconductor NPs like Au NPs[23], Ag NPs[24] and quantum dots[25] belong to the first type, which show properties like strong signal, photo-bleaching resistance and enhanced stability. Quantum dots were proved to be sensitive to H_2O_2 due to the quenching of its intrinsic photoluminescence. Research showed that glutathione-capped CdTe quantum dots were more sensitive to H_2O_2 than CdSe/ZnS QDs.[26] The second type of NPs is mainly polymer based structure, which is porous and biocompatible, acting as great carriers for traditional fluorescent probes. DCFDA enclosed ormosil NPs have been demonstrated to be superior to DCFDA without enclosure, which are more specific towards H_2O_2 when doing ROS detection.[27]

Heavy metals

Heavy metals are metallic elements that have relatively large atomic weight. They also occur naturally in our environment. Some heavy metals such as cobalt (Co), copper (Cu), chromium (Cr), iron (Fe), magnesium (Mg), manganese (Mn), nickel (Ni), selenium (Se) and zinc (Zn) are necessary nutrition elements for a healthy life. For instance, Cu is a core content in several oxidative stress related enzymes including catalase, superoxide dismutase and peroxidase.[28] However, heavy metals could cause toxic effects to cells when

the concentration exceed their normal level; various diseases such as Parkinson,[29] cancer[30], central nervous system disorders,[31] kidney stones[32] and cardiovascular disease[33] have been reported to be caused by exposure to heavy metals. The reason is probably due to their easiness of forming complex with biological molecules (DNA, RNA and protein) containing nitrogen, sulfur and oxygen.[34] Due to the high toxicity effects, heavy metals were strictly regulated by World Health Organization (WHO) and Environmental Protection Agency (EPA). Table 1.1 shows the standard regulation levels of seven heavy metals in drinking water. The concentrations allowed in drinking water for Cd, Hg, As and Pb are in the range of ppb level, while Cu and Zn are in ppm level. Various analytical techniques were developed and are continuously improved for metal detection. The standard methods such as atomic absorption spectroscopy, inductively coupled plasma-mass spectrometry and X-ray fluorescence spectroscopy are able to achieve a ppt and ppq level detection; however, these techniques require expensive and sophisticated equipments. Alternatively, cheaper and faster sensing methods based on molecule recognition are developing rapidly.

Table 1.1. Heavy Metals standards in Drinking Water Recommended by the WHO and EPA

Metal	WHO (mg/L)	EPA (mg/L)
Ni	0.07	0.04
Cu	2	1.3
Zn	3	5
Cd	0.003	0.005
Hg	0.001	0.002
Pb	0.01	0.015
As	0.01	0.01

The newly developed sensors could be divided into following types:

1. Electrochemical method. Adsorptive stripping analysis on mercury film electrode[35] is a very popular field for metal detection, which is more environmental friendly and efficient than solid mercury electrodes. And this method has been used to test Mo, Be Pb, Ni, Cr and U in various matrices including drinking water, seawater and biological sample. Besides, electrochemistry method was further printed into high throughput carbon electrodes, which are more favorable for on-site analysis of heavy metals.[36] Moreover, carbon nanotube modified electrodes were also successfully applied to heavy metal detection.[37-39]

2. Fluorescent dye based detection. Quite a large number of organic dye molecules were synthesized to target heavy metals.[40-42] These dye molecules usually show a fluorescent signal change upon binding with target metal ions. The recognition usually can be divided into cage based and binding based. And the advantage of using fluorescent dye for metal sensing is to do in-situ monitoring of metals within cells and animals.[43,44]

3. Nanoparticle (NP) based method. Nanoparticles were adopted here as either fluorescent reporter or carrier for metal sensing. Various nanoparticles have been reported

to be fluorescent and were applied for metal sensing, including gold NPs,[45,46] silver NPs,[47] quantum dots (QD),[48,49] carbon dots[50-52] and fluorescent polymer NPs.[53] Non-fluorescent nanoparticles are also useful here as a colorimetric reporter for detection of heavy metals[54-57] including Pb^{2+}, Cd^{2+}, Cu^{2+} and Hg^{2+}. Core shell nanoparticles were also widely synthesized and applied for heavy metal detection.[57-59]

Other than optical detection method, nanoparticles were reported to enhance the electrochemical detection of heavy metals when nanoparticles decorated electrodes were used. [38,55,60,61]

4. Biological molecules based sensing. Biomolecules such as DNA and protein were often used for metal detection due to the strong non-covalent coordination between them. DNA based detection of heavy metals were based on mainly two popular mechanisms: one is based on DNA hybridization and the other is DNAzyme. The most famous example for DNA hybridization is the Hg^{2+} mediated T-T mismatch,[62-64] which has been heavily adopted as a method for mercury detection. And DNAzymes are DNA molecules with the enzymatic capability of cleave another DNA or RNA strands when binding with certain metal coordinator. The cleavage process could be monitored by fluorescence change with proper labeling of the leaving strands. [48,65-68] Proteins were also quite often applied to metal detection due to strong coordination between metal and protein metal-binding motif. [69-71] Antibodies that can target metal-EDTA complexes were also reported for metal detection.[72,73]

Other than above methods, a lot of novel and interesting methods were also developed to target metal analysis, including paper-based sensing,[74,75] microfluidic device

sensing,[76,77] surface plasmon resonance sensing (SPR),[78] and chemiluminescent sensing.[79,80]

Histone post-transitional modifications

Histones are highly positively charged proteins that are densely packed with DNA to form a structure unit named nucleosomes. There are four subunits in histone proteins, namely H3, H4, H2a and H2b, forming an octamer structure. Without histone, DNA molecule will be very long and could not be efficiently enclosed inside nucleus. Other than this, histones also undergo post-transitional modifications (PTM), which play important roles in chromatin regulation. These modifications include methylation, acetylation, phosphorylation, ubiquitination, SUMOylation and more. Both H3 and H4 have long tails exposed outside of core histone and these tails are more prone to PTMs and contain most of the modification sites of histone. Meanwhile, H2a and H2b can also be modified, however, in a much smaller extent. The combination of different sites and modifications makes the histone modification study a very challenging and interesting field which has attracted great attention.

Histone acetylation was first reported in 1964.[81] From then on, it has been proved that acetylation was controlled by two groups of enzymes namely histone acetyltransferase and histone deacetylase. The acetylation process will neutralize the positive charge on amino group on lysine side chain, which will lead to weakened interaction between histone and DNA and result in a relaxed chromatin. The relaxed chromatin will allow the binding between DNA binding proteins and DNA which will further initiate downstream cellular

function. It has been reported that histone acetylation was associated with inflammatory disease,[82] cancer[83,84] and neurological and psychological disorders.[85]

Histone methylation is the process of adding a methyl group to the side chain amino group of lysine and arginine. Lysine could be mono-, di- or tri-methylated and for arginine, there could be mono- and symmetrical or asymmetrical di-methylation. Similar to acetylation, methylation level was also delicately controlled by two enzymes: methyl transferase and demethylase. Methylation was related to both transcriptional repression and activation. For example, trimethylation of lysine 4 would promote gene expression through recognition by transcription-activating effector molecules.[86] Lysine 9 di-methylation would cause a transcriptional silencing.[87]

Histone phosphorylation is the highly dynamic process and could take place on serine, threonine and tyrosine, as well as the N-terminal free amine group. Kinase and phosphatase are responsible for the control of phosphorylation level inside cell. Phosphorylation of histone will add negative charge to the histone, which will influence the chromatin structure. Most phosphorylation sites lie in the histone tails, because they are more accessible to large phosphorylation enzymes. And phosphorylation was reported to play a pivotal role in DNA fragmentation,[88] chromosome condensation,[89] and meiosis.[90]

Other histone modifications include ubiquitylation and sumoylation, which covalently add a much larger group of ubiquitin to histone lysine through a sequential action of three enzymes. [91] Sumoylation is related to ubiquitylation and the covalent attachment of small ubiquitin-like modifier molecules to lysine. And these two modifications were less studied and some researches have shown that they are related to gene activation and silencing.[92]

Environmental factors, such as nutritional supplements,[93] xenobiotic chemicals,[94] inorganic compounds[95], heavy metals,[96,97] pesticides[98] and low-dose radiation[99] have been shown to affect the epigenetics. When these factors enter cells, some were able to enhance ROS production. ROS play an important role in oxidation based removal of methyl groups from histone lysine[100] and also were reported to inhibit histone acetylation.[101]

Some of the heavy metals were reported to cause cancer though epigenetics. Nickel is one of the most abundant element on earth, and considered to be a potent carcinogen. However, the carcinogenesis is not a consequence of mutagenicity, but rather its ability to alter chromatin structure. Exposure of nickel could distort different histone modifications. For example, exposure of nickel was shown to increase H3K9me2,[102] H34K3me2 and H3K9me2 levels.[97] There are also reports show that nickel would inhibit H3 and H4 acetylation.[103,104] H3S10 phosphorylation can also be enhanced when nickel is added to the cell.[105] Chromium is another well-established human carcinogen and shows strong ROS generation capacity. Chromium was also reported to induce strong effects on histone methylation[106] and acetylation.[107]

Traditionally, histone modification analysis was mainly based on specific antibodies, and it is still the most popular method at present. However, there are some drawbacks presented in the use of antibodies in this field, such as high cost, cross-reactivity with other sites, variance between batches and possible influence of nearby sites. Recently, mass spectrometry (MS) has been applied into this field to address these problems. Different MS related methods have been applied to histone modifications studies, such as liquid chromatography Electrospray ionization mass spectrometry (LC-ESI-MS) and matrix

assisted laser desorption ionization-time of flight mass spectrometry (MALDI-TOF MS). MS is very powerful technique that could achieve not only confirmation of known histone modification sites, but discovery of unknown sites, quantification of modification levels and possibly the reading of the entire histone codes. However, MS still has some disadvantages including expensive equipment, high maintenance cost, long sample preparation procedures, and difficulty of spectrum interpretation.

Supramolecular chemistry is a field that focused on interesting noncovalent interactions between molecules, including hydrogen bonding, pi-pi interaction, electrostatic interaction, van der Waals force and hydrophobic interaction. The basis of the supramolecular chemistry is molecular recognition and host-guest interaction. The application of supramolecular chemistry mainly lies in the fields such as drug delivery,[108] sensing[109] and catalysis,[110] which rely on molecular recognition and binding. One of the ultimate goals of supramolecular chemistry is to use synthetic molecular to replace antibodies. There are already interesting researches completed to apply supramolecular chemistry into the field of histone modification analysis. The most commonly used molecule are Cyclodextrins (CDs), Calixarenes(CAs), cucurbituril (CBs) and their derivatives.[111] CAs were reported to be able to specifically target tri-methylated over non-methylated lysine like lysine 4, lysine 9, lysine 27 and lysine36, and this feature was further applied to sense protein binding interaction.[112,113] The strong interaction between trimethyllysine and CAs was due to the hydrophobic interaction between aromatic core of the binding pocket and the combination of cation−π interactions and electrostatic interactions. Small CA4 similar structure was also synthesized to target dimethyl-lysine in

lysozyme.[114] Another application was to conjugate CA4 to the stationary phase of an affinity column for isolation of methylated proteins.[115] CB6 and CB7 were also shown to recognize methylated lysine and arginine over non-methylated.[116]

These supramolecular hosts always show pan-specificity towards their targets, which means they can target a class of modifications, however, they cannot differentiate same modification but at different locations. This is due to the fact that these hosts are still much smaller than antibody, which could not sense the nearby and neighboring amino acids environment. To solve this problem, sensor arrays are usually adopted here to expand the application of these hosts to complex mixtures. Sensor arrays are also called "chemical nose", which combine different sensing elements into an array and the information collected for each element were gathered and processed to finally present different features. These features will be able to be used to represent more precisely the analytes. Sensor arrays have been adopted for sensing of odor,[117] gas,[118] cancer,[119] organic compounds,[120] soft drinks[121] and so on. Using arrays of sensors, the Hof group could achieve a discrimination of methylated, mono-, di-, and trimethylated lysine on a single histone tail sequence.[122] The Waters group were also able to differentiate different histone modifications, methylation sites and levels based on a four component sensor array.[123]

Scope of the dissertation

This dissertation was to introduce novel designs of analytical tools targeting toxicants like ROS, heavy metals as well as possible resulting biological effects – histone modifications – after exposure. **Chapter 2** is talking about the application of a novel hybrid microgel particles used for ROS sensing. The hybrid microgel is proved to be highly sensitive to H_2O_2, and it is further applied to the detection of two common heath related factors: blood sugar and blood cholesterol. **Chapter 3** is focusing on the synthesis of new synthetic host cavitand and its fluorescent guest. This guest and host system shows good sensitivity and specificity towards lysine 9 tri-methylation. A demethylase assay demonstrated the capability of these new strategy to do inhibitor screening for methylation enzymes. **Chapter 4** aimed to use a cavitand-guest based sensor array to test different histone modifications (methylation, acetylation, phosphorylation, and the mix of three), and the binding mechanism was analyzed and 14 peptides were tested later to show the high discrimination capability of this new method. In **Chapter 5** this sensor array was further adopted to test both demethylase and methyl transferase activity in situ. We show that our sensor array could discriminate different enzyme reactions based very similar substrates and products. **Chapter 6** focused on heavy metals detection with sensor array, where one more guest molecule DSMI was adopted here to enhance its capability of differentiate different metals. 17 metals were able to be distinguished within one run. Environmental samples were also used to verify the effectiveness of this sensor array design. **Chapter 7** is talking about some unfinished projects related to first 5 chapters and a conclusion is also made in this chapter.

Reference

(1) Sauer, H.; Wartenberg, M.; Hescheler, J. *Cell. Physiol. Biochem.* **2001**, *11*, 173-186.

(2) Gamaley, I. A.; Klyubin, I. V. In *Int. Rev. Cytol.*, Kwang, W. J., Ed.; Academic Press, 1999, pp 203-255.

(3) Cardoso, A. R.; Chausse, B.; da Cunha, F. M.; Luévano-Martínez, L. A.; Marazzi, T. B. M.; Pessoa, P. S.; Queliconi, B. B.; Kowaltowski, A. J. *Free Radic. Biol. Med.* **2012**, *52*, 2201-2208.

(4) Boveris, A.; Cadenas, E. *IUBMB Life* **2000**, *50*, 245-250.

(5) Cruthirds, D. L.; Novak, L.; Akhi, K. M.; Sanders, P. W.; Thompson, J. A.; MacMillan-Crow, L. A. *Arch. Biochem. Biophys.* **2003**, *412*, 27-33.

(6) Chandel, N. S.; Maltepe, E.; Goldwasser, E.; Mathieu, C. E.; Simon, M. C.; Schumacker, P. T. *Proceedings of the National Academy of Sciences* **1998**, *95*, 11715-11720.

(7) Pelicano, H.; Carney, D.; Huang, P. *Drug Resist. Updat.* **2004**, *7*, 97-110.

(8) Trachootham, D.; Alexandre, J.; Huang, P. *Nat. Rev. Drug Discov.* **2009**, *8*, 579-591.

(9) Bagchi, D.; Bagchi, M.; Hassoun, E. A.; Stohs, S. J. *Toxicology* **1995**, *104*, 129-140.

(10) Damian G. Deavall, E. A. M., Judith M. Horner, Ruth Roberts. *Journal of Toxicology* **2012**, *2012*, 13.

(11) Halliwell, B. *The American Journal of Medicine* **1991**, *91*, S14-S22.

(12) Yamamori, T.; Yasui, H.; Yamazumi, M.; Wada, Y.; Nakamura, Y.; Nakamura, H.; Inanami, O. *Free Radic. Biol. Med.* **2012**, *53*, 260-270.

(13) Kazuo Tsugane, K. K., Yasuo Niwa, Yasushi Ohba, Keishiro Wada, Hirokazu Kobayashi. *The Plant Cell* **1999**, *11*.

(14) T. K. Prasad, M. D. A., B. A. Martin, C. R. Stewart. *The Plant Cell* **1994**, *6*.

(15) Szatrowski, T. P.; Nathan, C. F. *Cancer Res.* **1991**, *51*, 794-798.

(16) Larissa M. Uusitalo, N. H. *Int. J. Mol. Sci.* **2012**, *9*.

(17) Kalyanaraman, B.; Darley-Usmar, V.; Davies, K. J. A.; Dennery, P. A.; Forman, H. J.; Grisham, M. B.; Mann, G. E.; Moore, K.; Roberts Ii, L. J.; Ischiropoulos, H. *Free Radic. Biol. Med.* **2012**, *52*, 1-6.

(18) Soh, N. *Anal. Bioanal. Chem.* **2006**, *386*, 532-543.

(19) Miller, E. W.; Albers, A. E.; Pralle, A.; Isacoff, E. Y.; Chang, C. J. *J. Am. Chem. Soc.* **2005**, *127*, 16652-16659.

(20) Alvarez, L.; Levin, C. H.; Merola, F.; Bizouarn, T.; Pasquier, H.; Baciou, L.; Rusconi, F.; Erard, M. *Photochem. Photobiol.* **2010**, *86*, 55-61.

(21) Tsourkas, A.; Newton, G.; Perez, J. M.; Basilion, J. P.; Weissleder, R. *Anal. Chem.* **2005**, *77*, 2862-2867.

(22) Oh, W.-K.; Jeong, Y. S.; Kim, S.; Jang, J. *ACS Nano* **2012**, *6*, 8516-8524.

(23) Lee, H.; Lee, K.; Kim, I.-K.; Park, T. G. *Adv. Funct. Mater.* **2009**, *19*, 1884-1890.

(24) Zhong, L.; Gan, S.; Fu, X.; Li, F.; Han, D.; Guo, L.; Niu, L. *Electrochim. Acta* **2013**, *89*, 222-228.

(25) Li, Y.; Li, B.; Zhang, J. *Luminescence* **2013**, *28*, 667-672.

(26) Yuan, J.; Guo, W.; Yin, J.; Wang, E. *Talanta* **2009**, *77*, 1858-1863.

(27) Kim, G.; Lee, Y.-E. K.; Xu, H.; Philbert, M. A.; Kopelman, R. *Anal. Chem.* **2010**, *82*, 2165-2169.

(28) Stern, B. R. *J. Toxicol. Environ. Health A* **2010**, *73*, 114-127.

(29) Uversky, V. N.; Li, J.; Fink, A. L. *J. Biol. Chem.* **2001**, *276*, 44284-44296.

(30) Hamilton, J. W.; Kaltreider, R. C.; Bajenova, O. V.; Ihnat, M. A.; McCaffrey, J.; Turpie, B. W.; Rowell, E. E.; Oh, J.; Nemeth, M. J.; Pesce, C. A.; Lariviere, J. P. *Environ. Health Perspect.* **1998**, *106*, 1005-1015.

(31) B L Vallee, a.; Ulmer, D. D. *Annu. Rev. Biochem.* **1972**, *41*, 91-128.

(32) Järup, L. *Br. Med. Bull.* **2003**, *68*, 167-182.

(33) *Journal of Toxicology* **2011**, *2011*.

(34) Aragay, G.; Pons, J.; Merkoçi, A. *Chem. Rev.* **2011**, *111*, 3433-3458.

(35) Economou, A.; Fielden, P. R. *TrAC Trends in Analytical Chemistry* **1997**, *16*, 286-292.

(36) Palchetti, I.; Laschi, S.; Mascini, M. *Anal. Chim. Acta* **2005**, *530*, 61-67.

(37) Morton, J.; Havens, N.; Mugweru, A.; Wanekaya, A. K. *Electroanalysis* **2009**, *21*, 1597-1603.

(38) Aragay, G.; Merkoçi, A. *Electrochim. Acta* **2012**, *84*, 49-61.

(39) Tuzen, M.; Saygi, K. O.; Soylak, M. *J. Hazard. Mater.* **2008**, *152*, 632-639.

(40) Domaille, D. W.; Que, E. L.; Chang, C. J. *Nat. Chem. Biol.* **2008**, *4*, 168-175.

(41) Zhang, J. F.; Zhou, Y.; Yoon, J.; Kim, J. S. *Chem. Soc. Rev.* **2011**, *40*, 3416-3429.

(42) Murkovic, I.; Wolfbeis, O. S. *Sensors and Actuators B: Chemical* **1997**, *39*, 246-251.

(43) Jiang, P.; Guo, Z. *Coord. Chem. Rev.* **2004**, *248*, 205-229.

(44) Yoon, S.; Albers, A. E.; Wong, A. P.; Chang, C. J. *J. Am. Chem. Soc.* **2005**, *127*, 16030-16031.

(45) Huang, C. C.; Yang, Z.; Lee, K. H.; Chang, H. T. *Angew. Chem.* **2007**, *119*, 6948-6952.

(46) Huang, C.-C.; Chang, H.-T. *Anal. Chem.* **2006**, *78*, 8332-8338.

(47) Lee, K.-S.; El-Sayed, M. A. *The Journal of Physical Chemistry B* **2006**, *110*, 19220-19225.

(48) Wu, C.-S.; Khaing Oo, M. K.; Fan, X. *ACS Nano* **2010**, *4*, 5897-5904.

(49) Han, B.; Yuan, J.; Wang, E. *Anal. Chem.* **2009**, *81*, 5569-5573.

(50) Li, H.; Zhai, J.; Tian, J.; Luo, Y.; Sun, X. *Biosens. Bioelectron.* **2011**, *26*, 4656-4660.

(51) Lu, W.; Qin, X.; Liu, S.; Chang, G.; Zhang, Y.; Luo, Y.; Asiri, A. M.; Al-Youbi, A. O.; Sun, X. *Anal. Chem.* **2012**, *84*, 5351-5357.

(52) Guo, Y.; Wang, Z.; Shao, H.; Jiang, X. *Carbon* **2013**, *52*, 583-589.

(53) Zhao, X.; Tapec-Dytioco, R.; Tan, W. *J. Am. Chem. Soc.* **2003**, *125*, 11474-11475.

(54) Kim, Y.; Johnson, R. C.; Hupp, J. T. *Nano Lett.* **2001**, *1*, 165-167.

(55) Xu, X.; Duan, G.; Li, Y.; Liu, G.; Wang, J.; Zhang, H.; Dai, Z.; Cai, W. *ACS Appl. Mater. Interfaces* **2014**, *6*, 65-71.

(56) Nath, N.; Chilkoti, A. *Anal. Chem.* **2002**, *74*, 504-509.

(57) Slocik, J. M.; Zabinski, J. S.; Phillips, D. M.; Naik, R. R. *Small* **2008**, *4*, 548-551.

(58) Sugunan, A.; Thanachayanont, C.; Dutta, J.; Hilborn, J. *Science and Technology of Advanced Materials* **2005**, *6*, 335-340.

(59) Vossmeyer, T.; Guse, B.; Besnard, I.; Bauer, R. E.; MüLLEN, K.; Yasuda, A. *Adv. Mater.* **2002**, *14*, 238-242.

(60) Gumpu, M. B.; Sethuraman, S.; Krishnan, U. M.; Rayappan, J. B. B. *Sensors and Actuators B: Chemical* **2015**, *213*, 515-533.

(61) Luo, X.; Morrin, A.; Killard, A. J.; Smyth, M. R. *Electroanalysis* **2006**, *18*, 319-326.

(62) Miyake, Y.; Togashi, H.; Tashiro, M.; Yamaguchi, H.; Oda, S.; Kudo, M.; Tanaka, Y.; Kondo, Y.; Sawa, R.; Fujimoto, T.; Machinami, T.; Ono, A. *J. Am. Chem. Soc.* **2006**, *128*, 2172-2173.

(63) Xue, X.; Wang, F.; Liu, X. *J. Am. Chem. Soc.* **2008**, *130*, 3244-3245.

(64) Darbha, G. K.; Singh, A. K.; Rai, U. S.; Yu, E.; Yu, H.; Chandra Ray, P. *J. Am. Chem. Soc.* **2008**, *130*, 8038-8043.

(65) Breaker, R. R.; Joyce, G. F. *Chem. Biol.* **1994**, *1*, 223-229.

(66) Wang, Z.; Lee, J. H.; Lu, Y. *Adv. Mater.* **2008**, *20*, 3263-3267.

(67) Liu, J.; Lu, Y. *J. Am. Chem. Soc.* **2003**, *125*, 6642-6643.

(68) Liu, J.; Lu, Y. *J. Am. Chem. Soc.* **2004**, *126*, 12298-12305.

(69) Dudev, T.; Lim, C. *Annual Review of Biophysics* **2008**, *37*, 97-116.

(70) Varriale, A.; Staiano, M.; Rossi, M.; D'Auria, S. *Anal. Chem.* **2007**, *79*, 5760-5762.

(71) Chen, P.; Greenberg, B.; Taghavi, S.; Romano, C.; van der Lelie, D.; He, C. *Angewandte Chemie International Edition* **2005**, *44*, 2715-2719.

(72) Blake, D. A.; Jones, R. M.; Blake, R. C.; Pavlov, A. R.; Darwish, I. A.; Yu, H. *Biosens. Bioelectron.* **2001**, *16*, 799-809.

(73) Khosraviani, M.; Pavlov, A. R.; Flowers, G. C.; Blake, D. A. *Environ. Sci. Technol.* **1998**, *32*, 137-142.

(74) Ratnarathorn, N.; Chailapakul, O.; Henry, C. S.; Dungchai, W. *Talanta* **2012**, *99*, 552-557.

(75) Chen, G.-H.; Chen, W.-Y.; Yen, Y.-C.; Wang, C.-W.; Chang, H.-T.; Chen, C.-F. *Anal. Chem.* **2014**, *86*, 6843-6849.

(76) Cate, D. M.; Adkins, J. A.; Mettakoonpitak, J.; Henry, C. S. *Anal. Chem.* **2014**, *87*, 19-41.

(77) Delaney, J. L.; Hogan, C. F.; Tian, J.; Shen, W. *Anal. Chem.* **2011**, *83*, 1300-1306.

(78) Hassani, A.; Skorobogatiy, M. *Opt. Express* **2006**, *14*, 11616-11621.

(79) Obata, H.; Karatani, H.; Nakayama, E. *Anal. Chem.* **1993**, *65*, 1524-1528.

(80) Bowie, A. R.; Achterberg, E. P.; Mantoura, R. F. C.; Worsfold, P. J. *Anal. Chim. Acta* **1998**, *361*, 189-200.

(81) Allfrey, V. G.; Faulkner, R.; Mirsky, A. E. *Proc. Natl. Acad. Sci. U. S. A.* **1964**, *51*, 786-794.

(82) Barnes, P.; Adcock, I.; Ito, K. *Eur. Respir. J.* **2005**, *25*, 552-563.

(83) Timmermann, S.; Lehrmann, H.; Polesskaya, A.; Harel-Bellan, A. *Cell. Mol. Life Sci.* **2001**, *58*, 728-736.

(84) Mahlknecht, U.; Hoelzer, D. *Mol. Med.* **2000**, *6*, 623.

(85) Taylor, J. P.; Taye, A. A.; Campbell, C.; Kazemi-Esfarjani, P.; Fischbeck, K. H.; Min, K.-T. *Genes Dev.* **2003**, *17*, 1463-1468.

(86) Bannister, A. J.; Kouzarides, T. *Methods Enzymol.* **2004**, *376*, 269-288.

(87) Gupta, S.; Kim, S. Y.; Artis, S.; Molfese, D. L.; Schumacher, A.; Sweatt, J. D.; Paylor, R. E.; Lubin, F. D. *The Journal of Neuroscience* **2010**, *30*, 3589-3599.

(88) Ajiro, K. *J. Biol. Chem.* **2000**, *275*, 439-443.

(89) Matsumoto, Y.-i.; Yasuda, H.; Mita, S.; Marunouchi, T.; Yamada, M.-a. *Nature* **1980**, *284*, 181-183.

(90) Wang, Q.; Wang, C.-M.; Ai, J.-S.; Xiong, B.; Yin, S.; Hou, Y.; Chen, D.-Y.; Schatten, H.; Sun, Q.-Y. *Cell Cycle* **2006**, *5*, 1974-1982.

(91) Hershko, A.; Ciechanover, A. *Annu. Rev. Biochem.* **1998**, *67*, 425-479.

(92) Minsky, N.; Oren, M. *Mol. Cell* **2004**, *16*, 631-639.

(93) Waterland, R. A.; Jirtle, R. L. *Mol. Cell. Biol.* **2003**, *23*, 5293-5300.

(94) Ho, S. M.; Tang, W. Y.; Belmonte de Frausto, J.; Prins, G. S. *Cancer Res.* **2006**, *66*, 5624-5632.

(95) Singh, K. P.; DuMond, J. W., Jr. *Int. J. Oncol.* **2007**, *30*, 253-260.

(96) Arita, A.; Costa, M. *Metallomics : integrated biometal science* **2009**, *1*, 222-228.

(97) Zhou, X.; Li, Q.; Arita, A.; Sun, H.; Costa, M. *Toxicol. Appl. Pharmacol.* **2009**, *236*, 78-84.

(98) Andersen, H. R.; Schmidt, I. M.; Grandjean, P.; Jensen, T. K.; Budtz-Jørgensen, E.; Kjærstad, M. B.; Bælum, J.; Nielsen, J. B.; Skakkebæk, N. E.; Main, K. M. *Environ. Health Perspect.* **2008**, *116*, 566-572.

(99) Koturbash, I.; Baker, M.; Loree, J.; Kutanzi, K.; Hudson, D.; Pogribny, I.; Sedelnikova, O.; Bonner, W.; Kovalchuk, O. *Int. J. Radiat. Oncol. Biol. Phys.* **2006**, *66*, 327-330.

(100) Chen, H.; Costa, M. *Biometals* **2009**, *22*, 191-196.

(101) Kang, J.; Zhang, Y.; Chen, J.; Chen, H.; Lin, C.; Wang, Q.; Ou, Y. *Toxicol. Sci.* **2003**, *74*, 279-286.

(102) Chen, H.; Ke, Q.; Kluz, T.; Yan, Y.; Costa, M. *Mol. Cell. Biol.* **2006**, *26*, 3728-3737.

(103) Broday, L.; Peng, W.; Kuo, M.-H.; Salnikow, K.; Zoroddu, M.; Costa, M. *Cancer Res.* **2000**, *60*, 238-241.

(104) Yan, Y.; Kluz, T.; Zhang, P.; Chen, H.-b.; Costa, M. *Toxicol. Appl. Pharmacol.* **2003**, *190*, 272-277.

(105) Ke, Q.; Li, Q.; Ellen, T. P.; Sun, H.; Costa, M. *Carcinogenesis* **2008**, *29*, 1276-1281.

(106) Sun, H.; Zhou, X.; Chen, H.; Li, Q.; Costa, M. *Toxicol. Appl. Pharmacol.* **2009**, *237*, 258-266.

(107) Xia, B.; Yang, L.-q.; Huang, H.-y.; Pang, L.; Hu, G.-h.; Liu, Q.-c.; Yuan, J.-h.; Liu, J.-j.; Xia, Y.-b.; Zhuang, Z.-x. *Toxicol. Lett.* **2011**, *205*, 140-145.

(108) Bae, Y.; Fukushima, S.; Harada, A.; Kataoka, K. *Angewandte Chemie International Edition* **2003**, *42*, 4640-4643.

(109) Ji, X.; Yao, Y.; Li, J.; Yan, X.; Huang, F. *J. Am. Chem. Soc.* **2013**, *135*, 74-77.

(110) Daniel, M.-C.; Astruc, D. *Chem. Rev.* **2004**, *104*, 293-346.

(111) Ma, X.; Zhao, Y. *Chem. Rev.* **2015**, *115*, 7794-7839.

(112) Daze, K. D.; Pinter, T.; Beshara, C. S.; Ibraheem, A.; Minaker, S. A.; Ma, M. C. F.; Courtemanche, R. J. M.; Campbell, R. E.; Hof, F. *Chemical Science* **2012**, *3*, 2695-2699.

(113) Beshara, C. S.; Jones, C. E.; Daze, K. D.; Lilgert, B. J.; Hof, F. *Chembiochem* **2010**, *11*, 63-66.

(114) McGovern, R. E.; Snarr, B. D.; Lyons, J. A.; McFarlane, J.; Whiting, A. L.; Paci, I.; Hof, F.; Crowley, P. B. *Chem Sci* **2015**, *6*, 442-449.

(115) Garnett, G. A. E.; Starke, M. J.; Shaurya, A.; Li, J.; Hof, F. *Anal. Chem.* **2016**, *88*, 3697-3703.

(116) Gamal-Eldin, M. A.; Macartney, D. H. *Org. Biomol. Chem.* **2013**, *11*, 488-495.

(117) Rakow, N. A.; Suslick, K. S. *Nature* **2000**, *406*, 710.

(118) Star, A.; Joshi, V.; Skarupo, S.; Thomas, D.; Gabriel, J.-C. P. *The Journal of Physical Chemistry B* **2006**, *110*, 21014-21020.

(119) Machado, R. F.; Laskowski, D.; Deffenderfer, O.; Burch, T.; Zheng, S.; Mazzone, P. J.; Mekhail, T.; Jennings, C.; Stoller, J. K.; Pyle, J. *Am. J. Respir. Crit. Care Med.* **2005**, *171*, 1286-1291.

(120) Zhang, C.; Suslick, K. S. *J. Am. Chem. Soc.* **2005**, *127*, 11548-11549.

(121) Zhang, C.; Suslick, K. S. *J. Agric. Food Chem.* **2007**, *55*, 237-242.

(122) Minaker, S. A.; Daze, K. D.; Ma, M. C. F.; Hof, F. *J. Am. Chem. Soc.* **2012**, *134*, 11674-11680.

(123) Peacor, B. C.; Ramsay, C. M.; Waters, M. L. *Chemical Science* **2017**, *8*, 1422-1428.

Chapter 2 Fluorescence Detection of Glucose and Cholesterol Based on ZnS/CuS Nanocomposite Hybrid Microgel Particles

Introduction

Diabetes mellitus is becoming a worldwide heath problem nowadays due to increasing obesity,[1] unhealthy lifestyle[2] and physical inactivity[3] among people. The diagnostic of diabetes is of pivotal importance since the consequence will cause serious lifelong influence on patients. Confirmation of diabetes needs at least one test result showing blood glucose level within the diabetic range.[4] And it is common that re-testing would be done later if previous result could not be achieved. Cholesterol is a major structural molecule of cell membranes, and is a precursor for biosynthesis of steroid hormones and vitamin D. Maintaining a proper level of cholesterol is essential for human health. It has been reported that high blood cholesterol level can increase the risk of atherosclerosis[5] and cardiovascular disease,[6] while low cholesterol concentration may lead to hypocholesterolemia, and finally cause hemorrhagic stroke.[7]

Numerous useful and interesting analytical methods were developed to determine concentrations of glucose and cholesterol, including colorimetric, fluorescent,[8] luminescence, electrochemical, surface plasma resonance, etc. Among these techniques, fluorescent detection was of great interest due to low cost, high sensitivity and easily applied for *in vitro* and *in vivo* detection. Depending on fluorescent compounds, fluorescent method can be further classified into organic fluorescent dye based and nanodots based (quantum dots, carbon dots, polymer dots). To achieve the fluorescence "turn-on" or "turn-

off', both enzymatic and non-enzymatic methods were developed. Enzymatic methods are extremely popular in this filed due to the two powerful enzymes, glucose oxidase and cholesterol oxidase. Oxygen consumption and hydrogen peroxide production from oxidation reaction were used as targets of analysis.

Microgels are small colloidal microspheres with porous hydrogel structure inside, and usually have diameters less than 1 μm. Microgel based techniques are becoming popular for applications in drug delivery, sensing and smart emulsifiers, due to advantages, including ease of fabrication, low cost, high biocompatibility, versatility and stimuli responsive. To further introduce optical, magnetic, catalytic and responsive features to microgel, inorganic small nanoparticles like gold, silver and iron oxide were loaded. In-situ synthesis of inorganic nanoparticles, including palladium, silver, cadmium sulfide and iron oxide, inside a microgel network has been reported. In-situ synthesis is more convenient to achieve a homogeneous distribution of inorganic nanoparticles and provide protection of these particles inside the microgel network.

In this paper, we designed a ZnS/CuS nanocomposite hybrid microgels and showed its high sensitivity in detection of glucose and cholesterol through oxidase catalyzed releasing of H_2O_2. *NIPAM-co-AA* microgel was first synthesized through radical polymerization of N-isopropylacrylamide (NIPAM) and acrylic acid (AA) with bis-acrylamide (BIS) as a crosslinker. In-situ synthesis of ZnS nanocluster or ZnS/CuS nanocomposite was achieved through adding Na_2S into Zn^{2+} and Cu^{2+} incorporated microgel. The strong coordination between the carboxyl groups in microgel and the sulfide nanoparticle could prevent unwanted leaking of nanoparticles. H_2O_2 as an oxidizing reagent was discovered to be able

to release Zn^{2+} from the sulfide nanocomposite, which will be captured immediately by Fluozin-3 (zinc specific turn-on fluorescent dye) and emit strong fluorescence. Furthermore, we show that ZnS/CuS nanocomposite microgel has better performance over ZnS. This method was successfully applied to H_2O_2 monitoring, serum glucose and cholesterol detection, and showed excellent analytical performance.

Scheme 2.1. Glucose and Cholesterol detection based on ZnS/CuS nanocomposite hybrid microgel.

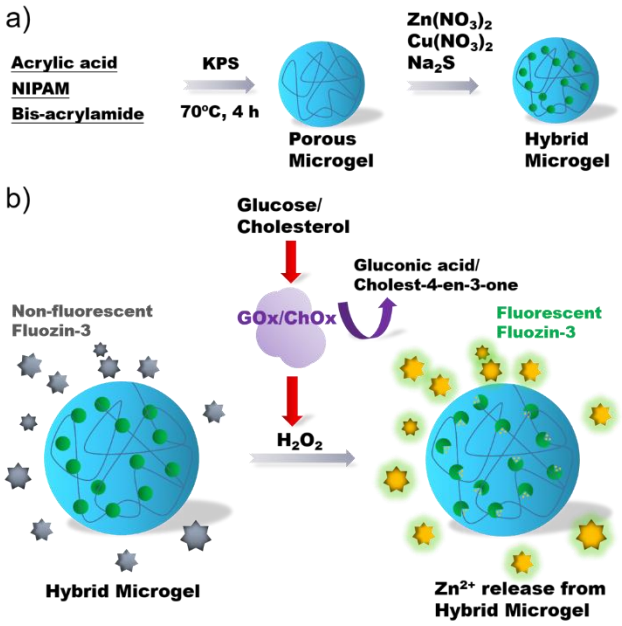

Results and discussion

Microgel particles with high density of carboxyl groups were first prepared by emulsion polymerization (Scheme 2.1), which serve as a perfect microreactor for in situ synthesis of small nanoparticles. The network structure (with voids between) can help both the nucleation and growth of the nanoparticles, and limit the nanoparticles to small sizes (less than 10 nm). The nanoparticles in the synthesized microgel also show much better stability comparing with nanoparticles prepared by other in solution methods with surface blocking and coating reagents. Meanwhile, the network will prevent large biomolecules, such as proteins and DNAs to penetrate, which is very useful feature when doing in situ sensing of complex biological media. In this design, H_2O_2 can easily diffuse through the gel network and release the Zn^{2+}, and fluozin-3 dye can be turned on upon binding with Zn^{2+}.

The synthesized ZnS hybrid microgel has an average diameter of 271.6 nm (Figure S2.1), while inner nanoparticles were clearly observed with diameters less than 5 nm (Figure 2.1), and no free external nanoparticles were observed. Previously, we have shown that the size of ZnS nanoclusters affects the efficiency of Zn^{2+} releasing by Ag^{+} cation exchange, and smaller sized nanoparticles show better efficiency.[11] However, even that is the case, for 44 nM ZnS nanoparticles, a microwave assisted process is still quite needed to reach an efficiency of 71.0%. A quick cation exchange test shows that this new ZnS hybrid microgel would reach almost complete exchange (95.2%) without any assistance (Table S2.1). Smaller size (~5 nm) surely play a role here, and another important factor is nanoparticle structure. Synthesis of nanoparticles in a microgel structure does not go through a high pressure hydrothermal process which makes the nanoparticle packed less dense and were more accessible by Ag^{+}. And the stability of ZnS microgel was tested, which shows no loss of Zn^{2+} for at least one week (Figure S2.2).

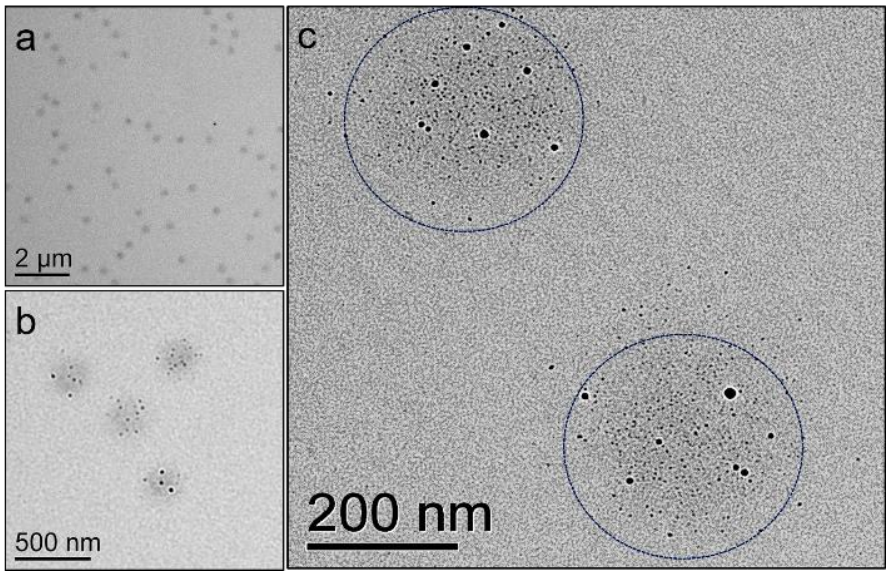

Figure 2.1 TEM images of ZnS hybrid microgel with different amplification power. The blue circled area in (c) is to show the enclosed nanoparticles inside the microgel.

ZnS microgel was first used for H_2O_2 detection. As Demonstrated in Figure 2.2a, an encouraging signal increase of fluozin-3's was first observed for ZnS microgel with the increase of H_2O_2. And for 80 mM of H_2O_2, the fluorescence signal was the same as cation exchange by Ag. This means H_2O_2 can achieve a complete releasing of Zn^{2+} from ZnS nanoparticles. We also tested the performance of ZnS nanoparticles with a diameter of 11.5±2.7 nm, which shows a similar performance (Figure 2.2b). We argue that zinc releasing is probably due to oxidation of sulfide by H_2O_2. Sulfide is a reducing reagent that can be oxidized by oxidizing reagent into S^0 and then SO_4^{2-} depending on the concentration and redox potential of oxidizing reagent (Equation 1 & 2).[12-14] This same zinc releasing were also observed for ZnSe nanoparticles (~5 nm diameter) (Figure S2.3).[10] ZnSe is more sensitive to H_2O_2, and the fluorescence signal saturated at much lower concentrations (800

μM) comparing to ZnS. This is because Se^{2-} process much greater reducing power than S^{2-} and can be easily oxidized to Se^0 when oxidants present.[15,16]

$$S^{2-} + 4\,H_2O_2 + 2\,H^+ \rightarrow S + 4\,H_2O \quad (1)$$

$$S^{2-} + 4\,H_2O_2 \rightarrow SO_4^{2-} + 4\,H_2O \quad (2)$$

Inspired by the oxidation based releasing phenomenon, we further added Cu^{2+} to the hybrid microgel during synthesis. We hypothesized that Cu^{2+} can enhance the sensitivity of H_2O_2 detection owing to the fact that Cu is a redox-active metal which can catalyze the formation of hydroxyl radicals (OH•) upon mixing with H_2O_2. OH• is a much stronger oxidation reagent with an oxidation potential of 2.8 V, while H_2O_2 has a value of 1.78 V. However, OH• has very short half-life (approximately 10^{-9} seconds) and a high reactivity, which means it could not diffuse far away from its site of generation. Therefore, the colocalization of Cu^{2+} with ZnS will be very important here. We synthesized ZnS/CuS nanocomposite hybrid microgels with different concentrations of Cu^{2+}, from 1% to 50% of Zn^{2+}. The performance of H_2O_2 detection was shown in Figure 2.3. 1% ZnS/CuS microgel (Figure 2.3 black) showed the best performance, and the detection limit was much lower than ZnS microgel. However, as increasing of Cu^{2+} ratio to 5% and 10% (Figure 2.3 red & blue), the performance dropped significantly. And the detection ability was completely lost at 50% ratio microgel.

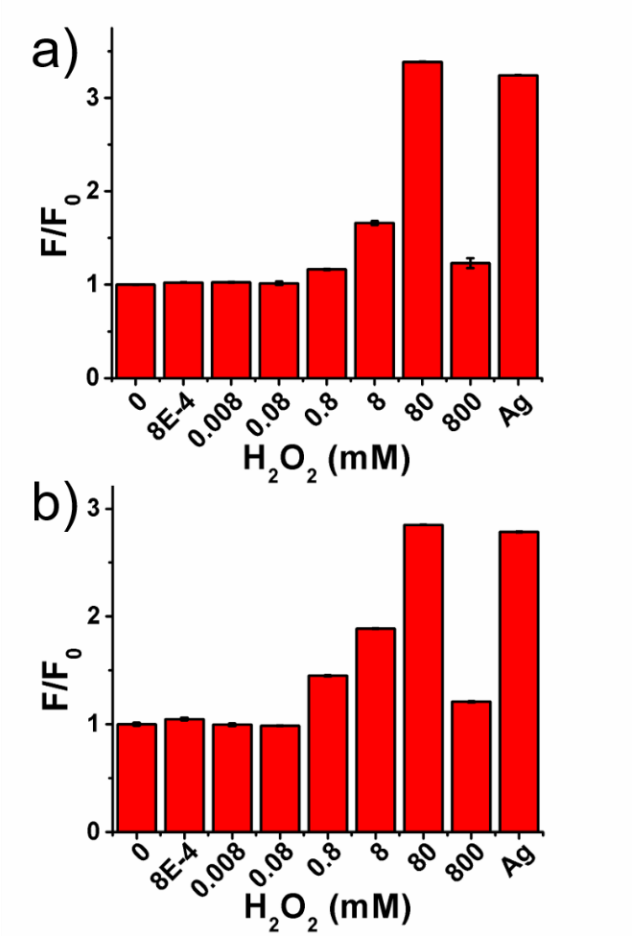

Figure 2.2 Fluorescence enhancement of a) ZnS hybrid microgel b) ZnS nanoparticles with addition of H_2O_2 and $AgNO_3$ [Fluozin-3] = 3 µM, PBS buffer, pH = 7.4, [$AgNO_3$] =100 µM.

To elucidate this phenomenon, we measured Zn and Cu concentration inside the microgel by first dissolving the metal sulfide with nitric acid and then quantifying with ICP-AES. The results (Figure S2.4) clearly indicated that along increasing of Cu ratio, the Cu concentration increased while the Zn concentration dropped significantly. This is not surprising result, because the stability constant of Cu^{2+} with monocarboxylic acids and several dicarboxylic acids were always larger than Zn^{2+}, which means the binding between Cu^{2+} and microgel will be stronger than Zn^{2+}.[17] Since the binding sites are limited, when

reaching equilibrium, more sites will be occupied by Cu^{2+}. The other reason could be due to the fact that CuS has much lower solubility ($K_{sp} = 1 \times 10^{-36}$) comparing with ZnS ($K_{sp} = 1 \times 10^{-23}$), which means it would be more stable during dialysis process.

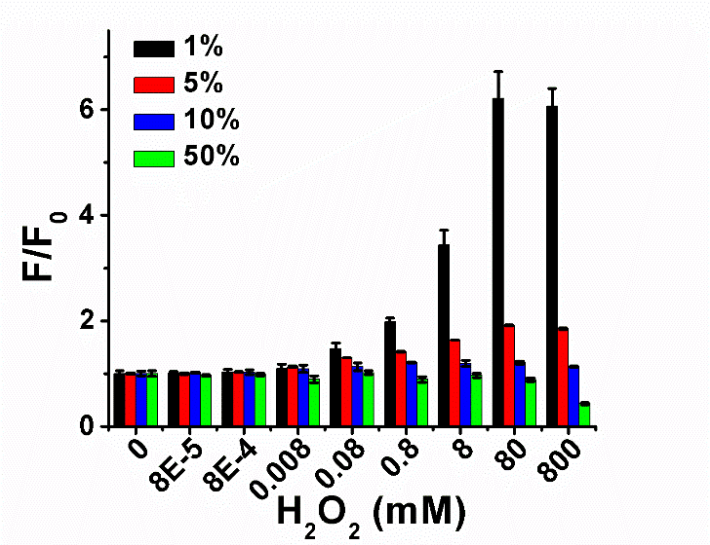

Figure 2.3 Fluorescence enhancement of ZnS/CuS nanocomposite with different ratios. [Fluozin-3] = 3 μM, PBS = 10 mM, pH = 7.4.

To find out if there are indeed OH• formation during the oxidation releasing of ZnS/CuS nanocomposite microgels. ABEI-H_2O_2 chemiluminescence (CL) system was adopted here to quantify the formation of OH•.[18] CL of the ABEI-H_2O_2 can be greatly enhanced when oxygen-related radicals such as OH•, $O2^{\bullet-}$ presents[19,20] As shown in Figure S2.5, CL intensity increased along with Cu ratio. And the CL intensity of no microgel control and ZnS microgel was nearly the same, however, CL intensity of 1% ZnS/CuS microgel was about 2.4 times of ZnS microgel, which indicates even with 1% copper, there are still much more OH• generated. This explains why 1% ZnS/CuS microgel is more sensitive towards H_2O_2.

Another important question is how the hybrid microgel respond to different oxidation reagents. Several of them were tested for ZnS microgel (Figure 2.4a) first, and it turned out that only ClO^- can induce a fluorescence turn-on. However, for 1% ZnS/CuS microgel

(Figure 2.4b), H_2O_2 and KO_2 also showed on fluorescence increase. And interestingly, Fenton reaction (Fe^{2+} & H_2O_2) did not show any effects and this is possibly due to the short half-life of OH•, which could not reach the nanoparticles before it is reduced. Glucose and iron species also did not show any effects.

To improve the performance of H_2O_2 detection further, Ethylenediaminetetraacetic acid (EDTA), a strong metal cation chelating agent, was added to the solution to lower down the background signal and enhance the signal to noise ratio. As shown in Figure S2.6, a great enhancement of S/N ratio was observed upon adding only 1 μM of EDTA. We further optimized the EDTA concentration, and 3 μM EDTA showed the best performance (S/N ratio) and was chosen for later studies (Figure S2.7). The calibration curve of H_2O_2 was shown in Figure 2.5. The detection limit was calculated to be ~80 nM, and the dynamic range is between 80 nM and 8 mM.

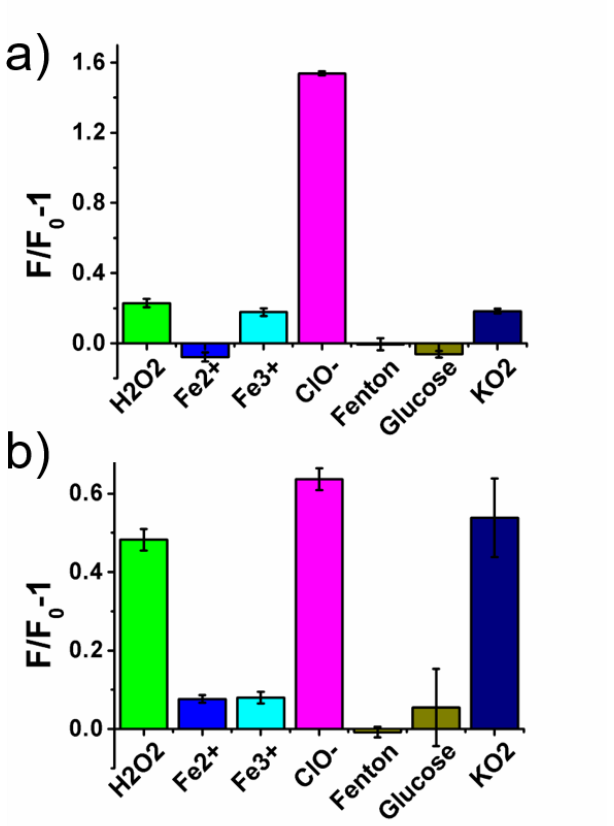

Figure 2.4 Specificity of a) ZnS hybrid microgel and b) 1% ZnS/CuS microgel with addition of different regents. [Fluozin-3] = 3 μM, PBS buffer, pH = 7.4, [All reagents] = 10 μM. For Fenton reaction, 10 μM of Fe^{2+} and 10 μM H_2O_2 was used, and KO_2 was used to generate $O2^{-\bullet}$.

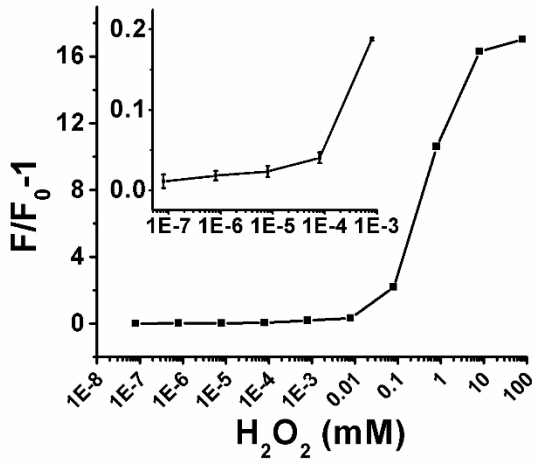

Figure 2.5 Calibration curve of 1% ZnS/CuS microgel with H_2O_2. [EDTA] = 3 μM.

GOx is a highly efficient oxidase, which oxidize glucose and release H_2O_2 as a by-product. By monitoring the concentration of H_2O_2, glucose level was able to be measured. Some necessary optimization was done first, including optimization of enzyme reaction time (Figure S2.8a) and enzyme concentration (Figure S2.8b). And it was found that 2 μg/mL GOx with 30 minutes' reaction time was the best reaction condition. The performance of glucose was determined by using 0-10 mM glucose solution in 1 x PBS buffer with optimum reaction condition (30 mins, 37 ºC) (Figure 2.6a). The inset shows the linear range is 0-1 mM, and the equation is $F/F_0-1 = 5.9[\text{glucose}]+1.1$, with $R^2 = 0.99$. And the detection limit calculated by three times standard deviation was 0.53 μM. To demonstrate our method's ability to do in situ monitoring of GOx activity, the time dependent enzyme reactions were carried out for 30 minutes with varying substrate concentrations (Figure 2.6b). The Michaelis–Menten constant K_m was calculated to be 0.54 mM using Lineweaver-Burke plot.[21]

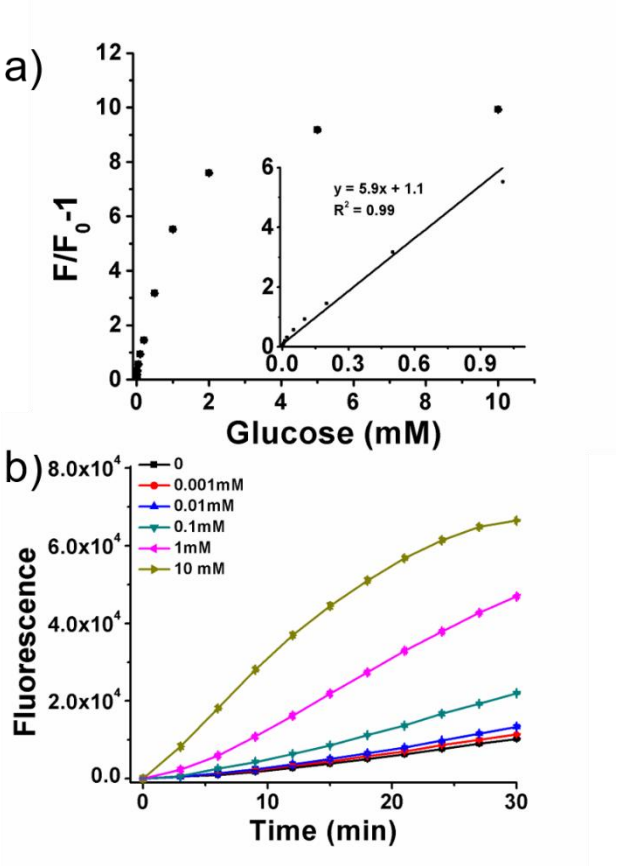

Figure 2.6 Calibration curve and continuous monitoring of GOx activity with 1% ZnS/CuS microgel. a) calibration curve of glucose with increasing concentration. b) continuous monitoring of GOx activity with different concentrations of glucose, from 0 to 10 mM.

Cholesterol measurement is complicated by the fact that cholesterol has poor solubility in aqueous buffer. Nonionic surfactants TX-100 was used here to improve the solvability. To dissolve the cholesterol, 5% TX-100 was first prepared in 1x PBS buffer, and a final concentration of 5 mM of cholesterol solid was added into the solution. And A10 minutes' incubation in a 70 ºC water bath was needed to make the cholesterol fully dissolved. The as prepared solution was diluted 10 times into 1x PBS (with 0.5% TX-100), and used for ChOx based reaction. We further optimized the EDTA concentration, since an large increase in background signal was observed when TX-100 was added. And increasing the

EDTA concentration to 6 μM will give a comparable signal to noise ratio as before (Figure S2.9). ChOx is quite like GOx, which oxidize cholesterol into cholest-4-en-3-one and produce H_2O_2 at the meantime. Due to the low solubility of cholesterol, a lower range of concentration (0-500 μM) was analyzed (Figure 2.7a). The linear range of cholesterol detection is 0-500 μM, and the equation is $F/F_0-1 = 0.017[\text{cholesterol}]+1.19$, with $R^2 = 0.98$. And the detection limit calculated by three times standard deviation was 0.77 μM. Similarly, our method could be applied to measurement of the enzyme activity of ChOx (Figure 2.7b). The K_m value was calculated to be 0.07 mM.

We further applied the ZnS/CuS hybrid microgel to quantify glucose and cholesterol concentration in human serum samples. Five serum samples with glucose concentration between 2.94 mM and 25.4 mM were measured, and our results showed a good matching with values provided on the products information (Table S2.2). And five cholesterol samples (total cholesterol 1.94 – 10.98 mM) were also chosen. To test the total cholesterol level in serum, another enzyme ChEx was used first to hydrolyze cholesterol esters in serum and then coupled with ChOx based detection. The results were also shown in Table S2.2.

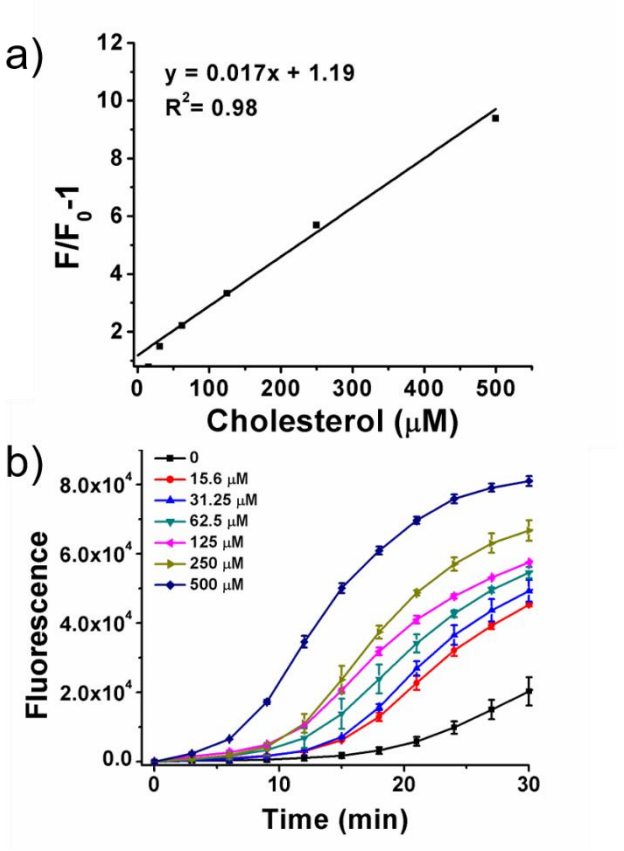

Figure 2.7 Calibration curve and continuous monitoring of ChOx activity with 1% ZnS/CuS microgel. a) calibration curve of Cholesterol with increasing concentration. b) continuous monitoring of ChOx activity with different concentrations of cholesterol, from 0 to 10 μM.

Conclusion

To summarize, we have designed a unique ZnS/CuS hybrid microgel system based on H_2O_2 triggered release of Zn^{2+}, which can illuminate the Fluozin-3 dye and shows a fluorescence turn-on. And adding a small amount of Cu into the ZnS microgel will greatly improve the performance of the system due to the formation of strong OH•. With all these improvements made, we were able to achieve a good detection limit and broad detection range of both glucose and cholesterol. And finally, the serum samples were measured and

showed great accuracy. And we expect this research could be possibly adopted to other fields of diagnostics with minor modification.

Experimental section

Materials. N-isopropylacrylamide (NIPAM), Acrylic acid (AA), bis-acrylamide (BIS), potassium persulfate (KPS), H_2O_2, $Zn(NO_3)_2$, $Cu(NO_3)_2$, Na_2S, H_2O_2, N-(aminobutyl)-N-(ethylisoluminol) (ABEI), D-glucose, Cholesterol, glucose oxidase (GOx), cholesterol oxidase (ChOx) and cholesterol esterase (ChEx) were purchased from Sigma-Aldrich, Inc. (Saint Louis, MO). $Ag(NO_3)$ and Sodium dodecyl sulfate (SDS) were purchased from Fisher Scientific (Waltham, MA). Human serum samples were purchased from Discovery Life Sciences Inc. and stored at -80ºC until use (Los Osos, CA). All chemicals were analytical regent grade and used without further purification. Ultrapure water with electric resistance > 18.2MΩ was produced by the Milipore Milli-Q water purification system (Billerica, MA).

Synthesis of microgel. Microgel was synthesized according to literature[9] with modifications. Briefly, 0.305 g NIPAM, 0.097 g AA, 0.03 g SDS and 4% (of total monomer) BIS were dissolved in 45 mL of ultrapure water inside a three-neck flask. The solution was purged with high purity nitrogen for 30 mins at room temperature and then the temperature was increased to 70 ºC. Freshly prepared KPS solution (0.01g in 5 mL) was added quickly to the flask and the solution was kept stirring for 4 hours at 70 ºC. A milk colored solution appeared after 4 hours, which is the synthesized microgel particles. The solution was dialyzed against ultrapure water with a 12-14 kD Spectra/Por molecularporous membrane tubing (Spectrum labs Inc., Rancho Dominguez, CA) to

remove nonreacted monomers and residual SDS for 2 days with changing of water every 4 hours. The gel solution was kept at room temperature until use.

Synthesis of ZnS and ZnS/CuS nanocomposite hybrid microgel. $COOH^-$ group of microgel solution was first determined by acid base titration. 3 mL above microgel solution was diluted 9 times into ultrapure water (final $[COOH^-]$ = 3 mM). Then $Zn(NO_3)_2$ and $Cu(NO_3)_2$ was added into above microgel solution very quick well stirring. The final molar ratio of Zn^{2+}: $COOH^-$ = 1:2, with varying Cu^{2+} ratio (from 0 to 50% of Zn^{2+}). pH was adjusted with 1 M KOH to finally 6.8 to ensure better coordination. After overnight incubation, above solution was dialyzed with water for 24 hours to remove unbounded metal ions. On the following day, Na_2S was added with a final concentration of 3 mM and the reaction continued for 2 hours at room temperature. Final product was dialyzed again for 24 hours to remove unreacted Na_2S and stored at room temperature. The hybrid microgels were characterized by TEM and NTA (Nanoparticles Tracking Analysis).

Synthesis of ZnS and ZnSe nanoparticles. Water soluable ZnS and ZnSe nanoparticles were fabricated according to our previous researches [10,11] and the size was determined by DLS.

ABEI-H_2O_2 chemiluminescence detection. 100 µM ABEI and different microgel solutions (ZnS and different ratios of ZnS/CuS microgel) were first mixed in pH 10 water solution. The chemiluminescence signal was acquired by a Promega GloMax-Multi+ Microplate Multimode Reader with online injection system. CL was measured immediately upon injection of H_2O_2. The injection rate is kept 500 µL/s for all measurements.

ICP-AES analysis. Inductively Coupled Plasma - Atomic Emission Spectrometer (ICP-AES) (Norwalk, CT) was employed to verify the quantities of Zinc and Copper concentration in microgels. The samples were treated with 10% HNO_3 before analysis. The instrument was first rinsed with 10% HNO_3 before injection. Standard solutions and all samples were measured in triplicate.

H_2O_2 measurements. Measurements was carried out in 96-well microplates. First, 10 µL of hybrid microgel was added into each well; then, 70 µL of H_2O_2 in PBS buffer (1x) was added and incubate for 15 minutes; Finally, 20 µL of Fluorezin-3 (final concentration 3 µM) with or without EDTA was added and mix for 5 minutes on a plate shaker. The plate was read on a fluorescence plate reader (Perkin Elmer Wallac 1420 Victor 2 Microplate Reader with the Ex/Em wavelengths at 485/530 nm).

Glucose and cholesterol measurement. Detection of glucose was done in two ways: separate reaction and one pot reaction. For separate reaction, glucose stock solution in water (50 mM) was diluted into PBS buffer (1x) and GOx was added to a final concentration of 2 µg/mL. After 30 minutes' reaction at 37 ºC, the solution was added into 1% ZnS/CuS hybrid microgel and measured similarly like H_2O_2 detection. The one pot reaction was carried out by adding microgels, glucose and GOx all in one well and fluorescence was recorded every 3 minutes on a plate reader.

Cholesterol detection was quite similar as glucose detection. Cholesterol stock solution was prepared by adding cholesterol solid (5 mM) into TX-100 solution (5%, v/v). A 5 minutes' incubation on 70ºC water bath is necessary for fully dissolving cholesterol. The measurements were also done in two ways as glucose. And a constant 0.5% TX-100 was

added to keep the cholesterol from precipitation. ChOx concentration is 20 μg/mL through all the experiments.

Serum sample measurement. For glucose detection, serum was first diluted 50 times into PBS, then GOx was added and after 30 minutes' incubation, the solution was filtered through a 3 kD ultra centrifugation filter with 10,000 g for 15 minutes. The filtration was tested by 1% ZnS/CuS hybrid microgel. As to cholesterol detection, serum was first diluted 50 times. ChEx and ChOx were both added to the serum and after 30 minutes, the solution was filtered and detected similarly as glucose.

Reference

(1) Lazar, M. A. *Science* **2005**, *307*, 373-375.

(2) Mozaffarian, D.; Peñalvo, J. L. *Am. J. Kidney Dis.*, *68*, 1-4.

(3) American Diabetes, A. *Clinical Diabetes : A Publication of the American Diabetes Association* **2015**, *33*, 97-111.

(4) Alberti, K. G.; Zimmet, P. Z. *Diabet. Med.* **1998**, *15*, 539-553.

(5) Wilson, P. W. F.; D'Agostino, R. B.; Levy, D.; Belanger, A. M.; Silbershatz, H.; Kannel, W. B. *Circulation* **1998**, *97*, 1837-1847.

(6) Jackson, R.; Lawes, C. M. M.; Bennett, D. A.; Milne, R. J.; Rodgers, A. *The Lancet* **2005**, *365*, 434-441.

(7) Orken, D. N.; Kenangil, G.; Uysal, E.; Gundogdu, L.; Erginoz, E.; Forta, H. *Clin. Neurol. Neurosurg.* **2010**, *112*, 668-671.

(8) Ma, J.-L.; Yin, B.-C.; Wu, X.; Ye, B.-C. *Anal. Chem.* **2017**, *89*, 1323-1328.

(9) Zhang, J.; Xu, S.; Kumacheva, E. *J. Am. Chem. Soc.* **2004**, *126*, 7908-7914.

(10) Yao, J.; Schachermeyer, S.; Yin, Y.; Zhong, W. *Anal. Chem.* **2011**, *83*, 402-408.

(11) Yao, J.; Han, X.; Zeng, S.; Zhong, W. *Anal. Chem.* **2012**, *84*, 1645-1652.

(12) Chavda, A.; Patel, M.; Mukhopadhyay, I.; Ray, A. *ACS Sustainable Chemistry & Engineering* **2016**, *4*, 2302-2308.

(13) Hasani, M.; Koleini, S. M. J.; Khodadadi, A. *Journal of Mining and Environment* **2016**, *7*, 1-12.

(14) Aydogan, S. *Chem. Eng. J.* **2006**, *123*, 65-70.

(15) Kang, M.; Chen, F.; Wu, S.; Yang, Y.; Bruggeman, C.; Charlet, L. *Environ. Sci. Technol.* **2011**, *45*, 2704-2710.

(16) Breynaert, E.; Scheinost, A. C.; Dom, D.; Rossberg, A.; Vancluysen, J.; Gobechiya, E.; Kirschhock, C. E. A.; Maes, A. *Environ. Sci. Technol.* **2010**, *44*, 6649-6655.

(17) Motoo, Y.; Kazuo, Y.; Hitoshi, O. *Bull. Chem. Soc. Jpn.* **1960**, *33*, 1067-1070.

(18) Liu, M.; Zhang, H.; Shu, J.; Liu, X.; Li, F.; Cui, H. *Anal. Chem.* **2014**, *86*, 2857-2861.

(19) Cui, H.; Zhang, Z.-F.; Shi, M.-J. *The Journal of Physical Chemistry B* **2005**, *109*, 3099-3103.

(20) Zhang, Z.-F.; Cui, H.; Lai, C.-Z.; Liu, L.-J. *Anal. Chem.* **2005**, *77*, 3324-3329.

(21) Wu, P.; He, Y.; Wang, H.-F.; Yan, X.-P. *Anal. Chem.* **2010**, *82*, 1427-1433.

Supporting information

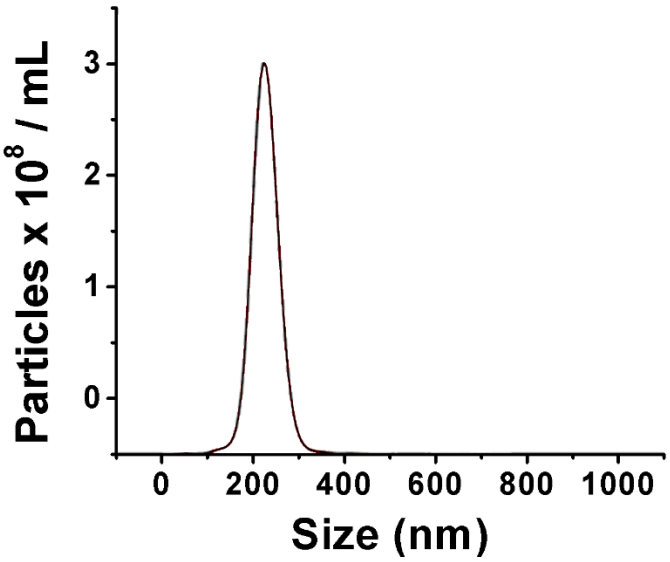

Figure S2.1 NTA measurements of size of ZnS microgel particles.

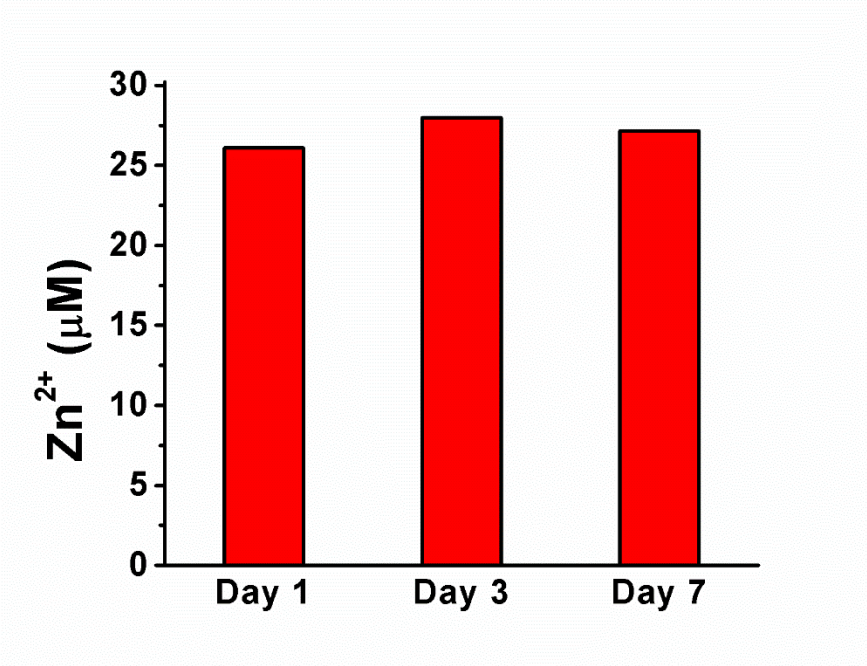

Figure S2.2 Stability of ZnS microgel. ZnS microgel was kept in PBS buffer and measurements were made on day 1, day 3 and day 7. The ZnS microgel was first washed three times (through a 30 kD filter) and measurements were done with Fluozin-3 and Ag.

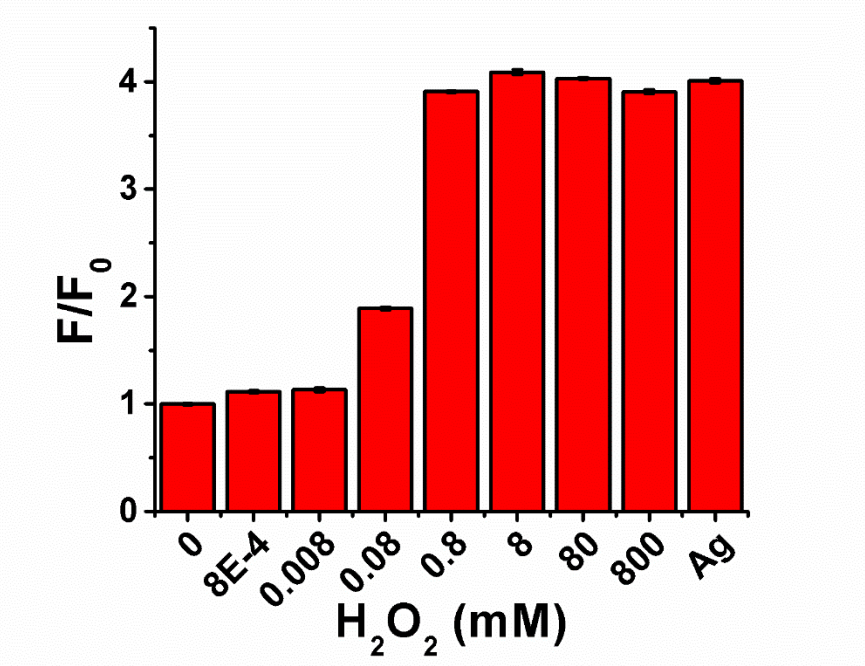

Figure S2.3 Fluorescence of ZnSe upon addition of H2O2. [Fluozin-3] = 3 μM, PBS buffer, pH = 7.4.

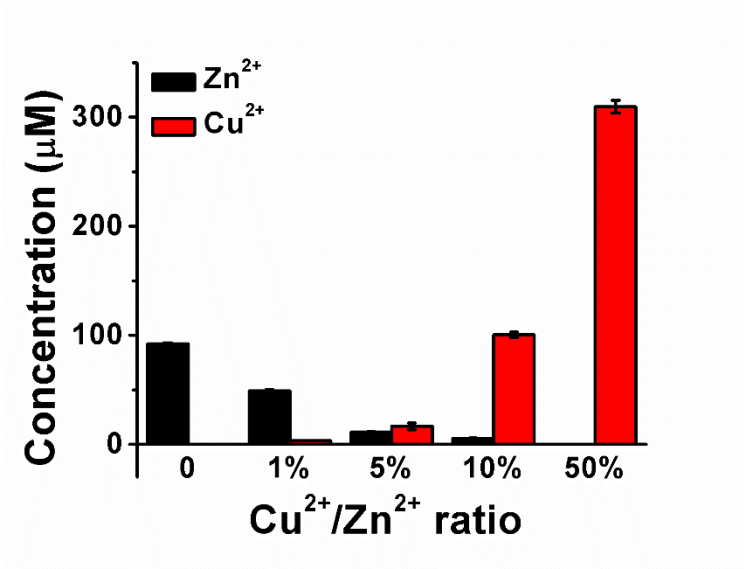

Figure S2.4 ICP-AES quantification of metal concentration in hybrid microgel with different Cu^{2+}/Zn^{2+} ratio.

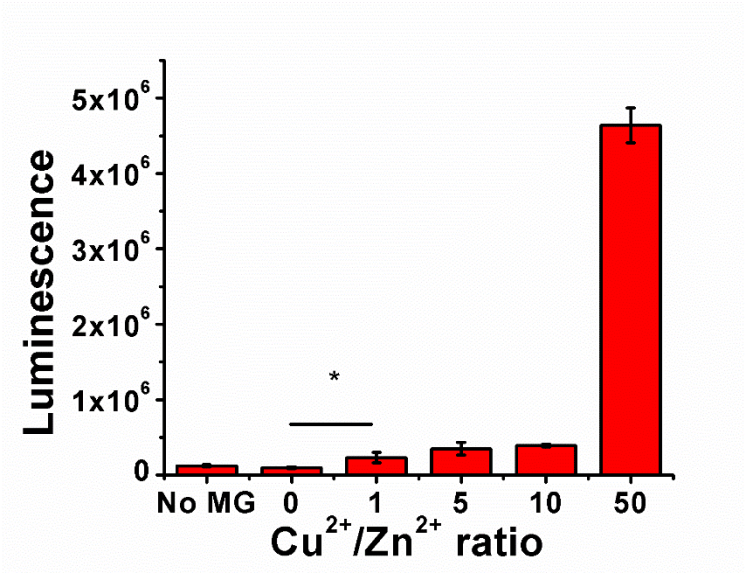

Figure S2.5 Chemiluminescence of different microgels with H_2O_2 and ABEI. [H_2O_2] = 1 mM, [ABEI] = 0.1 mM.

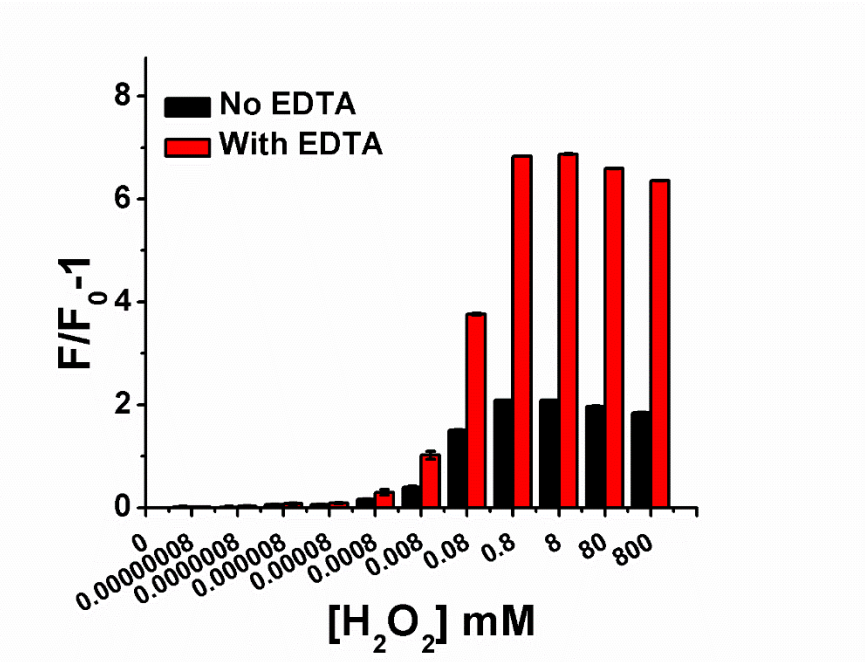

Figure S2.6 Fluorescence ratio change of 1% ZnS/CuS microgel upon adding H_2O_2 with and without the presence of EDTA. [EDTA] = 1 μM.

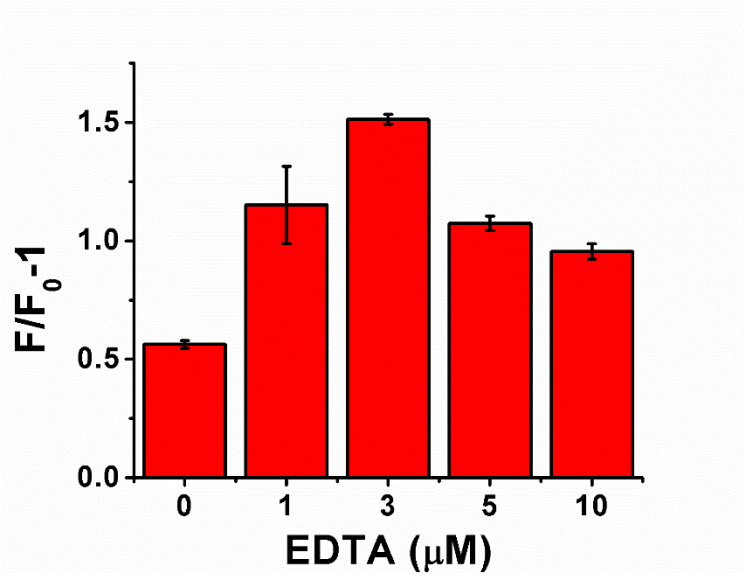

Figure S2.7 Fluorescence enhancement ratio (F/F_0-1) in response of H_2O_2 with different EDTA concentration. [H_2O_2] = 80 μM.

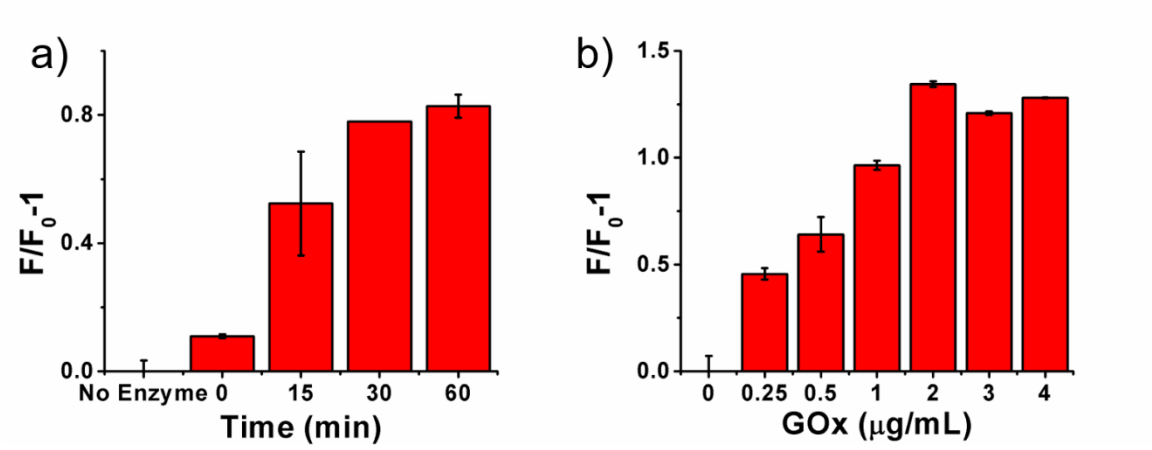

Figure S2.8 Time and enzyme concentration optimization. a) Fluorescence ratio change of 1% ZnS/CuS microgel with different enzyme reaction time. [GOx] = 1 μg/mL b) Fluorescence ratio change of 1% ZnS/CuS microgel with different GOx concentration, reaction time = 30 minutes.

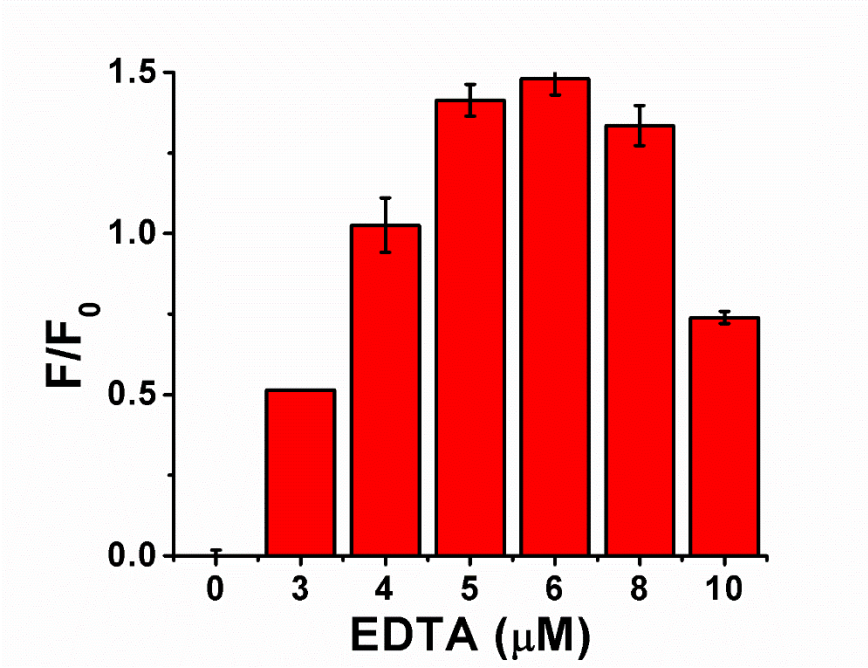

Figure S2.9 EDTA optimization for cholesterol detection.

Table S2.1 Cation exchange efficiency of ZnS microgel with addition of $AgNO_3$. Results obtained by ICP-AES.

	Total	**Cation exchange (100uM Ag)**	**Efficiency**
Zn^{2+}	27.41 µM	26.10 µM	95.2%

Table S2.2 Serum detection of glucose and cholesterol

Sample	Product Info. (Glucose mM)	This method (Glucose mM)	RSD
1	5.83	6.93	4.44%
2	25.4	25.86	1.79%
3	2.94	3.74	6.53%
4	16.11	17.61	4.07%
5	10.39	11.44	6.57%
Sample	Product Info. (Cholesterol mM)	This method (Cholesterol mM)	RSD
6	1.94	2.03	1.79%
7	3.37	3.87	1.08%
8	6.14	5.45	8.55%
9	10.98	11.08	1.08%
10	8.8	8.13	6.92%

Chapter 3 A Self-Aggregating Deep Cavitand Acts as a Fluorescence Displacement Sensor for Lysine Methylation

Introduction

The diversity of proteins in living cells is greatly increased by post-translational modifications (PTMs).[1] Histone modifications such as methylation play important roles in regulation of gene transcription, strongly impacting cellular development, and they also respond to different stimulations leading to the development of pathological conditions.[2] Monitoring PTM changes in cells is essential in epigenetics and systems biology for better understanding of the regulation mechanisms of cellular processes,[3] and for the treatment of diseases associated with epigenetic disruption.[4] Understanding how PTMs affect cell function and disease requires unambiguous detection of specific PTMs in complex mixtures, which remains a significant technical challenge, especially in a format amenable to automated high-throughput screening. Assays that employ antibodies[5a], commonly with radioisotope tagging,[5b] are available to detect methylation on peptides, but few are able to discriminate between mono- and dimethylated or di- and trimethylated residues, or to differentiate between closely related PTM sites. Moreover, immunodetection methods are cumbersome, especially in a high throughput environment.[6]

Synthetic receptors are an inviting solution to this problem, and there has been some elegant work recently published on the use of designed host molecules that bind to protein PTMs. The most notable targets are methylated lysine residues, which are substrates for simple receptors such as tetrasulfonatocalix[4]arene (CX4)[7] and cucurbit[7]uril (CB7)[8] as

well as more selective receptors designed either rationally[9] or through dynamic combinatorial selection.[10] The recognition of protein PTM targets often uses classical analytical techniques such as NMR and ITC: applications to sensing technologies require alternate readouts. The most common method for protein PTM sensing is indicator displacement assays,[7,11,12] which mainly exploit CX4 and CB7. These electron-rich cyclophanes and calixarenes cause charge-transfer induced quenching of the complexed fluorescent dyes. The analyte competes with the dye for binding to the cavity, and restores the fluorescence. These displacement sensors have been used for enzyme assays, and sensor arrays have also been constructed using a group of cyclophane receptors for detection of histone peptides carrying variable methylations at various positions.[7b] However, the dye-receptor interaction is shape and functional group-dependent, which limits the choice of dyes in sensor construction, and often requires specialized synthetic reporters. Here we describe a sensitive sensing system for peptide methylation and demethylase enzyme activity that functions with common, commercial fluorophores.

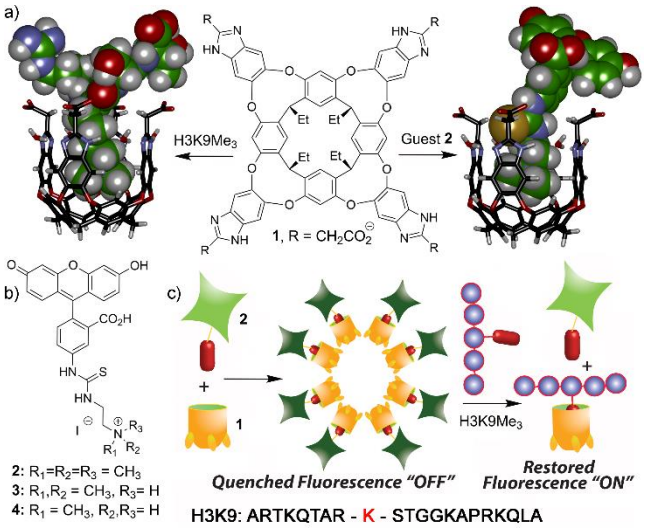

Figure 3.1 a) Structure of host 1 and minimized models of the 1•2 and the 1•(AR(KMe3)ST) host:guest complexes (SPARTAN); b) fluorescent guests 2-4; c) the aggregation-based sensing system.

Results and discussion

The host system used for this purpose is the self-folding, water-soluble deep cavitand **1** (Figure 3.1a). This is a versatile receptor, capable of selective recognition of a wide variety of substrates in aqueous,[13] biomimetic membrane[14] and living cell[14b] environments. Soft cations are the strongest guests, and binding affinities generally vary between mM and μM, with R-NMe_3^+ species such as acetylcholine showing the greatest affinity. As can be seen in Figure 3.1, the cavity is filled by the -$CH_2CH_2NMe_3^+$ group (e.g. from trimethyllysine, KMe_3), with the remainder of the target structure positioned above the cavitand rim. Cavitand **1** is unique amongst water-soluble receptors in that its *exterior* is quite hydrophobic, as well as that of its internal cavity. This leads to some unusual assembly behavior upon the recognition of mildly lipophilic trimethylammonium-containing species: while **1** forms a simple 1:1 complex with small molecules such as choline, larger species

that protrude out of the cavity can cause the receptor to aggregate into larger assemblies. This concept has been exploited by using **1** as sensing agent for acetylcholine, exploiting the lowered relaxivity of a bound Gd-containing guest for MRI detection.[15] This self-aggregation upon target binding introduces the possibility of a new strategy for indicator displacement assays. If fluorescence quenching of a bound dye can be effected upon aggregation, both the fluorophore and the binding anchor could be varied: as the fluorophore need not be inside the cavity, a far greater scope of reporters could be employed. In addition, the "binding handle" can be tailored to allow excellent specificity for desired targets.

Our initial tests were to determine a suitable fluorophore for the displacement assay. The requirements can be quite stringent: the binding of the indicator must be sufficiently robust as to be retained in a complex environment, but weaker than the binding of the selected target. The dye must be sufficiently lipophilic to confer aggregation, be quenched when bound (i.e. the fluorophores must be brought into close proximity upon aggregation), and turn on when released. In addition, long wavelength fluorescence is desirable for simple sensing, and water-solubility is essential. We tested a small range of water-soluble fluorescein-based dyes to determine their affinity and potential quenching range. Guests **2-4** were very simply synthesized in one or two steps from methylated ethylenediamine derivatives and commercial fluorescein isothiocyanate, and vary in their methylation state at the terminal nitrogen. NMe_3^+ species **2** is a well-established guest for **1** in lipid bilayer environments,[14] and $NHMe_2^+$ dye **3**, NH_2Me^+ dye **4** and fluorescein itself would be

expected to have increasingly smaller affinities for **1**, due to mismatches in shape and charge-fitting with the cavity of **1**.

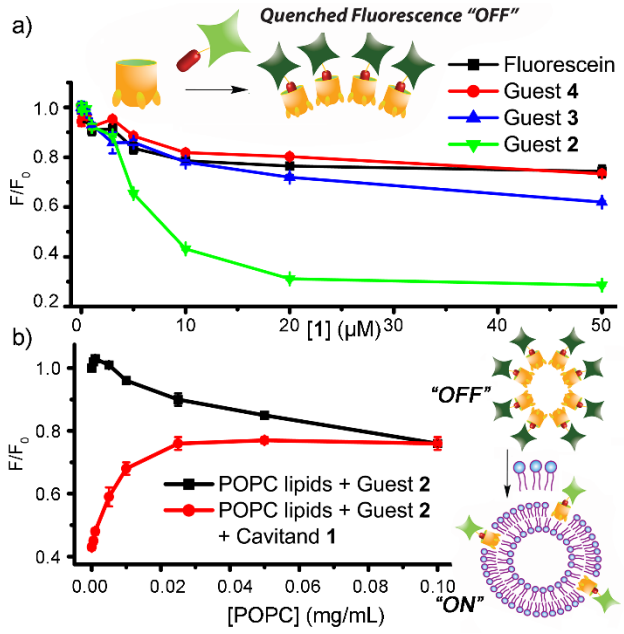

Figure 3.2 Aggregation-based Quenching. a) Relative fluorescence of 2-4 at 3 μM with increasing [1] in PBS buffer (10 mM phosphate, 150 mM NaCl, pH 7.4); b) Effect of POPC lipid vesicle concentration on the fluorescence of the 1•2 host:guest complex (20 μM 1, 3 μM 2).

As can be seen from Figure 3.2a, there is an obvious difference in behavior between the four dyes upon addition of increasing concentrations of cavitand **1** in phosphate buffered saline (PBS). While minimal changes in fluorescence were observed upon addition of **1** to fluorescein and NH_2Me^+ guest **4**, a slight decrease in fluorescence was observed for NMe_2H^+ guest **3**. However, when NMe_3^+ guest **2** was added, a strong loss in fluorescence was observed, reaching maximal quenching in the presence of 20 μM **1**, when only 30% of the original fluorescence was retained. The affinity of the various dyes was determined from these curves. The dissociation constant (K_d) of the **2•1** complex was estimated to be 17±10 μM by solving the complex dissociation equilibrium (see Supporting Information). The K_d values for NMe_2H^+ dye **3**, NH_2Me^+ dye **4** and fluorescein were at least 10 times larger than that of **2**, indicating weak or non-specific binding.

NMR analysis was consistent with the theory that the fluorescence loss observed upon addition of guest **2** to cavitand **1** was due to complexation-induced quenching via an aggregative mechanism.[15] When **2** was titrated into a D_2O solution of **1**, proton signals for both **1** and **2** disappear and broaden out (see Supporting Information, Figure S3.2), indicating the formation of large, slowly tumbling aggregates. Large aggregates show a size-dependent decrease in T2 and the concomitant introduction of dipolar coupling effects that broaden ^{1}H NMR signals.[16] In addition, new broad peaks appear, corresponding to expulsion of a THF molecule from the cavity of **1** (present in the cavity in the final isolation step[13]), illustrating that the host:guest recognition process occurs. Surface tension measurements (see Supporting Information) show a sharp reduction of the surface tension upon addition of **1** to a solution of **2**, something not observed upon increasing [**1**] or [**2**] alone. Evidently, upon association with **1** (even at μM concentrations), aggregation of the **1•2** complex occurs, positioning the fluorescein groups close to one another in the self-assembled (presumably micellar) aggregate, and self-quenching is observed. Indeed, greater quenching efficiency was obtained by increasing the concentration of the **1•2** complex while keeping the **1/2** ratio the same (see Supporting Information). By contrast, if the experiment was repeated in the presence of POPC vesicles, fluorescence recovery was observed (Figure 3.2b). Cavitand **1** self-embeds into these vesicles very easily,[14c] and this abrogates any *self*-association. The amount of **1** incorporated in a single vesicle is <5%,[14c] and no self-quenching of **2** can occur, corroborating the theory that the quenching of **2** upon binding in **1** is due to self-quenching between fluorophores upon aggregation of the **1•2** host:guest complex. The quenching should occur via a ground-state (i.e. static) mechanism,

rather than via a dynamic mechanism such as diffusional collision.[17] In fact, the flattening of the Stern-Volmer plot of F_0/F vs. [**1**] at high [**1**] indicated the presence of both free and bound **2** in the system**.** The quenching phenomenon was inversely related to temperature, with less quenching observed at higher temperature. Fluorescence lifetime measurements also showed that no change in the lifetime of **2** occurred when mixed with cavitand **1,** even at the optimal concentration ratio where $F/F_0 = 0.3$. All these experiments support the notion of static quenching.

This aggregation-based quenching mechanism is unique, and distinctly different to the standard indicator displacement assays that occur solely via host:guest quenching interactions.[12] This process is controlled by both the highly selective host behavior *and* self-aggregative properties of **1**. Only a selected few guests cause this aggregation: purely hydrophobic species (e.g. hydrocarbons) do not, nor do small charged species such as choline.[13] Only mildly lipophilic R-NMe_3^+ guests such as **2** have been shown to cause this aggregation.[15] As such, this phenomenon can be exploited to establish simple, homogeneous in-solution displacement assays for the detection of suitable substrates, if the substrate is a sufficiently good guest to displace the indicator **2**. As the measured K_d of **2** was ~17 μM, only strongly binding targets should be capable of this displacement, allowing the formation of a selective sensor.

As NMe_3^+-based substrates are the most strongly bound by **1**, we envisaged that this system would be an excellent candidate for the detection of lysine methylation PTMs. The specific, strong affinity of **2** for the host would ensure selective detection of trimethylated targets. Our initial tests involved the fluorescence detection of trimethylation on histone

H3 peptide fragments. The primary amino acid sequence of the H3 peptides used (amino acids 1-21) is shown in Figure 3.1. We initially focused on variably methylated peptides at the lysine 9 position. The sensor was constructed by mixing cavitand **1** and guest **2** at an optimized ratio of 6:1 in PBS, with [**2**] = 3 μM. Three H3 peptide fragments with methylations on K9 (from zero to three methyl groups: H3, H3K9Me and H3K9Me$_3$) were titrated into the system, and the fluorescence recovery analyzed with respect to peptide concentration (see Figure 3.3).

Gratifyingly, addition of the trimethylated peptide (H3K9Me$_3$) caused a significant recovery of the fluorescence signal upon addition of only 2 μM peptide. The fluorescence recovery reached a maximum at 5 μM peptide, and this effect was selective for the trimethylated NMe_3^+ guest, as would be expected from the previous affinity measurements. If the monomethylated peptide (H3K9Me) was added, some fluorescence recovery was observed, but to a far lower extent than for H3K9Me$_3$. In addition, the parent unmethylated peptide (H3K9) caused no recovery of the fluorescence signal within the initial concentration range of 0 to 5 μM. This indicator displacement assay is selective and quite robust in systems that mimic cell extraction: for example, the addition of the protease digest from human serum albumin (HSA digest, Figure 3.3) did not change the fluorescence of the sensor. Also, addition of a trypsin-digested cell lysate from mouse macrophages did not alter the response curve produced by H3K9Me$_3$ (see Supporting Information).

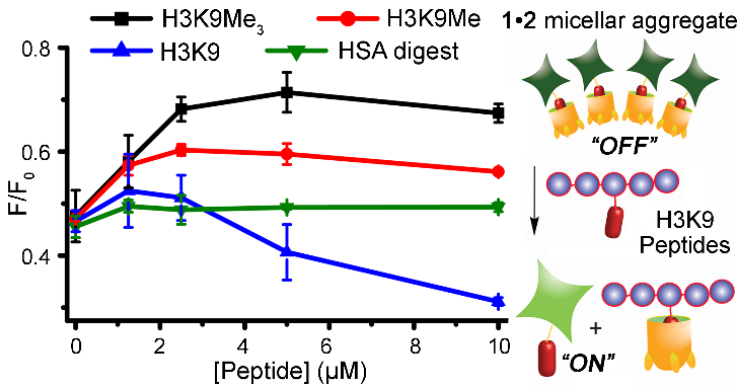

Figure 3.3 Fluorescence recovery induced by mixing modified (H3K9Me, H3K9Me3) or unmodified (H3K9) histone peptides (H3, 1-21), or the protease digest of human serum albumin (HSA) with the sensor system (PBS buffer, 20 μM 1, 3 μM 2).

To determine that the fluorescence recovery was due to selective cavity-based recognition rather than some other non-specific deaggregation process, we initially tested the affinity between cavitand **1** and H3K9Me$_3$) using affinity CE (see Supporting Information). Cavitand **1** was added to the running buffer (10 mM borate at pH 9.5) at increasing concentrations, and the electrophoretic mobility of the peptide was monitored. The migration time of the peptide gradually decreased with [**1**], and a neutral marker was used to indicate change in the electroosmotic flow (EOF). The net mobility shift ($\Delta\mu$) was plotted against [**1**], and the curve fitted to obtain K_d (H3K9Me$_3$) = 33.8 μM, consistent with the relative displacement results shown in Figure 3.3. Affinity measurements between **1** and unmethylated H3K9 were unsuccessful, as the highly cationic peptide irreversibly adhered to the capillary wall. The **1**•H3K9Me$_3$ binding limited this effect, allowing analysis.

The indicator displacement did show an unusual outcome at higher peptide concentrations, most strongly observed for the unmethylated H3K9. If the concentration of H3K9 was higher than 5 μM, the observed fluorescence *decreased* significantly (blue

curve, Figure 3.3). We speculated that this excess quenching could be the result of aggregation mediated by the electrostatic interaction between the cationic histone peptide and the anionic **1•2** complex. If true, the aggregation effect should be affected by the both salt concentration and type, i.e. show Hofmeister dependence. The Hofmeister series is well-established for its effects on protein solubility, but only recently has its effects on cavity-based molecular recognition been investigated.[18] We tested the effect on fluorescence quenching induced by the combination of **1**, **2**, and H3K9 in the presence of both "salting-in" (chaotropic) and "salting out" (kosmotropic) anions (Figure 3.4). A series of solutions were prepared by increasing [NaCl] from 0 to 1200 mM in 10 mM sodium phosphate (pH 7.4), or by fixing [NaCl] = 150 mM but varying the type of anion in the phosphate buffer. The sensor was constructed by mixing 3 μM guest **2** and 18 μM cavitand **1**, and the fluorescence was monitored with respect to [H3K9]. The initial observation was that the quenching process could be abrogated upon increasing [NaCl] (Figure 3.4a). As expected, increasing the ionic strength of the system reduced electrostatic interactions between the cationic peptide and the **1•2** complex. Salt concentration has been shown to disrupt the recognition of cationic proteins with **1** in membrane bilayers,[19] so this result was somewhat expected. The most interesting observation was in the presence of "salting-out" salts such as citrate, lowered fluorescence decrease is observed, corresponding to a lowered amount of aggregation with the cationic H3K9. This makes sense: as chaotropes make water more "water-like", increased binding of sodium ions to the external anionic carboxylates is observed, thereby reducing the net charge on the host (as has been shown by Gibb with his anionic host[18b]) and reducing the electrostatic attraction between **1** and

H3K9. Whereas the addition of 150 mM citrate completely removes any fluorescence loss due to aggregation (red line, Figure 3.4), sulfate (a weaker chaotrope) has a smaller effect (blue line), yet is still more effective than adding no salt at all. The slightly chaotropic chloride is the least effective additive. Most interestingly, addition of iodide *increases* the baseline fluorescence significantly (something not observed for the other salts). The most likely explanation is that the soft iodide anion has some affinity for the cavity itself,[18b] and competitively displaces **2**, regenerating the fluorescence.

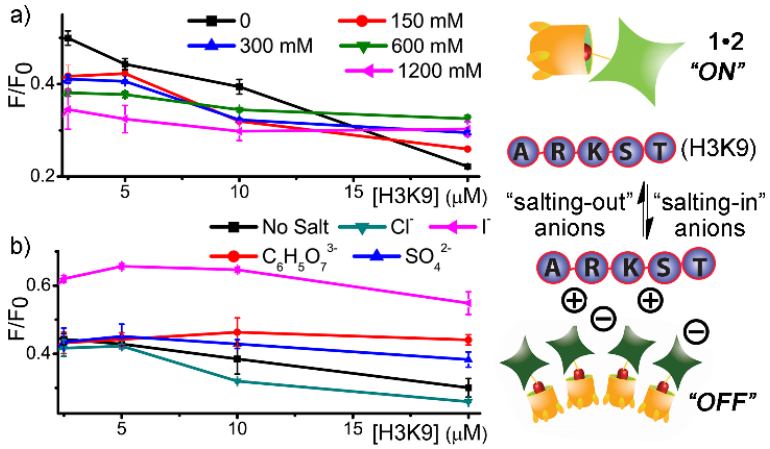

Figure 3.4 Hofmeister-dependent Aggregation. Effect of varying a) [NaCl] and b) anion type with [X-] = 150 mM on the fluorescence of the sensor (18 μM 1, 3 μM 2).

Interestingly, the electrostatically induced aggregation at higher peptide concentration was not significant with the trimethylated peptide H3K9Me$_3$, presumably due to the replacement of hard NH_3^+ ions with the softer, less H-bonding NMe_3^+. This leads to a large signal difference between the unmethylated and trimethylated peptides, in either no salt or PBS buffered condition ([NaCl] ≤ 150 mM), adding a second dimension to the sensing process *other than merely target affinity.* This feature makes our sensor ideal for monitoring enzymatic changes in peptide methylation-catalyzed histone-lysine N-methyltransferase or lysine demethylases. Known assays often rely on coupled chemical or enzyme reactions for signaling, or require target immobilization and separation.[20] As our sensor can clearly differentiate between trimethylated, monomethylated and non-methylated H3 peptides, it can directly monitor the methylation or demethylation processes in solution. The sensor was employed to monitor the reactivity of histone demethylase JMJD2E, which catalyzes the demethylation of histone H3 at lysine residue 9. Figure 3.5a shows the fluorescence trace of the demethylation assay. Upon mixing 10 μM of H3K9Me$_3$

with the **1•2** sensor (20 μM **1**, 3 μM **2**), the trimethylated peptide displaced the guest from the host, conferring fluorescence recovery on the system. The addition of 100 nM JMJD2E and its cofactors (1.5 mM ascorbate, 10 μM Fe^{2+}, and 50 μM 2-oxoglutarate) initiated the demethylation reaction. The observed fluorescence continuously decreased over time, as the demethylated products (either H3K9Me_2 or H3K9Me) have much lower affinity for **1** and are incapable of displacing **2**. The fluorescence decrease plateaued at 50 mins, after which no more demethylated product was generated. A control experiment showed that when the ratio of H3K9Me_3 and H3K9 was varied while keeping [peptide] = 20 μM, the fluorescence increased linearly with increasing fraction of H3K9Me_3 (Figure 3.5b). This indicates that the sensor can monitor changes in [H3K9Me_3] or [H3K9] during enzyme assays, and so we applied it to quantitate the effect of varying [JMJD2E] on demethylation of 20 μM H3K9Me_3 (Figure 3.5c), and tested the impact on enzyme activity from 2,4-dicarboxypyridine (2,4-PDCA), a 2-oxoglutarate analog and known inhibitor of JMJD2E (Figure 3.5d).[21] Higher sensor fluorescence was observed upon increasing [2,4-PDCA] (Figure 3.5d), fixing [JMJD2E] at 800 nM and t = 30 mins. The IC_{50} value was 7.4 μM, close to the literature value of ~ 3 μM.

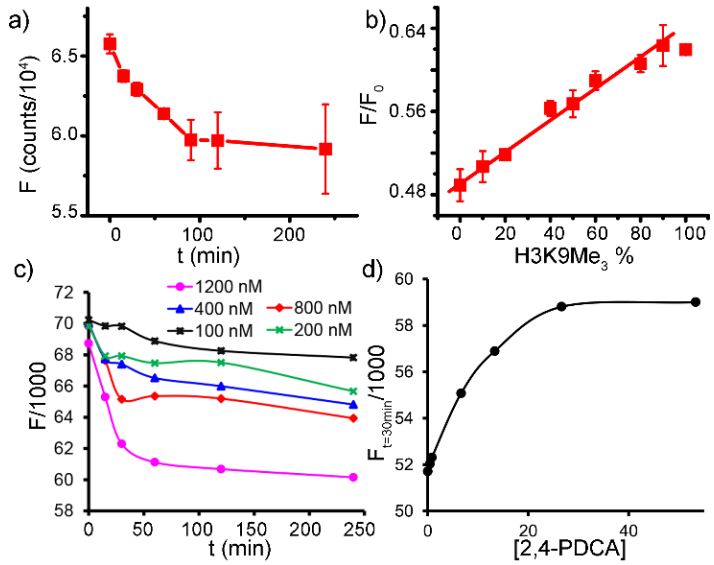

Figure 3.5 a) Sensor (20 μM 1, 3 μM 2) fluorescence in the presence of JMJD2E (800 nM); b) sensor response is dependent on methylation ratio; c) effect of varying [JMJD2E]; d) JMJD2E assay in the presence of PDCA inhibitor.

Conclusion

In conclusion, we have established a dual-mode aggregative indicator displacement sensing system for the detection of trimethylated peptides and determination of histone demethylase activity. The combination of selective recognition of suitably-sized NMe_3^+ salts and the targeted, reversible lipophilic aggregation of the host:guest complex provides a unique quenching mechanism that is not only dependent on affinity for sensitivity, but the lipophilicity of the host:guest sensor. In addition, aggregation can be controlled by the application of chaotropic anions in the analysis mixture, allowing a second level of discrimination between hard lysine groups and softer trimethyllysines. The aggregation-induced quenching mechanism gives higher flexibility in the selection of the signaling units, which are no longer limited to target-complementary dyes.

Experimental section

Synthesis of Fluorescein Guests:

Fluorescein isothiocyanate (25 mg, 0.64 mmol) was added to a 10 mL round bottom flask with stir bar. The system was purged and placed under nitrogen followed by addition of dry THF (1 mL). The corresponding amine (either N-methylethylenediamine or *unsym*-N,N-dimethylethylene-diamine was added (0.64 mmol) and the reaction was stirred at room temperature overnight. The reaction mixture was filtered and the product collected as a bright orange solid.

Monomethylated Guest 4: H NMR (500 MHz, D_2O): δ 7.55 (s, 2H), 7.40 (d, *J* = 8.0

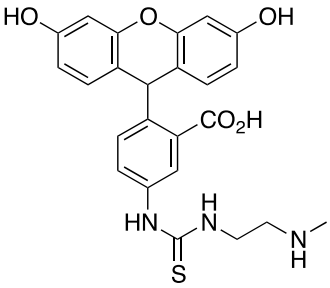

Hz, 2H), 7.15 (d, *J* = 8.9 Hz, 2H), 6.93 (d, *J* =8.0 Hz , 1H), 6.62 (dd, *J* = 8.9, 2.6 Hz, 2H), 6.54 (d, *J* = 2.6 Hz, 2H), 4.16 (s, 1H), 3.76 (s, 2H), 3.35 (t, 2H), 3.11 (s, 3H), 3.0 (t, 2H). ^{13}C NMR (125 MHz, D_2O): δ 180.7, 180.4, 173.1, 158.4, 140.4, 131.2, 130.1, 129.4, 122.9, 112.2, 103.6, 67.8, 66.5, 49.6, 37.5, 37.1, 33.2. ESI MH^+ *m/z* expected: 465.14, found: M^+= 464.1296.

Dimethylated Guest 3: ^{1}H NMR (700 MHz, DMSO-d_6): δ 8.23 (s, 2H), 7.75 (d, *J* = 8.0

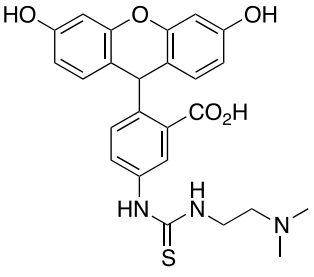

Hz, 2H), 7.09 (d, *J* = 8.0 Hz, 2H), 6.67 (d, *J* = 8.9 Hz, 2H), 6.60 (d, *J* = 2.1 Hz, 2H), 6.44 (dd, *J* = 8.9, 2.1 Hz, 2H), 5.75 (s, 1H), 3.60 (m, 2H), 3.50 (s, 2H), 2.66 (m, 2H), 2.19 (s, 6H). ^{13}C NMR (175 MHz, DMSO-d_6): δ 180.22, 168.78, 166.73, 158.65, 153.88,

152.10, 129.51, 128.86, 125.96, 116.18, 112.38, 110.48, 109.51, 102.34, 66.98, 59.49, 57.12, 45.12. ESI MH^+ *m/z* expected: 479.15, found: M^+= 478.1435.

Measurement of Fluorescence Quenching and Peptide Displacement:

In a typical quenching assay, 10 µL of the fluorescent guest (**2**, **3**, or **4**) (30 µM), 10 µL of the cavitand **1** (200 µM), and 80 µL of the 1×PBS (10 mM phosphate at pH 7.4 with 150 mM NaCl) were mixed in the 96-well plate, and incubated with mild shaking for 10 minutes. Followed, fluorescence was recorded in a Perkin Elmer Wallac 1420 Victor 2 Microplate Reader (PerkinElmer, Inc., Waltham, MA) with the EX/EM wavelengths at 485/535 nm. To observe the effect of fluorescence recovery induced by various histone peptides or the interfering peptides, 10 µL of the guest molecule (30 µM) was mixed with 10 µL of cavitand (200 µM) and 70 µL of PBS and incubated for 10 minutes; then 10 µL of the peptide solution was added to obtain the final peptide concentration in the range of 0 to 44 µM. Fluorescence reading was taken after 20 minutes.

One of the interfering samples tested was the digest prepared from HSA using the following procedure. First, 200 µL HSA (2 mg/mL) was denatured at 100 ^oC. Followed, 5 µL of DTT (Dithiothreitol, 200 mM), 20 µL of IAA (200 mM), and 20 µL of DTT (200 mM) were added sequentially and an incubation step of 30 minutes was applied after the addition of each reagent. At last, Trypsin equivalent to 2% of the protein mass was added to initiate the overnight incubation at 37 ^oC. The other interfering molecules tested were the lysate prepared from the Mouse Raw 264.7 macrophages. The cells were treated with the M-PER™ Mammalian Protein Extraction Reagent. The cell debris was removed by centrifugation at 14,000 ×g for 5 minutes, and the supernatant was collected and used after

quantifying the protein concentration by the Pierce BCA Protein Assay kit (Thermo Fisher).

To investigate the effect on peptide displacement from salt concentrations, the peptide displacement assay was carried out in 10 mM phosphate buffer (pH = 7.4) supplied with sodium chloride concentrations at 0, 150, 300, 600, and 1200 mM. The impact from the type of anions was studied using the sodium salt of citrate, sulfate, chloride, or iodide at the concentration of 150 mM, with the pH adjusted to 7.4 using sodium hydroxide.

Measurement of Enzyme Activity

Demethylation reaction mixture contained 1 mM ascorbic acid, 10 μM Fe^{2+} (ammonium ferrous sulfate), 50 μM 2-OG, 20 μM $H3K9Me_3$, and the demethylase, JMJD2E, at various concentrations. At different reaction duration, the mixture was heated in boiling water for 5 minutes to denature the enzyme and terminate the reaction. Then 50 μL of the reaction mixture at room temperature was mixed with 50 μL of the sensor solution that contained 40 μM cavitand **1** and 6 μM guest **2**, and incubated for 20 mins, prior to fluorescence measurement in the plate reader. Measurement of the IC_{50} value of the inhibitor 2,4-PDCA was carried out in the similar way, except for fixing the enzyme concentration at 800 nM and the reaction duration at 30 minutes. Various amounts of the inhibitor was spiked to the reaction solution with the final concentration reaching 53.3 μM. The IC_{50} value was found by fitting the plot of sensor fluorescence vs. inhibitor concentration to the exponential decay equation using Origin 8.0:

$$(F_0\text{-}F)/A = \exp(-x/t_1)$$

The value of t_1 was found to be 10.97 μM, with $R^2 = 0.9975$ and thus $IC_{50} = \ln(1/2) * t_1 =$ 7.4 μM.

Preparation of Liposomes

Liposomes used to break up the guest aggregation induced by binding with cavitand were prepared from 200 μL of 10 mg/mL POPC in chloroform. The solution was first dried under a nitrogen flow in a clean 2 mL volume glass bottle; and then 1 mL of 1×PBS was added and the mixture was allowed to sit on the bench for 15 minutes. Then the solution was vortexed vigorously for 1 minute. The mixture was further sonicated for 2 hours. The obtained liposome was kept at 4 ^{o}C before use.

Fluorescence Life Time Measurement

Time resolved measurements were performed with a 1 kHz Coherent Libra Ti:Sapphire regeneratively amplified laser system and a Hamamatsu C4334 Streakscope with 15 ps time resolution and 2.5 nm wavelength resolution. A beam splitter sent 50 percent of the 800 nm fundamental pulse into a frequency doubling BBO crystal to produce the 400 nm excitation beam. Integrated emission intensity was collected using front face detection with a 400 nm short pass filter in place before the streak camera. Filters were put in place before the streak camera in order to eliminate stray light. Using Time-Correlated Single Photon Counting (TCSPC), the amount of photons given off as a function of time were recorded. This was then be turned into a plot of natural log of signal versus time, in which the slope is relative to the fluorescence lifetime.

Capillary Electrophoresis

The 50 cm fused-silica capillary (75µm id, 365µm od; PolymicroTechnologies, Phoenix, AZ) with an effective length of 40 cm was sequentially rinsed at 20 psi with 0.1 M NaOH (2 min), deionized water (1 min), 0.1 M HCl (2 min), deionized water (1 min), and the running buffer (4 min) prior to injection. Different concentrations of cavitand **1** (0 µM-100 µM) were included in the running buffer of 17.5 mM phosphate (pH 7.4). DMSO at 0.01% was co-injected with 10 µM $H3K9Me_3$ to serve as the EOF marker. The sample was injected by pressure at 1 psi for 5 s. All CE separations were done at 25 kV with UV-absorption detection at 214 nm in room temperature.

Surface Tension Measurement

Surface tension was measured by the Fisher Surface Tensionmat (Fisher Scientific, Inc.) equipped with a platinum ring having a mean circumference of 6.004 cm. The ring and the plastic petri dish (30 × 10 mm) used as the solution container were cleaned with DI water three times before use. A stock cavitand **1** solution of 1 mg/mL was prepared. Aliquots of this stock solution were continuously added to 3 mL of 1× PBS (pH =7.4) and mixed well, while the surface tension was recorded after the addition of each aliquot. The surface tension of the cavitand/guest mixture was measured in the same way, with the stock solution being the mixture of **1** and **2** at a fixed molar ratio of 3 : 20 (stock [**1**] = 1 mg/mL).

Reference

(1) (a) Davidson, V.L. *Biochemistry* **2007**, *46*, 5283-5292. (b) Woodsmith, J.; Stelzl, U. *Curr. Opin. Struct. Biol.* **2014**, *24*, 34-44.

(2) Waldmann, T.; Schneider, R. *Curr. Opin.Cell Biol.* **2013**, *25*, 184-189.

(3)(a) Lee, S. *Toxicol. Res.* **2013**, *29*, 81-86. (b) Venuto, A.; de Marco, A. *J. Cell. Biochem.* **2013**, *114*, 510-513.

(4) (a) Walsh, C. T.; Garneau-Tsodikova, S.; Gatto, G. J., Jr. *Angew. Chem. Int. Ed.* **2005**, *44*, 7342-7372. (b) Wang, R.; Luo, M. *Curr. Opin. Chem. Biol.* **2013**, *17*, 729-737.

(5) (a) Carlson, S. M.; Moore, K. E.; Green, E. M.; Martin, G. M.; Gozani, O. *Nat. Protoc.* **2014**, *9*, 37-50. (b) Horiuchi, K.Y.; Eason, M.M.; Ferry J.J.; Planck, J.L.; Walsh, C.P.; Smith, R.F.; Howitz, K.T.; Ma, H. *Assay Drug Dev. Technol.* **2013**, *11*, 227-236.

(6)(a) Hattori, T.; Taft, J. M.; Swist, K. M.; Luo, H.; Witt, H.; Slattery, M.; Koide, A.; Ruthenburg, A. J.; Krajewski, K.; Strahl, B. D.; White, K. P.; Farnham, P. J.; Zhao, Y.; Koide, S. *Nat. Methods* **2013**, *10*, 992-995. (b) Rathert, P.; Dhayalan, A.; Ma, H.; Jeltsch, A. *Mol. Biosyst.* **2008**, *4*, 1186-1190.

(7) (a) Norouzy, A.; Azizi, Z.; Nau, W.M. *Angew. Chem. Int. Ed.* **2015**, *54*, 792–795. (b) Minaker, S.A.; Daze, K.D.; Ma, M.C.F.; Hof, F. *J. Am. Chem. Soc.* **2012**, *134*, 11674−11680.

(8) Gamal-Eldin, M.A.; Macartney, D.H. *Org. Biomol. Chem.* **2013**, *11*, 1234–1241.

(9) (a) Shaurya, A.; Dubicki, K. I.; Hof, F. *Supramol. Chem.* **2014**, *26*, 583-590. (b) Daze, K.D.; Hof, F. *Acc. Chem. Res.* **2013**, *46*, 937–945. (c) Daze, K.D.; Pinter, T.; Beshara, C.S.; Ibraheem, A.; Minaker, S.A.; Ma, M.C.; Courtemanche, R.J.; Campbell, R.E.; Hof, F. *Chem. Sci.* **2012**, *3*, 2695–2699. (d) Daze, K.D.; Ma, M.C.; Pineux, F.; Hof, F. *Org. Lett.* **2012**, *14*, 1512–1515.

(10) (a) Ingerman, L.A.; Cuellar, M.E.; Waters, M.L. *Chem. Commun.* **2010**, *46*, 1839–1841. (b) Pinkin, N.K.; Waters, M.L. *Org. Biomol. Chem.* **2014**, *12*, 7059-7067.

(11) Ghale, G.; Nau, W.M. *Acc. Chem. Res.* **2014**, *47*, 2150-2159.

(12) (a) Florea, M.; Kudithipudi, S.; Rei, A.; Gonzalez-Alvarez, M. J.; Jeltsch, A.; Nau, W. M. *Chem. Eur. J.* **2012**, *18*, 3521–3528. (b) Biedermann, F.; Hathazi, D.; Nau, W. M. *Chem. Commun.* **2015**, *51*, 4977-4980.

(13) Biros, S.M.; Ullrich, E.C.; Hof, F.; Trembleau, L.; Rebek, J., Jr. *J. Am. Chem. Soc.* **2004**, *126*, 2870-2876.

(14) (a) Liu, Y.; Liao, P.; Cheng, Q.; Hooley, R.J. *J. Am. Chem. Soc.* **2010**, *132*, 10383. (b) Ghang, Y.-J.; Schramm, M.P.; Zhang, F.; Acey, R.A.; David, C.N.; Wilson, E.H.; Wang, Y.; Cheng, Q.; Hooley, R.J. *J. Am. Chem. Soc.* **2013**, *135*, 7090-7093. (c) Ghang, Y.-J.; Lloyd, J.J.; Moehlig, M.P.; Arguelles, J.K.; Mettry, M.; Zhang, X.; Julian, R.R.; Cheng, Q.; Hooley, R.J. *Langmuir* **2014**, *30*, 10161-10166.

(15) Li, V.; Ghang, Y.-J.; Hooley, R.J.; Williams T.J. *Chem. Commun.* **2014**, *50*, 1375 - 1377.

(16) Cala, O.; Dufourc, E.J.; Fouquet E.; Manigand, C.; Laguerre, M.; Pianet, I. *Langmuir* **2012**, *28*, 17410-17418.

(17) Lakowicz, J.R. in *Principles of Fluorescence Spectroscopy*, Springer US: Boston, MA; 2006, p.p. 277-330.

(18) (a)Gibb, C. L. D.; Gibb, B. C. *J. Am. Chem. Soc.* **2011**, *133*, 7344-7347. (b) Carnegie, R. S.; Gibb, C. L.; Gibb, B. C. *Angew. Chem. Int. Ed.* **2014**, *53*, 11498-11500. (c) Gibb, C. L.; Oertling, E. E.; Velaga, S.; Gibb, B. C. *J. Phys. Chem. B.* **2015**, *119*, 5624-5638.

(19) Ghang, Y.-J.; Perez, L.; Morgan, M. A.; Si, F.; Hamdy, O. M.; Beecher, C. N.; Larive, C. K.; Julian, R. R.; Zhong, W.; Cheng, Q.; Hooley, R. J. *Soft Matter* **2014,** *10*, 9651-9656.

(20) (a)Kawamura, A.; Tumber, A.; Rose, N.R.; King, O.N.F.; Daniel, M.; Oppermann, U.; Heightman, T.D.; Schofield, C.J. *Anal. Biochem.* **2010**, *404*, 86-93. (b) Xu, W.; Podoll, J. D.; Dong, X.; Tumber, A.; Oppermann, U.; Wang, X. *J. Med. Chem.* **2013**, *56*, 5198-5202.

(21) (a) Tsukada, Y.-I.; Fang, J.; Erdjument-Bromage, H.; Warren, M. E.; Borchers, C. H.; Tempst, P.; Zhang, Y. *Nature* **2006**, *439*, 811-816. (b) Kaniskan, H. Ü.; Konze, K. D., Jin, J. *J. Med. Chem*. **2015**, *58*, 1596-1629.

Supporting information

1. Supporting Figures

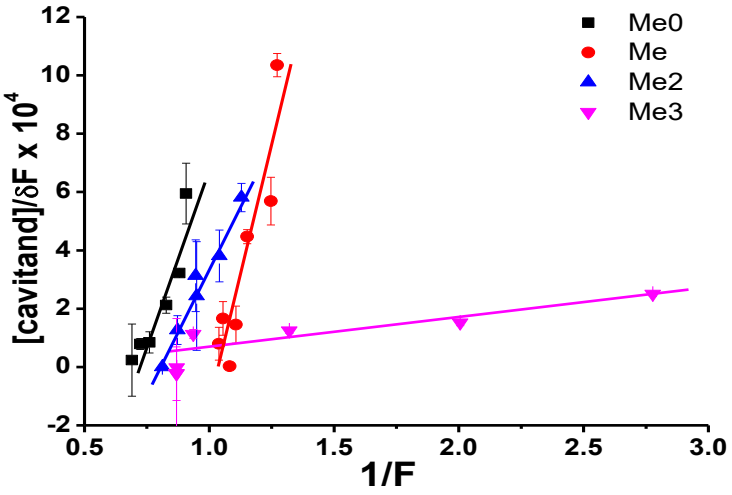

Guest	K_d (μM)
Fluorescein (Me0)	149 ± 19
Me (Guest 4)	406 ± 263
Me2 (Guest 3)	183 ± 18
Me3 (Guest 2)	17 ± 10

Figure S3.1 The linear plots for determination of the dissociation constants (K_d) for complexes formed between various guest molecules and cavitand.

The plot was fitted to:

$$[\text{cavitand}]/\Delta F = K_d\,(1/F) + [\text{Guest}]_0/F_0,$$

in which ΔF was the fluorescence difference measured with (F) or without cavitand (F_0); and $[\text{Guest}]_0$ was the concentration of the guest molecule. The slope of the plot was the K_d.

The guest concentration remained at 3 μM during the titration with increasing cavitand concentration at 0.10, 0.50, 1, 3, 5, 10, 20, and 50 μM. Two assumptions were used to obtain the linear relationship between [cavitand]/ΔF and 1/F: 1) the binding between the guest and cavitand 1 was at a 1:1 ratio; and 2) the quenching was complete so that any cavitand-bound guest would yield zero fluorescence and F was proportional to the concentration of the unbound guest. The K_d values obtained from two independent measurements (each concentration was repeated three time in each measurement, and the results from one of the measurements were shown here) were listed in the table.

NMR Analysis

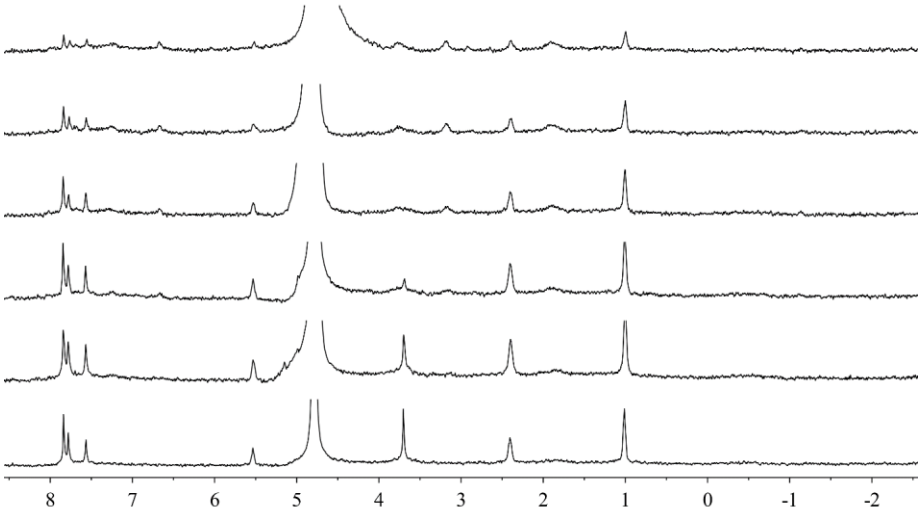

Figure S3.2 ^{1}H NMR spectra of the titration of trimethylammonium guest **2** into a solution of cavitand **1** (400 MHz, 298 K, D_2O, [**1**] = 2 mM). Bottom spectrum = **1**. Other spectra = five sequential additions of 0.2 molar equivalents of **2**. Proton signals for both **1** and **2** are lost upon addition of **2**, indicating the formation of large slow tumbling aggregates, and no free **2** is observed (see Fig S3.5), indicating strong **1**:**2** association.

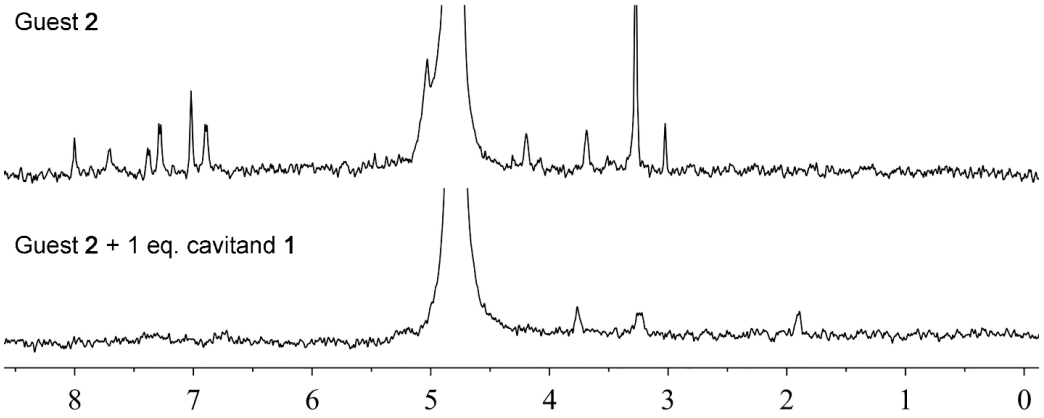

Figure S3.3 ^{1}H NMR spectra of the addition of cavitand **1** into a solution of trimethylammonium guest **2** (400 MHz, 298 K, D_2O, [**2**] = 0.25 mM). Proton signals for both **1** and **2** are lost upon addition of **2**, indicating the formation of large slow tumbling aggregates.

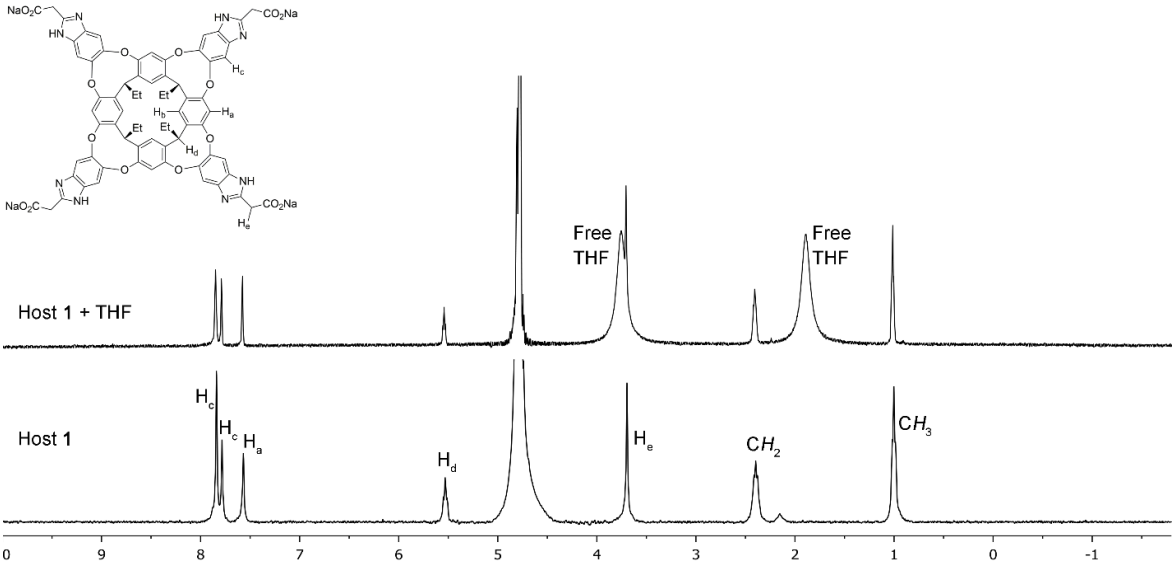

Figure S3.4 Labeled ^{1}H NMR spectra of cavitand **1** and cavitand **1** with free THF (400 MHz, 298 K, D_2O, [**1**] = 2 mM).

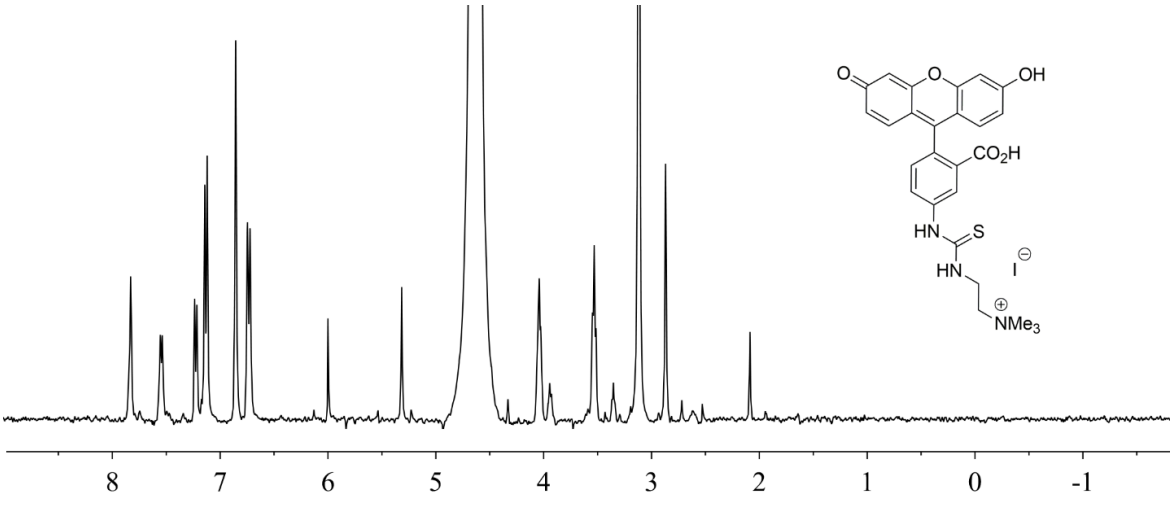

Figure S3.5 ^{1}H NMR spectrum of guest **2** (400 MHz, 298 K, D_2O, [**1**] = 1 mM)

Surface Tension Measurement

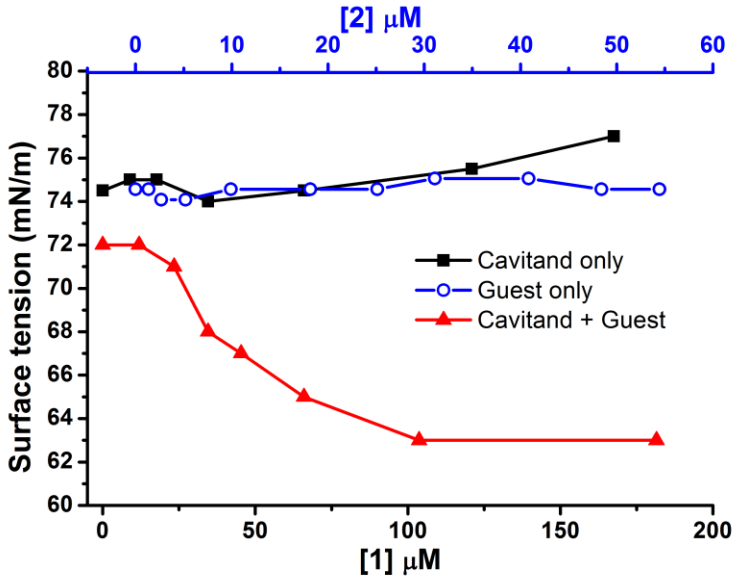

Figure S3.6 The surface tension decreased significantly with increasing [**1**] while keeping the molar ratio of **2** : **1** at 3 : 20, indicating the "surfactant-like" behavior of the 2•1 complex.[3]

However, the surface tension did not change if only the cavitand or the guest was present. The surface tension of the complex solution reached the lowest point at [**1**] = 100 μM, indicating formation of the micelle-like structure decreased the number of complex molecules at the air-solution interface. This phenomenon supported the hypothesis of aggregate formation upon guest-cavitand interaction.

Optical Measurements

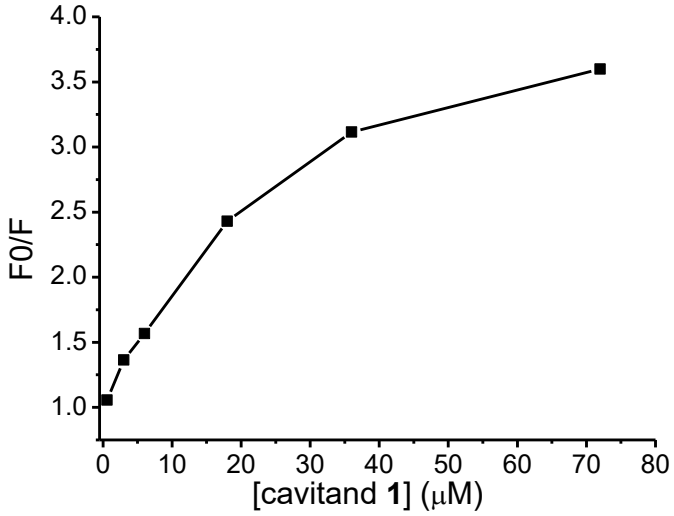

Figure S3.7 The fluorescence decreased with increasing both concentrations of guest **2** and cavitand **1** while keeping the guest : cavitand ratio at 1 : 6.

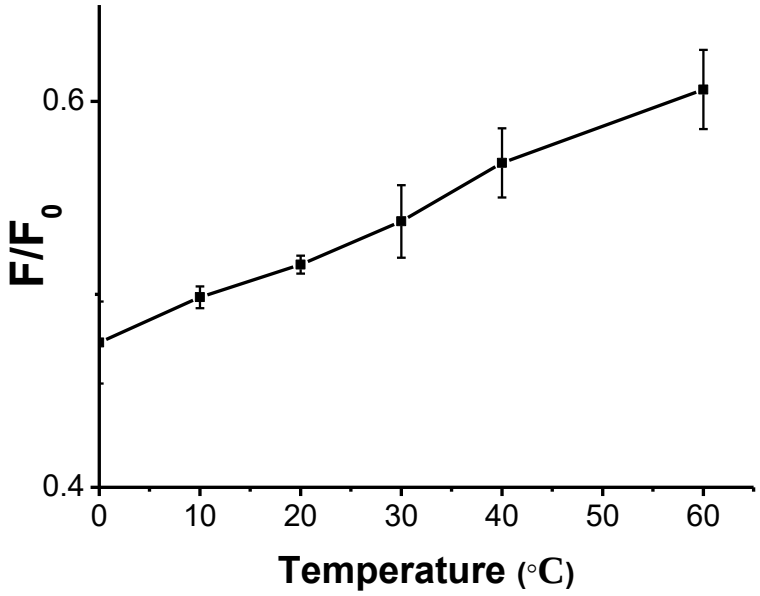

Figure S3.8 Temperature effect on quenching. The sensor solution contained 3 μM guest **2** (30 μM and 20 μM cavitand **1** in 1×PBS, and the solution was cooled or heated to different temperatures. Higher the temperature was, less quenching was observed.

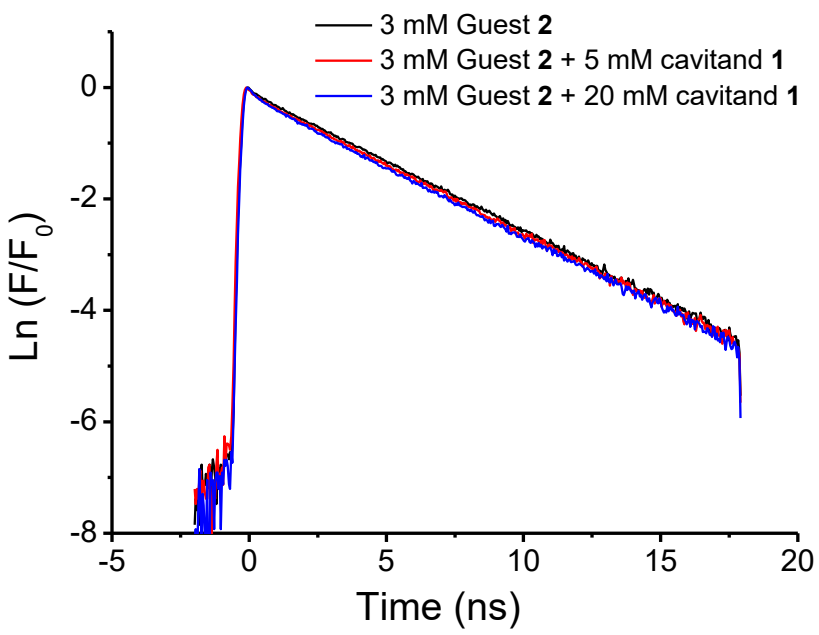

Figure S3.9 Fluorescence lifetime measurement for Guest **2** with or without the presence of cavitand **1**.

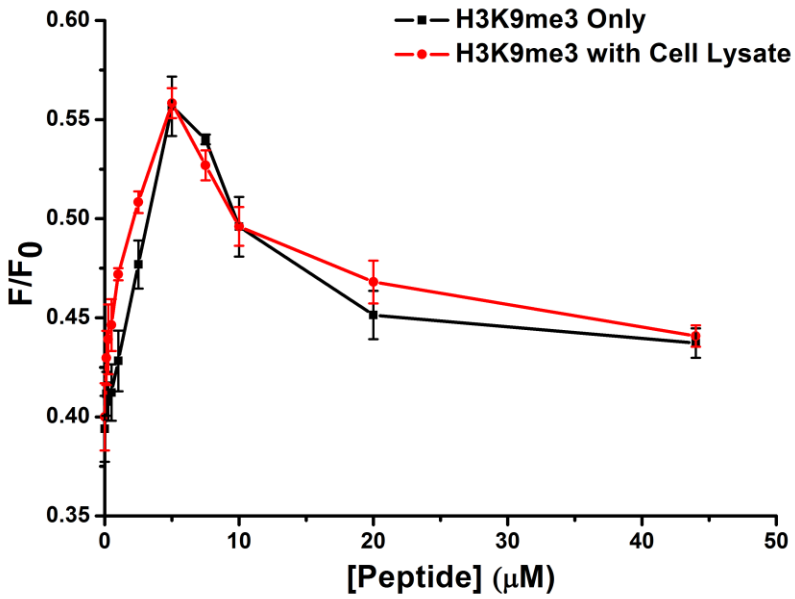

Figure S3.10 Fluorescence recovery induced by adding the trimethylated peptide ($H3K9Me_3$) to the sensor system (PBS buffer, 20 μM 1, 3 μM **2**), with or without the presence of 0.1 mg/mL cell lysate digest prepared from Mouse Raw 264.7 macrophages.

Affinity Measurement via Capillary Electrophoresis

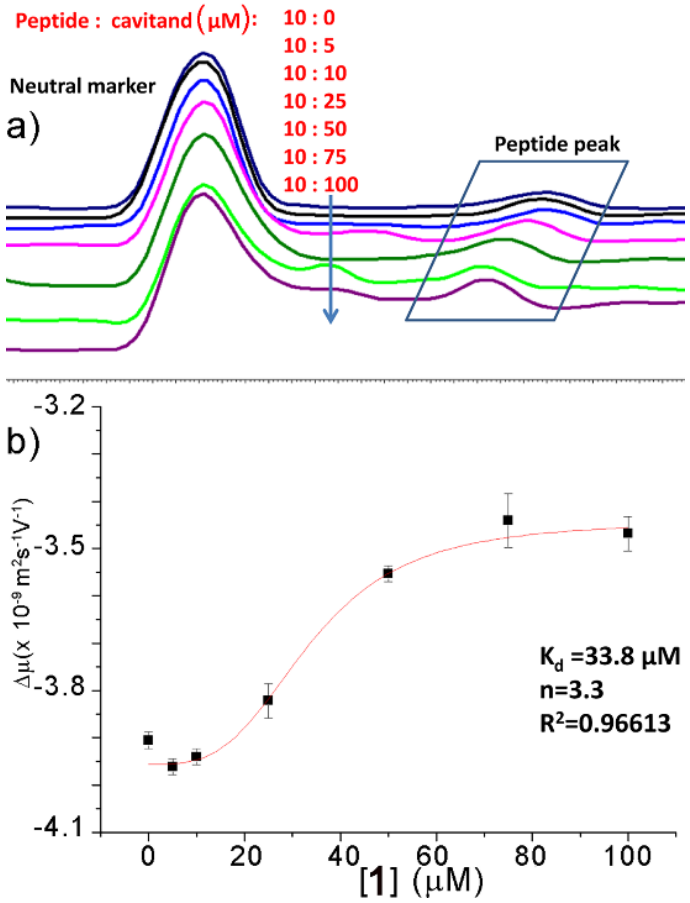

Figure S3.11 a) Electropherograms (λ = 280 nm detection) show the H3K9Me$_3$ ("peptide") peak shifts towards the neutral marker with increasing [**1**]; b) Mobility shift curve (Δμ vs. [**1**]), showing K_d and binding cooperativity n.

Chapter 4 Site Selective Reading of Epigenetic Markers by a Dual-Mode Synthetic Receptor Array

Introduction

The diversity of proteins in living cells is greatly increased by post-translational modifications (PTMs).[1] These PTMs change protein structure, leading to substantial effects on enzyme activity, protein-protein interaction and protein subcellular localization, impacting almost all dynamic cellular processes. Although great effort has been invested to identify PTMs in the proteome, it remains challenging due to their low abundance, highly dynamic modification states, and large variety in modification type and location.[2] A major challenge is the discrimination between similar PTMs, especially positional variations in a single type of modification, and the detection of different modifications in a single target. Synthetic receptors provide an inviting solution to this problem, as they are cheap, easily synthesized, and can show selectivity for binding different residues on protein scaffolds.[3]

The major limitation in molecular recognition of biological targets using synthetic receptors is the lack of selectivity when compared to natural systems, especially antibodies.[4] Whereas small molecule hosts must be synthesized from the ground up, natural systems can employ highly evolved superstructures and complex synthetic machinery to access receptors that show exquisite selectivity to small changes in environment.[5] In contrast, small molecule hosts are generally based on stable, easily accessible macrocyclic systems that function in water, such as cyclodextrins,[6] cyclophanes,[7] cucurbit[n]urils,[8] and

calixarenes.[9] These simple cavity-based species can recognize hydrophobic small molecules,[6a] peptide fragments[7a] and in some cases, even intact proteins.[3] Some hosts have been applied toward the recognition and analysis of PTM proteins and peptides,[10] and employed in arrays for differential analysis.[9c] The most widely applied and successful small molecule hosts for biomacromolecules are tetrasulfonatocalixarene (CX4) and cucurbit[7]uril, (CB7). While the parent macrocycles have impressive recognition capabilities, synthetic variations are extremely difficult.[11] Other hosts can be more easily varied, but their effectiveness is far more limited. The true difference between antibodies and small molecule receptors is the ability to recognize not only the residue of direct interaction, but to be able to discriminate based on *adjacent* residues and the surrounding environment. Antibodies are specific to residue *location*, not just residue type, whereas synthetic receptors show pan-specificity for the encapsulated functional group. Discrimination between highly similar PTMs, dual modifications of the same type, or positional variations between identical PTMs is extremely challenging, as most synthetic receptors often only have one recognition component: that of the PTM group itself (e.g. phosphate).[12] Most receptors are not sufficiently selective to allow discrimination between identical PTMs in different environments, as that requires selective secondary interactions.

The solution to this problem is to employ not one receptor, but multiple, variably functionalized receptors at once. An array formed from multiple receptors can provide multi-mode recognition to maximize signal differences from small variations in guest molecules, enabling more selective target discrimination. This technique has been used to create a "chemical nose" for small molecules in a variety of optical sensing applications.[13]

Targets such as glycoproteins,[14] phosphorylated peptides[15] and sugars[16] can be discriminated using a functional group sensitive chemical sensors.[17] The combined responses from selective interaction between many individual receptors and analytes generate a distinct pattern (fingerprint) for each analyte that can be analysed using a variety of multivariate statistic tools such as principal component analysis (PCA)[18] or linear discriminant analysis (LDA).[19] A pioneering example of this concept was shown by the Hof group,[9c] which used a lucigenin:CX4 indicator displacement assay to read methylation PTMs in histone peptide fragments, based on selective recognition of methylated arginine and lysine residues. The challenge in further application of this system is the lack of variability of the CX4 receptors. For maximal target discrimination, multiple variables in host binding motif are required. Dual, orthogonal recognition motifs in a single receptor scaffold could achieve more complex target discrimination via pairing an "anchor" recognition motif with secondary effects. The most obvious strategy is to pair shape-based recognition (via a synthetic cavity) with H-bonding and charge matching. Dual-mode binding is a well-established phenomenon in supramolecular chemistry, whereby a cavity-based host is combined with a second recognition element that allows further discrimination.[20] Cucurbit[n]urils are the best example of this: some extremely high affinities can be observed with suitably sized alkylammonium species, based on a combination of properly oriented hydrogen bonds and hydrophobic interactions.[21] The lack of tunability of CBs limits their use in a multi-mode binding array, however. The best combination of tunability and target affinity in aqueous supramolecular hosts lies with deep, self-folding cavitands. Here we show that a suite of upper rim functionalized self-

folding deep cavitands can be applied as fluorescent displacement sensors in an array-based format, and show exquisite selectivity in discriminating between highly similar small molecule targets and positional variations in histone peptides carrying lysine methylation, phosphorylation and acetylation PTMs. The discrimination occurs via multiple different recognition/displacement phenomena, rather than a simple cavity-based recognition process.

Results and Discussion

We focused on self-folding deep cavitands based on benzimidazole scaffolds, as these hosts are water-soluble and can be easily varied at the upper rim, introducing groups of varying size, hydrophobicity and charge, while keeping the target binding cavity constant. Cavitands such as **1** are flexible, [22] but are held in a kinetically stable "vase-like" conformation (Figure 4.1a) in the presence of water. This host shows good selectivity for soft R-NMe_3^+ cations such as choline or trimethyllysine.[23] Choline has a K_d of ~50 μM in pure D_2O solution, driven by favourable cation-π interactions with electron rich walls: analogous targets such as dimethylammonium salts or NEt_4^+ ions are poor shape matches for the cavity. These hosts are well-suited for recognizing lysine trimethylation PTMs, as the trimethylammonium group in KMe_3 fits well in the cavitand, and other methylations (KMe_0, KMe_1 and KMe_2) show much weaker affinity. In this study, we employed three specific cavitands (Figure 4.1a): anionic **1**,[23b] neutral **2**[24] and cationic **3**.[25] While the cavity size is identical in each host, the upper rim functions vary in size, charge, hydrophobicity and H-bonding capability.

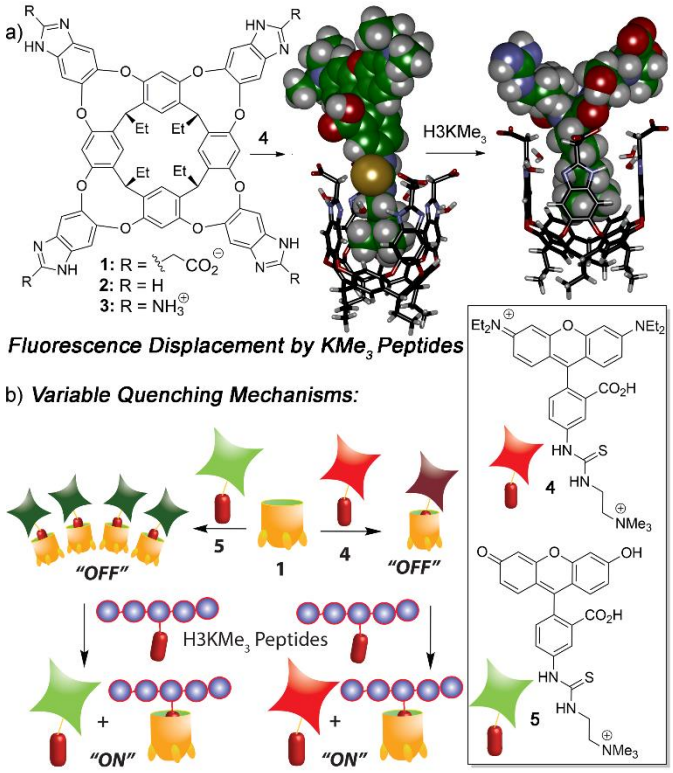

Figure 4.1 a) Structure of hosts 1-3 and minimized models of the 1•4 and the 1•(AR(KMe3)ST) host:guest complexes (SPARTAN); b) Illustration of the FDA processes and structure of Rhodamine B guest 4 and Fluorescein guest 5.

We have previously shown that the tetracarboxylate deep cavitand **1** is capable of recognizing lysine trimethylation PTMs on Histone H3 peptide fragments via selective fluorescence displacement.[26] The binding of fluorescein guest **5** in host **1** causes aggregation of the lipid-like host (Figure 4.1b) and concomitant aggregation-based quenching of the guest. Fluorescence recovery occurs upon displacement of **5** by the desired KMe_3 target.[26] While this sensing system was effective for discriminating between histone KMe_3 and $KMe_{0/1/2}$, the more challenging task of site-selective discrimination requires more variables, and so we synthesized the simple Rhodamine B variant, guest **4**. Guest **4** was synthesized from nitro-Rhodamine B in two steps (see ESI for procedures and

characterization). Surprisingly, despite its similarities to guest **5**, RhB guest **4** showed remarkable differences in binding behaviour: the affinity for cavitands **1-3** is stronger, and the quenching does not rely on an aggregative mechanism, but occurs upon simple 1:1 complex formation.

When guest **4** (3 μM) was mixed with cavitand **1**, **2** or **3** in phosphate buffer, a strong loss in fluorescence was observed in each case. Fluorescence reached a minimum at [**1**] = 4 μM, with 20% of the original fluorescence retained (Figure 4.2a). Cavitands **2** and **3** showed stronger quenching than **1**: the guest fluorescence continued to drop to only 7% and 2% of the original value with increasing [cavitand] up to 10 μM for **2** and **3**, respectively.

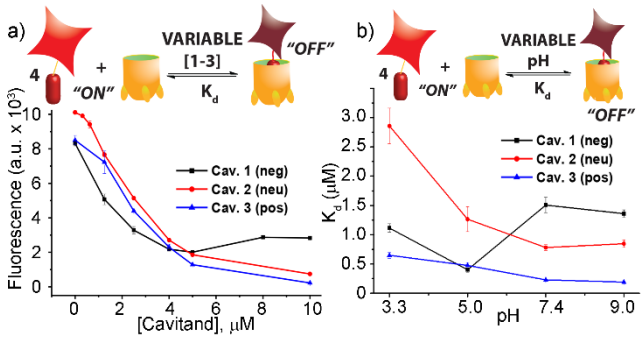

Figure 4.2 a) Fluorescence quenching of 3 μM guest 4 with varying cavitand [1-3] in 80 mM phosphate buffer, pH = 7.4; b) pH-dependent affinity of guest 4 for cavitands 1-3 in 80 mM different buffers (citrate buffer, pH = 3.3; phosphate buffer, pH = 5.0; phosphate

Fluorescence life-time measurements supported a static quenching mechanism for the interaction between guest **4** and all three cavitands (see Figure S4.2). The Stern-Volmer equation was therefore used to calculate the dissociation constants (K_d) for the host-guest pairs, using a 1:1 binary complex formation model. Since the protonation state for all three cavitands and guest **4** varies with pH, we measured the fluorescence quenching curves at various pH values, pH 3.3, 5.0, 7.4, and 9.0, and evaluated the dependence of K_d on pH. As shown in Figure 4.2b and Table 4.1, RhB guest **4** shows extremely strong affinities for all three hosts **1-3**, with K_d values in the micro- and sub-micromolar range. Cavitands **2** and **3** both show increasing affinity for **4** at increasing pH, but tetracarboxylate host **1** shows greatest affinity at pH 5.0. The weakest affinity is seen for **2•4** at pH 3.3, with K_d = 2.86 μM, and the strongest affinity is between **4** and cationic **3** at pH 9.0. In that case, the dissociation constant is 190 nM, which is an affinity usually only seen between suitable guests and CB[n],[11,21b] rather than flexible cavitand hosts.

Table 4.1 Dissociation constants (Kd, μM) for guest 4 in hosts 1-3 in varying pH conditions.

Host	pH 3.3	pH 5.0	pH 7.4	pH 9.0
1	1.11 ± 0.07	0.40 ± 0.04	1.51 ± 0.13	1.36 ± 0.06
2	2.86 ± 0.30	1.27 ± 0.21	0.78 ± 0.05	0.85 ± 0.06
3	0.65 ± 0.05	0.48 ± 0.04	0.23 ± 0.04	0.19 ± 0.02

These strong affinities are extremely encouraging for the application of the RhB guest-cavitand pairs in fluorescence displacement assays of biorelevant target binding. The high degree of quenching reduces the background signal in the absence of displacement, and only strongly bound guests are capable of displacing **4**, inducing large signal change, reducing "false positive" hits. Importantly, guest **4** does not show any variation in emission efficiency at varying pH (see Figure S4.3). The constant native emission of displaced **4** in various media enables the use of different binding media as array elements, to provide selective, pH responsive guest recognition. The fact that the displacement can occur in aqueous buffered solutions makes the assay simple and highly biocompatible.

To analyse the scope of the array, and to determine how effective the array is at discriminating extremely small differences in target, we focused on a suite of synthetic small molecule targets. The array was constructed by incorporating the three cavitands (**1-3**) and their complexes with the two fluorescent guests (**4** and **5**) at different pHs (pH 3.3, 5.0, 7.4, and 9.0 for guest **4**; and pH 7.4 and 9.0 for guest **5**), with a total of 14 variables. The concentrations of cavitand and fluorescent guest were maintained at 4 and 3 μM, respectively. Variable pH was achieved by addition of 70 mM of the sodium citrate (pH

3.3), phosphate (pH = 5.0 and 7.4), and carbonate (pH 9.0). Figure 4.3 shows the initial small molecule targets for testing: these have large differences in some cases, with a series of NMe_3^+ (**6-13**) and $NHMe_2^+$ (**14-18**) anchors.

More subtle variations are also included in the two substrate pools, with the variations positioned such that they interact closely with the upper rims of cavitands **1-3**. These include cationic ammonium groups varying in position and pK_b (**8**, **9**), neutral, yet H-bonding groups (**6**, **7**), anionic guests (**10-12**), and guests with lipophilic chains (**13**). The NMe_2H^+ guests **14-18** mirror these variations as well. The guests were mixed with each sensor solution in 96-well plates at a fixed concentration of 100 μM, to ensure detectable displacement signal, even for very weak competitors. The fluorescence was measured in a plate reader before (F_{min}) and after mixing (F) and compared with the original fluorescence of **4** and **5** (F_{max}), to determine the % of guest displaced $(F-F_{min})/F_{max}$. Comparison of these percentages attained allows analysis of the relative affinities of the target guest screen, with greater displacement indicating higher target affinity. Even though **4** and **5** are much better guests than the small molecule targets, sufficient displacement occurs, allowing mechanistic analysis of the recognition process.

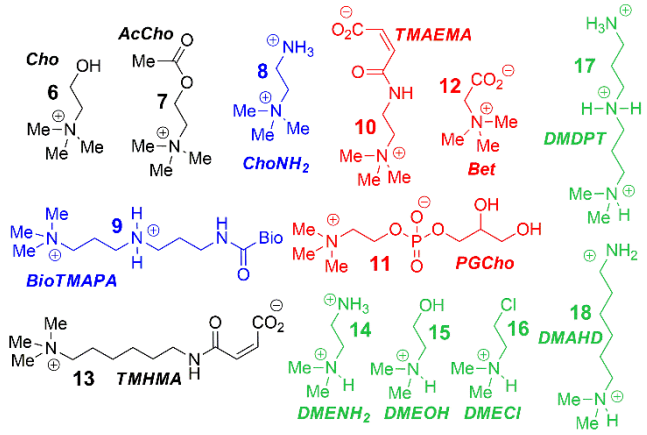

Figure 4.3 Small molecule guest scope.

The screening data shown in Figures 4.4 and 4.6 (as well as Figure S4.4) illustrate the sensitivity of the system to extremely small differences in guest properties. Figure 4.4a shows the simplest discrimination between two R-NMe_3^+ guests (choline **6** and cholamine **8**), and two less favoured R-NMe_2H^+ guests (N,N-dimethylethylenediamine **14** and N,N-dimethylethanolamine **15**), and provides a stark illustration of the effect of pH and cavitand type on four extremely similar guests. As expected,[23b] the maximal displacement of guest **4** from cavitand **1** occurs with the two R-NMe_3^+ guests, which show > 12% and ~8% increase upon addition of **6** and **8** respectively at pH 7.4. More displacement (22%) is seen at pH 9.0 for guest **6**. For cavitands **2** and **3**, which display stronger affinities to guest **4**, a lower overall percent displacement is obtained. Despite this, R-NMe_3^+ guests **6** and **8** gave greater displacement than the R-NMe_2H^+ guests **14** and **15** in general, which only displaced less than 5% of **4** at basic pH conditions and negligible or even negative changes at acidic pH conditions for all three hosts. This is consistent with their lower affinity for **1-3**, illustrating that discrimination between these large variations is simple.

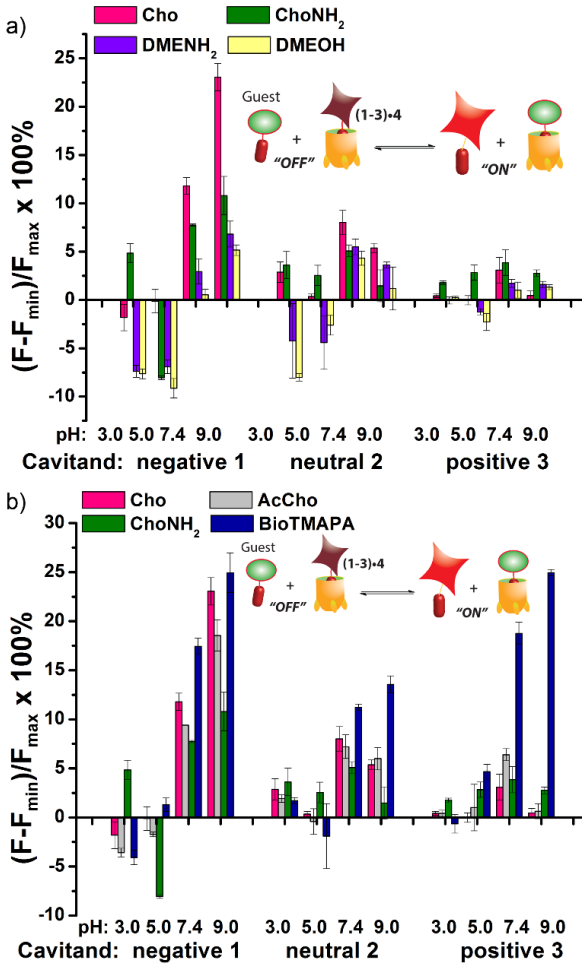

Figure 4.4 Small Molecule Indicator Displacement. a) R-NMe3+ vs RNMe2H+ discrimination for guests 6, 8, 14, 16; b) Discrimination between highly similar R-NMe3+ guests 6-9. Error bars calculated from three repeat experiments. For negative 1, [guest 4] = 3 μM and [c avitand **1**] = 4 μM, and for neutral **2** and positive **3**, [guest **4**] = 3 μM, [cavitand **2** or **3**] = 5 μM. [small molecule] = 100 μM.

Figure 4.4b shows the application of the array to more challenging discrimination between highly similar targets, namely four different R-NMe_3^+ guests: **6** and **8**, as well as acetylcholine **7** and ammonium BioTMAPA guest **9**. Variation of only a single group from OH (in **6**) to NH_2 (in **8**) leads to noticeable *pH-dependent* differences in binding, especially to cavitand **1,** even though the binding anchors are identical. In acidic media (both pH 3.3

and 5.0), minimal displacement of **4** was observed for all guests **6**-**9**. This could be partially attributed to the higher affinity of the fluorescent guest **4** to cavitand **1** at acidic pH than at higher pHs (see Figure 4.2b). At neutral and basic pH, much higher percentages of fluorophore **4** than that observed under the acidic conditions were displaced by **6**-**9** from all three hosts, with cavitand **1** showing the largest changes. The most interesting observation is that BioTMAPA **9** shows a larger displacement effect than choline **6** and acetylcholine **7** for **2** and **3**, even though the upper rims are ostensibly charge "mismatched".

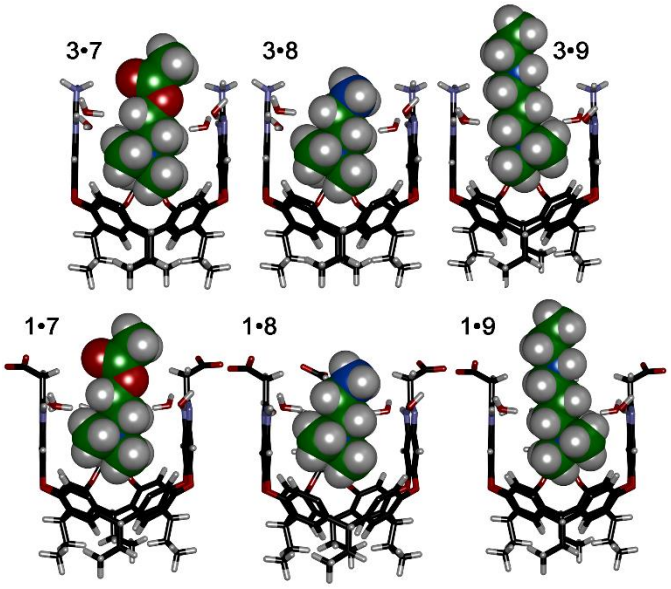

Figure 4.5 Minimized structures of the complexes between cavitands 1 and 3 (front walls removed for clarity), and guests 7, 8 and 9 (structure of 9 shortened for clarity), SPAR TAN, AM1 forcefield.

The interplay between solvation, charge matching effects and H-bonding between the four guests **6-9** and cavitands **1-3** is complex, and the individual effects on affinity are challenging to extract. The increase in host capabilities for neutral guests in neutral **2** at basic pH has been previously described as due to a "tightened" hydrogen bonding seam that shrinks the cavity size and increases non-covalent space-filling and CH-π interactions with bound guest.[27] However, both **1** and **3** contain upper rim groups that can also display variable protonation states, as can guests **8** and **9**. Variations in protonation state of some or all of the CO_2^-/CO_2H groups in **1**, or the NH_2/NH_3^+ groups in **3** in differing pH conditions, as well as variations in guest protonation state will affect the affinity. Figure 4.5 shows minimized structures of the complexes formed between hosts **1** and **3**, and guests **7-9**, and illustrates that these affinity variations are most likely due to upper rim charge matching, rather than variations in steric or shape-fitting effects. The NMe_3^+ group fits

snugly in the binding pocket, positioning the OH, NH_3^+ and NH_2R^+ groups of **6, 8** and **9** in proximity with the upper rim host functions. For example, the only difference in upper functionality between **8** and **9** is that the amine in **9** is more basic (calculated pKa for **9** is 9.81, and for **8** is 7.88) and is positioned one atom higher in the cavitand upon binding than **8**. At pH 7.4 when both **8** and **9** are protonated, the ammonium group in **9** is better positioned for favourable H-bonding and charge matching with the anionic CO_2^- groups in host **1**.

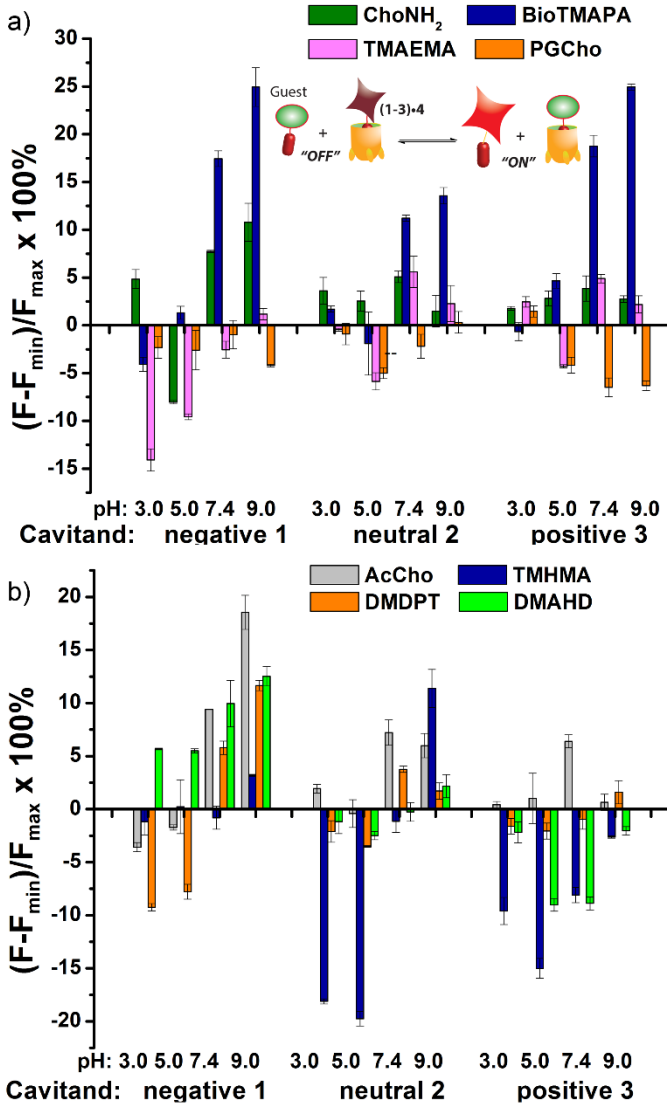

Figure 4.6 Small Molecule Indicator Displacement. a) Discrimination between anionic and cationic R-NMe3+ guests 8-11; b) Discrimination between neutral and lipophilic guests 7, 13, 17, 18. Error bars calculated from three repeat experiments. For negative 1, [guest **4**] = 3 µM and [cavitand **1**] = 4 µM, and for neutral **2** and positive **3**, [guest **4**] = 3 µM, [cavitand **2** or **3**] = 5 µM. [small molecule] = 100 µM.

The relatively large change in fluorescent signal upon displacement enabled the use of a competition assay for closer examination of the binding affinity of these compounds to cavitand **1**. By adding 0-5 mM of these small molecules to the mixture of **4** and **1** at fixed

concentrations under these two pHs, fluorescence vs [guest] titration curves were obtained. Using standard methods for determination of inhibitor binding constant in protein-ligand-inhibitor binding assays (see Experimental Section), the dissociation constants (K_i) of the complexes formed between cavitand **1** and guests **6**-**9** were calculated (see Table S4.2 for a list of calculated K_i values). The K_i for **9** (K_i = 10.5 μM) is greater than that of **8** (K_i = 16.5 μM) at pH 7.4. At pH 9.0, cholamine **8** is completely deprotonated, causing a mismatch that lowers the affinity dramatically (K_i = >100 μM). The more basic BioTMAPA **9** is still partially protonated at this pH and while its affinity drops, it is only lowered to 69.6 μM. The affinities of the upper rim-neutral choline **6** (K_i = 9.9, 10.2 μM) and acetylcholine **7** (K_i = 13.9, 11.4 μM) for cavitand **1** are unaffected by charge mismatching, and remain similar at both pH 7.4 and 9.0. Larger structural variations in guest lead to more obviously explainable affinity variations, as shown in Figure 4.6a. This series pairs guests with cationic groups at the upper rim (**8** and **9**) with guests displaying anionic groups (phosphatidyl-glycerol (PGCho) **11** and maleamate guest (TMAEMA) **10**). These effects are most pronounced for anionic host **1**. Whereas cationic guests **8** and **9** show strong affinity for **1**, these two anionic guests (**10** and **11**) positions its carboxyl or phosphate group directly at the carboxylates in **1** and shows no affinity at all under neutral and basic conditions for all three cavitands, suggesting that the phosphate or carboxyl group is also repelled by the electron-rich walls of the hosts.

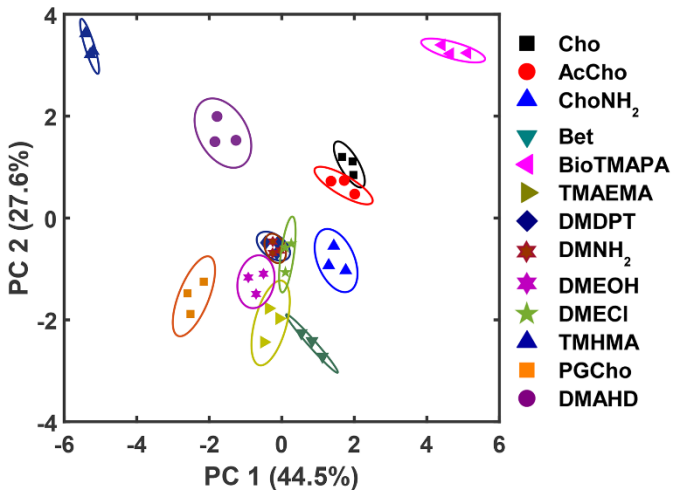

Figure 4.7 PCA plot for the small molecule screen. Each symbol represents one repeat of the measurement, and each molecule was tested 3 times, giving 3 identical symbols for each guest. The error ellipses were obtained at 95% confidence interval.

As well as shape, charge and H-bond matching between host and guest, either in the cavity or at the upper rim, other effects can occur under select conditions, leading to unusual displacement results, as shown in Figure 4.6b. Guests **13** (TMHMA) and **18** (DMAHD) are more lipophilic than their smaller counterparts, as they have n-hexyl groups in their interior structure. Addition of guest **13** at low pH causes a significant *lowering* of fluorescence, most notably with the complexes of **4** and cavitands **2** and **3**. This effect is also seen to a lesser extent with TMAEMA **10** with cavitand **1** (Figure 4.6a). Competitive binding of guest process causes the fluorescence of **4** to recover upon displacement, so the presence of *increased quenching* upon guest addition was surprising. However, this phenomenon can be explained by aggregative effects. The extra fluorescence decrease only occurs for lipophilic R-NMe_3^+ or R-NMe_2H^+ guest at acidic pH, conditions that neutralize the carboxylate group in **13**, for example. Protonated **13** is structurally similar to dodecyl-NMe_3^+, which is a surfactant and forms micelles at millimolar concentrations. Evidently

13 also forms micelles, which incorporate the **2•4** complex, causing additional aggregation-based quenching of **4**.[26] While unexpected, this phenomenon provides another variable for discrimination of lipophilic guests, one that is not dependent on cavity-based recognition.

The wide variety of individual effects at play in this system, from the pH-dependent affinity of the fluorophores for the different cavitands, to guest matching and mismatching with the host upper rims and unexpected aggregation effects, is illustrated by Principal Component Analysis (PCA), as shown in Figure 4.7. The scores plot was obtained by subjecting the displacement percentages measured with the rhodamine sensor to PCA. The responses acquired with the fluorescein sensor did not confer significant contribution to the final grouping effect and thus were not included in PCA. The first two principal components (PC) of the analysis summarized more than 70% of the total variance in the dataset, and successfully grouped the compounds based on their structural differences, with error ellipses shown, obtained at the 95% confidence interval. For instance, the three "strongest binders" (the $R–NMe_3^+$ guests **6, 7,** and **9**) locate in the upper-right panel, well separated from the $R–NHMe_2^+$ guests, as well as the more weakly bound $R–NMe_3^+$ guests (**8**, and **10-13**) by PC1 and PC2. Most of the $R–NHMe_2^+$ guests (**14-17**) locate close to each other, indicating that our sensors are not able to discriminate them due to their weak affinity to the hosts.

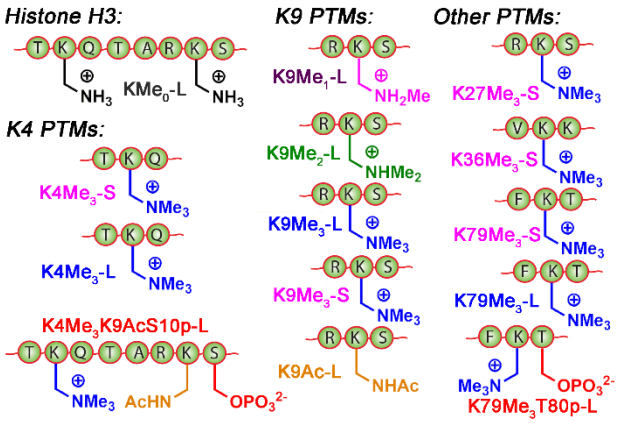

Figure 4.8 Variably modified peptides used in this study. L = 20/21 amino acid residues. S = 10-15 amino acid residues. See SI for full peptide sequences.

The small molecule screen illustrates the potency of the sensor system in detecting small differences in guest structure. By incorporating 3 different cavitands in 4 different pH environments, discrimination can be achieved between groups as similar as OH/NH_2, or even two different $R_2NH_2^+$ groups that display identical cavity binding handles. The sensitivity to non-cavity-based effects such as aggregation, H-bonding and charge matching is an encouraging sign of the array's ability to sense remote differences in target structure, not merely cavity-based recognition of a specific group. We next applied this sensor array to discriminate between various PTMs from peptides derived from Histone H3. The 14 peptides (see Table S4.3 for full peptide sequences) are illustrated in Figure 4.8, and provide a variety of challenges for discrimination by the sensor array. Some of the variations are quite large, such as varying the methylation state at K9 from 0/1/2/3 methyl groups ($K9Me_0$ - $K9Me_3$). Other differences are more subtle, including changing the position of the trimethylation PTM on the backbone. Five major methylation sites K4, K9, K27, K36, and K79 were analysed. The overall size of the peptide chain could be varied while retaining *identical* methylation level and position. For example, both 21 (denoted as

long, L) and 11 (short, S) amino acid fragments of $K4Me_3$, $K9Me_3$ and $K79Me_3$ were tested. Finally, non-methylation PTMs were tested including lysine acylations and serine/threonine phosphorylations, including the presence of remote dual or triple modifications on the same peptide. As the small molecule study showed weak response at acidic pHs, the peptide assay was performed in neutral (pH 7.4) and basic (pH 9.0) conditions only. In addition, as RhB guest was the most effective, the peptide assay only involved cavitands **1-3** and guest **4**. Side-by-side comparisons of the fluorescence recovery for the various different peptide groupings is shown in Figure 4.9, and the corresponding PCA analysis in Figure 4.10.

The initial test was the simplest: discriminate between varying methylation levels at the same position (Figure 4.9a). As predicted by the small molecule screen, the sensors showed excellent selectivity for different lysine methylation levels. The affinity of the tested peptides was far stronger than the small molecules, and only 10 μM peptide was added to the **1-3•4** sensors (as opposed to 1 mM small molecule) to give the responses shown in Figure 4.9. The control H3K9 peptides (1-21) displaying zero and mono-methylation at the K9 position caused negligible displacement with all of the cavitand **1-3•**RhB guest **4** sensors at this concentration. In contrast, as much as 10% and 15% of guest **4** was displaced by the di- ($K9Me_2$) and tri-methylated ($K9Me_3$) peptides at pH 9.0. The largest signal difference between $K9Me_2$ and $K9Me_3$ was observed with the negative cavitand **1**, although all three hosts showed significant discrimination.

The more challenging task is to discriminate *identical* modifications in different positions, and this is shown in Figure 4.9b, using the short peptides (10-15 amino acids)

with trimethylation PTMs at K4, K9, K27, K36, and K79. Cavitand **3** was not particularly effective at discriminating between these positionally variable KMe_3 modifications, but the other hosts were far more successful. The **1•4** sensor effectively discriminated three trimethylation sites at both pH 7.4 and 9.0, with the percent displacement decreasing between K4 > K27 > K36. However, negligible response was observed for $K9Me_3$-S and $K79Me_3$-S. Fortunately, the largest percent displacement in this case (~15%) was obtained with $K79Me_3$ and the neutral cavitand **2** at pH 9.0. While individual cavitands are not capable of fully discriminating the five different positional variations by themselves, the combination of the three hosts is successful.

These signal differences are interesting, as they illustrate the effects of remote structure on the recognition process. For example, the lysine residues at K9 and K27 share the same adjacent amino acids with the sequence of -RKS-, yet show significant displacement differences, especially with **1**. In addition, whereas the long, 21 amino acid $K9Me_3$ gave strong fluorescence recovery with **1•4**, the *short* 15 amino acid $K9Me_3$ showed no displacement of **4** and much lower affinity for **1**, despite the immediately adjacent amino acids and the KMe_3 binding target being identical. This suggests that other, *remote* factors are important components of the displacement, and those factors affect the differently functionalized hosts differently.

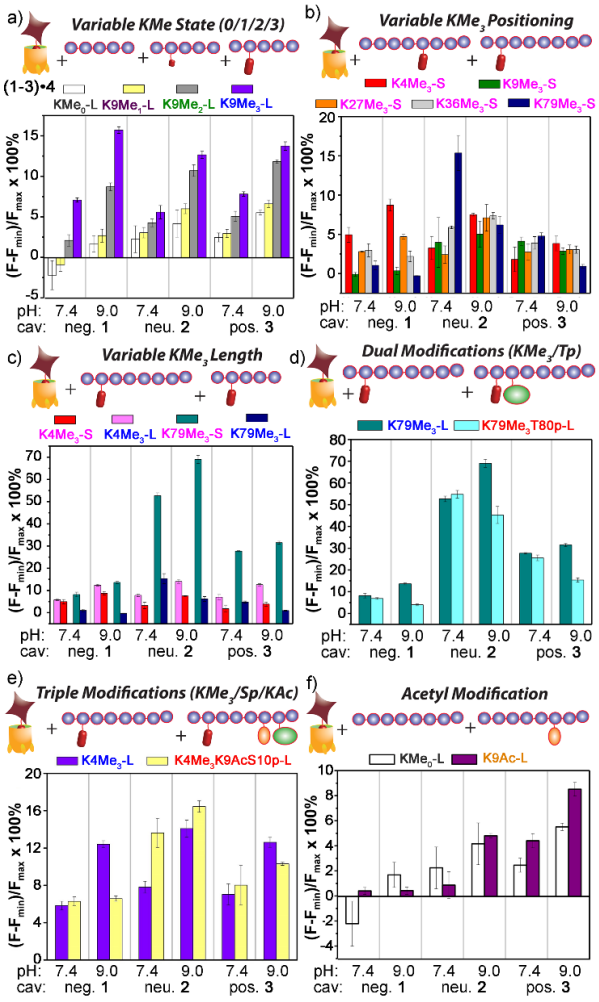

Figure 4.9 Peptide Discrimination via Fluorescence Recovery. Percent displacement plots grouped the peptides based on a) Lys methylation state; b) Lys methylation site; c) length; and presence of other modifications, such as d) nearby phosphorylation; e) remote acetylation and phosphorylation; and f) Lys acetylation in the absence of methylation. For negative **1**, [guest **4**] = 3 µM and [cavitand **1**] = 4 µM; and for neutral **2** and positive **3**, [guest **4**] = 3 µM, [cavitand **2** or **3**] = 5 µM. [peptide] = 10 µM.

The remote variations in peptide property suggested that the assay could be able to discriminate between identical modifications, at identical positions, in peptide fragments of varying length, as shown in Figure 4.9c. Short and long versions of $K4Me_3$ and $K79Me_3$ were tested, and again, a wide disparity in the effectiveness of the different cavitands was

observed. In this case, anionic cavitand **1** showed quite poor selectivity, but cationic **3** and especially neutral **2** showed exceptional discrimination between the different length peptides. K79Me$_3$-L (a.a. 69-89) caused almost 70% displacement of **4** from **2** at pH 9.0. This affinity is all the more remarkable for the fact that the short K79Me$_3$-S (a.a. 73-83) peptide shows almost zero displacement of **4** from **2**, despite the only variations in structure occurring remotely, over 6 amino acid residues distant from the host interaction! The K4Me$_3$ variants could be slightly discriminated, but far less effectively so.

As well as detecting remote changes in peptide structure, the sensor system can detect the presence of other, non-methylation modifications remote from the KMe$_3$ site, as shown in Figures 4.9d and 4.9e. Two multiply modified peptides were compared with their single KMe$_3$ equivalents. K79Me$_3$ contains an adjacent threonine residue, and so K79Me$_3$-L was tested against K79Me$_3$T80p-L. In addition, K4Me$_3$-L was compared with K4Me$_3$K9AcS10p-L. This variant has no differences in adjacent residues, but incorporates acetyl and phosphoryl groups at residues 9 and 10, remote from K4Me$_3$. Threonine phosphorylation in K79Me$_3$T80p-L decreased its affinity to all cavitands at pH 9.0 with respect to K79Me$_3$-L, most probably resulting from repulsion between the cavitand and the negatively charged phosphate group. The charge of the phosphate group appears not to be the overriding control factor, as the drop in signal was greatest for cavitand **2**: presumably the larger OPO_3^{2-} group provides a steric barrier to target binding.

These results indicate that the large, structurally variable peptides have more complex interactions with the hosts than the small molecules **6-18**. While the selectivity for KMe$_3$ is consistent with cavity-based recognition (Figure 4.9a), a solely host:guest type

interaction does not explain the sensitivity to peptide length, and suggests other factors are in play. These variables are most likely due to either (or both) charge and hydrophobicity variations. For example, K27Me$_3$-S has much higher hydrophobicity than the other short peptides used here (i.e. K4/9/36/79Me$_3$-S), as reflected by its GRAVY score, i.e. the hydrophobicity index for peptides calculated from the amino acid composition (see ESI Table S4.3). Hydrophobicity is not the only global factor to be considered: the pI of the peptides varies as well. K79Me$_3$-S has the lowest pI (4.56) among the 14 peptides tested and carries negative charge at neutral and basic pHs, while the other peptides have pIs close to or larger than 10 and are positively charged under the conditions of the assay. The specific examples from Figure 4.9c can also be compared: K79Me$_3$-L (a.a. 69-89) has a far higher hydrophobicity and positive charge (GRAVY = -0.518, pI = 9.98) than K79Me$_3$-S (a.a. 73-83, GRAVY -0.927, pI 4.56), commensurate with the large differences in displacement observed, especially with the **2•4** sensor. The less well-distinguished K4Me$_3$ pair are far more similar in charge/hydrophobicity as their pI and GRAVY scores are far closer (12.83, -1.448 for K4Me$_3$-L, 12.02, -1.890 for K4Me$_3$-L).

To provide a more accurate description of these unusual selectivities, fluorescence titration experiments similar to those performed for small molecules **6-9** were performed on the K79Me$_3$ peptide pairing shown in Figure 4.9d (i.e. K79Me$_3$T80p-L and K79Me$_3$) and neutral cavitand **2** (see Experimental Section and Figure S4.9). Interestingly, curve fitting analysis that assumes a 1:1 binding model was unsuccessful for these peptides. In contrast, the peptide curves fit very well to the Hill equation, indicating that a *multivalent* interaction is occurring, with multiple cavitands binding to a single peptide. The analysis

shows that phosphorylation at the adjacent amino acid does not change the microscopic association constant k between the peptide and host, but alters the binding cooperativity. The n value for K79Me$_3$-L binding to host **2** is 3.1, indicating positive cooperativity, but that of K79Me$_3$T80p-L reduces to 0.6, indicating negative cooperativity. The much large n value leads to the larger apparent K for peptide-cavitand binding. A similar phenomenon was also observed for binding between the long di- and trimethylated K9 peptides, K9Me$_2$-L and K9Me$_3$-L, to cavitand **1**, in which the n value changes from 2.3 to 0.8.

The low solubility of the cavitands (especially **2**) in water precludes analysis of exactly where the second interaction is occurring. These hosts are well-known to bind a range of lipophilic small molecules,[22] so interactions with exposed phenylalanine or leucine sidechains would be most likely. Other small molecule hosts show selectivity for Phe residues, so hydrophobic targeting is plausible, albeit much weaker than the NMe$_3^+$ residue binding. We have also previously shown that host **1** can bind proteins at membrane bilayer interfaces via charge-based interactions.[28] As the neutral cavitand **2** is the host that is most capable of non-KMe$_3$ recognition, however, it is most likely that hydrophobic association is the dominant factor here.

If the secondary modifications occurred on remote sites, as in K4Me$_3$K9AcS10p-L, the effect on target affinity was less predictable, but even more pronounced. The combination of acetylation and phosphorylation reduces the overall charge of the peptide, and K4Me$_3$K9AcS10p-L shows increased displacement of **4** from neutral cavitand **2** when compared to K79Me$_3$-L. This trend is similar to what observed between the low pI peptide H3K79Me$_3$-S and the other high pI peptides in Figure 4.9b: the drop in peptide positive

charge increased the percent displacement with the neutral cavitand. The effect was reversed with anionic cavitand **1** at pH 9.0, however, with K79Me_3-L showing stronger affinity than K4Me_3K9AcS10p-L. Again, varying the nature of cavitand has often contradictory effects on the affinity of remotely varied peptides. The origin of the selectivity is not always immediately apparent, but combining these effects into a single array allows for exquisite, almost antibody-like reading of epigenetic markers in Histone fragments.

These results introduce another question: our original assumption was that the cavitand required a substrate with an NMe_3^+ (or at least NMe_2H^+) group to effect displacement of **4**. Can the system detect non-methylation PTMs? This was tested with the control H3 peptide and H3K9Ac (Figure 4.9f). In this case, no NMe_3^+ groups are present at all, but the two peptides display different charge states in solution. Interestingly, cavitand **1** was incapable of discrimination, but cavitands **2** (at pH 9.0) and **3** (at both pH values) showed observable, albeit small, differences in fluorescence recovery between H3 and H3K9. These more hydrophobic hosts were far more sensitive to peptide hydrophobicity, and the multivalent association modes allowed remote discrimination between targets.

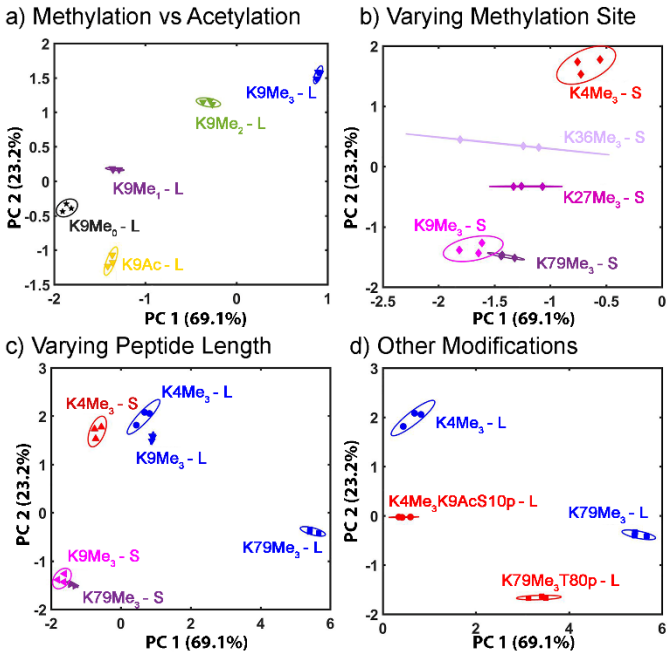

Figure 4.10 Peptide Discrimination PCA. Zoom-in scores plot for peptides a) with various degrees of methylation or acetylation; b) with varying methylation sites; c) with different peptide lengths; d) with phosphorylation and/or acetylation near the trimethylated site. Note - shapes/colors in a) correspond to the peptide assignment in b-d). The error ellipses were obtained at 95% confidence interval.

The displacement plots were also analyzed via PCA (see Figure 4.10 and ESI). The large impact on the target binding due to peptide size causes a clustering effect in the full peptide PCA panel (see ESI for full PCA plot). This full screen uses the signals from all cavitands **1-3**, with guest **4**, at pH 7.4 and 9.0. In this global screen, the short trimethylated peptides locate on the same panel as the long, non-, mono-, di-methylated, or acetylated peptides. The first PC summarizes more than 75% of the overall variance of the data set, PC 1, shows exceptional discrimination between that peptide series and the trimethylated long peptides. If PCA was carried out on separated groups of peptides, i.e., the long and short groups, clear separation of peptides carrying different levels of methylation and varied modifications was achieved on the scores plots (Figure 4.10). Separation of different

methylation states was simple and clear, as expected (Figure 4.10a). Methylation state is easily discriminated by both PC 1 and PC 2 (Figure 4.10b). For the long peptides (Figure 4.10c), the trimethylated peptides locate on the right panel, separated from those with lower levels of methylation or acetylation by PC1, which represents the major trend of the data and indicates that our array is most powerful at discriminating different methylation levels, as expected. The vertical axis, PC 2, is most effective at separating different modification positions: little variation in PC 1 is observed for K4/9/27/36/79Me_3, but they are highly variable in PC 2. In addition, PC 2 is most effective at separating other modifications (Figure 4.10d). Additional phosphorylation and/or acetylation also moves the peptide downward, i.e. their PC2 values become more negative. The subtle changes in the displacement data from Figure 4.9 are easily distinguished in the PCA, illustrating the power of the sensing system for small changes in peptide PTMs.

Conclusion

In conclusion, we have shown that variably functionalized self-folding deep cavitands are capable of highly selective discrimination between substrates containing small, or remote structural differences. Multiple different factors contribute to this discrimination: the hosts contain both a deep, electron-rich cavity that is capable of selective R-NMe_3^+ binding and charged upper rim functional groups, conferring dual-mode selectivity on target recognition. By pairing the hosts with strongly bound fluorescent indicators, a pH responsive fluorescence displacement assay can be created, which combines variable fluorophore affinity with variable guest binding in different pH conditions to provide a highly sensitive assay. The lipophilic nature of the hosts also introduces a self-aggregative

quenching phenomenon that adds an additional variable to the arrayed sensor. Principal component analysis provides a simple method of target discrimination. The range of targets that can be analysed is extensive: small molecules with single atom variations in structure can be differentiated, centred around a R-NMe_3^+ motif.

The system is most effective when analysing histone peptide post-translational modifications. By employing an arrayed suite of different host molecules, positionally selective recognition of peptide PTMs is possible. The hosts are capable of discriminating between different lysine methylation states, as expected, but are also affected by remote changes in peptide hydrophobicity and overall charge, allowing differentiation of identical methylation PTMs at varying positions on the peptide. Varying adjacent amino acid residues can be discriminated by the combined sensor array, allowing detection of variables remote to the targeted binding site, and this effect can be extended to the detection of non-methylation PTMs such as phosphorylation or acetylation. In addition, the sensor is affected by global changes in structure, so is capable of discriminating between identical PTMs, at identical positions on amino acid fragments that vary only in peptide backbone length. Binding selectivity for small molecule synthetic receptors is usually limited to recognition of the targeted function, but in this arrayed system, the synergistic application of multiple variables allows dual-mode deep cavitands to approach levels of recognition selectivity usually only seen with natural antibodies. Further applications of this sensor system to the recognition of protein modifications in cellular extracts are underway in our laboratories.

Experimental section

General. Molecular modelling (semi-empirical calculations) was performed using the AM1 force field using SPARTAN. Cavitands 1[23b] and 2,[24] and guest 5[25] were synthesized according to literature procedures. See ESI for synthesis and characterization of new molecules (3, 4, 9, 10, 13). Solvents were dried through a commercial solvent purification system (Pure Process Technologies, Inc.). All Histone H3 (purity > 95%) peptides were purchased from Anaspec and used as received. All curve fittings were performed with Origin 8.0. PCA was performed with XLSTAT (Addinsoft) with default settings. Scores plots with error ellipses were created in MatLab.

Measurement of fluorescence quenching and guest-cavitand binding. The quenching assay was carried out by mixing 10 μL of the fluorescent guest 4 (30 μM), 10 μL of the cavitand (1, 2, or 3) (0 – 400 μM), 70 μL of the incubation buffer at a selected pH in the 96-well plate, adding water to bring the total volume up to 100 μL, and incubating with mild shaking for 15 mins. Variable pH was obtained by adding 70 mM (final concentration in the mixture) sodium salt of citrate (pH 3.3), phosphate (pH 5.0 and 7.4), and carbonate (pH 9.0). The fluorescence signal (F) was recorded in a Perkin Elmer Wallac 1420 Victor 2 Microplate Reader (PerkinElmer) with the Ex/Em wavelengths at 530/605 nm. Dissociation constants were obtained by the Stern-Volmer equation,[29] with F_0 being the fluorescence with no cavitand:

$$F_0/F = 1 + 1/K_d\,[\text{Cavitand}]$$

Small molecule and peptide screening and K_i calculation. The fluorescence displacement assay was conducted with a 96-well plate. Each well contained the sensor

solution – a mixture of 10 μL of the fluorescent guest 4 (30 μM), 10 μL of the cavitand (1 at 40 μM; 2 or 3 at 50 μM), and 70 μL of the buffer (pH 3.3, 5.0, 7.4, and 9.0 obtained with the same buffer components as described above). Then 10 μL of H_2O (as the control for obtaining the minimum fluorescence, F_{min}), the peptide (100 μM), or the small molecule guest (1 mM) was added to each well. There were also wells containing guest 4 or 5 under the exact buffer environment but no cavitand or competitor added, for measurement of F_{max}. The fluorescence was acquired after 15 minutes' incubation under mild shaking. For small molecules, the displacement assay was also performed with the sensor formed between the cavitand 1 and fluorescent guest 5 at pH 7.4 and 9.0, following the exact same procedure.

To achieve the fluorescence recovery curves for K_d measurement of selected competitors, i.e. the small molecule 6-9, or the peptide series of H3K9 ($K9Me_0$, Me_1, Me_2, and Me_3) and H3K79 ($K79Me_3$ and $K79Me_3T80p$), 10 μL of the competitor solution was added to the sensor solution (at pH 7.4 or 9.0) to obtain the final concentration of 0 - 5 mM (for small molecules) or 0 – 20 μM.

Calculation of the K_d of the small molecule guest 6-8 followed the typical approach for determination of inhibitor binding constant in protein-ligand-inhibitor binding assays:[30] firstly, the titration curve of fluorescence against small molecule concentration were obtained; then the IC_{50} value (the "inhibitor" concentration giving half maximum response) was obtained by fitting the curve to the exponential decay equation:

$$F = A * \exp(- [guest]/t_1)$$

where IC_{50} = ln (1/2) * t_1. At last, the K_i value which is equivalent to the dissociation constant of the complex formed by the small molecule and the cavitand was obtained by the following equation:

$$K_i = IC_{50} / ([L]_{50} / K_d + [cavitand]_0 / K_d + 1)$$

where $[L]_{50}$ is the concentration of the free small molecule at 50% inhibition (approximated to be the starting small molecule concentration), $[cavitand]_0$ is the cavitand concentration at 0% inhibition, and K_d is the dissociation constant for the cavitand 1 - guest 4 complex.

To evaluate peptide binding to the cavitand, we assumed one peptide could bind to multiple cavitands, and the equilibrium constant k was obtained by fitting with the fluorescence vs. [peptide] to the Hill equation:

$$F = F_{min} + (F_{max} - F_{min}) * [peptide]^n/(k^n + [peptide]^n).$$

The “n” represents binding cooperativity.

Reference

(1) (a) Davidson, V. L. Biochemistry 2007, 46, 5283-5292. (b) O'Mal-ley, B. W.; Qin, J.; Lanz, R. B. Curr. Opin. Cell Biol. 2008, 20, 310-315. (c) Woodsmith, J.; Stelzl, U. Curr. Opin. Struct. Biol. 2014, 24, 34-44.

(2) (a) Cerny, M.; Skalak, J.; Cerna, H.; Brzobohaty, B., J. Proteomics 2013, 92, 2-27. (b) Olsen, J. V.; Mann, M., Mol. Cell. Prot. 2013, 12, 3444-3452.

(3) Smith, L.C.; Leach, D.G.; Blaylock, B.E.; Ali, O.A.; Urbach, A.R. J. Am. Chem. Soc. 2015, 137, 3663-3669

(4) (a) Kimura, H.; Hayashi-Takanaka, Y.; Goto, Y.; Takizawa, N.; Nozaki, N. Cell Struct. Funct. 2008, 33, 61–73. (b) Rothbart, S.B.; Dickson, B.M.; Raab, J.R.; Grzybowski, A.T.; Krajewski, K.; Guo, A.H.; Shanle E.K.; Josefowicz, S.Z.; Fuchs, S.M.; Allis, C.D.; Magnuson, T.R.; Ruthenburg, A.J.; Strahl, B.D. Mol. Cell. 2015, 59, 502-511. (c) Hattori, T.; Taft, J.M.; Swist, K.M.; Luo, H.; Witt, H.; Slattery, M.; Koide, A.; Ruthenburg, A.J.; Krajewski, K.; Strahl, B.D.; White, K.P.; Farnham, P.G.; Zhao, Y.; Koide, S. Nat. Methods 2013,10, 992-995. (d) Egelhofer, T.A.; Minoda, A.; Klugman, S.; Lee, K.; Kolasinska-Zwierz, P.; Alekseyenko, A.A.; Cheung, M.-S.; Day, D.S.; Gadel, S.; Gorchakov, A.A. et al. Nat. Struct. Mol. Biol. 2011, 18, 91-93.

(5) Hayashi-Takanaka, Y.; Yamagata, K.; Wakayama, T.; Stasevich, T.J.; Kainuma, T.; Tsurimoto, T.; Tachibana, M.; Shinkai, Y.; Kurumizaka, H.; Nozaki, N.; Kimura, H. Nucleic Acids Res. 2011, 39, 6475-6488.

(6) (a) Rekharsky, M.V.; Inoue, Y. Chem. Rev. 1998, 98, 1875-1917. (b) Breslow, R.; Yang, Z.; Ching, R.; Trojandt, G.; Odobel, F. J. Am. Chem. Soc. 1998, 120, 3536-3537.

(7) (a) Ingerman, L. A.; Cuellar, M. E.; Waters, M. L. Chem. Commun. 2010, 46, 1839-1841. (b) Pinkin, N. K.; Waters, M. L. Org. Biomol. Chem. 2014, 12, 7059-7067.

(8) (a) Barrow, S.J.; Kasera, S.; Rowland, M.J.; del Barrio, J.; Scherman, O.A. Chem. Rev. 2015, 115, 12320-12406. (b) Gamal-Eldin, M.A.; Macartney, D.H. Org. Biomol. Chem. 2013, 11, 1234–1241.

(9) (a) McGovern, R.E.; Fernandes, H.; Khan, A.R.; Power, N.P.; Crow-ley, P.B. Nat. Chem. 2012, 4, 527-533. (b) Norouzy, A.; Azizi, Z.; Nau, W.M. Angew. Chem. Int. Ed. 2015, 54, 792–795. (c) Minaker, S.A.; Daze, K.D.; Ma, M.C.F.; Hof, F. J. Am. Chem. Soc. 2012, 134, 11674−11680. (d) Garnett, G.A.E.; Starke, M.J.; Shaurya, A.; Li, J.; Hof, F. Anal. Chem. 2016, 88, 3697−3703.

(10) (a) Daze, K.D.; Hof, F. Acc. Chem. Res. 2013, 46, 937–945. (b) Daze, K.D.; Pinter, T.; Beshara, C.S.; Ibraheem, A.; Minaker, S.A.; Ma, M.C.; Courtemanche, R.J.; Campbell,

R.E.; Hof, F. Chem. Sci. 2012, 3, 2695–2699. (c) Daze, K.D.; Ma, M.C.; Pineux, F.; Hof, F. Org. Lett. 2012, 14, 1512–1515.

(11) Lucas, D.; Minami, T.; Iannuzzi, G.; Cao, L.; Wittenberg, J. B.; An-zenbacher, P., Jr.; Isaacs, L. J. Am. Chem. Soc. 2011, 133, 17966-17976.

(12) Conway, J.H.; Fiedler, D. Angew. Chem. Int. Ed. 2015, 54, 3941–3945.

(13) (a) Hennig, A.; Bakirci, H.; Nau, W.M. Nat. Methods 2007, 4, 629-632. (b) You, L.; Zha, D.; Anslyn, E.V. Chem. Rev. 2015, 115, 7840−7892.

(14) Wright, A.T.; Griffin, M.J.; Zhenlin, Z.; McCleskey, S.C.; Anslyn, E.V.; McDevitt, J.T. Angew. Chem. Int. Ed. 2005, 44, 6375-6378.

(15) (a) Zhang, T.; Edwards, N.Y.; Bonizzoni, M.; Anslyn, E.V. J. Am. Chem. Soc. 2009, 131, 11976-11984. (b) Wright, A.T.; Anslyn, E.V.; McDevitt, J.T. J. Am. Chem. Soc. 2005, 127, 17405-17411.

(16) Edwards, N.Y.; Sager, T.W.; McDevitt, J.T.; Anslyn, E.V. J. Am. Chem. Soc. 2007, 129, 13575-13583.

(17) (a) Ghale, G.; Nau, W.M. Acc. Chem. Res. 2014, 47, 2150-2159. (b) Umali, A. P.; Anslyn, E.V. Curr. Opin. Chem. Biol. 2010, 14, 685–692.

(18) (a) Jiang, Z.; Le, N.D.B.; Gupta, A.; Rotello, V.M. Chem. Soc. Rev. 2015, 44, 4264-4274. (b) Ashby, J.; Flack, K.; Jimenez, L.A.; Duan, Y.; Khatib, A.-K.; Somlo, G.; Wang, S.E.; Cui, X.; Zhong, W. Anal. Chem. 2014, 86, 9343-9349.

(19) Jurs, P.C.; Bakken, G.A.; McClelland, H.E. Chem. Rev. 2000, 100, 2649–2678.

(20) (a) Hooley, R.J.; Restorp, P.; Rebek, J., Jr. Chem. Commun. 2008, 44, 6291-6293. (b) Mettry, M.; Moehlig, M.P.; Hooley, R.J. Org. Lett. 2015, 17, 1497-1500.

(21) (a) Lagona, J.; Mukhopadhyay, P.; Chakrabarti, S.; Isaacs, L. An-gew. Chem. Int. Ed. 2005, 44, 4844-4870. (b) Rekharsky, M. V.; Mori, T.; Yang, C.; Ko, Y. H.; Selvapalam, N.; Kim, H.; Sobransingh, D.; Kaifer, A. E.; Liu, S. M.; Isaacs, L.; Chen, W.; Moghaddam, S.; Gilson, M. K.; Kim, K. M.; Inoue, Y. Proc. Natl. Acad. Sci. U.S.A. 2007, 104, 20737-20742.

(22) Hooley, R.J.; van Anda, H.J.; Rebek, J., Jr. J. Am. Chem. Soc. 2007, 129, 13464-13473.

(23) (a) Hof, F.; Trembleau, L.; Ullrich, E. C.; Rebek, J., Jr. Angew. Chem. Int. Ed. 2003, 42, 3150-3153. (b) Biros, S. M.; Ullrich, E. C.; Hof, F.; Trembleau, L.; Rebek, J., Jr. J. Am. Chem. Soc. 2004, 126, 2870-2876.

(24) Rafai Far, A.; Shivanyuk, A.; Rebek, J., Jr. J. Am. Chem. Soc. 2002, 124, 2854-2855.

(25) Soberats, B.; Sanna, E.; Martorell, G.; Rotger, C.; Costa, A. Org Lett. 2014, 16, 2480-2483.

(26) Liu, Y.; Perez, L.; Mettry, M.; Easley, C.J.; Hooley, R.J.; Zhong, W. J. Am. Chem. Soc. 2016, 138, 10746–10749.

(27) Schramm, M.P.; Hooley, R.J.; Rebek, J., Jr. J. Am. Chem. Soc., 2007, 129, 9773-9779.

(28) Ghang, Y.-J.; Perez, L.; Morgan, M. A.; Si, F.; Hamdy, O. M.; Beecher, C. N.; Larive, C. K.; Julian, R. R.; Zhong, W.; Cheng, Q.; Hooley, R. J. Soft Matter 2014, 10, 9651-9656.

(29) Lakowicz, J.R. in Principles of Fluorescence Spectroscopy, Springer US, 2006, pp 277-330.

(30) (a) Hulme, E.C.; Birdsall, N.J.M. Strategy and Tactics in Receptor-Binding Studies. In Receptor–Ligand Interactions: A Practical Ap-proach, Hulme, E.C. ed., Oxford University Press, 1992, pp 63–176. (b) Cer, R. Z.; Mudunuri, U.; Stephens, R.; Lebeda, F. J. Nucleic Acids Res. 2009, W441–W445.

Supporting Information

1.General Information

^{1}H and ^{13}C NMR spectra were recorded on either a Varian Inova 400 MHz NMR spectrometer, or a Bruker 500 MHz NMR spectrometer. All NMR spectra processed using MestReNova by Mestrelab Research S.L. Proton (^{1}H) chemical shifts are reported in parts per million (δ) with respect to tetramethylsilane (TMS, δ=0), and referenced internally with respect to the protio solvent impurity. ^{13}C chemical shifts are reported in parts per million (δ) and referenced internally with respect to ^{12}C solvent signal. Deuterated NMR solvents were obtained from Cambridge Isotope Laboratories, Inc., Andover, MA, and used without further purification. Mass spectra were recorded by electrospray ionization on an LTQ-XL linear ion trap mass spectrometer (Thermo Scientific, San Jose, CA). MALDI spectra were obtained using an AB Sciex TOF/TOF 5800 MALDI mass spectrometer with positive ion mode. Infrared spectra were recorded on a Bruker Alpha FTIR spectrometer. Melting points were collected using the melting point apparatus from Stanford Research Systems (SRS) Digimelt MPA 160. All materials were purchased from Sigma Aldrich (St. Louis, MO), Fisher Scientific (Fairlawn, NJ), or TCI (Tokyo, Japan) and were used as received.

2. Experimental Procedures

Synthesis of New Molecules:

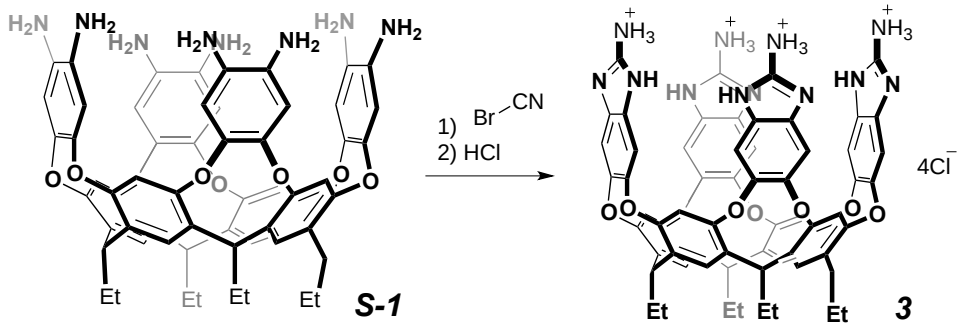

Ammonium Cavitand 3: Following a procedure slightly modified from published methods:[1] Octaamine cavitand ***S-1*** (454 mg, 0.44 mmol) in EtOH was stirred for 15 min at room temperature under N_2 atmosphere. A solution of cyanogen bromide (300 mg, 2.83 mmol) in EtOH was added drop wise over 15 min. The reaction mixture was stirred for 24 h at room temperature. The mixture was then cooled to 0 ^{o}C and basified to pH ~9. Solvent was removed by rotatory evaporation. The solid was redissolved in MeOH and 2 drop of 1M HCl was added, a white precipitate was formed. The cavitand was obtained as red solid (232 mg, 45% yield). ^{1}H NMR (500 MHz, DMSO-d_6), δ: 12.1 (s, 8H), 8.7 (s, 8H), 7.79 (s, 4H), 7.74 (s, 8H), 7.65 (s, 4H), 5.33 (t, J = 7.8 Hz, 4H), 2.24 (m, 8 H), 0.85 (t, J = 7.2 Hz, 12H); ^{13}C NMR (125 MHz, DMSO-d_6) δ: 155.9, 152.0, 148.7, 135.6, 127.1, 125.3, 117.1, 107.4, 35.7, 25.2, 19.8, 12.4; m.p. > 300 ^{o}C (decomp). MALDI-MS: $C_{64}H_{53}N_{12}O_8^+$ [M - 4Cl - 3H]$^+$: expected: 1117.4104; found: 1117.3110. Data is consistent with previous publication.[1]

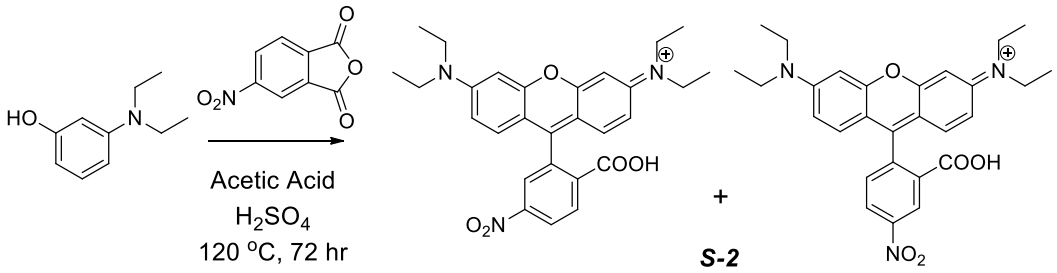

5/6 Nitro Rhodamine B S-2: To a stirred solution of 3-diethylaminophenol (1.0 g, 5.18 mmol) in glacial acetic acid (100 ml) was added concentrated H_2SO_4 catalyst (5-drops) followed by 4-nitrophthalic anhydride (1.71 g, 10.36 mmol). The reaction mixture was refluxed for 72 h. After cooling, the reaction was diluted into water (300 ml) and extracted with DCM (30 ml × 3). The solvent (DCM) was removed *in vacuo* to afford a mixture (47:53 %) of 5/6-nitro rhodamine B ***S-2*** (43%, 1.09g, 2.23 mmol) as a dark purple solid. ^{1}H NMR (400 MHz, $CDCl_3$, 25 °C, $CDCl_3$ = 7.26 ppm): 5-Nitro-rhodamine B: δ (ppm) = 12.33 (s, 1H), 9.11 (dd, *J* = 10.8, 2.3 Hz, 1H), 8.48 – 8.45 (m, 1H), 8.43 (dd, *J* = 8.3, 2.2 Hz, 1H), 8.24 (d, *J* = 8.6 Hz, 1H), 7.11 (d, *J* = 9.5 Hz, 1H), 6.91 (dd, *J* = 8.2, 2.1 Hz, 1H), 6.82 (t, *J* = 5.8 Hz, 1H), 6.16 – 6.10 (m, 2H), 3.35 (t, *J* = 7.1 Hz, 8H), 1.16 (q, *J* = 6.9 Hz, 12H). 6-Nitro-rhodamine B: δ (ppm) = 12.28 (s, 1H), 8.93 (d, *J* = 2.3 Hz, 1H), 8.33 (dd, *J* = 8.6, 2.2 Hz, 1H), 8.20 (t, *J* = 2.4 Hz, 1H), 7.53 (d, *J* = 8.3 Hz, 1H), 7.05 (d, *J* = 9.4 Hz, 1H), 6.75 (d, *J* = 9.1 Hz, 1H), 6.72 (d, *J* = 2.1 Hz, 1H), 6.05 (td, *J* = 9.0, 2.5 Hz, 2H), 3.37 (t, *J* = 7.1 Hz, 8H), 1.16 (q, *J* = 6.9 Hz, 12H). Data is consistent with previous publication.[1]

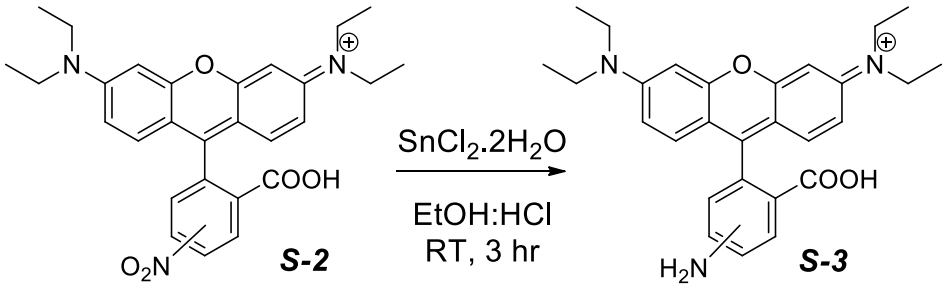

5/6 Amino Rhodamine B S-3: 5/6-nitro-rhodamine B ***S-2*** (1.09g, 2.23 mmol) was dissolved in EtOH:HCl (4:1, 50ml) along with $SnCl_2 \cdot 2H_2O$ (1.01g, 4.47 mmol). The resulting mixture was stirred at room temperature for 3 h, followed by dilution into H_2O (100 ml) and extraction with DCM (10 ml × 3). The solvent (DCM) was removed *in vacuo* to afford a mixture (51:49 %) of 5/6-amino-rhodamine B chloride as a deep magenta solid (90%, 0.92 g, 2.01 mmol). ^{1}H NMR (400 MHz, $CDCl_3$, 25 °C, $CDCl_3$ = 7.26 ppm): 5-Amino-rhodamine B: δ (ppm) = 12.49 (s, 1H), 8.93 (d, *J* = 1.8 Hz, 1H), 8.46 (d, *J* = 1.9 Hz, 1H), 7.91 (d, *J* = 8.6 Hz, 1H), 6.93 (d, *J* = 9.1 Hz, 1H), 6.76 (s, 1H), 6.69 (d, *J* = 2.2 Hz, 1H), 6.14 (dd, *J* = 8.0, 2.2 Hz, 3H), 3.42 – 3.34 (m, 8H), 1.19 (dd, *J* = 11.7, 7.0 Hz, 12H). 6-Amino rhodamine B: δ (ppm) = 12.24 (s, 1H), 8.44 (d, *J* = 1.9 Hz, 1H), 7.55 (d, *J* = 8.3 Hz, 1H), 6.83 (d, *J* = 8.8 Hz, 1H), 6.74 (s, 1H), 6.67 (d, *J* = 2.3 Hz, 1H), 6.50 (d, *J* = 2.2 Hz, 1H), 6.10 – 6.02 (m, 3H), 3.42 – 3.34 (m, 8H), 1.19 (dd, *J* = 11.7, 7.0 Hz, 12H). ESI-MS: *m/z* for $C_{28}H_{32}N_3O_3$ (M^+) calculated 458.2438, found 458.2668. Data is consistent with previous publication.[1]

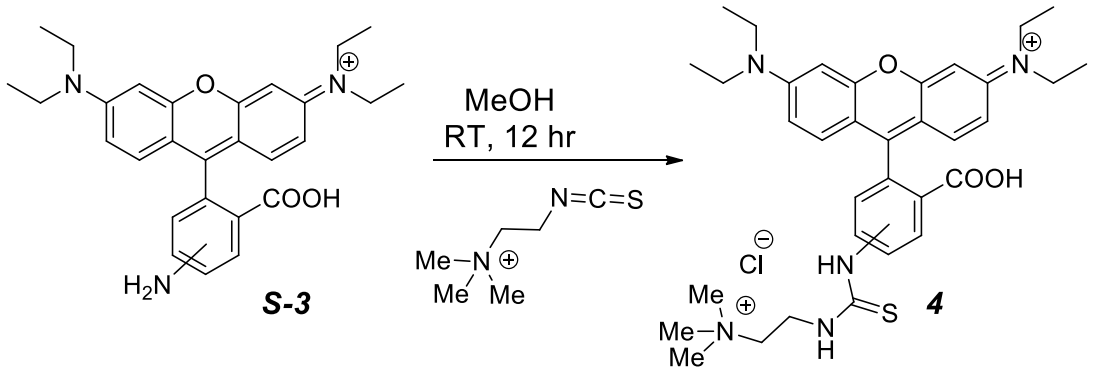

5/6 Rhodamine B guest 4: 5/6-Amino-Rhodamine B ***S-3*** (25 mg, 0.05 mmol) along with 2-isothiocyanato-N,N,N-trimethylethanaminium iodide[3] (15 mg, 0.05 mmol) was dissolved in MeOH (3 ml), and the resulting mixture was stirred at room temperature for 12 h. The solvent was removed *in vacuo* to yield the Rhodamine B Guest **4** as a bright purple solid. ^{1}H NMR (400 MHz, DMSO-d_6, 25 $^\circ$C, DMSO-d_6 = 2.50 ppm): Para-rhodamine B Guest (**4**): δ (ppm) = 12.59 (s, 1H), 12.23 (s, 1H), 8.65 (d, *J* = 2.3 Hz, 1H), 8.39 (dd, *J* = 6.1, 3.9 Hz, 1H), 7.70 (d, *J* = 8.5 Hz, 1H), 7.11 (d, *J* = 10.7 Hz, 1H), 6.90 – 6.85 (m, 1H), 6.81 (d, *J* = 3.2 Hz, 1H), 6.36 (d, *J* = 2.3 Hz, 1H), 6.21 (d, *J* = 2.4 Hz, 1H), 6.20 – 6.14 (m, 2H), 3.90 (s, 9H), 3.40 (t, *J* = 6.9 Hz, 2H), 3.17 (q, *J* = 6.9 Hz, 8H), 1.21 (t, *J* = 6.9 Hz, 2H), 1.10 (t, *J* = 6.9 Hz, 12H). Meta-rhodamine B Guest (**4**): δ (ppm) = 12.50 (s, 1H), 12.18 (s, 1H), 8.49 (dd, *J* = 8.3, 2.4 Hz, 1H), 7.93 (d, *J* = 8.5 Hz, 1H), 7.60 (d, *J* = 2.0 Hz, 1H), 6.97 (d, *J* = 9.5 Hz, 1H), 6.83 (d, *J* = 3.3 Hz, 1H), 6.63 (dd, *J* = 8.6, 2.3 Hz, 1H), 6.09 (d, *J* = 2.5 Hz, 2H), 6.07 (d, *J* = 2.4 Hz, 1H), 6.03 (d, *J* = 2.4 Hz, 1H), 3.90 (s, 9H), 3.38 (t, *J* = 6.9 Hz, 2H), 3.17 (q, *J* = 6.9 Hz, 8H), 1.21 (t, *J* = 6.9 Hz, 2H), 1.10 (t, *J* = 6.9 Hz, 12H). MALDI-TOF MS: *m/z* $C_{34}H_{47}ClN_5O_4S$ ($[M+Cl+H_2O]^+$) calculated 656.3032, found: 656.0713.

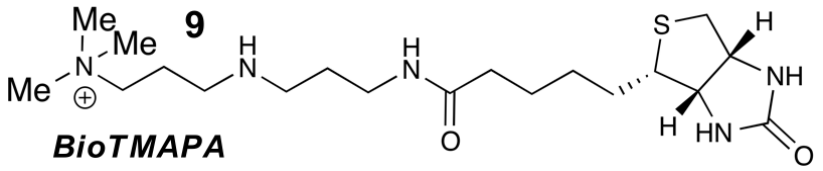

N^1-(3-biotinamidopropyl)-N^3,N^3,N^3-trimethylpropane-1,3-diaminium Iodide (BioTMAPA) 9: To a stirred solution of NHS Biotin (100 mg, 0.293 mmol) in dry THF (3 mL) under nitrogen was added N,N-dimethyl-propylenediamine (0.296 mmol). The reaction mixture was stirred at room temperature for 18 h, then concentrated via solvent removal *in vacuo*, followed by trituration with diethyl ether and hexanes. The resulting precipitate was vacuum filtered, washed with diethyl ether then hexanes, before being dried under vacuum. The solid was redissolved in dry THF (2 mL) under nitrogen, followed by the addition of iodomethane (41.6 mg, 18.2 µL, 0.293 mmol). The reaction mixture was stirred at room temperature for 4 h, then triturated with dry dichloromethane and hexanes. The precipitate was vacuum filtered, yielding a white solid (85 mg, 55% yield). ^{1}H NMR (400 MHz, D_2O): δ 4.63 (td, *J* = 8, 4 Hz, 1H), 4.46 (td, *J* = 8, 4 Hz, 1H), 3.47 (m, 2H), 3.35 (m, 2H), 3.32 (t, *J* = 7 Hz, 2H), 3.20 (s, 10H), 3.12 (t, J = 7, 2H), 3.06 (m, 4H), 2.31 (t, *J* = 7 Hz, 2H), 1.89 (m, 2H), 1.66 (m, 4H), 1.44 (m, 2H). ^{13}C NMR (100 MHz, DMSO-d_6): δ 172.9, 162.7, 63.7, 61.0, 59.2, 55.4, 54.9, 52.3, 45.9, 45.2, 36.2, 35.2, 28.4, 28.2, 27.8, 25.2, 21.6. ESI-MS: *m/z* $C_{19}H_{38}N_5O_2S$ for (M^+) calculated 400.6043, found 400.2982. $[\alpha]_D^{20}$ +0.073^o (c 0.05, MeOH). IR 3267.65, 1649.02, 1643.39, 1455.91, 1230.49, 1073.36 cm^{-1}. Melting Point: 125 ^{o}C.

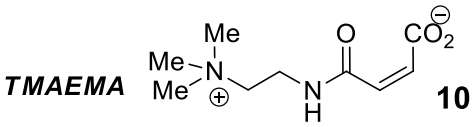

(Z)-4-oxo-4-((2-(trimethylammonio)ethyl)amino)but-2-enoate (TMAEMA) 10: Maleic anhydride (500 mg, 5.10 mmol) was added to a 100 mL round bottomed flask followed by diethyl ether (50 mL). *N*,*N*-Dimethylethylenediamine (5.10 mmol, 450 mg, 511µL) was then added dropwise while stirring at room temperature. After 10 min a precipitate was observed, and the resulting solid was vacuum filtered. In a 250 ml round bottom flask, 100 mg (0.540 mmol) of solid was dissolved in DMF (3 mL), followed by the addition of methyl iodide (76.6 mg, 33.6 µL, 0.54 mmol). The mixture was stirred at room temperature for 4 hours. An observed precipitate was then vacuum filtered, followed by purification via washing with diethyl ether then hexanes, to yield a yellow-white solid (125 mg, 10 % yield). ^{1}H NMR (400 MHz, D_2O): δ 6.51 (d, *J* = 12 Hz, 1H), 6.36 (t, *J* = 11 Hz, 1H), 3.80 (t, *J* = 7 Hz, 2H), 3.57 (t, *J* = 7 Hz, 2H), 3.22 (s, 9H). ^{13}C NMR (100 MHz, D_2O): δ 221.3, 220.1, 132.5, 129.8, 64.0, 53.5, 33.7. ESI-MS *m/z* $C_9H_{17}N_2O_3$ expected: 201.2429, found: $[MH]^+$ = 201.1350. IR 3427.16, 1716.51, 1628.48, 1523.53, 1476.55, 1209.11, 1077.11 cm^{-1}. Melting Point: 154 ^{o}C.

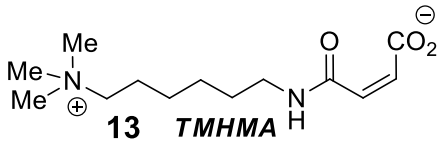

13 *TMHMA*

(Z)-4-oxo-4-((2-(trimethylammonio)hexyl)amino)but-2-enoate (TMHMA) 13:

To a stirred solution of maleic anhydride (170 mg, 1.73 mmol) in diethyl ether (10 mL) was added 6-(dimethylamino)hexylamine (300 µL, 1.73 mmol) dropwise. The reaction mixture was stirred at room temperature for 10 minutes, until a noticeable precipitate had formed. The resulting solid was then vacuum filtered, washed with diethyl ether, and dried. The purified solid (84 mg, 0.347 mmol) was dissolved in DMF (1 mL) along with methyl iodide (49 mg, 22.0 µL, 0.35 mmol), and the reaction mixture was stirred at room temperature for 4 h, until a precipitate had formed. The solid was then filtered, followed by purification via washing with diethyl ether then hexanes, to afford a thick orange oil (90 mg, 68 % yield). ^{1}H NMR (400 MHz, D_2O): δ 6.48 (d, *J* = 12.4 Hz, 1H), 6.30 (d, *J* = 12.2 Hz, 1H), 3.32 (m, 4H), 3.12 (s, 9H), 1.82 (q, *J* = 7 Hz, 2H), 1.59 (q, *J* = 7, 2 Hz), 1.42 (m, 2H). ^{13}C NMR (100 MHz, D_2O): δ 169.2, 167.3, 133.5, 130.3, 66.8, 53.1, 39.7, 27.8, 25.7, 25.2, 22.4. ESI-MS *m/z* $C_{13}H_{25}N_2O_3$ expected: 257.3492, found: $[MH]^+$ = 257.1549. IR 3433.54, 1710.3, 1629.09, 1561.95, 1476.44, 1216.68 cm^{-1}.

NMR Data:

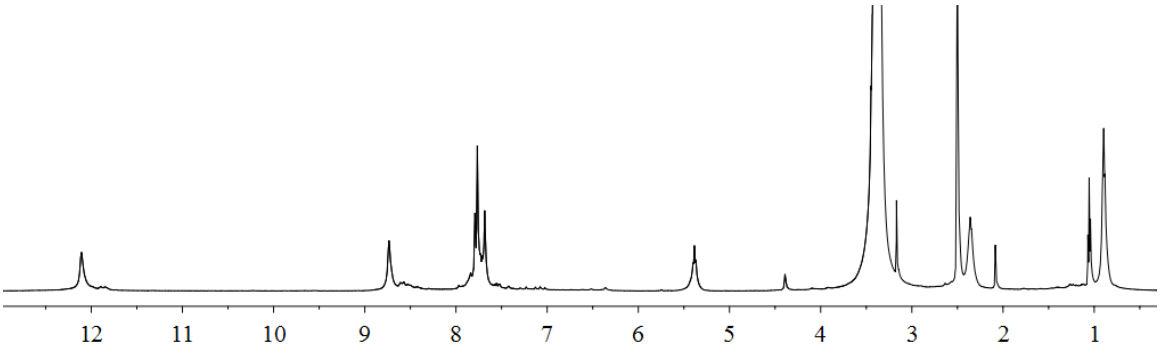

Figure S4.1 ^{1}H NMR spectrum of positive cavitand **3** (500 MHz, DMSO-d_6, 64 scans, δ 14.0 – -2.0 ppm sweep width).

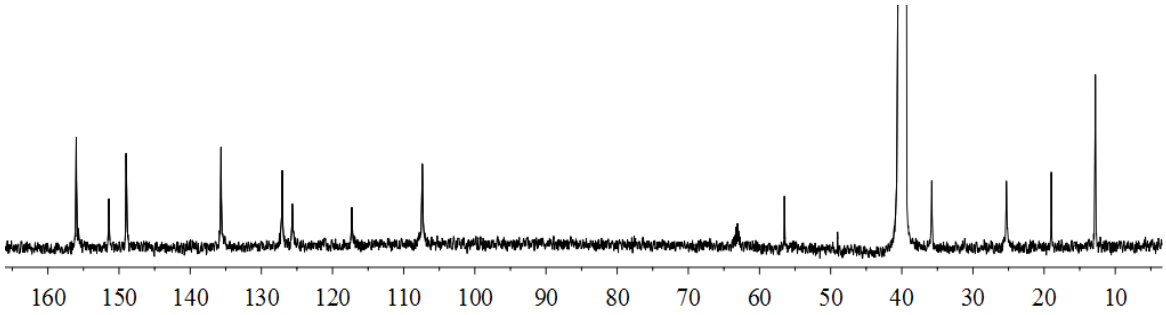

Figure S4.2 ^{13}C NMR spectrum of positive cavitand **3** (125 MHz, DMSO-d_6, 1024 scans, δ 220 – -10 ppm sweep width).

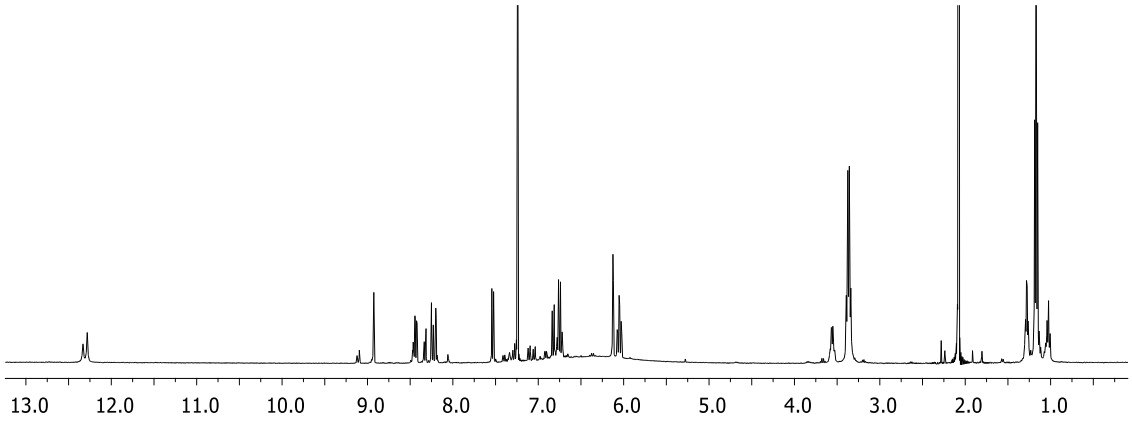

Figure S4.3 ^{1}H NMR spectrum of 5/6-nitro-rhodamine B **S-2** (400 MHz, $CDCl_3$, 64 scans, δ 14.0 – -2.0 ppm sweep width).

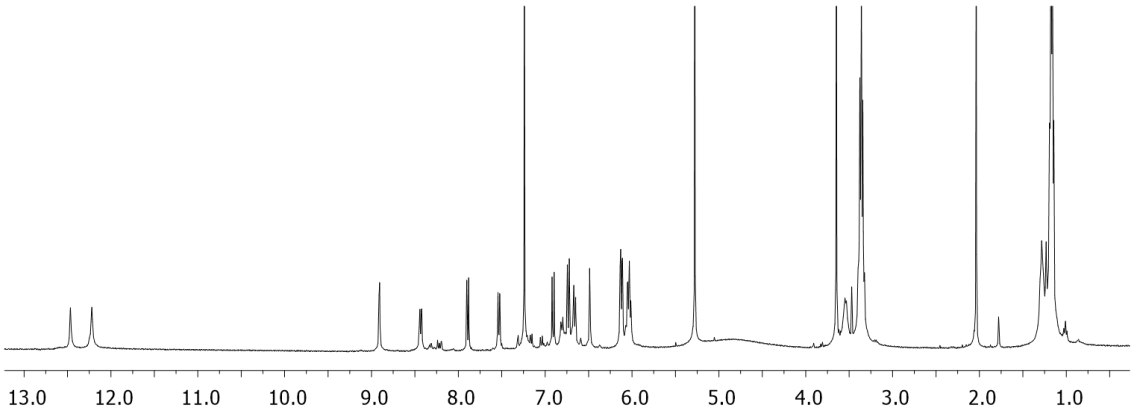

Figure S4.4 ^{1}H NMR spectrum of 5/6-amino-rhodamine B **S-3** (400 MHz, $CDCl_3$, 64 scans, δ 14.0 – -2.0 ppm sweep width).

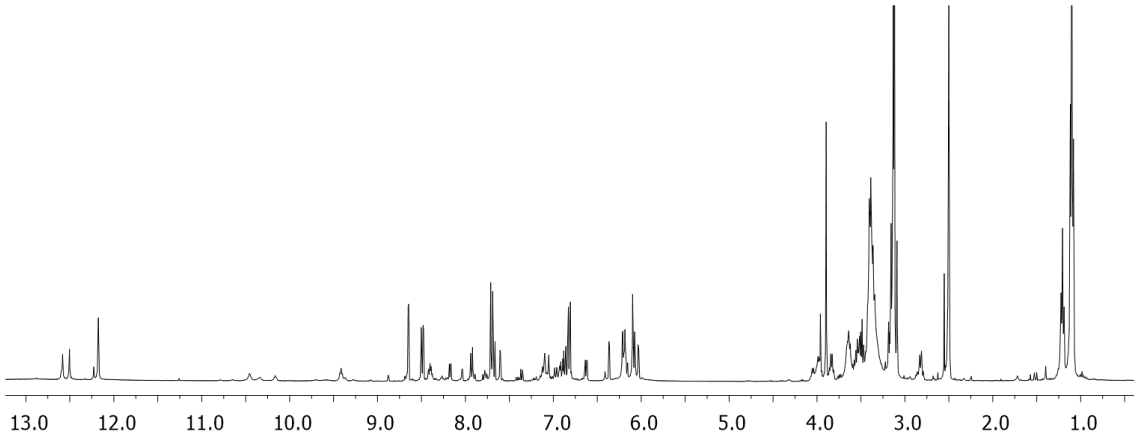

Figure S4.5 ^{1}H NMR spectrum of rhodamine B guest **4** (400 MHz, DMSO-d_6, 64 scans, δ 14.0 –-2.0 ppm sweep width).

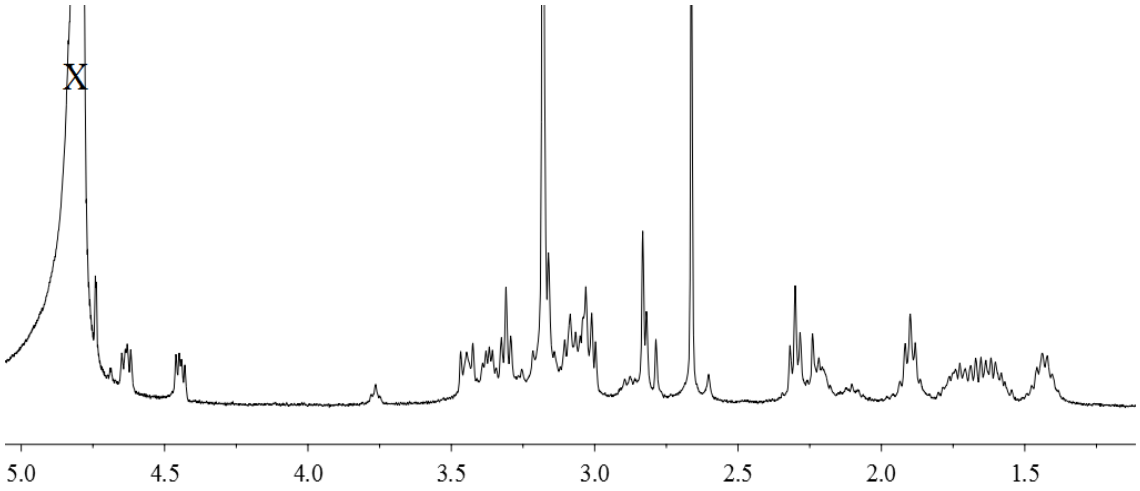

Figure S4.6 ^{1}H NMR spectrum of N^{1}-(3-biotinamidopropyl)-N^{3},N^{3},N^{3}-trimethylpropane-1,3-diaminium Iodide (BioTMAPA) **9**. (400 MHz, D_2O, δ 14.0 – -2.0 ppm sweep width, 64 scans).

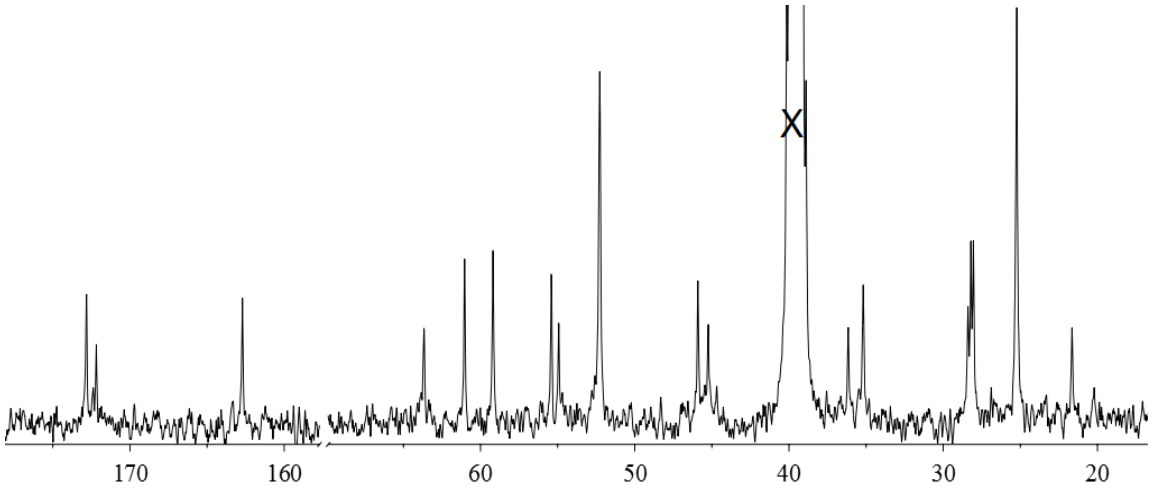

Figure S4.7 ^{13}C NMR spectrum of N^1-(3-biotinamidopropyl)-N^3,N^3,N^3-trimethylpropane-1,3-diaminium Iodide (BioTMAPA) **9** (100 MHz, DMSO-d_6, δ 220 – -10 ppm sweep width, 512 scans).

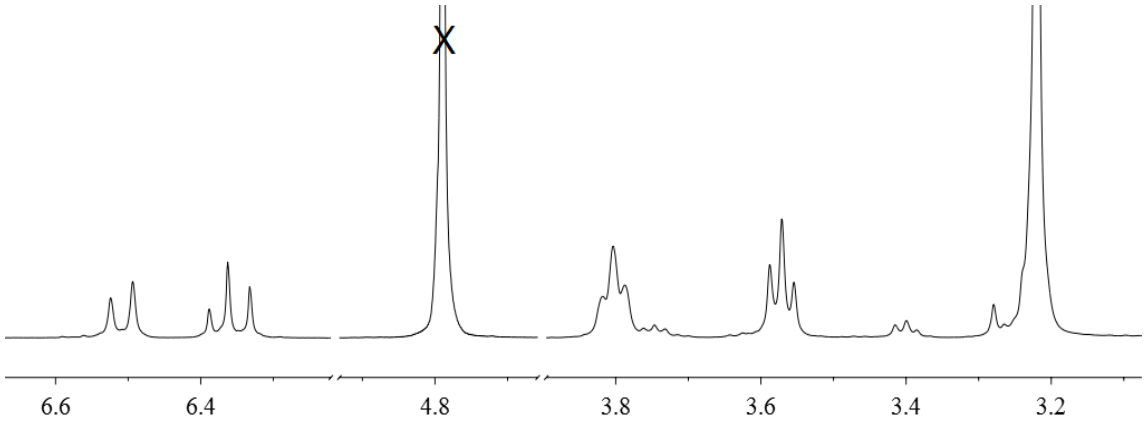

Figure S4.8 ^{1}H NMR spectrum of (Z)-4-oxo-4-((2-(trimethylammonio)ethyl)amino)but-2-enoate (TMAEMA) **10**. (400 MHz, D_2O, δ 14.0 – -2.0 ppm sweep width, 64 scans).

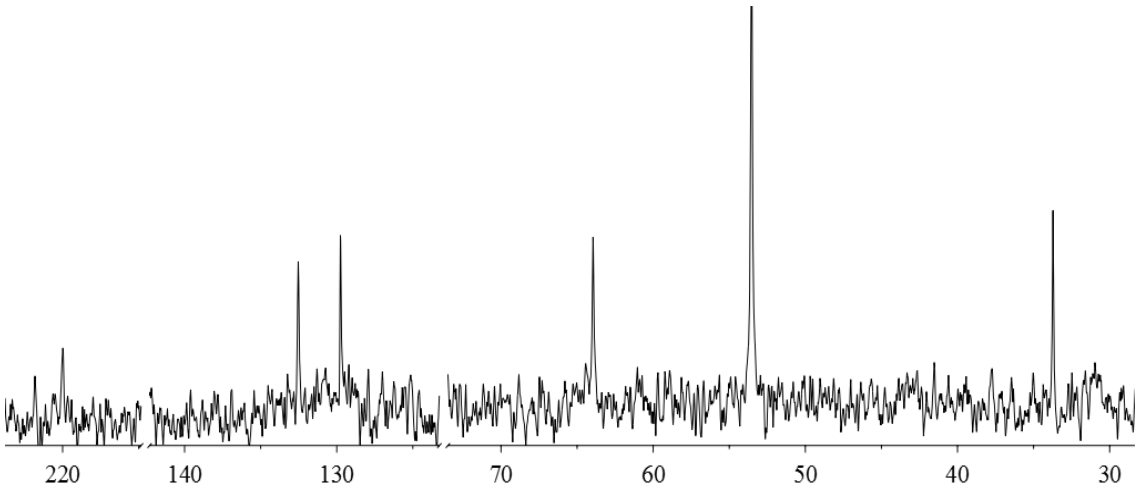

Figure S4.9 ^{13}C NMR spectrum of (Z)-4-oxo-4-((2-(trimethylammonio)ethyl)amino)but-2-enoate (TMAEMA) **10** (100 MHz, $CDCl_3$, δ 220 – -10 ppm sweep width, 512 scans).

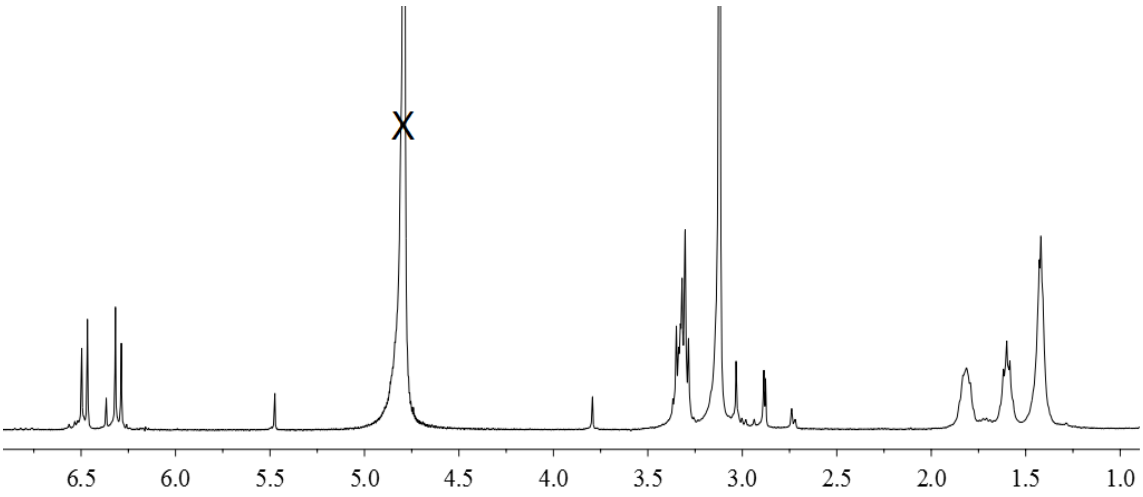

Figure S4.10 ^{1}H NMR spectrum of (Z)-4-oxo-4-((2-(trimethylammonio)hexyl)amino)but-2-enoate (TMHMA) **13**. (400 MHz, D_2O, δ 14.0 – -2.0 ppm sweep width, 64 scans).

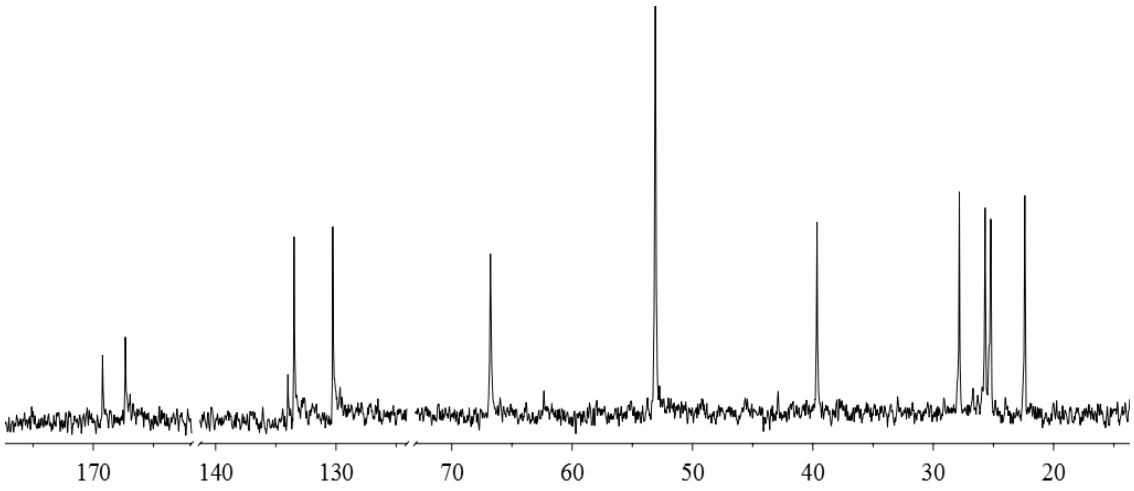

Figure S4.11 ^{13}C NMR spectrum of (Z)-4-oxo-4-((2-(trimethylammonio)hexyl)amino)but-2-enoate (TMHMA) **13** (100 MHz, $CDCl_3$, δ 220 – -10 ppm sweep width, 512 scans).

Mass Spectral Data:

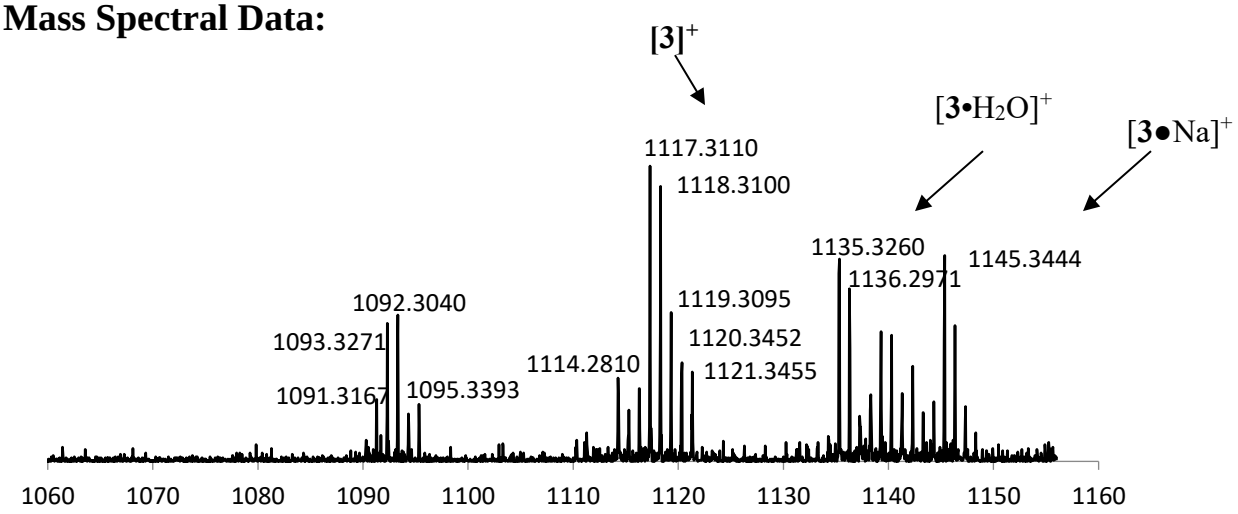

Figure 4.12 MALDI-TOF MS spectrum of positively charged cavitand **3.**

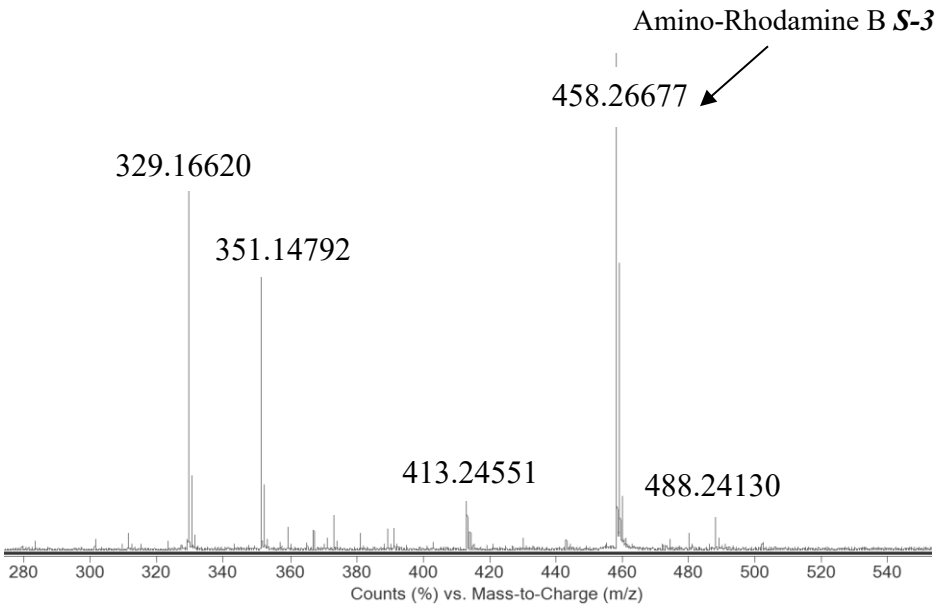

Figure 4.13 ESI-MS spectrum of 5/6-amino-rhodamine B **S-3.**

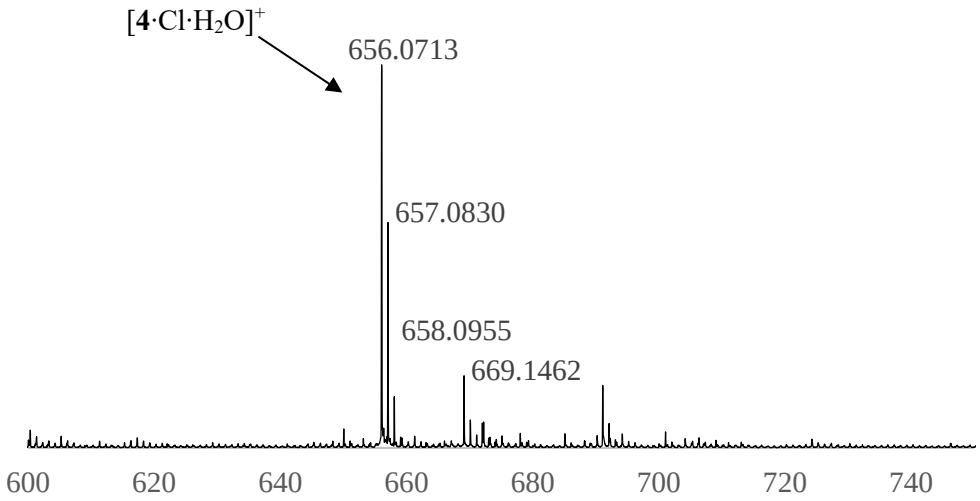

Figure 4.14 MALDI-TOF MS spectrum of rhodamine B guest **4.**

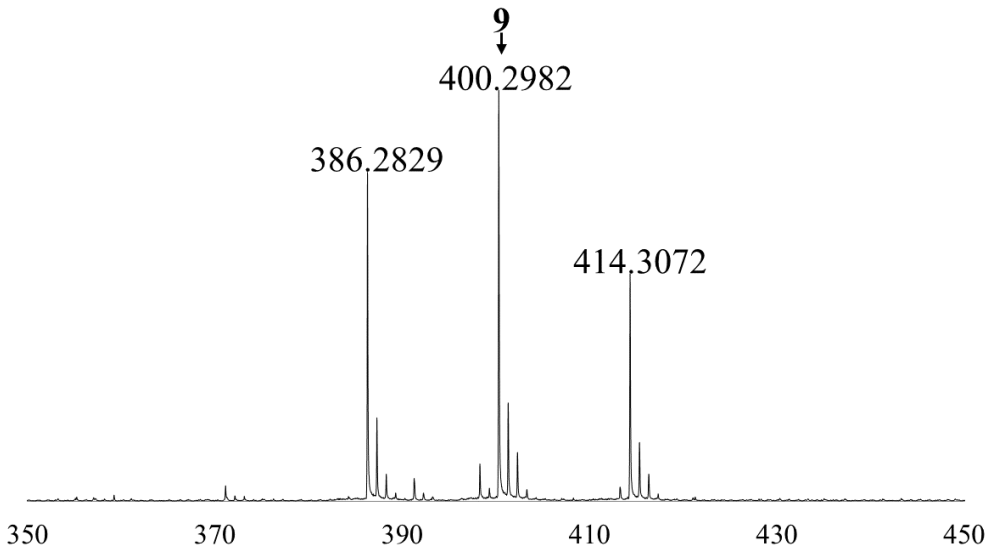

Figure 4.15 ESI-MS spectrum of N^1-(3-biotinamidopropyl)-N^3,N^3,N^3-trimethylpropane-1,3-diaminium Iodide (BioTMAPA) **9**.

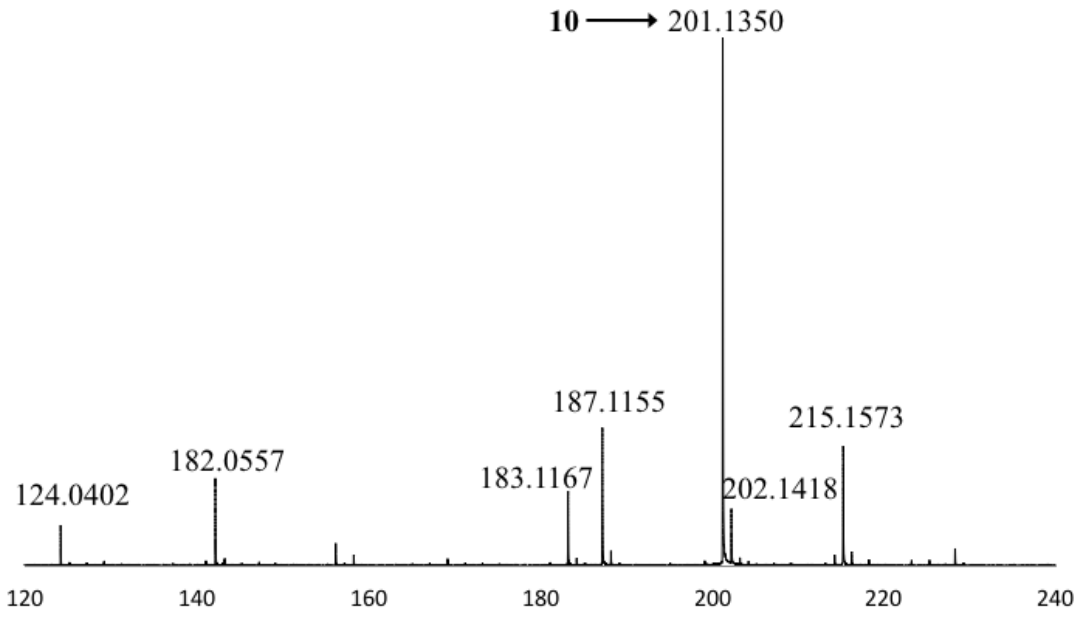

Figure 4.16 ESI-MS spectrum of (Z)-4-oxo-4-((2-(trimethylammonio)ethyl)amino)but-2-enoate (TMAEMA) **10**.

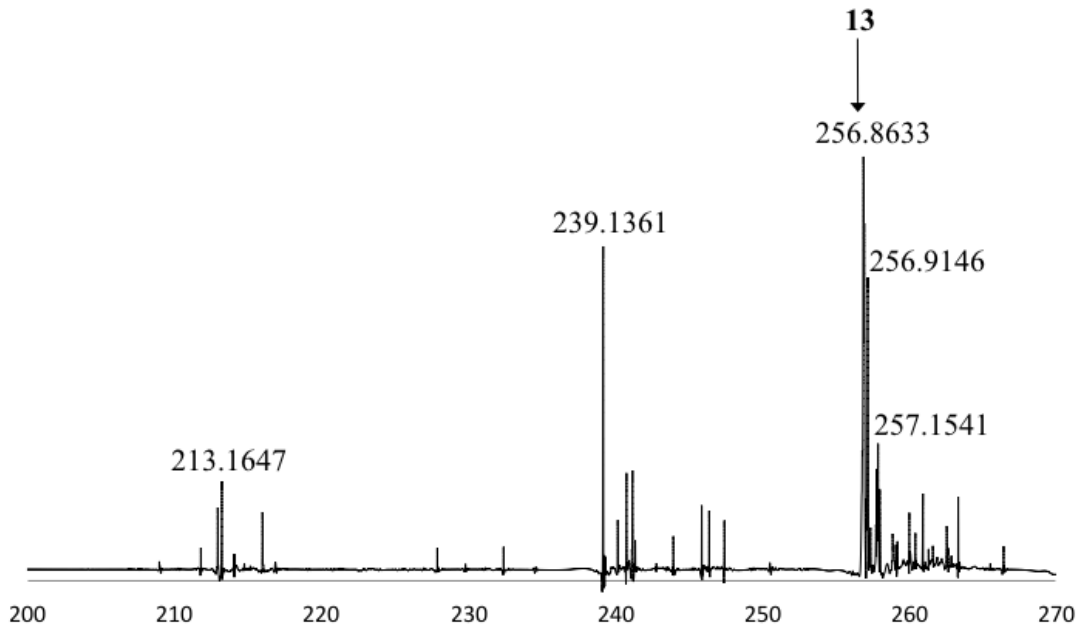

Figure 4.17 ESI-MS spectrum of (Z)-4-oxo-4-((2-(trimethylammonio)hexyl)amino)but-2-enoate (TMHMA) **13.**

3. Supporting Figures

Rhodamine B Guest 4 Optical Properties

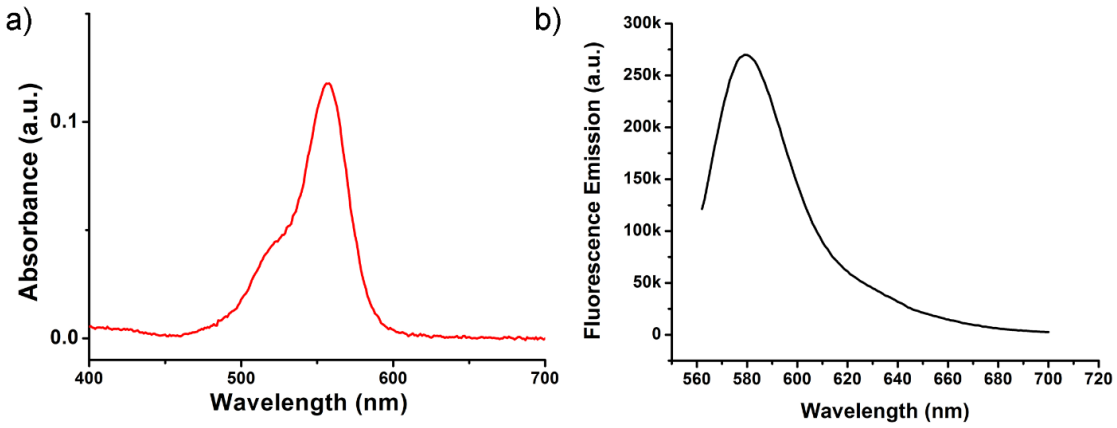

Figure 4.18 a) Absorption and **b)** fluorescence emission (excitation at λ = 557 nm) spectrum of guest **4** at 3 μM in water.

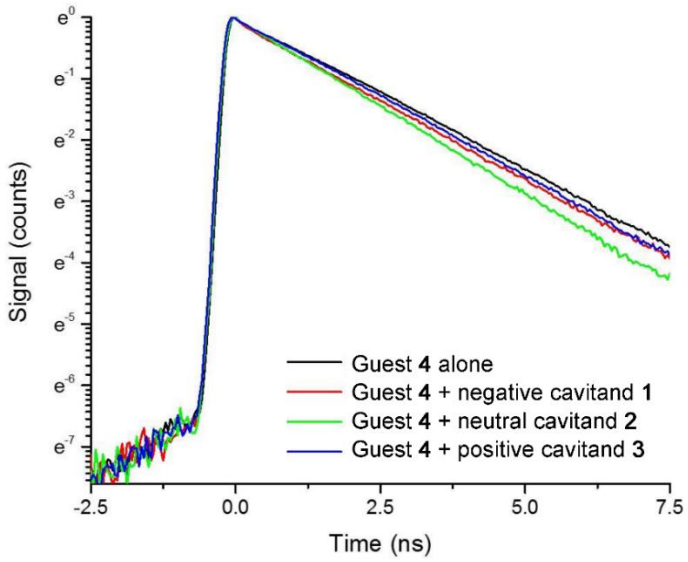

Figure 4.19 Fluorescence lifetime measurement for Guest **4** at 3 µM with or without the presence of cavitand **1, 2 or 3** at 4 µM in phosphate buffer pH 7.4.

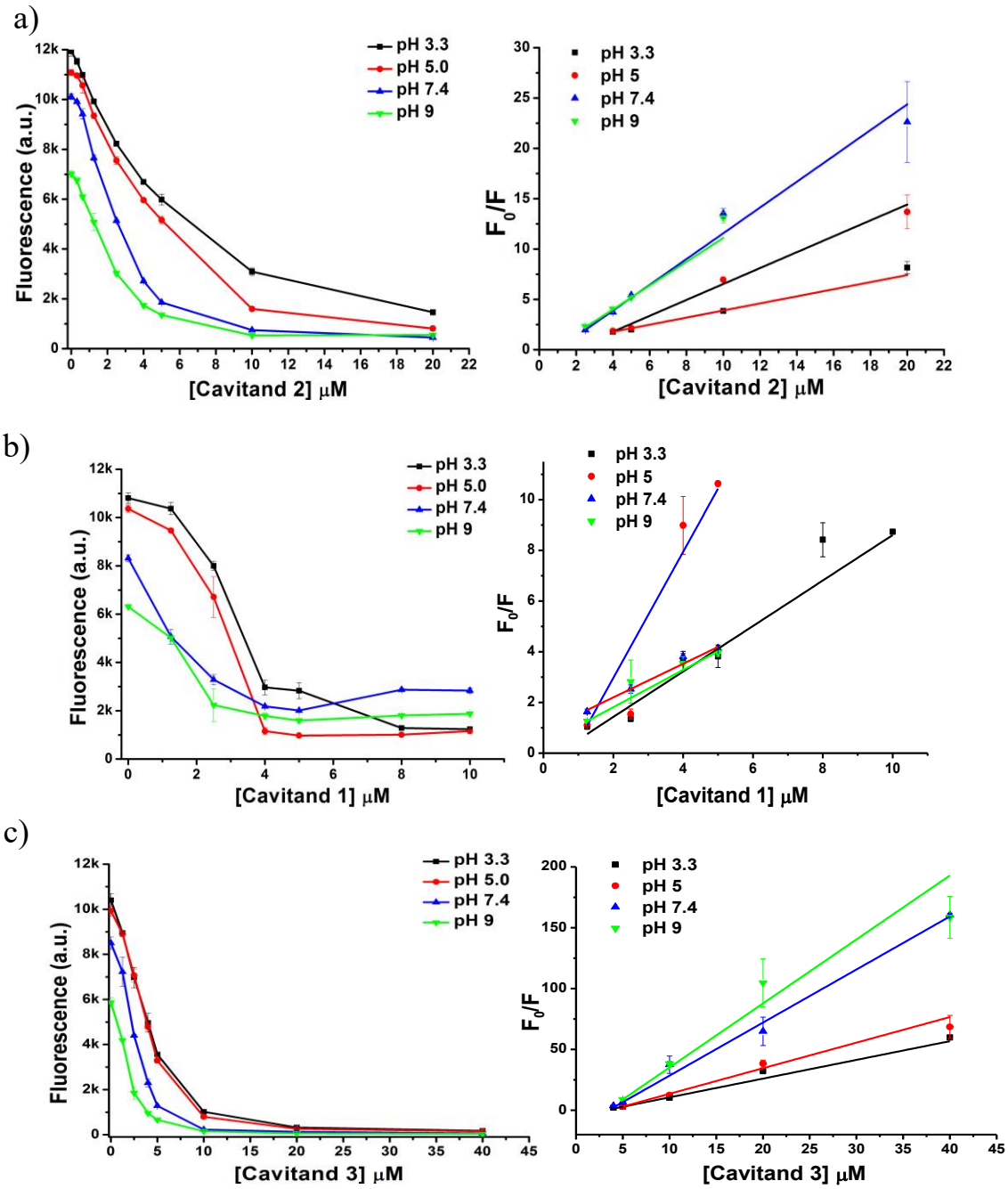

Figure 4.20 The fluorescence quenching (left) and Stern-Volmer fitting (right) curves of guest **4** at 3 μM with increasing concentrations of cavitand a) **1**; b) **2** and c) **3**. The measurement was conducted in various pH: 3.3, 5.0, 7.4, and 9.0.

Small Molecule Displacement Data

Table S4.1 The pKa values of the functional groups indicated by the arrows in the picture.

Guest	pKa
8	7.88
9	9.81
10	3.59
12	2.26
13	3.91
14	9.48
17	8.34 (terminal); 10.1 (internal)
18	10.35

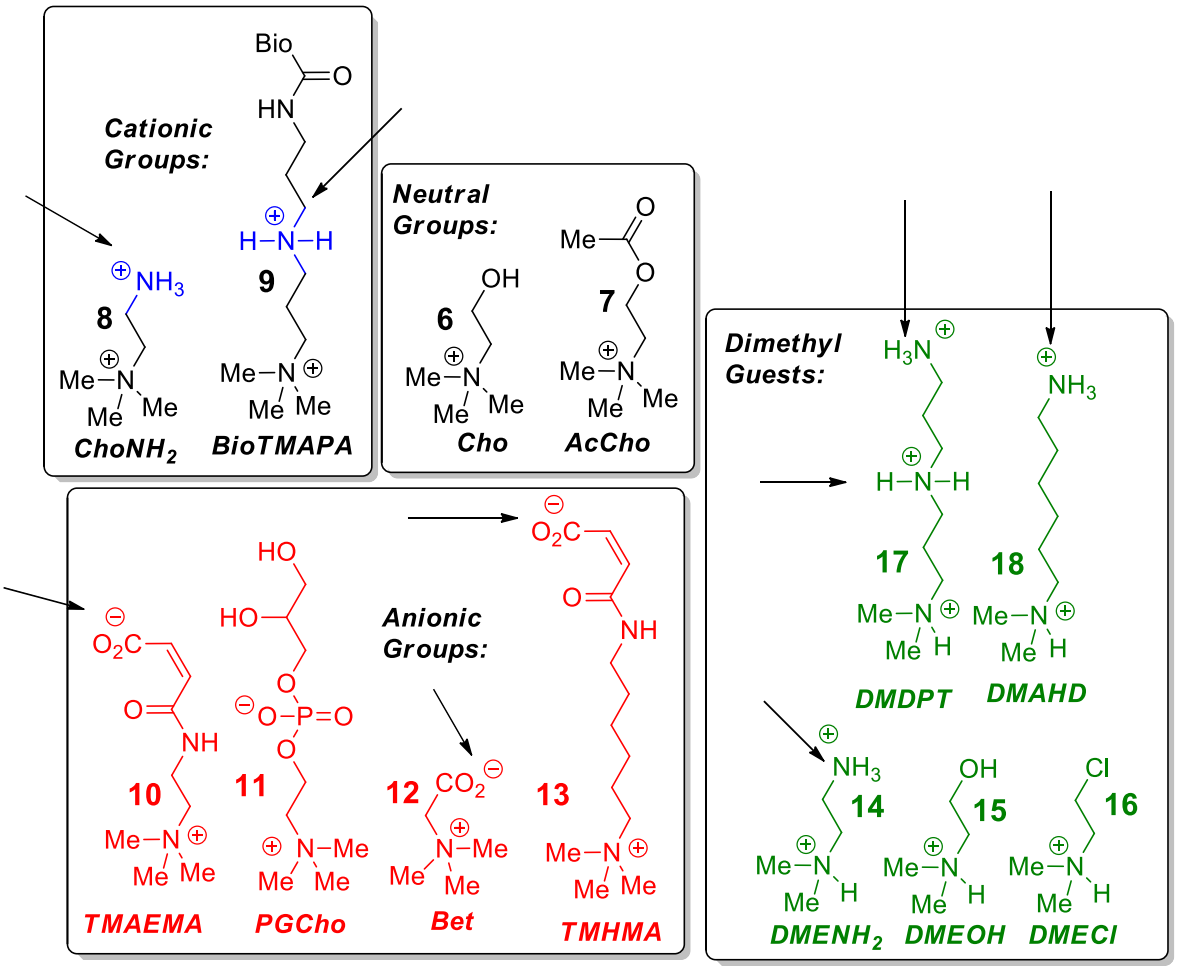
Cationic Groups:
Bio
HN
8
9
ChoNH2
BioTMAPA
Neutral Groups:
6
7
Cho
AcCho
Anionic Groups:
10
11
12
13
TMAEMA
PGCho
Bet
TMHMA
Dimethyl Guests:
17
18
DMDPT
DMAHD
14
15
16
DMENH2
DMEOH
DMECl

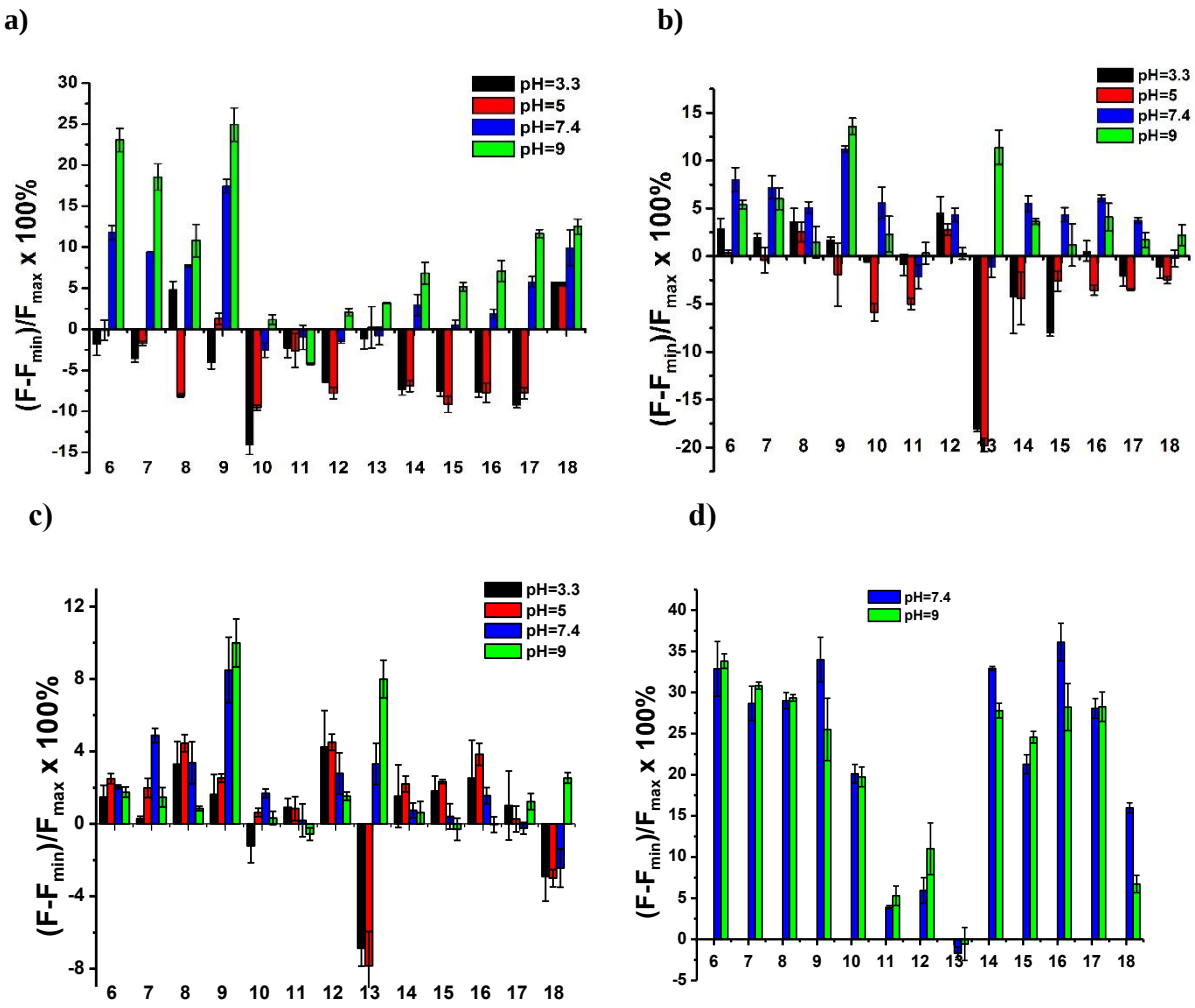

Figure S4.21 The complete screening data for the small molecule guests using our fluorescent guest-cavitand array. The sensor elements were constructed by pre-incubating guest **4** at 3 μM with a) cavitand **1** at 4 μM; b) cavitand **2** at 5 μM; and c) cavitand **3** at 4 μM in the solutions of 4 pH values: 3.3, 5.0, 7.4, and 9.0. In addition, the array included the sensor formed by d) fluorescein guest **5** at 3 μM with cavitand **1** at 20 μM at pH 7.4 and 9.0.

a)

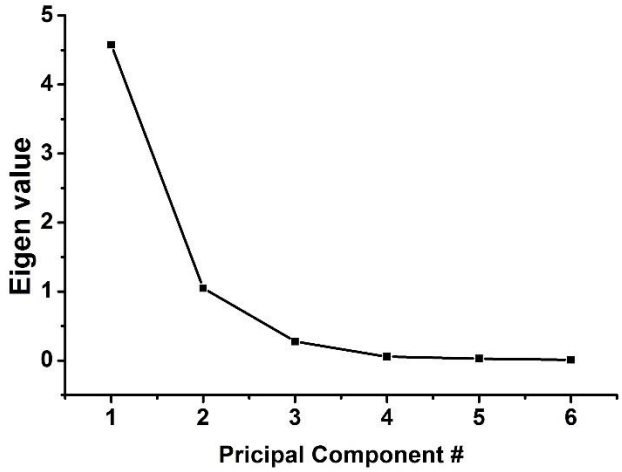

b)

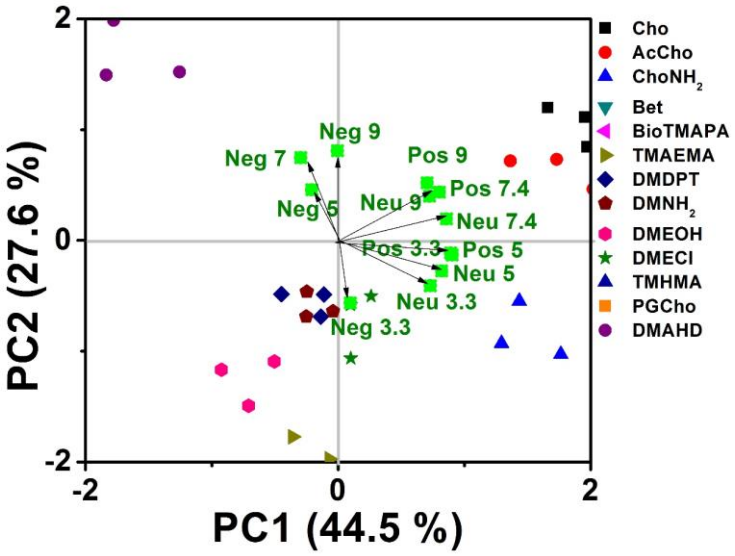

Figure S4.22 a) The Scree plot of PCA on the screening data of small molecule guests, used to determine the appropriate number of principal components.

After the first two components, there is a minimal change in the remaining eigenvalues, indicating that the first two components summarized the majority of the variations within the data set. b) The factor loading plot that describes the relationship between original

variables and subspace dimensions. The scale was enlarged compared to the PCA plot shown in Fig. 4.7 to clearly show the location of each variable on this plot. From the plot, we can tell that the sensor elements at neutral and basic pH conditions had key contribution to the location of the small molecule guests at the upper panel of the score plot. Cavitands **2** and **3** contribute more to the differentiation between the R-NMe_3^+ and R-$NHMe_2^+$.

a) **b)**

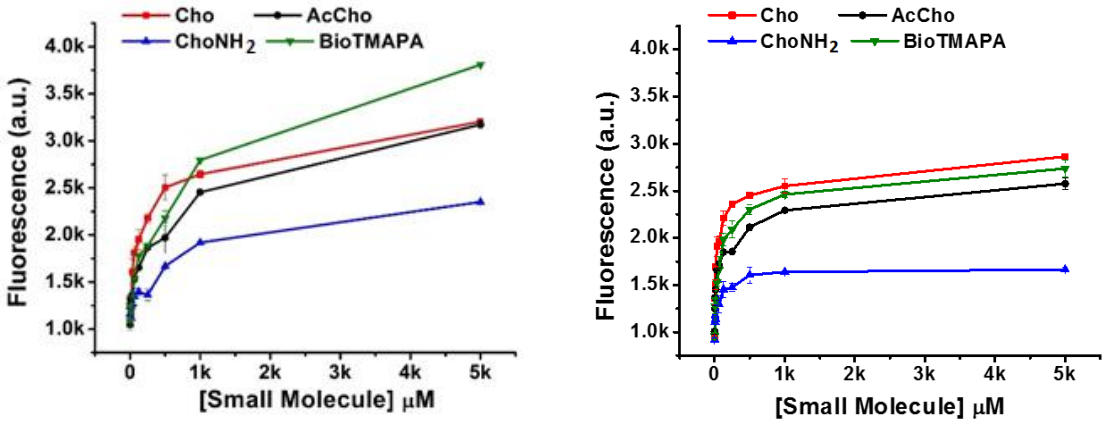

Figure S4.23 Fluorescence recovery induced by mixing four selected small molecule guests at increasing concentrations from 0 to 5 mM with the sensor of **1•4** at **a)** pH 7.4 and **b)** pH 9.0.

Table S4.2 The IC_{50} and K_d values of the four selected small guest molecules (**6-9**) calculated as described in Methods section from the fluorescence recovery curves shown in Fig. S4.6.

IC_{50} (µM)				
Small molecule	**Cho 6**	**AcCho 7**	**$ChoNH_2$ 8**	**BioTMAPA 9**
pH 7.4	40.9 ± 4.9	56.0 ± 8.9	66.4 ± 12.2	43.2 ± 6.6
pH 9	44.5 ± 6.4	49.4 ± 15.3	N/A	289.2 ± 21.9
K_d (µM)				
Small molecule	**Cho 6**	**AcCho 7**	**$ChoNH_2$ 8**	**BioTMAPA 9**
pH 7.4	9.9±0.6	13.9±1.6	16.5±2.4	10.5±1.0
pH 9	10.2±1.0	11.4±3.1	N/A	69.6±4.7

Peptide Displacement Data:

a)

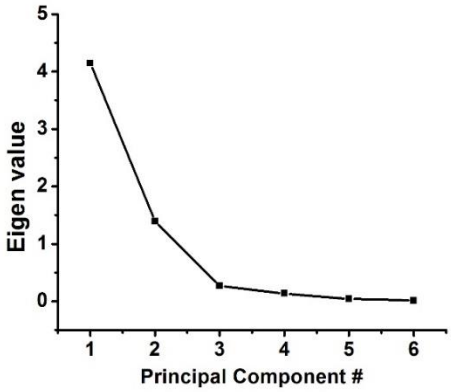

b)

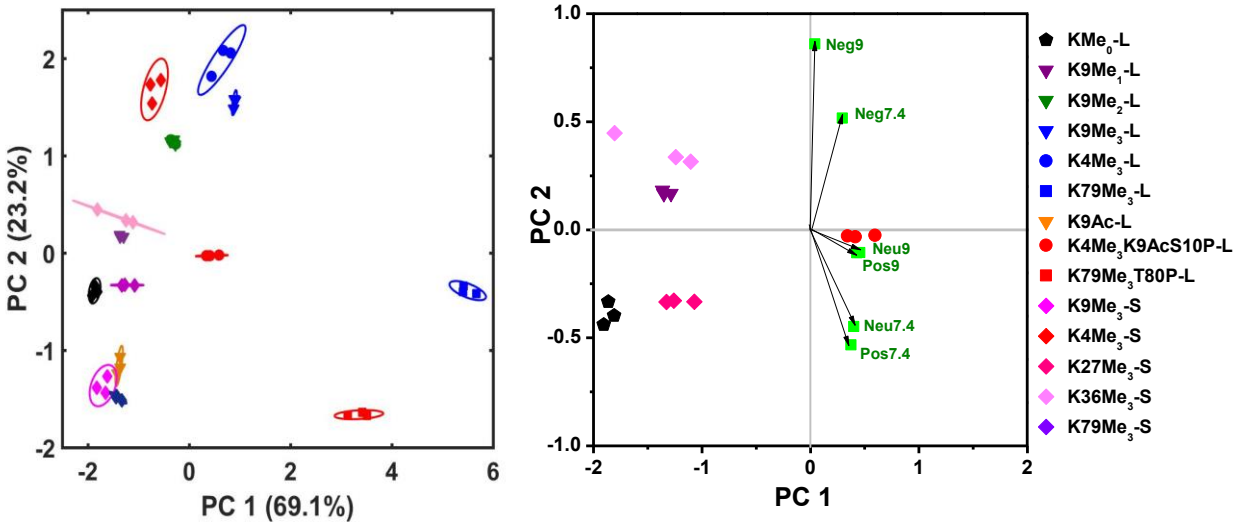

Figure S4.24 a) The Scree plot and b) the score plot (left) containing all 14 peptides as shown in groups in Fig. 4.10, and the corresponding factor loading plot (right; with enlarged scale to clearly show the positions of all variables) of PCA for the screening data of peptides to determine of the appropriate number of principal components.

We can tell from the scree plot that the first two principal components are appropriate in summarizing the major variance within the data set. The factor loading plot indicates all

variables contribute to the differentiation of the trimethylated long peptides from the di-, mono-, and non-methylated long peptides, as well as from the short peptides. The sensor elements of **1•4** at pH 7.4 and 9.0, and **2•4** at pH 9.0 contribute more to the location of the peptides in the upper panel in this dimension, and the sensor elements of **2•4** at pH 7.4, and **3•4** at pH 7.4 and 9.0 contribute to the location of the guests in the lower panel. The error ellipses were obtained at 95% confidence interval.

Table S4.3 The list of peptides used in our study and their sequence, pI, and GRAVY score.

No.	Peptides	Sequence (No modification shown)	pI	GRAVY
1	H3(1-21)	ARTKQTARKSTGGKAPRKQLA	12.31	-1.448
2	H3K9(Me1)(1-21)	ARTKQTARK(Me1)STGGKAPRKQLA	12.31	-1.448
3	H3K9(Me2)(1-21)	ARTKQTARK(Me2)STGGKAPRKQLA	12.31	-1.448
4	H3K9(Me3)(1-21)	ARTKQTARK(Me3)STGGKAPRKQLA	12.31	-1.448
5	H3K9(Ac) (1-20)	ARTKQTARK(Ac)STGGKAPRKQL	12.83	-1.610
6	H3K4(Me3)(1-21)	ARTK(Me3)QTARKSTGGKAPRKQLA	12.83	-1.448
7	H3K4(Me3)K9(Ac)S10(P) (1-21)	ARTK(Me3)QTARK(Ac)S(P)TGGKAPRKQLA	12.83	-1.448
8	H3K79(Me3),amide	RLVREIAQDFK(Me3)TDLRFQSSAVK-NH2	9.98	-0.518
9	H3K79(Me3)T80(P),Biotin (69-89)	RLVREIAQDFK(Me3)T(P)DLRFQSSAVK(Biotin)	9.98	-0.518
10	H3K9(Me3) (3-17)	TKQTARK(Me3)STGGKAPR	12.02	-1.727
11	H3K4(Me3)(1-10)	ARTK(Me3)QTARKS	12.02	-1.890
12	H3K27(Me3) (23-34)	KAARK(Me3)SAPATGG	11.17	-0.750
13	H3K36(Me3)(31-41)	STGGVK(Me3)KPHRY	10.29	-1.500
14	H3K79(Me3) (73-83)	EIAQDFK(Me3)TDLR	4.56	-0.927

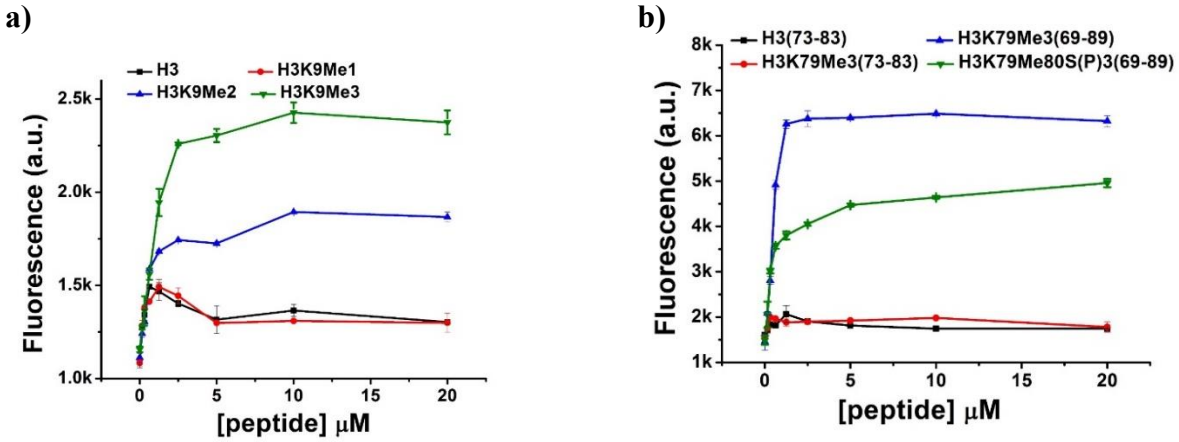

Figure S4.25 Fluorescence recovery induced by mixing a) the H3K9 (1-21) peptide series with different methylation levels with the sensor of **1•4** (3 and 4 μM, respectively) at pH 9.0, and the H3K79 series with the sensor of **2•4** (5 and 4 μM, respectively) at pH 9.0. Peptide concentrations increased from 0 to 20 μM.

Table S4.4 Dissociation constants obtained by fitting the fluorescence recovery curves shown in Fig. S4.8 to the Hill equation as described in the Methods section.

Parameter	H3K79Me$_3$(69-89)	H3K79Me$_3$T80(P)(69-89)	H3K9Me$_2$(1-21)	K9Me$_3$(1-21)
k (μM)	0.50±0.04	0.42±1.39	0.41±1.00	0.96±0.18
n	3.08	0.62	0.77	2.27
R^2	0.9972	0.9783	0.9095	0.9924

Chapter 5 Site-Selective Sensing of Histone Methylation Enzyme Activity via an Arrayed Supramolecular Tandem Assay

Introduction

Histone post-translational modifications (PTMs) play important roles in regulation of gene expression.[1] Methylations occur primarily at lysine and arginine residues on the histone backbone,[2] affecting transcriptional regulation,[3] heterochromatin assembly, and cell cycle progression.[4] Site-specific lysine methylations are created by lysine methyltransferases (KMT) and removed by lysine demethylases (KDM).[5] As dynamic control of histone methylation regulates numerous cellular processes, mechanistic study of their function is essential for understanding epigenetic regulation and its effect on disease progression. This requires assays that are able to differentiate not only methylation states, but also the *positions* of methylation. Most site-specific assays rely on antibodies to recognize the changes in methylation situation,[6] but their specificity at differentiating methylation sites and states is unsatisfactory.[7] In addition, their high cost is not compatible for high-throughput screening and the synthetic peptide substrate often requires immobilization.[8]

Supramolecular tandem assays that employ small molecule synthetic receptors as host molecules for the targets of interest are an enticing alternative to antibody-based enzyme assays.[9] Water-soluble hosts such as sulfonated calixarenes (CXs),[10] cucurbiturils (CBs)[11] or cyclophanes[12] can recognize the substrates or byproducts of enzymatic reactions, and be paired with fluorescence displacement assays (FDAs) for selective, *in situ* monitoring of

the process. This small molecule approach has many advantages, such as high sensitivity, simple, rapid detection and low cost.[13] A number of enzymatic targets have been monitored using small molecule FDAs,[14] such as cholinesterases,[14a] decarboxylases,[14b-d] protease,[15] histone deacetylase[12] and lysine methyltransferase.[16]

These advantages are offset by one specific weakness, especially when compared to antibody-based assays: site selectivity. Small molecule receptors generally only recognize a single type of functional group. While excellent selectivities for a specific group type are possible,[17] differentiating identical modifications at different positions is extremely challenging. This limitation means that large amounts of enzymes are required, and that critical enzyme functions cannot be investigated, such as cross-reactivity over multiple methylation sites and interference from non-substrate peptides. Effective *in vitro* assays of methylation enzyme activity require both *site-selective* molecular recognition and an optical readout of the KMT or KDM activity. Arrayed cyclophane/calixarene host molecules have been shown to selectively recognize K and R methylations,[12b,17] but a site-selective enzyme assay sensor is as yet unknown. Here we show that an FDA sensing system based on deep cavitand synthetic receptors can be used to monitor the site-selective function of multiple histone methylation enzymes.

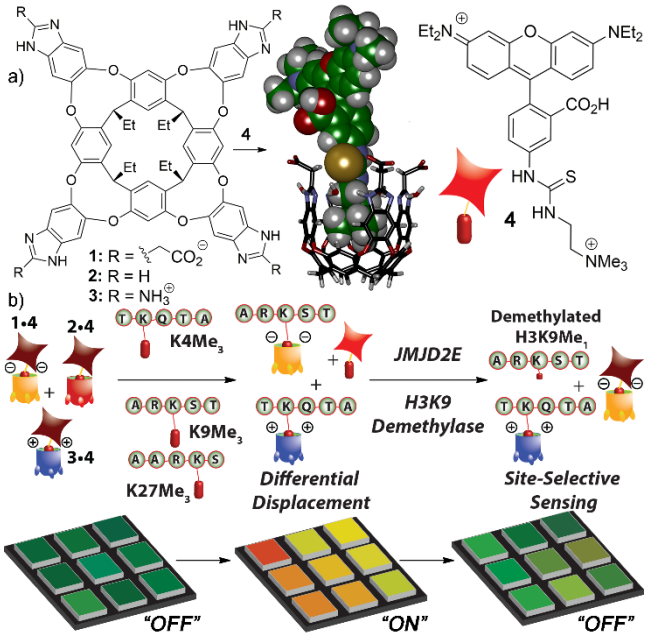

Figure 5.1 a) Structure of hosts 1-3, guest 4 and a minimized model of the 1•4 host:guest complex (SPARTAN); b) Supramolecular tandem assay for a lysine demethylase enzyme.

Results and Discussion

Water-soluble deep cavitands[18] such as **1-3** (Figure 5.1) are useful for recognition and sensing of biomolecules. We have previously shown that the combination of cavitand **1** and a suitable fluorophore allows sensing of Kme_3 peptides via FDA.[19] This concept can be extended to allow *site-selective* Kme_3 recognition by the application of cavitands **1-3** in an array-based format,[20] followed by discrimination via Principal Component Analysis (PCA).[21] The sensor can discriminate Kme_3 residues at different positions on peptides, and even sense remote changes in peptide structure. The sensitivity of the system to methylation site and state suggests that it would be capable of site-selective monitoring of methylation enzyme activity (Figure 5.1).

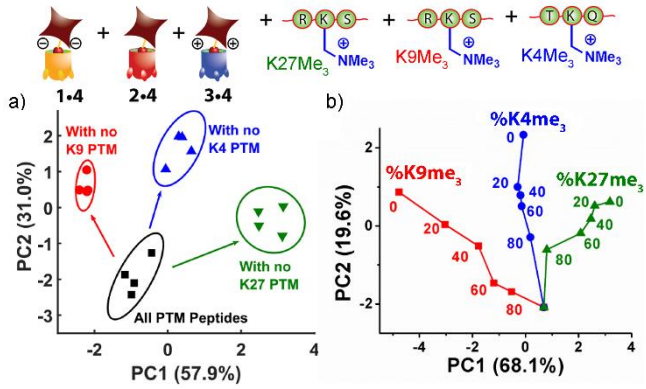

Figure 5.2 Site-selective sensing in peptide mixtures. a) Scores plot of the selective recognition of Kme_3 peptides in a peptide mixture with the **(1-3)•4** sensor; b) PCA scores plot of a lysine demethylase reaction mimic. [**4**] = 3 μM, [**1**] = 4 μM, [**2,3**] = 5 μM, 50 mM phosphate buffer at pH = 7.4 or 50 mM carbonate buffer at pH = 9.0, [peptide] = 2 μM. Ellipses drawn at 95% confidence.

Initially, we established the ability of the sensor system to discriminate between methylations in peptide mixtures (Figure 5.2, see Supporting Information for full peptide sequences). Three different histone H3 peptides with trimethylation (Kme_3) modifications at different positions ($H3K4me_3$, $H3K9me_3$, $H3K27me_3$) were combined and added to an array of hosts **1-3** and fluorophore **4**. The array was constructed by incorporating the three cavitands (**1**-**3**, 4 μM) and their complexes with guest **4** (3 μM) at two different pHs (pH 7.4 and 9.0), for a total of 6 variables. The peptides were mixed with each sensor solution per well in a 96-well plate at a fixed concentration of 2 μM, and the relative fluorescence recovery detected for each well. Analysis of the array readouts (4 separate runs) was performed by PCA, and the scores plot is shown in Figure 5.2a. The selectivity was tested by switching a single Kme_3 peptide from the mixture with its non-methylated control. The 6-variable **(1-3)•4** array can detect the absence of each methylation ($K4me_3$, $K9me_3$, $K27me_3$) in the peptide mixture. We also performed a mimic of the enzymatic

demethylation process[12b] by varying the proportion of each Kme_3 peptide versus the corresponding non-methylated peptide (Figure 5.2b) in 20% increments. As the proportion of each Kme_3 peptide decreased, a continuous movement of the clusters towards each end product in the PCA plot was observed, indicating the suitability of the sensor for the analysis of the product mixtures during enzymatic reaction. The sensor is also functional in the presence of cell extracts. H3(1-21), H3K4me_3, H3K9me_3, and H3K27me_3 can be well separated on the scores plot (see Supporting Information) after 2 μM (~ 4 μg/mL) of the peptide was spiked into the protease digest of Calf Histone at 100 μg/mL.

Of course, discrimination of the products and intermediates is not the only requirement for a successful enzyme assay. A simple array should provide optimal signal to minimize enzyme and substrate consumption, and must function in the presence of cofactors and a mixture of potential substrates. The (**1**-**3**)•**4** sensor (at 4 and 3 μM respectively) could detect as little as 22 nM of H3K9me_3 and was responsive to change in [peptide] up to 10 μM at pH 7.4. The detection performance was not affected by the presence of a complex peptide mixture prepared by digesting bovine histones at a concentration of 5-250 fold of the H3K9me_3 peptide (see Supporting Information). The sensor system was also tolerant to the presence of other chemicals required for JMJD2E catalyzed demethylation (2-oxoglutarate (2-OG), Fe^{2+}, and ascorbate) and HMT methylation (S-adenosyl-methionine (SAM) and byproduct S-adenosyl-homocysteine (SAH)). Sodium ascorbate (0.5 mM) and Fe^{2+} (6 μM) only slightly increased (~5%) quenching of the guest **4** fluorescence by the cavitand **1**, and 2-OG (50 μM) had no effect at all. Addition of SAM did not induce any change to sensor fluorescence within the concentration range (0-100 μM) required for enzyme assays. None

of these additives had any effect on the fluorescence recovery profiles upon displacement of **4** by target peptides, nor did up to 0.5% DMSO. Finally, the tolerance of the system to repeated exposure with UV light was tested. Figure S5.5 shows that guest **4** is somewhat susceptible to photobleaching, with a 15% loss of signal observed after 225 mins continuous exposure to UV light, cavitand **1** acts as a protecting agent and only <5% loss of signal was observed for the **1•4** complex. The fluorescence recovered by $H3K9me_3$ was also stable over 120 mins under the same conditions.

The sensor was applied to monitor the reactions catalyzed by two histone methylation enzymes: the lysine demethylase JMJD2E, and the lysine methyltransferase PRDM9. Both of these enzymes specifically act on a single lysine residue: JMJD2E catalyzes the demethylation of histone H3 at lysine residue 9, and PRDM9 catalyzes the trimethylation of H3 at lysine residue 4 (Figure 5.3). By adding JMJD2E to a 2 μM $H3K9me_3$ solution with 50 μM 2-OG, 6 μM Fe^{2+} and 0.5 mM ascorbate, the enzyme activity can be monitored over time by the fluorescence changes in the single component **1•4** sensor ([**1**] = 3 μM, [**4**] = 4 μM, Figure 5.3a-b). As the demethylation reaction proceeds, the concentration of $H3K9me_3$ decreases, leading to less displacement of the guest **4** from cavitand **1**, and thus lower fluorescence. The simple **1•4** sensor was able to monitor the JMJD2E reactivity with as little as 200 nM enzyme, with a 10% fluorescence decrease observed after 20 mins reaction. The reaction process was confirmed by MALDI-TOF MS analysis of the mixture at individual time points (Figure 5.3b, same conditions as for the FDA analysis). At time zero, only $H3K9me_3$ (m/z = 2297.05) was detected. $H3K9me_1$ (m/z = 2269.0) and

H3K9me$_2$ (m/z = 2283.0) appeared at time = 10 min, and complete conversion to the product H3K9me$_1$ occurred after 2h.

The same concept can be applied to monitor methyltransferase activity. In this case, the Kme$_3$ product formed by trimethylation of the H3 peptide at K4 by PRDM9 displaces fluorophore **4** from host **1**, causing continuous fluorescence increase. Mixing 200 nM PRDM9 with 2 μM H3K4, 100 μM SAM and 1 mM dithiothreitol (DTT), the sensor fluorescence increased rapidly within the first 15 minutes and leveled off afterwards (Figure 5.3c,d). MALDI-TOF-MS also confirmed that the initial fluorescence recovery within 5 min of reaction was mainly caused by the production of H3K4me$_1$. The amount of H3K4me$_2$ and H3K4me$_3$ started to increase significantly after t = 10 min. With continuous conversion of H3K4me$_1$ and H3K4me$_2$ to H3K4me$_3$, only H3K4me$_3$ was detected at t > 30 min, at which time the fluorescence recovery of the **1•4** sensor reached a plateau.

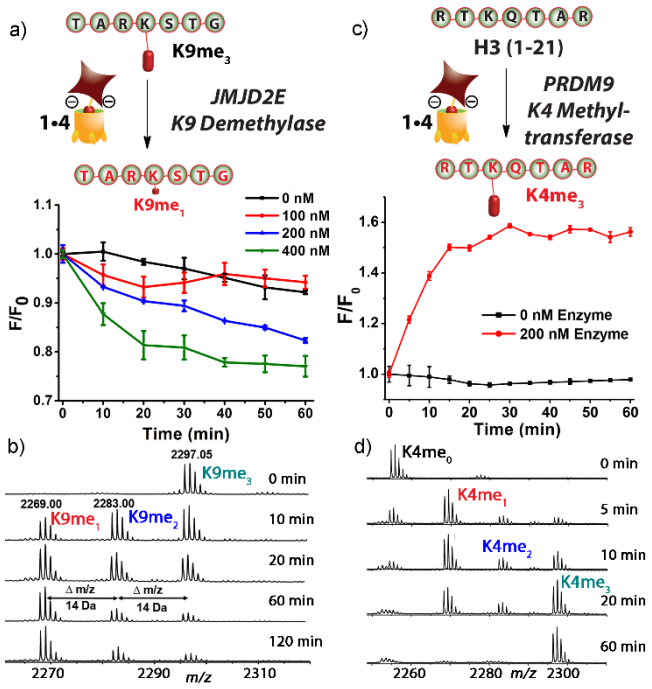

Figure 5.3 Enzyme Activity Monitoring with a single component sensor. a) [JMJD2E] dependence on fluorescence response; b) MALDI-MS identification of the demethylation products over time, [**4**] = 3 μM, [**1**] = 4 μM, [peptide] = 2 μM, , **[**2-OG] = 50 μM, [Fe^{2+}] = 6 μM; [ascorbate] = 0.5 mM; c) [PRDM9] dependence on fluorescence response; d) MALDI-MS identification of the methylation products over time, [**4**] = 3 μM, [**1**] = 4 μM, [peptide] = 2 μM, [PRDM9] = 200 nM, [SAM] = 100 μM [DTT] = 1 mM.

The simple **1•4** assay allows single substrate analysis, but the more exciting challenge is to monitor the *site-selective* function of the methylation enzymes in a substrate mixture. The full six-component array composed of the three host:guest complexes **(1-3)•4**, at pH 7.4 or pH 9.0 was capable of distinguishing different methylation sites in histone peptide mixtures (Figure 5.2). Having separately shown enzyme monitoring and site-selective Kme_3 sensing, we combined the two systems to sense a specific peptide substrate for the methylation enzyme from a mixture of peptides. We prepared identical enzyme reaction mixtures as above, but used a mixture of peptides as the substrates instead of one. The reaction catalyzed by JMJD2E was supplied with 2 μM of $H3K9me_3$, $H3K4me_3$, and

H3K27me$_3$ (along with 50 μM 2-OG, 6 μM Fe^{2+} and 0.5 mM ascorbate), and PRDM9 was mixed with 2 μM of H3(1-21), H3(23-34) (along with 100 μM SAM and 1 mM DTT). The reactions were terminated at various time points by incubating in boiling water for 5 minutes to deactivate the enzyme, the individual components of the **(1-3)•4** sensor array (4 μM host, 3 μM **4**) added and the fluorescence analyzed. While the initial Kme$_3$ sensor utilized 6 elements to achieve the selective detection of different methylation sites, we found that addition of the sensors present at pH 9.0 did not further enhance the separation of different peptides on the scores plot compared to using only the pH 7.4 sensors. We therefore only used three elements of the array for monitoring the enzyme reaction with the peptide mixtures, i.e. **(1-3)•4** at pH 7.4. For monitoring the site-selective JMJD2E demethylation process, four controls were prepared in the presence of all cofactors and deactivated JMJD2E: the peptide mixtures of H3(1-21) + K4me$_3$ + K27me$_3$, K9me$_3$ + K4me$_3$ + H3 (23-34), and K9me$_3$ + H3(1-21) + H3K27me$_3$, as well as the product K4me$_3$ + K27me$_3$ + K9me$_1$, illustrating the scores plot position of the "correct" H3K9me$_1$ demethylated target, and incorrect demethylation at either K4 or K27. For monitoring the site-selective methylation process with PRDM9, the three controls were K4me$_3$ + H3 (23-34), K9me$_3$ + H3 (23-34), and H3 (1-21) + H3K27me$_3$, validating that the sensor can track the site-selective enzymatic reaction.

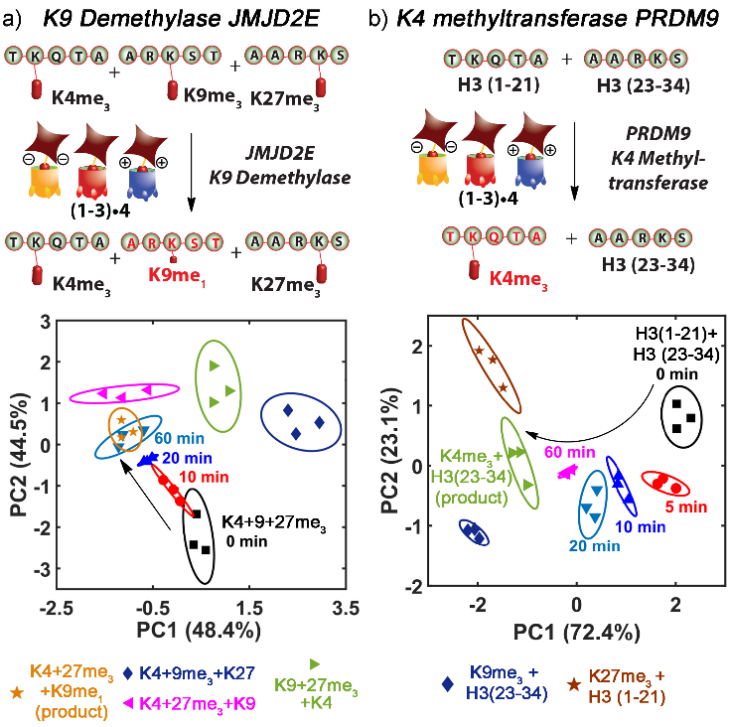

Figure 5.4 Site-selective enzyme assays. a) PCA scores plot of the selective demethylation of $K9me_3$ in a mixture of $K4me_3$, $K9me_3$ and $K27me_3$ peptides by JMJD2E with the **(1-3)•4** sensor; b) PCA scores plot of the selective methylation of $K4me_3$ in a mixture of H3 (1-21) and H3 (23-24) peptides by PRDM9 with the **(1-3)•4** sensor. [**4**] = 3 μM, [**1**] = 4 μM, [**2,3**] = 5 μM, in 50 mM phosphate (pH 7.4). Ellipses drawn at 95% confidence.

The sensor responses terminated at various time points were subjected to PCA, together with the controls (Figure 5.4). As the JMJD2E-catalyzed demethylation reaction proceeds, the reaction mixture moves towards the position where $K9me_1$ + $K4me_3$ + $K27me_3$ is located, and further away from the other two controls, indicating that the enzyme acts on only the K9 methylation site, but not K4 nor K27. The analysis is not only capable of distinguishing incorrect reaction products, but also the state of the product: fully demethylated K9 is distinguishable from $K9me_1$. Similarly, since PRDM9 only adds methyl groups to the K4 position, the reaction mixture catalyzed by PRDM9 moved

towards the control containing $K4me_3$, and not the other controls with K9 or K27 methylation. Each mixture was separated from each other (at 95% confidence), except for the demethylation reaction mixture at t = 60 min and the product mixture of $K9me_1$ + $K4me_3$ + $K27me_3$. The significance in group separation was confirmed by hierarchical cluster analysis (HCA) and one-way MANOVA, respectively (see Supporting Information).

Conclusion

In conclusion, we have employed supramolecular receptors to site-selectively recognize specific peptide modifications from a mixture of peptides in real enzymatic reactions. The activity of both histone methyltransferase and demethylase on specific methylation sites can be monitored. The sensitive molecular recognition capabilities of tailored deep cavitands provides site-selective discrimination between K methylations at different positions on the peptide backbone in a complex reaction mixture, and in the presence of interfering peptides. The sensor provides a quick and easy way to monitor the methylation or demethylation process catalyzed by histone PTM enzymes in a high-throughput manner, without requiring any sophisticated instrumentation or rigorous sample preparation.

Experimental section

1. General Information

Cavitands **1**,[1,4] **2**,[2,4] **3**[3,4] and guest **4**[4] were synthesized and characterized according to literature procedures. ^{1}H and ^{13}C NMR spectra were recorded on a Bruker 400 MHz NMR spectrometer. All NMR spectra were processed using MestReNova by Mestrelab Research S.L. Deuterated NMR solvents were obtained from Cambridge Isotope Laboratories, Inc., Andover, MA, and used without further purification. Mass spectra were recorded by electrospray ionization on an LTQ-XL linear ion trap mass spectrometer (Thermo Scientific, San Jose, CA). Solvents were dried through a commercial solvent purification system (Pure Process Technologies, Inc.). MALDI-MS spectra were obtained using an AB Sciex TOF/TOF 5800 MALDI mass spectrometer in the positive ion mode. Molecular modelling (semi-empirical calculations) was performed using the AM1 force field using SPARTAN.

All Histone H3 (purity > 95%) peptides (non-, mono-, di-, tri- Methylated) were purchased from Anaspec and used as received. Jumonji domain containing 2E (JMJD2E) and its inhibitor 2,4-dicarboxypyridine(2,4-PDCA) were purchased from Cayman Chemical (Ann Arbor, MI). Recombinant PRDM9 (191-414) protein was purchased from Active Motif (Carlsbad, CA). All other materials, including Rhodamine B, L-Ascorbic acid (ascorbate), ammonium ferrous sulfate, 2-oxoglutarate (2-OG), calf histone, S-(5'-Adenosyl)-L-methionine chloride (SAM) and S-(5'-Adenosyl)-L-homocysteine (SAH) were purchased form Sigma Aldrich (St. Louis, MO), Fisher Scientific (Fairlawn, NJ), or TCI (Tokyo, Japan) and were used as received.

Principal component analysis (PCA), Jackknife validation and Hierarchical clustering analysis (HCA) were completed with RStudio (Version 1.0.136), an integrated development environment (IDE) for R (version 3.3.2). Fluorescence data was first stored as an excel file, and then read into a matrix in RStudio. The internal function "princomp()" was used to perform PCA; the 'lda()' function was called for Jackknife Validation with the "CV" set as "true". One replicate was left out of the training set, and the LDA classifier was fitted on the input data. The output was recorded in a two-dimensional table. HCA was done with two steps: the Euclidean distance between any two objects within the dataset was first calculated and recorded into a two-dimensional matrix; then the matrix was used as the input for the built-in HCA function "hclust()", and the result was drawn with the "plot()" function.

One-way multivariate analysis of variance (one-way MANOVA) was completed with IBM SPSS Statistics 24.0. A post-hoc test was used here to show the significance of difference between any two objects. A p-value (shown as "sig." in the result table) < 0.05 was considered to be of significant difference.

Confidence ellipses were drawn with the data obtained from PCA using Matlab (version R2016b). The ellipse was drawn using a self-developed script. The full Matlab scripts are available upon request.

2. Experimental Procedures

Fluorescence displacement assay with PTM peptides. In general, the displacement assay was carried out by mixing 10 μL of the fluorescent guest **4** (30 μM), 10 μL of the cavitand (40 μM for **1,** 50 μM for **2** or **3**), 70 μL of the incubation buffer (phosphate pH 7.4 or carbonate pH 9) in the 96-well plate, adding 10 μL of histone H3 peptides to bring the total volume up to 100 μL, and incubating with mild shaking for 15 mins at room temperature. The fluorescence signal (F) was recorded in a Perkin Elmer Wallac 1420 Victor 2 Microplate Reader (PerkinElmer) with the Ex/Em wavelengths at 530/605 nm.

The calf histone was digested with chymotrypsin following protocols below. First, 1,000 μL of calf thymus histones (2 mg/mL) was denatured at 100 ^{o}C for 10 min. Then, 10 μL of DTT (Dithiothreitol, 200 mM), 20 μL of IAA (200 mM), and 20 μL of DTT (200 mM) were added sequentially and an incubation step of 30 min was applied after the addition of each reagent. At last, chymotrypsin equivalent to 1:50 of the protein mass was added to initiate the overnight incubation at 37 ^{o}C. Gel electrophoresis was employed to confirm that the digestion was completed and no histone protein bands were detected. The digestion product was used as a mimic of complex histone peptide environment.

PTM Enzyme activity assay. K9 Demethylation catalyzed by JMJD2E was performed by mixing ascorbic acid (500 μM), Fe^{2+} (ammonium ferrous sulfate, 6 μM), 2-OG (50 μM), H3K9me_3(1-21) (2 μM), and JMJD2E at various concentrations, in Tris buffer (50 mM, pH 8.2). Similarly, K4 methylation was carried out by mixing the methyl transferase PRDM9 at various concentrations with H3K4me_3(1-21) (2 μM), SAM (100 μM), DTT (1 mM) and NaCl (100 mM) in Tris buffer (50 mM, pH 8.5). The **1•4** sensor

([**1**] = 3 μM, [**4**] = 4 μM) was also added to each reaction mixture for *in situ* monitoring of the enzymatic process. The fluorescence was recorded by the plate reader every 5 min. The inhibition effect of 2,4-PDCA on JMJD2E was monitored using the same enzymatic mixture, except for fixing [JMJD2E] at 400 nM and the reaction duration at 30 min. Various amounts of 2,4-PDCA were spiked to the reaction solution with the highest concentration reaching 53.3 μM. The IC_{50} value was found by fitting the plot of sensor fluorescence vs. inhibitor concentration to the exponential decay equation using Origin 8.0:

$$(F_0\text{-}F)/A = \exp(-x/t_1)$$

The value of exponential constant t1 was found to be 10.6 μM, with $R^2 = 0.9751$ and thus $IC_{50} = \ln(1/2) * t_1 = 7.35$ μM.

When using the cavitand array for the study of the enzyme reaction, the demethylation or methylation reaction was first carried out as described above without adding the (**1-3)•4** (at 4 and 3 μM respectively) sensors. A small aliquot of the reaction solution was taken out and heated at 100 ºC for 5 min to deactivate the enzyme. The aliquot was split equally and added to the solutions containing the (**1-3)•4** sensors, and incubated for 15 min. For the array containing 6 sensor elements, the three (**1-3)•4** sensors were present in two buffer systems – the phosphate buffer (50 mM) at pH 7.4 and the carbonate buffer (50 mM) at pH 9.0. For the array containing 3 sensor elements, only the phosphate buffer was used. Fluorescence was measured by a Perkin Elmer Wallac 1420 Victor 2 Microplate Reader (PerkinElmer) with the Ex/Em wavelengths at 530/605 nm. Each measurement was repeated 3 times.

MALDI-TOF MS analysis. The enzymatic reaction was carried out exactly as described above for the fluorescence displacement measurements. Aliquots were taken out at various time points and heated to deactivate the enzyme. A saturated solution of α-cyano-4-hydroxycinnamic acid (CHCA) was prepared in the 1:1 mixture of pure acetonitrile and 0.1% formic acid, and used as the matrix. A mixture of 0.5 μL of the matrix and 0.5 μL of the reaction aliquot was spotted on a stainless steel Opti-TOF™ 96 targets plate, and allowed to dry completely before introducing into the mass spectrometer. Analysis was carried out on an AB Sciex 5800 TOF/TOF proteomics analyzer with a laser irradiation at a repetition frequency of 1000 Hz. A laser intensity index of 2800 was used for sample ionization and the MS spectra were acquired in the positive reflector mode within the mass range from 500 to 3,000 Da.

Reference

(1) Klose, R. J.; Zhang, Y. *Nat. Rev. Mol. Cell. Biol.* **2007**, *8*, 307-318.

(2) Tsukada, Y.-i.; Fang, J.; Erdjument-Bromage, H.; Warren, M. E.; Borchers, C. H.; Tempst, P.; Zhang, Y. *Nature* **2006**, *439*, 811-816.

(3) Stewart, M. D.; Li, J.; Wong, J. *Mol. Cell. Biol.* **2005**, *25*, 2525-2538.

(4) Nakayama, J.; Rice, J. C.; Strahl, B. D.; Allis, C. D.; Grewal, S. I. *Science* **2001**, *292*, 110-113.

(5) Jenuwein, T.; Laible, G.; Dorn, R.; Reuter, G. *Cell Mol. Life Sci.* **1998**, *54*, 80–93.

(6) Huq, M. D. M.; Ha, S. G.; Barcelona, H.; Wei, L.-N. *J. Proteome Res.* **2009**, *8*, 1156-1167.

(7) Rathert, P.; Dhayalan, A.; Ma, H.; Jeltsch, A. *Mol. BioSyst.* **2008**, *4*, 1186-1190.

(8) Rathert, P.; Zhang, X.; Freund, C.; Cheng, X.; Jeltsch, A. *Chem. Biol.*, **2008**, *15*, 5–11.

(9) Dsouza, R. N.; Hennig, A.; Nau, W. M. *Chem.-Eur. J.* **2012**, *18*, 3444-3459.

(10) (a) McGovern, R. E.; Snarr, B. D.; Lyons, J. A.; McFarlane, J.; Whiting, A. L.; Paci, I.; Hof, F.; Crowley, P. B. *Chem. Sci.* **2015**, *6*, 442-449. (b) Garnett, G. A. E.; Starke, M. J.; Shaurya, A.; Li, J.; Hof, F. *Anal. Chem.* **2016**, *88*, 3697-3703. (c) Tabet, S.; Douglas, S. F.; Daze, K. D.; Garnett, G. A. E.; Allen, K. J. H.; Abrioux, E. M. M.; Quon, T. T. H.; Wulff, J. E.; Hof, F. *Bioorg. Med. Chem.* **2013**, *21*, 7004-7010.

(11) Barrow, S. J.; Kasera, S.; Rowland, M. J.; del Barrio, J.; Scherman, O. A. *Chem. Rev.* **2015**, *115*, 12320−12406.

(12) (a) Gober, I. N.; Waters, M. L. *J. Am. Chem. Soc.* **2016**, *138*, 9452–9459. (b) Peacor, B. C.; Ramsay, C. M.; Waters, M. L. *Chem. Sci.* **2017**, 8, 1422-1428.

(13) Ghale, G.; Nau, W. M. *Acc. Chem. Res.* **2014**, *47*, 2150-2159.

(14) (a) Guo, D.-S.; Yang, J.; Liu, Y. *Chem.-Eur. J.* **2013**, *19*, 8755−8759. (b) Hennig, A.; Bakirci, H.; Nau, W. M. *Nat. Methods* **2007**, *4*, 629−632. (c) Praetorius, A.; Bailey, D. M.; Schwarzlose, T.; Nau, W. M. *Org. Lett.* **2008**, 10, 4089−4092. (d) Nau, W. M.; Ghale, G.; Hennig, A.; Bakirci, H.; Bailey, D. M. *J. Am. Chem. Soc.* **2009**, *131*, 11558−11570.

(15) Ghale, G.; Ramalingam, V.; Urbach, A. R.; Nau, W. M. *J. Am. Chem. Soc.* **2011**, *133*, 7528−7535.

(16) Florea, M.; Kudithipudi, S.; Rei, A.; González-Álvarez, M. J.; Jeltsch, A.; Nau, W. M. *Chem.-Eur. J.* **2012**, *18*, 3521-3528.

(17) (a) Ingerman, L. A.; Cuellar, M. E.; Waters, M. L. *Chem. Commun.* **2010**, *46*, 1839-1841. (b) James, L. I.; Beaver, J. E.; Rice, N. W.; Waters, M. L. *J. Am. Chem. Soc.* **2013**, *135*, 6450−6455. (c) Minaker, S. A.; Daze, K. D.; Ma, M. C. F.; Hof, F. *J. Am. Chem. Soc.* **2012**, *134*, 11674-11680. (d) Beaver, J.E.; Waters, M.L. *ACS Chem. Biol.* **2016**, *11*, 643–653.

(18) Biros, S. M.; Ullrich, E. C.; Hof, F.; Trembleau, L.; Rebek, J. *J. Am. Chem. Soc.* **2004**, *126*, 2870-2876.

(19) Liu, Y.; Perez, L.; Mettry, M.; Easley, C. J.; Hooley, R. J.; Zhong, W. *J. Am. Chem. Soc.* **2016**, *138*, 10746-10749.

(20) Liu, Y.; Perez, L.; Mettry, M.; Gill, A. D.; Byers, S. R.; Easley, C. J.; Bardeen, C. J.; Zhong, W.; Hooley, R. J. *Chem. Sci.* **2017**, *8*, 3960- 3970.

(21) Jurs, P. C.; Bakken, G. A.; McClelland, H. E. *Chem. Rev.* **2000**, *100*, 2649-2678.

Supporting Information

Supporting tables

Table S5.1 The list of peptides used in our study and their sequence.

Abbreviation	Peptides	Sequence (No modification shown)
H3(1-21)	H3(1-21)	ARTKQTARKSTGGKAPRKQLA
K9me$_1$	H3K9(me$_1$)(1-21)	ARTKQTARK(me$_1$)STGGKAPRKQLA
K9me$_2$	H3K9(me$_2$)(1-21)	ARTKQTARK(me$_2$)STGGKAPRKQLA
K9me$_3$	H3K9(me$_3$)(1-21)	ARTKQTARK(me$_3$)STGGKAPRKQLA
K4me$_3$	H3K4(me$_3$)(1-21)	ARTK(me$_3$)QTARKSTGGKAPRKQLA
H3(23-34)	H3(23-34)	KAARKSAPATGG
K27me$_3$	H3K27(me$_3$) (23-34)	KAARK(me$_3$)SAPATGG
K36me$_3$	H3K36(me$_3$)(31-41)	STGGVK(me$_3$)KPHRY

Supporting Figures

Sensor Optimization

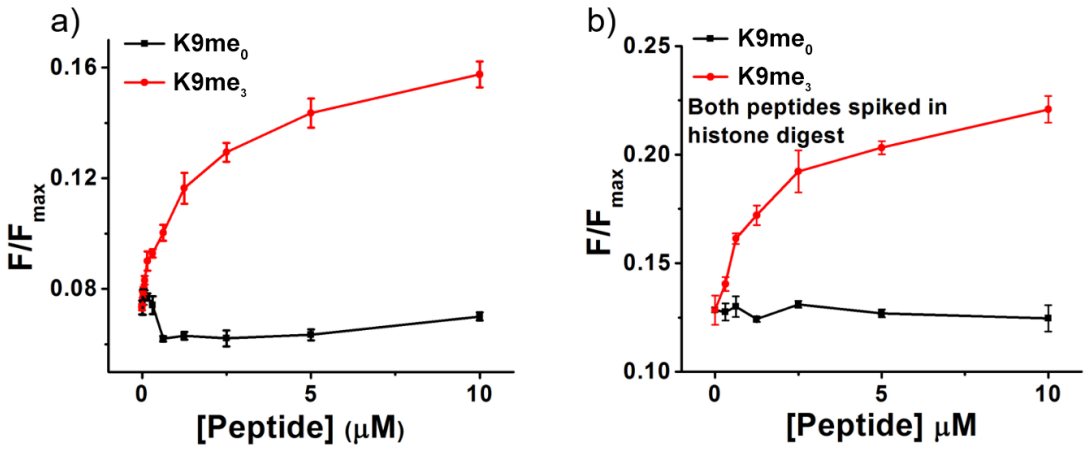

Figure S5.1 $K9me_0$ and $K9me_3$ peptide competition with **1•4** in (**a**) phosphate buffer (50 mM, pH 7.4), or (**b**) phosphate buffer spiked with the calf thymus type II-A histone digest (0.1 mg/mL). F_{max} represents the fluorescence of guest **4** without cavitand **1**.

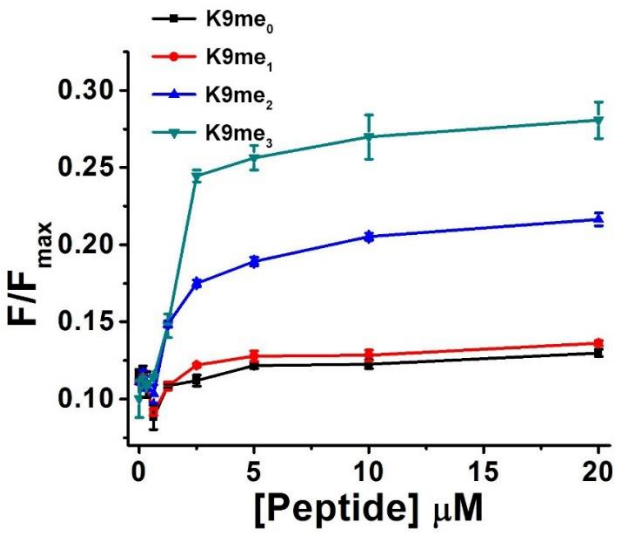

Figure S5.2 Competition curve of $K9me_0$, $K9me_1$, $K9me_2$ and $K9me_3$ with **1•4** (cavitand **1** = 4 μM, guest **4** = 3 μM) in phosphate buffer (50 mM, pH = 7.4).

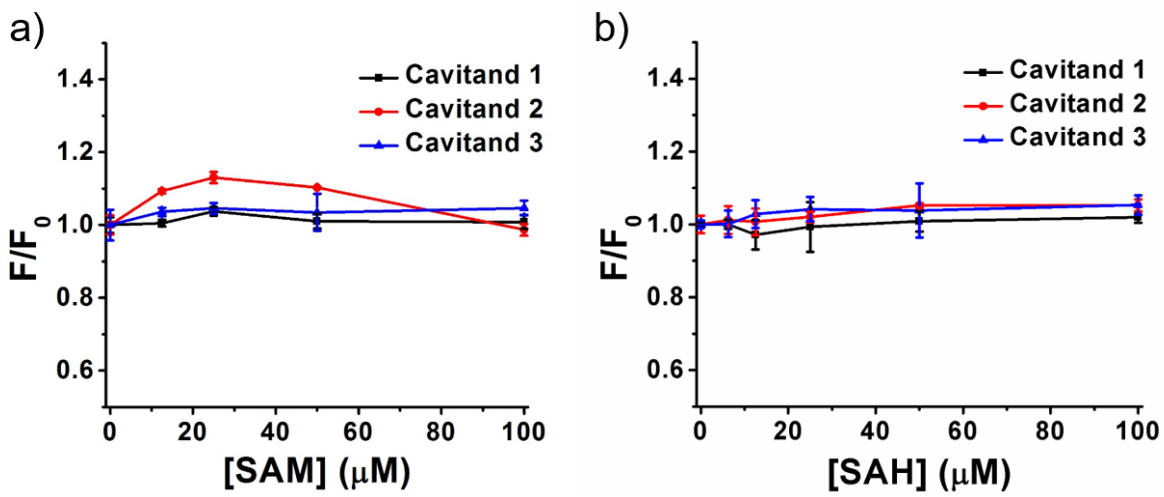

Figure S5.3 Influence of (a) S-(5'-Adenosyl)-L-methionine (SAM) and (b) S-(5'-Adenosyl)-L-homocysteine (SAH) on the fluorescence of **1•4, 2•4** and **3•4** (cavitand **1** = 4 μM, cavitand 2 = 5 μM, cavitand 3 = 5 μM, guest **4** = 3 μM) in phosphate buffer (50 mM, pH = 7.4). F_0 represents the fluorescence of **1•4**, **2•4** or **3•4.**

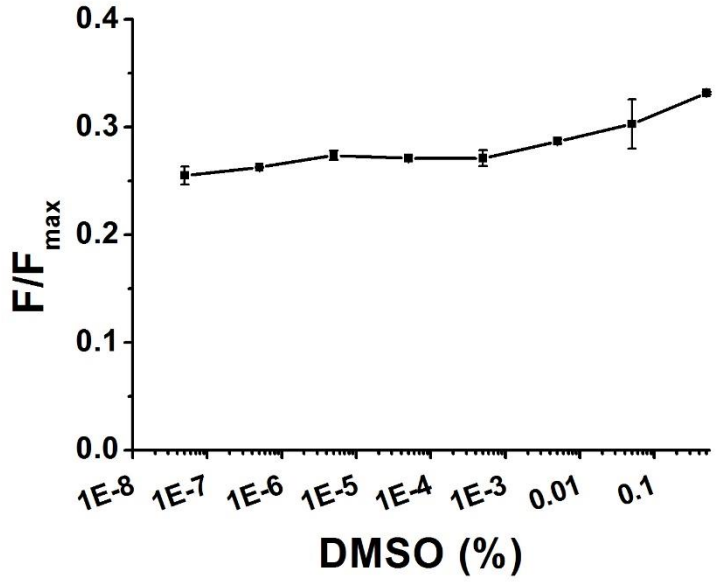

Figure S5.4 Impact of DMSO concentration on the fluorescence of sensor **1•4** (cavitand **1** = 4 μM, guest **4** = 3 μM) in phosphate buffer (50 mM, pH = 7.4).

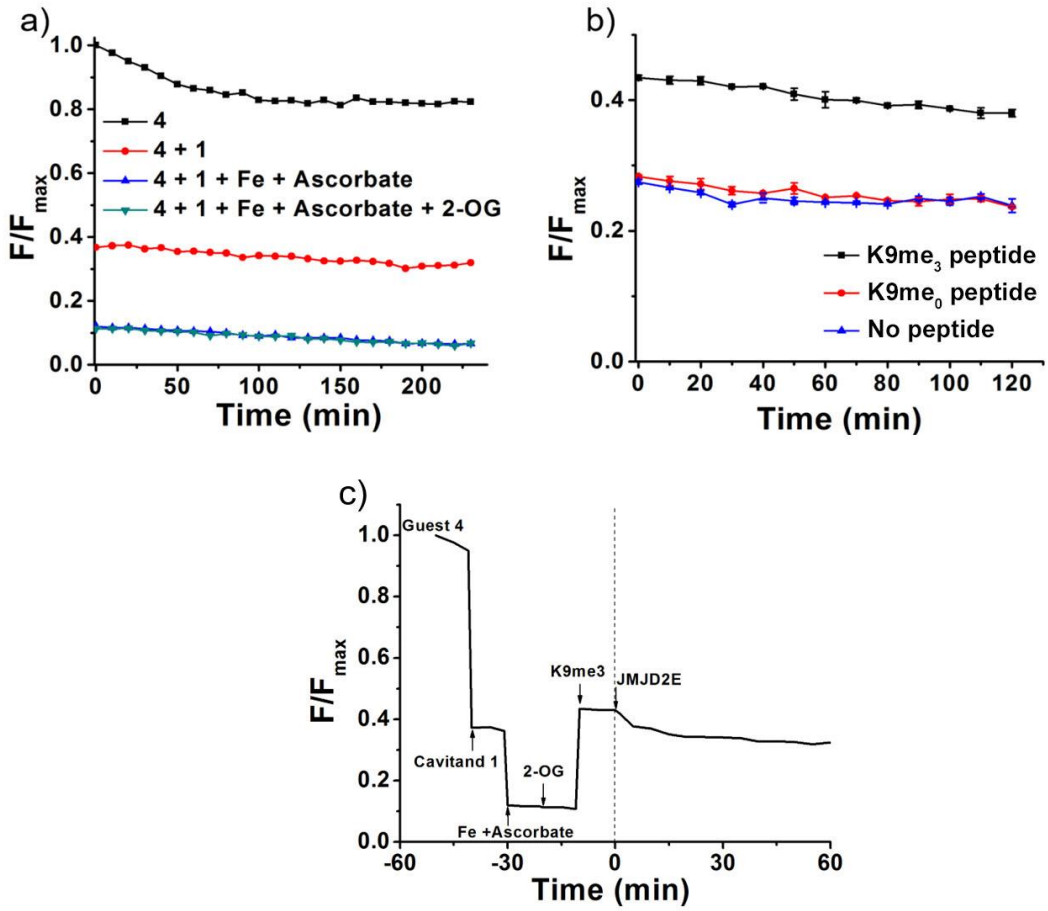

Figure S5.5 Stability of guest **4** and **1•4** in (**a**) the solutions containing the chemicals used in the reaction catalyzed by JMJD2E; and (**b**) with the peptide substrates upon continuous light exposure (λ_{ex} = 530 nm). The background buffer was still 50 mM phosphate at pH 7.4, and the sensor was composed of 3 μM guest **4** and 4 μM cavitand **1**. The concentrations for Fe^{2+}, ascorbate, and 2-OG were 6 μM, 0.5 mM, and 50 μM, respectively. (c) The fluorescence vs. time curve for the enzymatic assay catalyzed by JMJD2E collected as each component was added. [peptide] = 2 μM, [JMJD2E] = 200 nM.

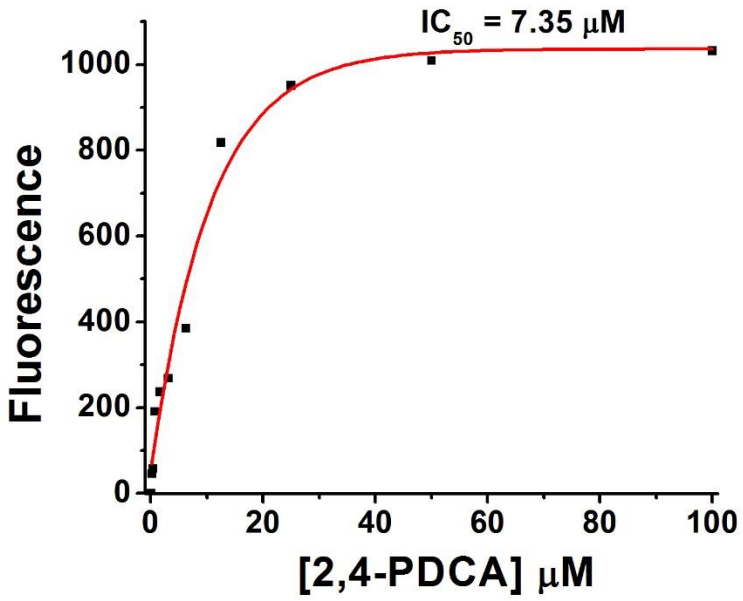

Figure S5.6 Investigation of 2,4-PDCA inhibition on JMJD2E. The fluorescence of the **1•4** sensor (cavitand **1** = 4 μM, guest **4** = 3 μM) increased with the addition of 2,4- PDCA from 0 to 100 μM to the enzyme reaction mixture containing ascorbate (500 μM), Fe^{2+} (ammonium ferrous sulfate, 6 μM), 2-OG (50 μM), H3K9me3(1-21) (2 μM), and 400 nM JMJD2E in Tris buffer (50 mM, pH 8.2).

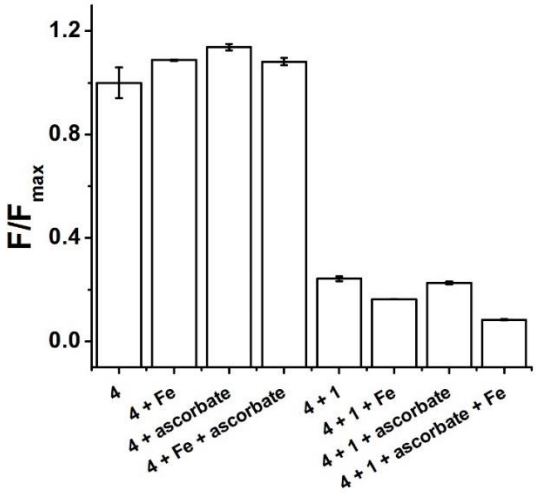

Figure S5.7 Influence of the chemical additives in the JMJD2E demethylation reaction on the fluorescence of guest **4** itself and complex **1•4**. Cavitand **1** = 4 μM, guest **4** = 3 μM, Fe^{2+} = 6 μM, ascorbate = 1 mM.

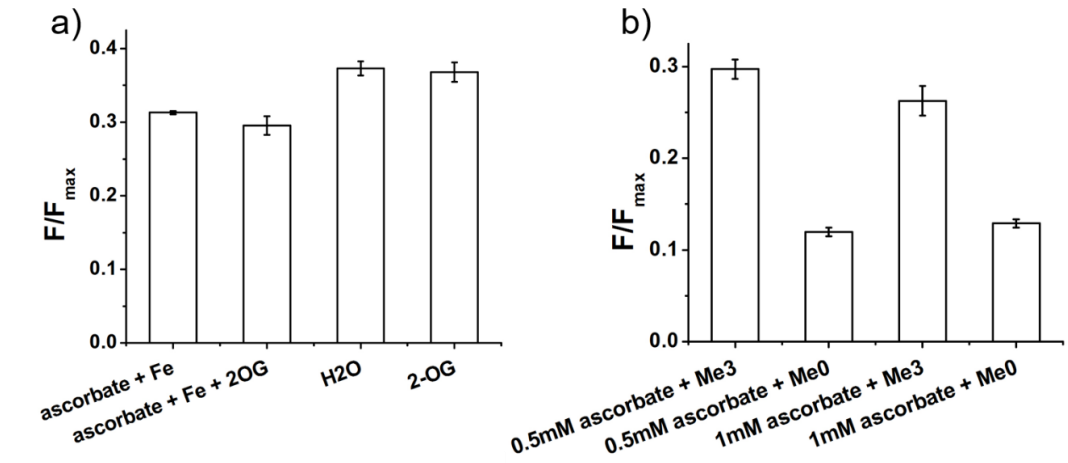

Figure S5.8 Impacts of (**a**) 2-OG (50 µM), Fe^{2+} and (**b**) ascorbate (1 or 0.5 mM) on the fluorescence of sensor **1•4** (cavitand **1** = 4 µM, guest **4** = 3 µM).

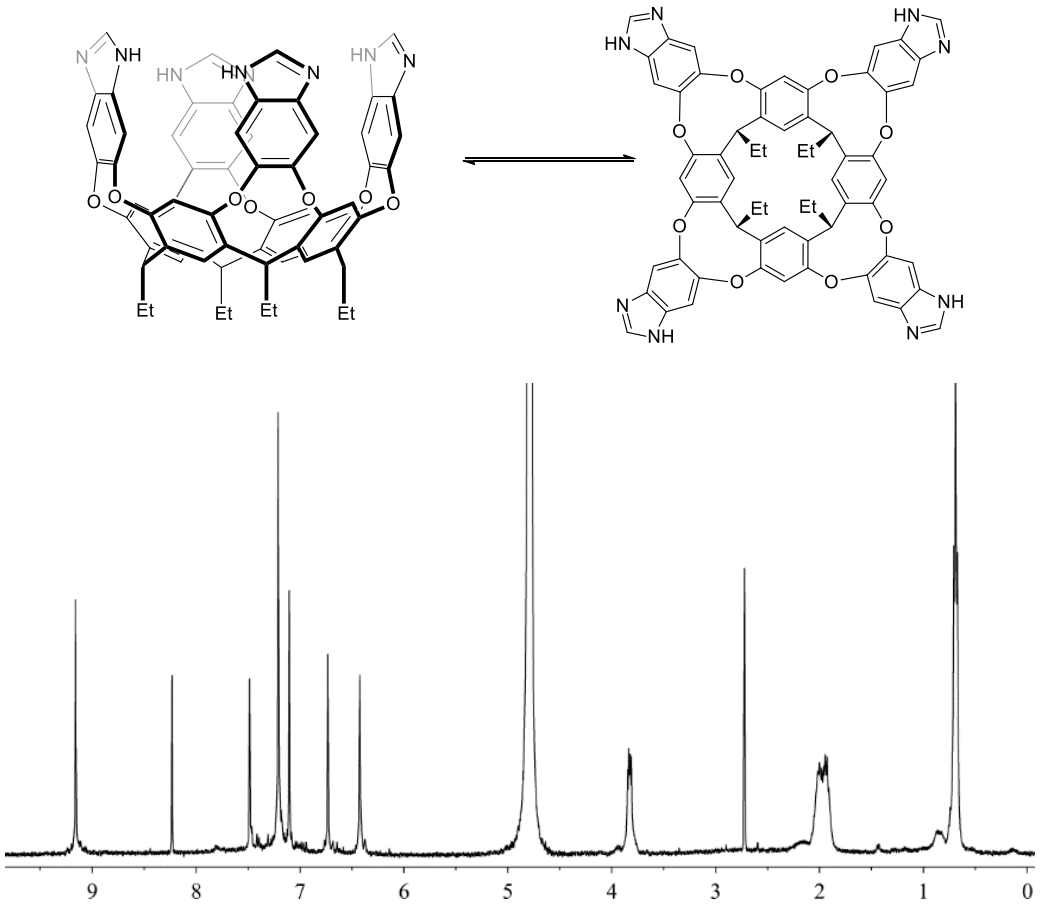

Figure S5.9 ^{1}H NMR spectrum of cavitand **2** in D_2O (400 MHz, 1 mM **2**, 298K).

Peptide Mixture Analysis

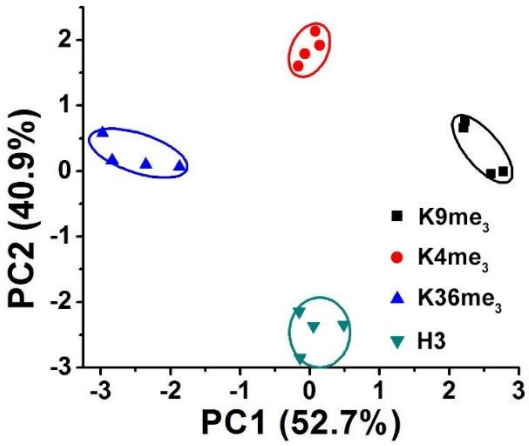

Figure S5.10 The Scores plot from PCA on the data obtained from four peptides in presence of histone digest (0.1 mg/mL) using the 6-element cavitand array. The plot was produced by PCA analysis using 6 factors: **1•4, 2•4** and **3•4** with two pHs (7.4 and 9).

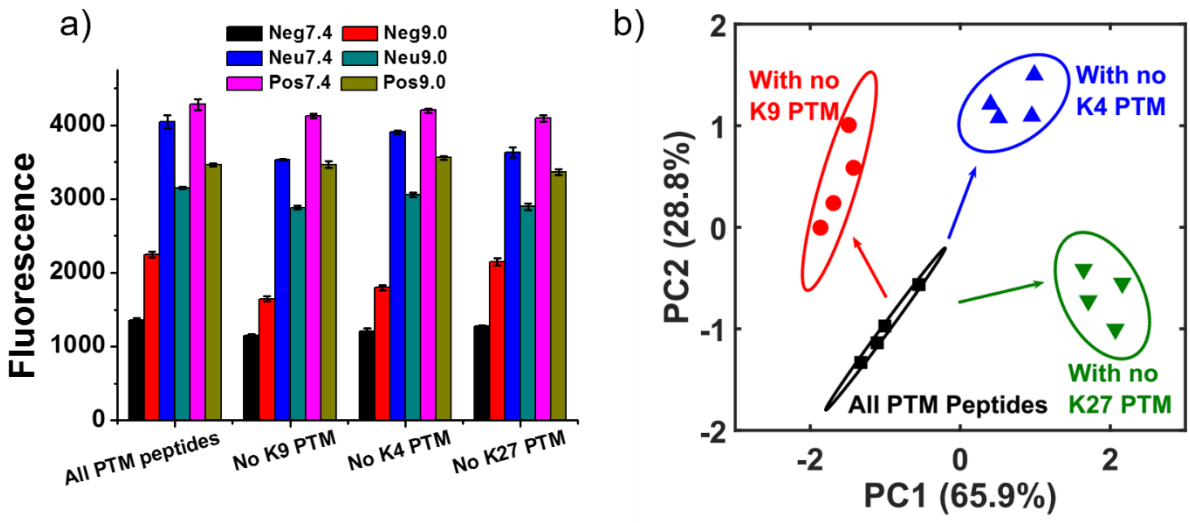

Figure S5.11 a) Raw fluorescence data used for PCA analysis in Figure 5.2a, showing the selective recognition of Kme_3 peptides in a peptide mixture with the **(1-3)•4** sensor, [**4**] = 3 μM, [**1**] = 4 μM, [**2**,**3**] = 5 μM, 50 mM phosphate buffer at pH = 7.4 or 50 mM carbonate buffer at pH = 9.0, [peptide] = 2 μM; b) PCA scores plot for the same experiment using only 3 factors (cavitands **1**, **2** and **3**, pH 7.4 only) as opposed to 6 (which is shown in Figure 5.2a).

Table S5.2 Factor Loadings table of the PCA data shown in Figure 5.2a.

Factor loadings	**PC1**	**PC2**
cavitand **1**, pH 7.4	**0.819**	**-0.509**
cavitand **1**, pH 9.0	**0.686**	**-0.696**
cavitand **2**, pH 7.4	**0.922**	**0.208**
cavitand **2**, pH 9.0	**0.924**	**0.255**
cavitand **3**, pH 7.4	**0.791**	**0.352**
cavitand **3**, pH 9.0	**0.203**	**0.928**

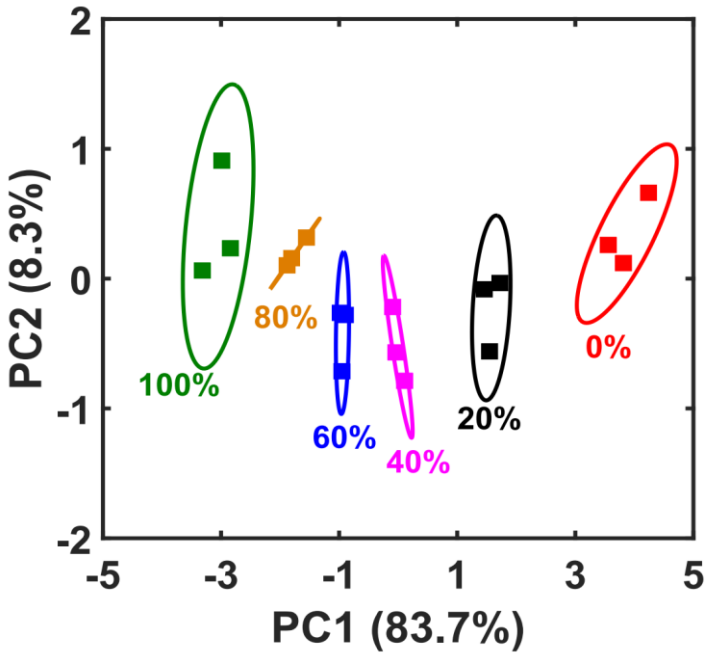

Figure S5.12 PCA scores plot with 3 repeats for the variation of K9me$_3$ in a K4/9/27me$_3$ mixture the selective recognition of K9me$_3$ peptides in a peptide mixture with the **(1-3)•4** sensor; this data is that of the red line in Figure 5.2b, showing all repeats. Ellipses drawn at 95% confidence.

Enzyme Reaction Analysis

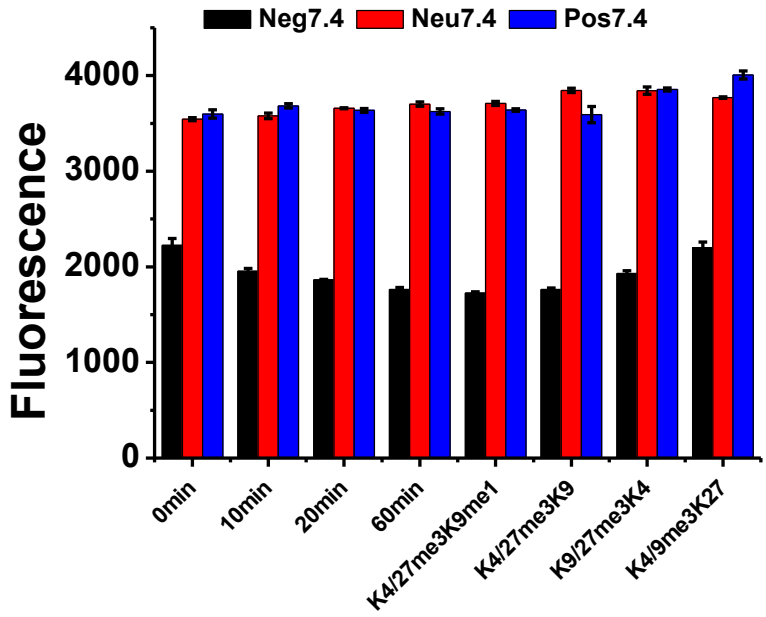

Figure S5.13 Raw fluorescence data used for PCA analysis in Figure 5.4a, showing the selective sensing of JMJD2E activity. [**4**] = 3 μM, [**1**] = 4 μM, [**2**,**3**] = 5 μM, [peptide] = 2 μM, [JMJD2E] = 200 nM, [2-OG] = 50 μM, [Fe^{2+}] = 6 μM; [ascorbate] = 0.5 mM in 50 mM phosphate (pH 7.4).

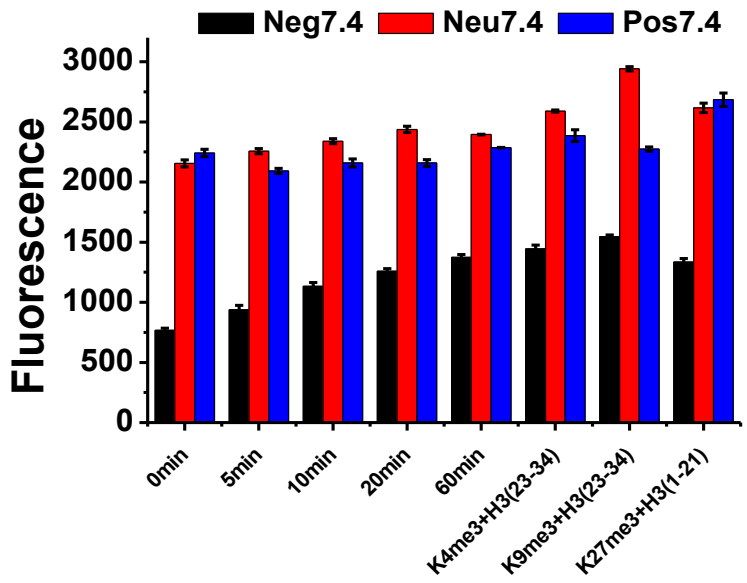

Figure S5.14 Raw fluorescence data used for PCA analysis in Figure 5.4b, showing the selective sensing of PRDM9 activity. [**4**] = 3 µM, [**1**] = 4 µM, [**2**,**3**] = 5 µM, [peptide] = 2 µM, [PRDM9] = 200 nM, [SAM] = 100 µM, [DTT] = 1 mM, in 50 mM phosphate (pH 7.4).

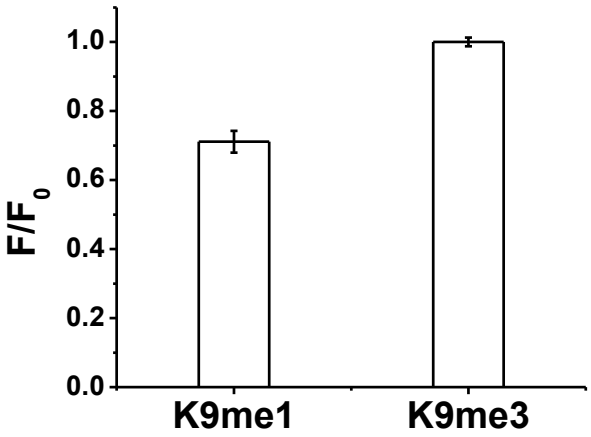

Figure S5.15 Relative fluorescence change of **1•4** after adding $K9me_1$ and $K9me_3$ at pH 7.4. [**4**] = 3 μM, [**1**] = 4 μM, [peptide] = 2 μM, in 50 mM phosphate (pH 7.4).

Statistical Validation

Hierarchical cluster analysis (HCA) was performed to determine the distance between the groups within our dataset. The Dendrogram for the dataset that included the demethylation reaction catalyzed by JMJD2E is shown in Fig. S5.15. The following conclusions can be drawn from the plot, all agreeing with the PCA result:

1. Most of the three repeats of the same sample have good similarity to each other, i.e. joining each other at a low dissimilarity value around 50, except for one of the repeats for K4/27me$_3$K9.

2. The reaction mixture with the longest reaction time t=60 min has high similarity to the end product K4/27me$_3$K9me$_1$. The MALDI measurement also showed that, the substrate/product ratio no longer changed after 60 min, and the reaction should have reached equilibrium at this point.

3. The reaction mixture collected at t = 10 and 20 min have higher similarity to each other, than with other reaction time duration at 0 and 60 min, but definitely we can differentiate the reaction mixtures collected at t = 0, 10-20 min, and 60 min.

4. The three standard peptide mixtures containing a single non-methylated peptide non-methylated, (i.e. K4/27me$_3$K9, K4/9me$_3$K27, and K9/27me$_3$K9) are far apart from each other because they are the leaves on the branches that only join at high dissimilarity values > 400.

The Dendrogram for the data set that included the methylation reaction catalyzed by PRDM9 shown in Figure S5.16 also clearly indicated that our method can differentiate the reaction mixtures measured at different reaction time duration. Each of the two adjacent

time points (0 & 5 min, 10 & 20 min, 60 & end product) have some similarity to each other, joining each other at a medium dissimilarity value of ~300, but these three groups are significantly different from each other, and only join at dissimilarity value > 600. The three standard peptide mixtures are also very different from each other.

The NANOVA test (Table S5.3) on the PC1 and PC2 values of the samples indicates whether the 7 groups of objects in our dataset can be significantly separated by these values at 95% confidence interval. We can see from the result that the only object pair that cannot be differentiated by either PC1 or PC2 is the t=60 min and the end product K4/27me_3K9me_1. All other groups can be significantly differentiated by at least one of the PC values at 95% confidence interval.

The NANOVA test (Table S5.4) for the samples describing the methyltransferase action shows that all groups can be differentiated significantly with 95% confidence interval by PC1, although PC2 cannot tell apart the reaction mixtures collected at various durations.

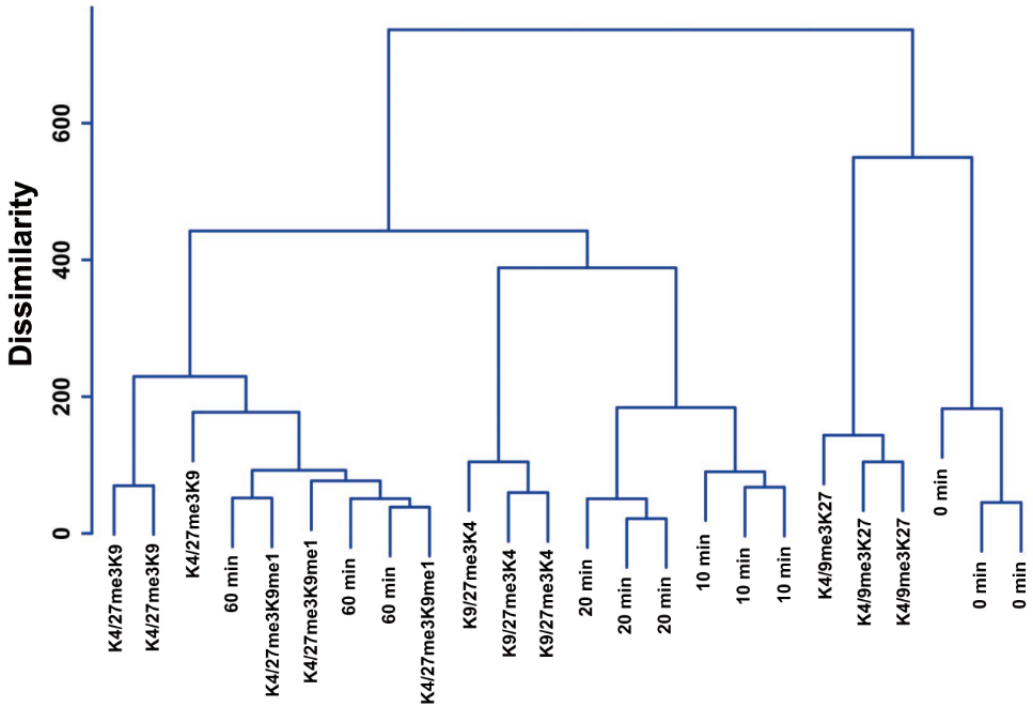

Figure S5.16 Hierarchical cluster analysis of the fluorescence data shown in Figure S5.13.

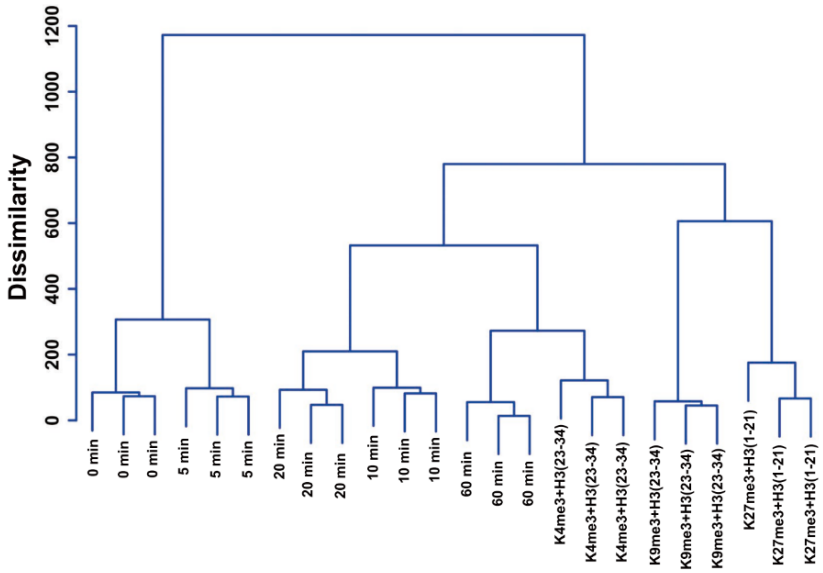

Figure S5.17 Hierarchical cluster analysis of the fluorescence data shown in Figure S5.14.

Table S5.3 Jackknife analysis of the fluorescence data shown in Figure S5.13.

	0 min	10 min	20 min	60 min	K4/27me$_3$ K9me1	K4/27me$_3$ K9	K9/27me$_3$ K4	K4/9me$_3$ K27	%Correct
0 min	**3**	**0**	**0**	**0**	**0**	**0**	**0**	**0**	**100**
10 min	**0**	**3**	**0**	**0**	**0**	**0**	**0**	**0**	**100**
20 min	**0**	**0**	**3**	**0**	**0**	**0**	**0**	**0**	**100**
60 min	**0**	**0**	**0**	**1**	**2**	**0**	**0**	**0**	**33**
K4/27me$_3$K9me$_1$	**0**	**0**	**0**	**3**	**0**	**0**	**0**	**0**	**0**
K4/27me$_3$K9	**0**	**0**	**0**	**0**	**1**	**2**	**0**	**0**	**67**
K9/27me$_3$K4	**0**	**0**	**0**	**0**	**0**	**0**	**3**	**0**	**100**
K4/9me$_3$K27	**0**	**0**	**0**	**0**	**0**	**0**	**0**	**3**	**100**
Total	**3**	**3**	**3**	**1**	**0**	**2**	**3**	**3**	**75**

Table S5.4 Jackknife analysis for the fluorescence data shown in Figure S5.14.

	0 min	5 min	10 min	20 min	60 min	K4me$_3$+ H3(23-34)	K9me$_3$+ H3(23-34)	K27me$_3$+ H3(1-21)	%Correct
0 min	**3**	**0**	**0**	**0**	**0**	**0**	**0**	**0**	**100**
5 min	**0**	**3**	**0**	**0**	**0**	**0**	**0**	**0**	**100**
10 min	**0**	**0**	**3**	**0**	**0**	**0**	**0**	**0**	**100**
20 min	**0**	**0**	**0**	**3**	**0**	**0**	**0**	**0**	**100**
60 min	**0**	**0**	**0**	**0**	**3**	**0**	**0**	**0**	**100**
K4me$_3$+ H3(23-34)	**0**	**0**	**0**	**0**	**0**	**3**	**0**	**0**	**100**
K9me$_3$+ H3(23-34)	**0**	**0**	**0**	**0**	**0**	**0**	**3**	**0**	**100**
K27me$_3$+ H3(1-21)	**0**	**0**	**0**	**0**	**0**	**0**	**0**	**3**	**100**
Total	**3**	**3**	**3**	**3**	**3**	**3**	**3**	**3**	**100**

Table S5.5 Results from NANOVA analysis for the %K9me$_3$ data presented in Fig. S5.12. The analysis is based on the observed means of three repeats.
*: The mean difference is significant at the .05 level.

Dependent Variable	(I) Sample	(J) Sample	Mean Difference (I-J)	Sig.	Dependent Variable	(I) Sample	(J) Sample	Mean Difference (I-J)	Sig.
PC1	0%	100%	6.9200*	0	PC2	0%	100%	-0.055	0.824
		20%	2.2944*	0			20%	.5723*	0.035
		40%	3.8787*	0			40%	.8714*	0.004
		60%	4.8146*	0			60%	.7658*	0.008
		80%	5.6179*	0			80%	0.1547	0.533
	100%	0%	-6.9200*	0		100%	0%	0.055	0.824
		20%	-4.6256*	0			20%	.6273*	0.023
		40%	-3.0414*	0			40%	.9264*	0.002
		60%	-2.1055*	0			60%	.8208*	0.005
		80%	-1.3021*	0			80%	0.2096	0.402
	20%	0%	-2.2944*	0		20%	0%	-.5723*	0.035
		100%	4.6256*	0			100%	-.6273*	0.023
		40%	1.5842*	0			40%	0.2991	0.239
		60%	2.5201*	0			60%	0.1935	0.438
		80%	3.3235*	0			80%	-0.4176	0.109
	40%	0%	-3.8787*	0		40%	0%	-.8714*	0.004
		100%	3.0414*	0			100%	-.9264*	0.002
		20%	-1.5842*	0			20%	-0.2991	0.239
		60%	.9359*	0			60%	-0.1056	0.669
		80%	1.7393*	0			80%	-.7167*	0.012
	60%	0%	-4.8146*	0		60%	0%	-.7658*	0.008
		100%	2.1055*	0			100%	-.8208*	0.005
		20%	-2.5201*	0			20%	-0.1935	0.438
		40%	-.9359*	0			40%	0.1056	0.669
		80%	.8034*	0			80%	-.6112*	0.026
	80%	0%	-5.6179*	0		80%	0%	-0.1547	0.533
		100%	1.3021*	0			100%	-0.2096	0.402
		20%	-3.3235*	0			20%	0.4176	0.109
		40%	-1.7393*	0			40%	.7167*	0.012
		60%	-.8034*	0			60%	.6112*	0.026

Table S5.6 Results from NANOVA analysis for the data presented in Fig. S5.13. The analysis is based on observed means. *: The mean difference is significant at the .05 level. The highlighted cells showed the ones not significantly different from each other.

Dependent Variable	(I) Sample	(J) Sample	Mean Difference (I-J)	Sig.	Dependent Variable	(I) Sample	(J) Sample	Mean Difference (I-J)	Sig.
PC1	0min	10min	.5397*	0.019	PC2	0min	10min	-1.1110*	0
		20min	1.0543*	0			20min	-1.8407*	0
		60min	1.4563*	0			60min	-2.3975*	0
		K4/27Me3K9	1.5369*	0			K4/27Me3K9	-3.4479*	0
		K4/27Me3K9me1	1.5174*	0			K4/27Me3K9me1	-2.5784*	0
		K4/9Me3K27	-2.1249*	0			K4/9Me3K27	-2.7589*	0
		K9/27Me3K4	-0.4085	0.067			K9/27Me3K4	-3.6267*	0
	10min	0min	-.5397*	0.019		10min	0min	1.1110*	0
		20min	.5146*	0.025			20min	-.7297*	0.007
		60min	.9167*	0			60min	-1.2865*	0
		K4/27Me3K9	.9972*	0			K4/27Me3K9	-2.3369*	0
		K4/27Me3K9me1	.9777*	0			K4/27Me3K9me1	-1.4674*	0
		K4/9Me3K27	-2.6646*	0			K4/9Me3K27	-1.6479*	0
		K9/27Me3K4	-.9482*	0			K9/27Me3K4	-2.5157*	0
	20min	0min	-1.0543*	0		20min	0min	1.8407*	0
		10min	-.5146*	0.025			10min	.7297*	0.007
		60min	0.4021	0.071			60min	-.5568*	0.032
		K4/27Me3K9	.4826*	0.034			K4/27Me3K9	-1.6072*	0
		K4/27Me3K9me1	.4631*	0.04			K4/27Me3K9me1	-.7377*	0.007
		K4/9Me3K27	-3.1792*	0			K4/9Me3K27	-.9182*	0.001
		K9/27Me3K4	-1.4628*	0			K9/27Me3K4	-1.7860*	0
	60min	0min	-1.4563*	0		60min	0min	2.3975*	0
		10min	-.9167*	0			10min	1.2865*	0
		20min	-0.4021	0.071			20min	.5568*	0.032
		K4/27Me3K9	0.0806	0.703			K4/27Me3K9	-1.0504*	0
		K4/27Me3K9me1	0.0611	0.772			K4/27Me3K9me1	-0.1809	0.456
		K4/9Me3K27	-3.5812*	0			K4/9Me3K27	-0.3614	0.146
		K9/27Me3K4	-1.8648*	0			K9/27Me3K4	-1.2292*	0
	K4/27Me3K9	0min	-1.5369*	0		K4/27Me3K9	0min	3.4479*	0
		10min	-.9972*	0			10min	2.3369*	0
		20min	-.4826*	0.034			20min	1.6072*	0
		60min	-0.0806	0.703			60min	1.0504*	0
		K4/27Me3K9me1	-0.0195	0.926			K4/27Me3K9me1	.8695*	0.002
		K4/9Me3K27	-3.6618*	0			K4/9Me3K27	.6890*	0.01
		K9/27Me3K4	-1.9454*	0			K9/27Me3K4	-0.1789	0.46
	K4/27Me3K9me1	0min	-1.5174*	0		K4/27Me3K9me1	0min	2.5784*	0
		10min	-.9777*	0			10min	1.4674*	0
		20min	-.4631*	0.04			20min	.7377*	0.007
		60min	-0.0611	0.772			60min	0.1809	0.456
		K4/27Me3K9	0.0195	0.926			K4/27Me3K9	-.8695*	0.002
		K4/9Me3K27	-3.6423*	0			K4/9Me3K27	-0.1805	0.456
		K9/27Me3K4	-1.9259*	0			K9/27Me3K4	-1.0484*	0
	K4/9Me3K27	0min	2.1249*	0		K4/9Me3K27	0min	2.7589*	0
		10min	2.6646*	0			10min	1.6479*	0
		20min	3.1792*	0			20min	.9182*	0.001
		60min	3.5812*	0			60min	0.3614	0.146
		K4/27Me3K9	3.6618*	0			K4/27Me3K9	-.6890*	0.01
		K4/27Me3K9me1	3.6423*	0			K4/27Me3K9me1	0.1805	0.456
		K9/27Me3K4	1.7164*	0			K9/27Me3K4	-.8679*	0.002
	K9/27Me3K4	0min	0.4085	0.067		K9/27Me3K4	0min	3.6267*	0
		10min	.9482*	0			10min	2.5157*	0
		20min	1.4628*	0			20min	1.7860*	0
		60min	1.8648*	0			60min	1.2292*	0
		K4/27Me3K9	1.9454*	0			K4/27Me3K9	0.1789	0.46
		K4/27Me3K9me1	1.9259*	0			K4/27Me3K9me1	1.0484*	0
		K4/9Me3K27	-1.7164*	0			K4/9Me3K27	.8679*	0.002

Table S5.7 Results from NANOVA analysis for the data presented in Fig. S5.14. The analysis is based on observed means. *: The mean difference is significant at the .05 level.

Dependent Variable	(I) Sample	(J) Sample	Mean Difference (I-J)	Sig.	Dependent Variable	(I) Sample	(J) Sample	Mean Difference (I-J)	Sig.
PC1	0min	10min	1.2091*	0	PC2	0min	10min	1.1604*	0
		20min	1.7910*	0			20min	1.4644*	0
		5min	.3188*	0.024			5min	1.1145*	0
		60min	2.2972*	0			60min	.9226*	0
		K27me3+H3(1-21)	3.8322*	0			K27me3+H3(1-21)	-.8462*	0
		K4me3+H3(23-34)	3.2656*	0			K4me3+H3(23-34)	.7739*	0
		K9me3+H3(23-34)	4.1897*	0			K9me3+H3(23-34)	1.9304*	0
	10min	0min	-1.2091*	0		10min	0min	-1.1604*	0
		20min	.5818*	0			20min	0.304	0.095
		5min	-.8903*	0			5min	-0.0459	0.792
		60min	1.0881*	0			60min	-0.2378	0.185
		K27me3+H3(1-21)	2.6231*	0			K27me3+H3(1-21)	-2.0066*	0
		K4me3+H3(23-34)	2.0565*	0			K4me3+H3(23-34)	-.3865*	0.039
		K9me3+H3(23-34)	2.9806*	0			K9me3+H3(23-34)	.7700*	0
	20min	0min	-1.7910*	0		20min	0min	-1.4644*	0
		10min	-.5818*	0			10min	-0.304	0.095
		5min	-1.4721*	0			5min	-0.3499	0.058
		60min	.5063*	0.001			60min	-.5418*	0.006
		K27me3+H3(1-21)	2.0412*	0			K27me3+H3(1-21)	-2.3106*	0
		K4me3+H3(23-34)	1.4746*	0			K4me3+H3(23-34)	-.6905*	0.001
		K9me3+H3(23-34)	2.3988*	0			K9me3+H3(23-34)	.4660*	0.015
	5min	0min	-.3188*	0.024		5min	0min	-1.1145*	0
		10min	.8903*	0			10min	0.0459	0.792
		20min	1.4721*	0			20min	0.3499	0.058
		60min	1.9784*	0			60min	-0.1919	0.28
		K27me3+H3(1-21)	3.5134*	0			K27me3+H3(1-21)	-1.9607*	0
		K4me3+H3(23-34)	2.9468*	0			K4me3+H3(23-34)	-0.3406	0.065
		K9me3+H3(23-34)	3.8709*	0			K9me3+H3(23-34)	.8159*	0
	60min	0min	-2.2972*	0		60min	0min	-.9226*	0
		10min	-1.0881*	0			10min	0.2378	0.185
		20min	-.5063*	0.001			20min	.5418*	0.006
		5min	-1.9784*	0			5min	0.1919	0.28
		K27me3+H3(1-21)	1.5349*	0			K27me3+H3(1-21)	-1.7688*	0
		K4me3+H3(23-34)	.9684*	0			K4me3+H3(23-34)	-0.1487	0.399
		K9me3+H3(23-34)	1.8925*	0			K9me3+H3(23-34)	1.0078*	0
	K27me3+H3(1-21)	0min	-3.8322*	0		K27me3+H3(1-21)	0min	.8462*	0
		10min	-2.6231*	0			10min	2.0066*	0
		20min	-2.0412*	0			20min	2.3106*	0
		5min	-3.5134*	0			5min	1.9607*	0
		60min	-1.5349*	0			60min	1.7688*	0
		K4me3+H3(23-34)	-.5666*	0			K4me3+H3(23-34)	1.6201*	0
		K9me3+H3(23-34)	.3575*	0.013			K9me3+H3(23-34)	2.7767*	0
	K4me3+H3(23-34)	0min	-3.2656*	0		K4me3+H3(23-34)	0min	-.7739*	0
		10min	-2.0565*	0			10min	.3865*	0.039
		20min	-1.4746*	0			20min	.6905*	0.001
		5min	-2.9468*	0			5min	0.3406	0.065
		60min	-.9684*	0			60min	0.1487	0.399
		K27me3+H3(1-21)	.5666*	0			K27me3+H3(1-21)	-1.6201*	0
		K9me3+H3(23-34)	.9241*	0			K9me3+H3(23-34)	1.1565*	0
	K9me3+H3(23-34)	0min	-4.1897*	0		K9me3+H3(23-34)	0min	-1.9304*	0
		10min	-2.9806*	0			10min	-.7700*	0
		20min	-2.3988*	0			20min	-.4660*	0.015
		5min	-3.8709*	0			5min	-.8159*	0
		60min	-1.8925*	0			60min	-1.0078*	0
		K27me3+H3(1-21)	-.3575*	0.013			K27me3+H3(1-21)	-2.7767*	0
		K4me3+H3(23-34)	-.9241*	0			K4me3+H3(23-34)	-1.1565*	0

Chapter 6 Selective Heavy Element Sensing with a Simple Host:Guest Fluorescent Array

Introduction

Heavy metals such as chromium, lead, and mercury pose a persistent risk to ecosystems, [1] and are also a threat to human health, causing severe issues such as memory loss, learning deficits, blindness and deafness, kidney damage and cancers.[2,3] In addition, employment of rare earth (RE) metals including lanthanides and actinides in industry has been increasing. These elements can cause mutations and cancers, and radioactivity imposes acute danger to human beings and ecosystems. Therefore, it is of paramount importance to sensitively and selectively monitor toxic heavy and RE metal contents in the environment.[4,5] The challenge in monitoring heavy metal pollutants lies in the complexity of environmental samples, and calls for simple survey techniques that can detect multiple metals selectively and sensitively, in a fast and high-throughput manner. [6,7] The most selective probes for metal ions are DNA-based, and can be employed in fluorescence-based assays for sensitive metal detection.[8-17] However, few are found for RE metals[8,9,15,16] and they are rarely applied to monitor complex metal mixtures, due to their synthetic complexity and cost. Electrochemical sensors have been developed for heavy or RE metals, but display relatively poor sensitivity and selectivity.[18,19] Small molecule metal sensors are attractive due to their simplicity and scalability,[20,21] but can be limited in their selectivity. Selective discrimination between ions that have extremely similar charges, electron configurations and coordination geometries is challenging. Whereas transition metals

display varying coordination geometries and numbers, the coordination chemistry of the RE metals is quite consistent across the series, with the largest differences being in effective ionic radius (EIR) and charge:size ratio. Those differences are small: La^{3+} and Yb^{3+} are only separated by 0.2 Å in size, and adjacent rare earths are exceptionally similar in EIR.[22,23] As a result, the RE metals are challenging targets for selective optical sensing by small molecule systems, especially at low concentrations. For example, while the concentration of uranyl ion in seawater is only 3 ppb,[24] contaminated waste streams in rivers can contain as high as 11.5 ppm,[25] and sensors that can function in that range are highly applicable for environmental remediation.[26]

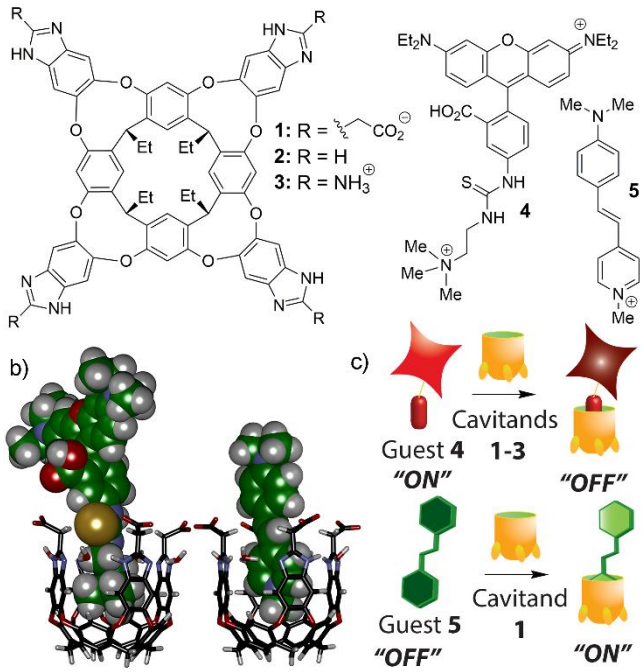

Figure 6.1 a) Structure of hosts 1-3, guests 4 and 5; b) minimized models of the 1•4 and 1•5 host:guest complexes (SPARTAN); c) Illustration of the turn-on and turn-off fluorescence detection processes.

One method to increase the sensitivity of optical sensors is to combine multiple detectors into a sensor array.[27-33] Each array element can respond to several metals and a number of such elements are combined to yield a signal pattern from all the metals in the sample. The patterns from all array elements can be treated by discriminant analysis[34,35] to extract the quantitative information about the analytes and selectively recognize the presence of multiple metals in the mixture. While some arrayed optical sensors for heavy metals are known,[30] selective discrimination of highly similar metals is challenging, and analysis of RE metals via these techniques is limited. Even with arrayed sensors, the strategy of combining a metal coordinator and a covalently appended fluorophore for "turn-off" sensing is limited by the selectivity of metal ion coordination.

Here we offer an alternative strategy: instead of applying optical sensors that only use "single-mode" detection, i.e. coordination of the metal to a specific ligand, and monitoring the change in emission of an appended fluorophore, one can exploit a series of host:fluorophore complexes that are affected by the presence of small amounts of metal ions in aqueous solution in different ways. The sensing candidates are shown in Figure 6.1: the hosts are water-soluble deep cavitands, molecules that display a defined cavity capable of binding suitably sized and charged species in aqueous solution.[36-41] By varying the charge and H-bonding abilities at the upper rim while maintaining the internal cavity, selective host:guest interactions can be enhanced, and pH-responsive recognition is possible.[42,43] The molecular recognition properties of cavitands **1-3** are affected by numerous factors, including salt concentration and type, pH, and the presence of surfactants. These subtle changes in environment can alter the binding affinity of fluorescent guests in the hosts, giving a simple optical readout of affinity changes. By combining variably functionalized hosts with different fluorescent guests at varying pH in an arrayed format, a "chemical nose" sensor[44-49] can be created that is capable of highly selective discrimination of similar ionic species at micromolar concentration in buffered water.

The sensing applications performed to date have involved detecting species that bind inside the host cavity and displace the target fluorophore, such as post-translationally modified peptides.[42] The sensitivity of the system to environmental variations suggested that other interactions could be exploited for detection. The multiple carboxylate groups in **1** are in close proximity to each other, and are easily capable of free rotation to chelate a

metal ion, allowing effective binding, even in aqueous solution. Here we show that a simple array of host:fluorophore complexes is capable of selective sensing and discrimination of highly similar heavy metal ions, including lanthanide and actinide salts in aqueous solution, via multiple fluorescence enhancement and quenching mechanisms.

Results and Discussion

We investigated two reporter molecules: RhB guest **4**, which contains a trimethylammonium (R-Me_3^+) group for binding in hosts **1**-**3**, and dimethylaminostyrylmethylpyridinium iodide (DSMI) **5**. Guest **4** displays the fluorescent Rhodamine B group above the cavity of the hosts, and strong intermolecular fluorescence quenching is observed via photoinduced electron transfer.[43] The affinity of **4** for cavitands **1**-**3** varies from 2.8 μM (**2**, pH 3.3) to 190 nM (**3**, pH 9.0), and >98% quenching of the fluorescence of **4** is observed upon binding. DSMI **5** has a size, shape and charge profile that suggest it would be an excellent guest for **1-3** in water, and it is well-known to display enhanced fluorescence upon binding in hydrophobic environments, such as the cavity of host molecules hexasulfonatocalix[6]arene[53,54] or cucurbit[7]uril.[55] Interestingly, DSMI **5** behaves quite differently to RhB guest **4**: upon its binding to anionic cavitand **1**, a strong *enhancement* in fluorescence of **5** is observed. The maximal fluorescence increase is over 30-fold at pH 3.3, which is far larger than the observed increase seen when bound in CX6[53] or CB7 (Figure S6.1, Supporting Information).[55] The enhancement is pH dependent: the maximum increase was close to 20-fold at pH 5.0 and 7.4, while at pH 9.0 less than 5-fold increase was observed (72.6 μM **1**, 1.5 μM **5**, 100 mM phosphate or carbonate buffer adjusted to the corresponding pH, see Figure S6.2). The excitation and emission occurred

at λ = 485 nm and 605 nm, respectively, and the combination of 1.5 µM DSMI **5** with 20 µM of cavitand **1** were chosen as the optimal sensing conditions (Figures S6.3 & S6.4). The dissociation constant K_d (**5•1**) was found to be 23.1 µM through non-linear regression analysis of the fluorescence enhancement curve at pH 7.4 (Figure S6.5), an order of magnitude lower than that of **4•1**. The lower affinity of **5** necessitated the use of an excess of **1** to reach saturation in fluorescence change for sensing purposes (Figure S6.4). The **5•1** complex was quite stable and the fluorescence was not affected by the presence of liposomes (see Figure S6.6). Interestingly, the fluorescence of DSMI **5** was not enhanced by cavitands **2** or **3** in aqueous solution, suggesting that both shape and charge-based complementary interactions are required for strong binding between DSMI **5** and cavitand **1**.

The individual host:guest combinations were exposed to micromolar concentrations of a series of heavy metal salts in buffered aqueous solution. Tris and Bis-Tris buffers (20 mM) were used to minimize the presence of competitive ions in the system, and focus solely on the metal-host interaction. The metal screen consisted of five general groups, as shown in Figure 6.2: alkaline earths ($Ca^{2+,}$ Mg^{2+}), early transition metals (Mn^{2+} - Cu^{2+}), group IIB/IVA transition metals (Zn^{2+}, Cd^{2+}, Hg^{2+}, Pb^{2+}), rare earths (La^{3+}, Ce^{3+}, Er^{3+}) and actinides (Th^{4+}, UO_2^{2+}). Our preliminary test included 7 sensor elements: cavitands **1-3** [3 µM] with guest **4** [4 µM] at pH 5.0 and 7.4, and **5•1** at pH 7.4 ([**1**] = 20 µM, [**5**] = 1.5 µM). The relevant metal chloride salt at 50 µM (except for Th^{4+} and UO_2^{2+}, where the acetate was used) was added to each element, followed by monitoring the fluorescence changes. It was observed that three host:fluorophore combinations, **4•1** at both pH 5.5 and 7.4, and **5•1**

at pH 7.4 gave the greatest signal changes. Fluorescence displacement/enhancement effects were observed with the cavitand **2**/**3**•guest **4** pairing, but the effects were more subtle (see Figure S6.7 for the full screening data). As a result, we simplified the array design, employing only tetracarboxylate cavitand **1**. The results are shown in Figure 6.2, with the metals arranged from left to right in the order of increasing atomic number in each plot.

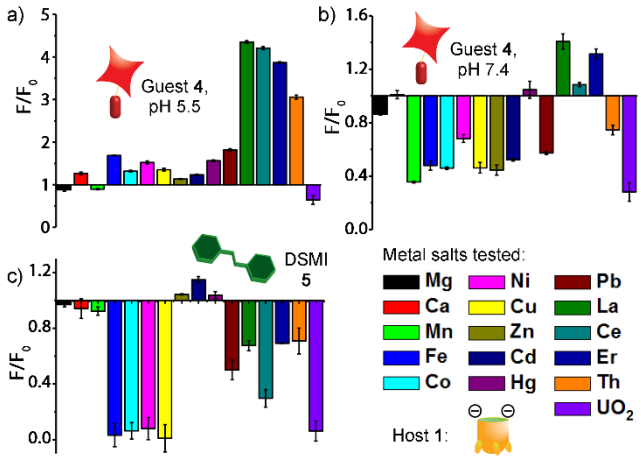

Figure 6.2 Fluorescence response change on metal addition to host:fluorophore complexes. [metal] = 50 μM; sensor 4•1: [1] = 4 μM, [4] = 3 μM, in 20 mM Tris (pH 7.4) or Bis-Tris (pH 5.5) titrated to the corresponding pH with nitric acid; sensor 5•1: [1] = 20 μM, [5] = 1.5 μM, in 20 mM Tris (pH 7.4).

The largest fluorescence recovery (≥ 4-fold) was seen with guest **4** at pH 5.5 (Figure 6.2a) when the sensor was mixed with the lanthanides and actinides, La^{3+}, Ce^{3+}, Er^{3+}, and Th^{4+}. However, this sensor did not respond to the transition and main group metals, exhibiting little change in fluorescence. The same quenching effect by UO_2^{2+} was also observed at pH 7.4. Interestingly, the same sensor (3 μM **1**, 4 μM **4**, 20 mM Tris, Figure 6.2b) at the more basic pH of 7.4 displayed a very different response profile with greater variation in signal, with ~60% loss of fluorescence for early TMs, Cd^{2+}, Pb^{2+} and actinides, but minimal change for alkaline earths and Hg^{2+}, plus fluorescence *recovery* for the lanthanides. UO_2^{2+} was the only species that reduced the sensor fluorescence by 40~50% at both pH 5.5 and pH 7.4. The emission intensity of the DSMI: host complex **5•1** (20 μM **1**, 1.5 μM **5**, pH 7.4, 20 mM Tris) was decreased by the addition of metals (Figure 6.2c). Strong (almost 100%) loss of DSMI fluorescence enhancement was observed with Fe^{2+},

Co^{2+}, Ni^{2+}, Cu^{2+}, as well as UO_2^{2+}, while the lanthanides and actinides induced loss in fluorescence varying from 30% (La^{3+}, Er^{3+}, Th^{4+}) to 70% (Ce^{3+}). Minimal change occurred to the sensor's fluorescence for alkaline earths, Mn^{2+} and the group IIB transition metals.

The widely varying effects of addition of only micromolar amounts of metal ions on the fluorescence profile of the host:guest complexes are unusual and interesting. Importantly, the variation in sensor fluorescence is a *host*-mediated process: the fluorescence of guests **4** and **5** was not changed significantly upon addition of 50 μM metal in the absence of cavitand **1** (see Figure S6.8). This makes sense: both guests **4** and **5** are cationic, and will have minimal contact with metal ions in aqueous solution at the low concentrations used. There was one exception, however: UO_2^{2+} showed strong native quenching of both **4** and **5** at pH 5.0 and 7.4, with ~ 20% and ~50% loss of fluorescence respectively.

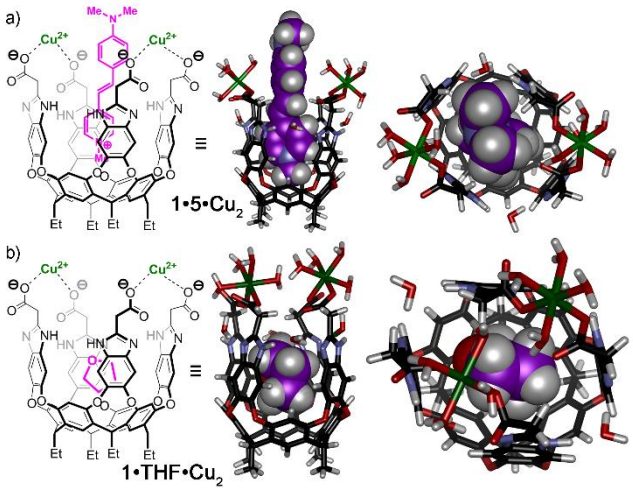

Figure 6.3 Minimized structures of a) 1•5•Cu2 and b) 1•THF•Cu2, indicating the effect on metal orientation in the presence of large and small guests (SPARTAN, AM1 forcefield).

The large signal change to the cavitand-guest system induced by the metals was unexpected, especially at micromolar concentrations in buffered water: host **1** only contains weakly coordinating carboxylate groups at the upper rim for metal complexation. Upon closer inspection of the structure (Figure 6.3), it becomes obvious that the carboxylate groups are in suitable proximity to each other to allow chelating interactions with large metal ions, increasing the target affinity.[56] Figure 6.3 shows minimized structures of complexes between host **1** and Cu^{2+} in the presence and absence of guests **4** and **5** (see Figure S6.18 for the **1•4•Cu2** model). The freely rotating carboxylates allow bidentate metal binding in multiple orientations. In the presence of guest, the metals can be positioned away from the cavity. However, in the absence of the large fluorophore (Figure 6.3b), the metals reside above the cavity: metal complexation is possible in the presence of fluorophore, but lowers the fluorophore affinity due to steric interactions

between the metal and the protruding guest. While these models are certainly not the only coordination modes possible (such as a 1:1 metal•cavitand complex, for example), they illustrate that metal coordination is tolerated by the **1•4** and **1•5** complexes and that the fluorophore affinity for **1** will be altered by metal binding.

This modeling allows some conclusions to be drawn that explain the variable changes in response upon metal binding. The changes are subtle in some cases, and exact mechanistic analysis of each interaction is impractical, but some possibilities are illustrated in Figure 6.4. The analysis can be split into three separate cases - **1•4** at either pH 5.5 or pH 7.4, and **5•1**. The sensing of the metal in each case is mediated by the interaction of the newly added metal with the upper rim of the cavitand, and this effect is greatest for anionic **1** at pH 7.4. Guest **4** is strongly quenched by **1**, and its affinity is strongly pH-dependent.[43] Two competing factors are at play in the **4•1** system, which give competing responses (Figure 6.4a). The interaction of the added metal salt with the cavitand can bring this metal species into close proximity with bound **4**, causing additional quenching (and *lowered* fluorescence) via the heavy atom effect.[57] Alternatively, the metal interaction with **1** can interfere with the host:guest event, lessening the affinity of **4** for host **1**, releasing the guest into free solution and causing an *increase* in fluorescence. These two effects are both participating at pH 5.5 and 7.4, but the proportion of each effect varies. The fluorescence changes with the DSMI **5•1** sensor are different: in the majority of cases, a strong loss of fluorescence is observed upon addition of metal. The interactions of metal ions with host **1** are similar to those described as above, and the two competing mechanisms are still occurring. However, as DSMI shows enhanced fluorescence upon binding in **1**, both heavy

metal-based quenching of the **5•1** complex and expulsion of **5** from the cavitand upon host:metal interaction cause a loss of fluorescence enhancement in **5** (Figure 6.4b).

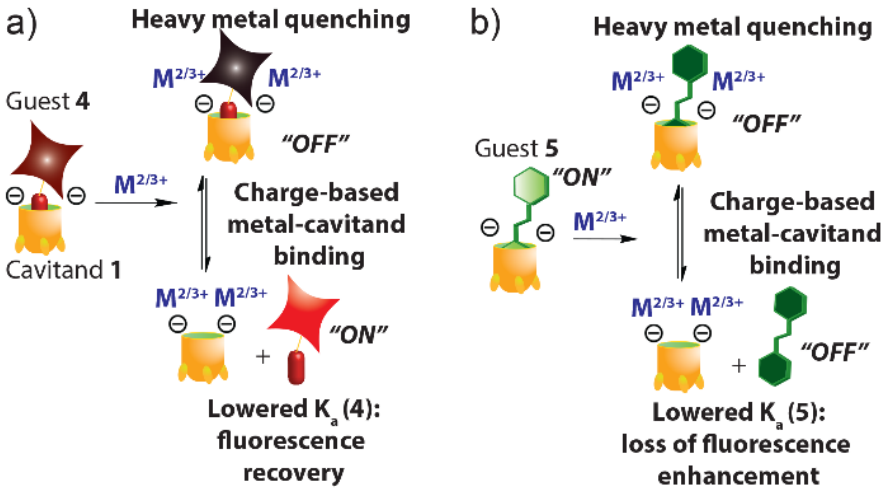

Figure 6.4 Illustration of the various sensing mechanisms involved in the recognition processes with the 1•4 and 1•5 complexes.

To corroborate these theories, calibration curves of fluorescence response vs. metal concentration were constructed for the metals that caused the most significant response ($F/F_{max} \geq 2$ or ≤ 0.5) in the three sensors: **1•4** at pH 5.5 or 7.4, and **1•5** at pH 7.4 (Figure S6.9). Based on the potential interaction models proposed in Figure 6.4, we attempted to fit the curves with two simple binding models (see Experimental Section). The first model is the metal-cavitand-guest complex formation model, in which the titration curves of these metals were fitted with the Hill equation[52] by viewing the **1•4** complex as a single "macromolecule". The resultant macroscopic dissociation constant, labeled as "K_d^{MC}", serves as an index to compare the relative binding affinity of the metals to the **1•4** complex, as has been used for analysis of other host:guest indicator displacement systems.[20] The second model is the displacement model used for determination of inhibitor affinity to proteins.[58,59] This assay allows monitoring of ligand displacement from the protein-ligand

complex by small molecule inhibitors, and this fitting gives the dissociation constant of the metal-cavitand complex, marked as K_d^D. These simple models may not reflect the complete binding situation, because the final fluorescence changes depend on multiple binding events, including the strength of the **1**•M^{2-4+} interaction and the efficiency of the guest quenching by the metal. However, the responses for certain metals are dominated by a single interaction type, and are amenable to fitting by one of the simple models.

At pH 7.4, the early transition metals (Mn^{2+} - Zn^{2+}), the heavy metals (Pb^{2+} and Cd^{2+}), as well as UO_2^{2+}, reduced the **1•4** sensor fluorescence by more than 50%, indicating that formation of the stable **M^{2+}•1•4** complex could be the dominant effect. Indeed, fitting the binding curves to the Hill equation was successful with R^2 = 0.99 (Table 6.1a,c; Figure S6.10), while the no fit was seen with the displacement model. The tested metals all showed a positive cooperativity "n" between 1 and 2, indicating that binding of the first metal cation could facilitate the binding of the subsequent ions. The K_d^{MC} values were relatively consistent, ranging from 0.7±0.1 μM (Cu^{2+}) to 3.8±1.4 μM (Fe^{2+}). The strong affinity of these metals to the **1•4** complex is expected, as host **1** will display (on average) a bis-anionic charge under these conditions, allowing strong charge matching with the metal cations. This strong binding was also persistent and observable in mass spectrometry: both Cu^{2+} and UO_2^{2+} formed stable complexes with cavitand **1**, detectible by surface-enhanced laser desorption/ionization (SELDI) assisted with graphene oxide (see Figure S6.14). The MS data clearly showed that these two cations could coordinate with cavitand **1** at 1:1, 2:1, and 3:1 stoichiometries, when mixing 10 μM of cavitand **1** and 100 μM of the metal cation.

Table 6.1 Metal Affinity Constants for the 4•1 Complex Sensor.

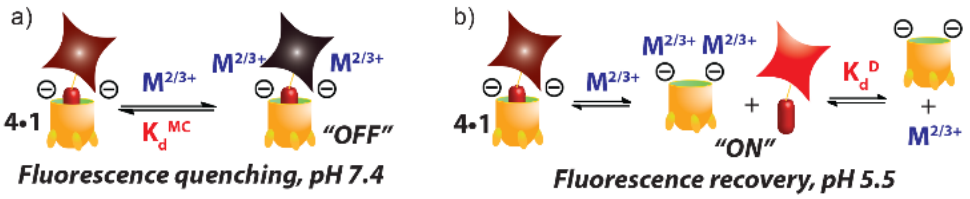

Metal	KdMC, µM	n
Fe2+	3.8±1.4	2.1
Co2+	2.0±0.4	2.7
Zn2+	2.7±0.8	2.0
Cu2+	0.7±0.1	1.4
Cd2+	2.5±0.3	2.3
Pb2+	1.3±0.3	2.0
UO22+	1.4±0.2	1.1

Metal	KdD, µM
La3+	1.0±0.1
Ce3+	1.1±0.1
Er3+	0.9±0.1
Th4+	1.1±0.1

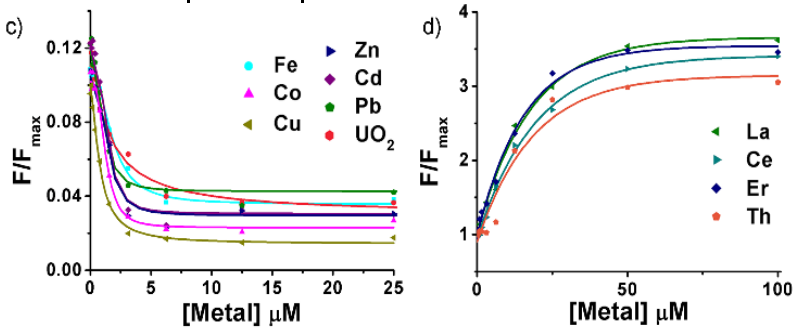

[a] [1] = 3 µM, [4] = 4 µM, pH 7.4, 20 mM Tris. KdMC determined via Hill equation,[52] KdD determined via enzyme inhibitor model.[58] c) calibration curves for Hill analysis; d) calibration curves for inhibitor analysis.

At pH 5.5, only the lanthanides induced sufficiently large fluorescence enhancement of the **1•4** sensor to allow fitting (Table 6.1b,d, Figure S6.11). These binding curves fit well with the displacement model, resulting in K_d^D values around 1 µM, consistent with the theory that fluorescence enhancement occurs via displacement of **4** and concomitant loss

of quenching. The K_d^D values may not represent the true dissociation constant between metal and cavitand, because of the overly simplified assumption of a 1:1 binding stoichiometry, but this analysis corroborates the fluorophore displacement concept. The oxophilic Ln^{3+} ions are the only ions capable of strong affinity for **1** in its partially protonated state.

The analysis of the DSMI **5•1** sensor was more complex. Since we could not determine whether complex formation or displacement were the contributing factors (as both mechanisms cause guest **5** quenching), we fitted the binding curves of the ions that induce > 50% fluorescence reduction (the early transition metals (Fe^{2+}-Cu^{2+}), Pb^{2+}, Ce^{3+}, and UO_2^{2+}) with both models. Interestingly, fitting to the Hill equation was more successful than the displacement model (Table 6.2; Figure S6.12). The K_d^{MC} values ranged from ranging from 8.7±1.7 μM (Cu^{2+}) to 1.9±0.6 mM (Ce^{3+}), indicating much greater variance in binding affinity for the **5•1** sensor than with the **4•1** sensor. Only Pb^{2+} and Ce^{3+} showed good fitting with the displacement model. The large K_d^{MC} values found for these two cations using the complex formation model indicated the relatively low stability of the **M^{2+}•1•5** complex, displacing guest **5** due to the high affinity of the metal for the host.

Table 6.2 Metal Affinity Constants for the **5•1** Complex Sensor.[a]

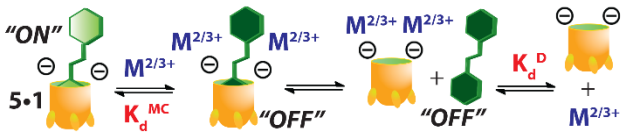

Metal	K_d^{MC}, µM	n	K_d^{D}, µM
Fe^{2+}	58 ± 14	2	N/A
Co^{2+}	200 ± 40	2.7	N/A
Ni^{2+}	73 ± 14	2.5	N/A
Cu^{2+}	8.7 ± 1.7	1.6	N/A
Pb^{2+}	(1.3±0.3) × 10^3	1.5	12.2±1.7
Ce^{3+}	(1.9±0.6) × 10^3	2.3	2.7±0.1
UO_2^{2+}	4.9 ± 0.5	1.1	N/A

[a][1] = 20 µM, [5] = 1.5 µM, pH 7.4, 20 mM Tris. KdMC determined via Hill equation,52 KdD determined via enzyme inhibitor model.58 Red = best fit with the inhibitor model.

The calibration curves typically exhibit linear response ranges between 0-10 or 0-20 µM, before reaching plateau at higher metal concentration. Using the linear regression equation and the 3σ method, the limits of detection (LOD) of each sensor for individual metals were found to be between 1.2-0.07 µM, with a linear range (see Figure S6.13). The lowest LOD of 0.07 µM is observed for Cu^{2+} with the **4•1** sensor at pH 7.4. The LOD of heavy metals ranges from 1.3 (Th^{4+}) to 0.31 µM (Er^{3+}) with the **1•4** sensor at pH 5.5. The limit of quantitation (LOQ, calculated using the 10σ method, see Figure S6.16) for either the cation (Ce^{3+} or Th^{4+}) alone, or the mixture of La^{3+}/Er^{3+}/Ce^{3+}/Th^{4+} at equal molarity were quite similar, around 1-2 µM, even when spiked in the environmental water sample collected from Lake Evans, Riverside, CA.

The multiple different interactions and quenching mechanisms between the various metals and sensor components are ideal for analysis by discriminant methods. Each sensor

responds to multiple metals, which induces subtle fluorescence changes sensitive to the type and concentration of the metals. Linear discriminant analysis (LDA)[10] was chosen as the discriminant technique here, as it can yield dimensional components optimized to maximize the differentiation among sample classes, as opposed to unsupervised pattern recognition tools like principal component analysis (PCA).[10] As a baseline control, the fluorescence profiles obtained by incubating the metal salts on free, uncomplexed guests **4** and **5** were subjected to LDA (Figure 6.5a). As expected, the fluorophores are incapable of effectively discriminating the metal salts in the absence of cavitand. The only outlier is UO_2^{2+}, which can be easily identified in the scores plot, due to its strong native quenching ability. All other metals, including light and heavy metals are unclustered and indistinguishable.

In contrast, when only a 3-component cavitand:fluorophore sensor array was used, excellent discrimination of almost all the metal ions can be achieved. When LDA was applied to the data set from Figure 6.2 (with **4•1** at pH 5.5/7.4, and **5•1**), the scores plot shown in Figure 6.5b is obtained. In each case, three repeats were taken for each sample, and these three repeated measurements of the same metal were included well within the 95% confidence ellipses, showing good reproducibility of our measurement. The not-overlapping ellipses reveal good separation of different metals by our sensor array. Most importantly, the metals with the highest structural similarity, i.e. La^{3+}, Ce^{3+}, Er^{3+}, and Th^{4+}, are extremely well-separated from each other. In addition, the scores plot shows three main clusters of metals. All the lanthanides are located in the left panel on the scores plot (LD1 < 0), away from the other metals which displayed LD1 > 0. The upper right panel (LD2

>0) was occupied by the early transition metals metals $Fe^{2+}/Co^{2+}/Ni^{2+}/Cu^{2+}$ and the outlier UO_2^{2+}, while the lower right panel (LD2 < 0) contained mainly the IIA/ IIB metals ($Mg^{2+}/Ca^{2+}/Zn^{2+}/Cd^{2+}/Hg^{2+}$).

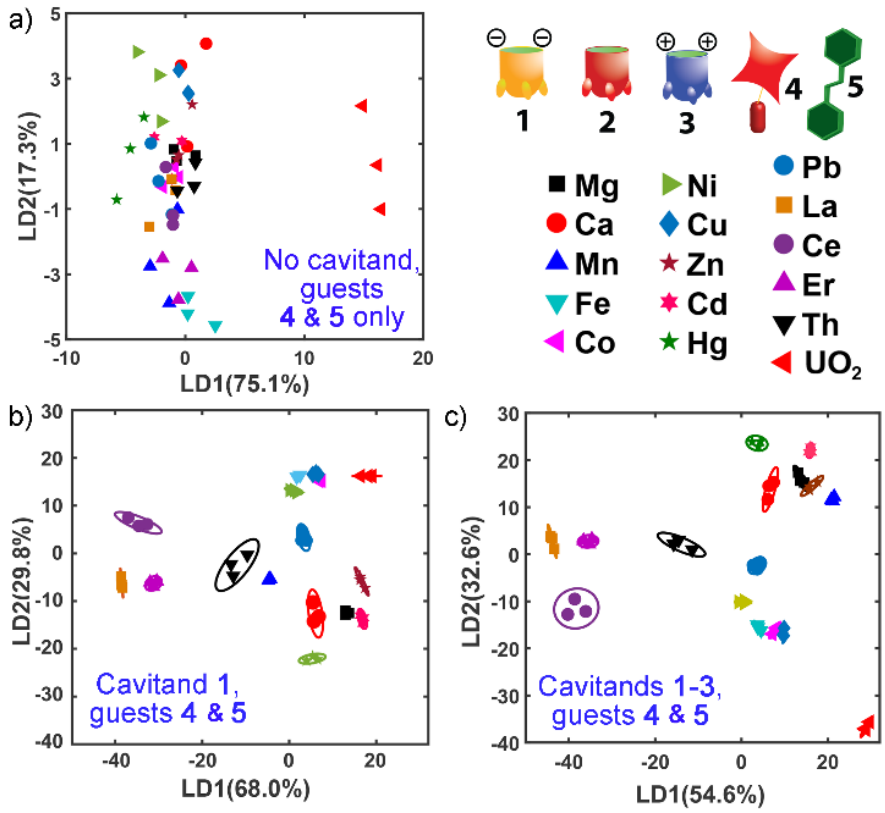

Figure 6.5 Metal salt identification *via* Linear Discriminant Analysis. a) Scores plot of the metal screen with a cavitand-free screen, [**4**] = 3 μM, [**5**] = 1.5 μM; b) Scores plot of the metal screen with the 3 factor sensor array containing **4•1** ([**1**] = 4 μM, [**4**] = 3 μM) in pH 7.4 or pH 5.5 buffer, and sensor **5•1** ([**1**] = 20 μM, [**5**] = 1.5 μM, pH 7.4); c) Scores plot of the metal screen with the 7 factor sensor array containing **4•1/4•2/4•3** ([**1**] = 4 μM, [**2**] = 3 μM, [**3**] = 3 μM, [**4**] = 3 μM) in pH 7.4 or pH 5.5 buffer, and sensor **5•1** ([**1**] = 20 μM, [**5**] = 1.5 μM, pH 7.4). pH 7.4 = 20 mM Tris, pH 5.5 = 20 mM Bis-Tris.

The full 7-factor sensor array was also applied to the metal screen, and the LDA scores plot is shown in Figure 6.5c. This array included four more variables, the sensors formed by the neutral and cationic cavitands **2** and **3** with the rhodamine guest **4** at two pHs. While the individual effects of these hosts were much more subtle, the array with more variables was more tolerant to random signal variation, and thus the 95% ellipses enclosing the three repeats of each metal were much narrower. The extended array still gave out excellent separation among the trivalent inner transition metals, with some improvement in the

discrimination of the VIIIB/IB metals. However, Pb^{2+} and Mn^{2+} were much closer to the IIA/IIB cluster and the separation among the metals within this cluster were poorer.

The metal discrimination was also tested with Hierarchical Cluster Analysis (HCA) on the simple 3-factor sensor. On the resultant dendrogram (see Figure 6.6a), all three repeats for the same metal were clustered well with very small dissimilarity (< 100), and three main clusters with dissimilarity close to 2,000 were found: the VIIIB/IB metals (Fe^{2+}/Ni^{2+}/Co^{2+}/Cu^{2+}), the IIA/IIB groups (Ca^{2+}/Mg^{2+} /Zn^{2+}/Hg^{2+}/Cd^{2+}), and the inner transition metals (La^{3+}/Er^{3+}/Th^{4+}). Pb^{2+} and UO_2^{2+} were clustered with the VIIIB/IB metals, and Mn^{2+} was included in the IIA/IIB group, agreeing with their relative locations on the LDA score plot.

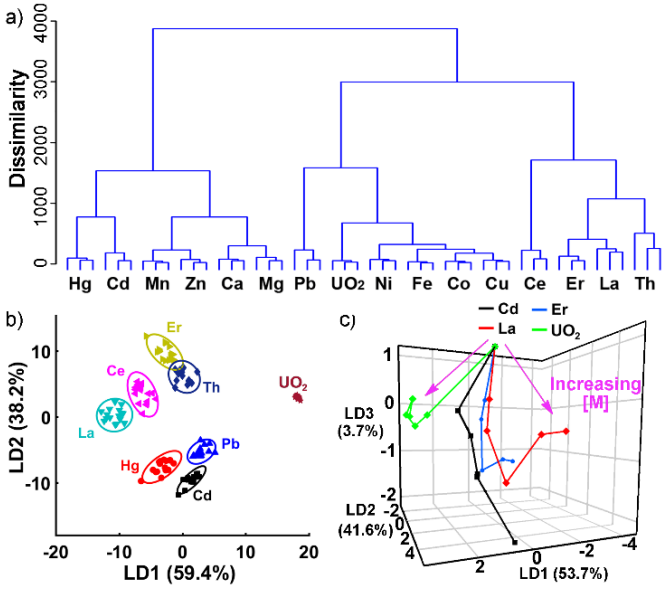

Figure 6.6 a) Hierarchical cluster analysis; b) metal identification and c) quantification by the 3 factor sensor array containing **4•1** ([**1**] = 4 μM, [**4**] = 3 μM) in 20 mM Tris (pH 7.4) or Bis-Tris (pH 5.5) buffer, and sensor **5•1** ([**1**] = 20 μM, [**5**] = 1.5 μM, in 20 mM Tris, pH 7.4). [Metal] in (c) = 0, 0.8, 1.6, 3.1, 6.3, 12.5, 25.0, 50.0, 100.0 μM.

Both the LDA and HCA results support that the observed fluorescence profiles are closely related to metal properties. Even with just three array variables, the simple sensor system can not only discriminate between metals with different coordination behavior, but can also discriminate between highly similar metals while allowing their grouping and analysis. To further evaluate the simple 3-component sensor capabilities for the discrimination of environmentally relevant heavy metals (Hg^{2+}, Cd^{2+}, Pb^{2+}) and the lanthanides/actinides (UO_2^{2+}, La^{3+}, Er^{3+}, Ce^{3+}, Th^{4+}), we performed a more detailed analysis of these species. Figure 6.6b shows the score plot from LDA of these 8 metals, with significantly more repeats (n = 16). Despite the extensive number of repeats used, the 95% ellipses showed either zero or minimal (Er^{3+}/Th^{4+}) overlap on the score plot, meaning that these metals can be differentiated with 95% confidence using our sensor array coupled

with LDA. In addition, Jackknife analysis showed that each metal can be assigned to the correct group with 100% accuracy (see Table S6.1).

Of course, the most important and challenging task is to detect these metals in a complex mixture of ions, as would be observed in an environmental sample. Quantifying one metal ion in the presence of other metal ions is challenging without pre-treatment and sophisticated instruments like ICP-AES or ICP-MS, due to the cross-reactivity between the recognition probes. Metal quantitation using our array was tested by measuring the fluorescence responses with increasing concentrations of each metal when mixed with the sensors. Indeed, when the metal concentration increased from 0 to 100 μM in tap water, the position of the sample on the 3D-score plot resulted from LDA of the fluorescence profiles would move towards different directions depending on the identity of the metal (Figure 6.6c). Increasing metal concentrations moved all samples downward in the LD3 direction, but different metals projected toward different direction on the LD1-LD2 plane. For instance, increasing [Cd^{2+}] moved the location of the metal sample to a more positive LD2 location with little change in LD1, while higher [UO_2^{2+}] moved it towards more positive LD1 and more negative LD2 with small change in LD3 direction. No overlap was observed between the trajectories of individual metals, indicating good capability of sensor in recognizing the elevated concentration of one metal in tap water. This confirms that the array is capable of quantitating the heavy and inner transition metals in aqueous solutions.

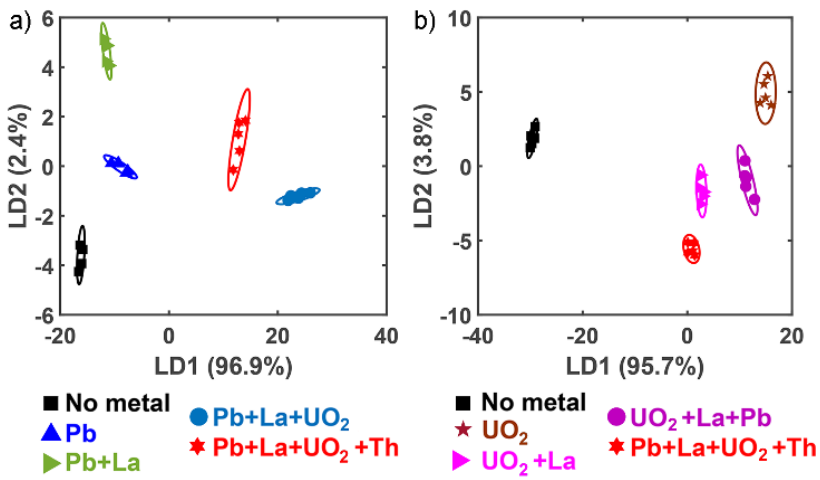

Figure 6.7 Metal salt identification in Mixtures. LDA Scores plots identifying a) Pb^{2+}; b) UO_2^{2+} in the presence of other salts in commercial tap water with the three factor sensor array containing **4•1** ([**1**] = 4 μM, [**4**] = 3 μM) in pH 7.4 or pH 5.5 buffer, and sensor **5•1** ([**1**] = 20 μM, [**5**] = 1.5 μM, pH 7.4). [Metal] = 20 μM, pH 7.4 = 20 mM Tris, pH 5.5 = 20 mM Bis-Tris.

To illustrate the efficacy of the sensor towards environmentally relevant mixtures, we prepared a series of samples with increasing complexity. The first set of samples was created by spiking several metals, each with a final concentration of 2 μM, to unpurified tap water and testing the samples with our 3-factor sensor array, with a focus on detecting the environmentally important ions Pb^{2+} and UO_2^{2+} in mixtures containing the similarly sized metals at comparable molarity. The fluorescence patterns were subject to LDA and the resultant score plots were shown in Figure 6.7 (the score plot with 11 mixtures displayed in Figure S6.15; raw fluorescence data in Figure S6.17). We can see from Figure 6.7a that the co-presence of the inner transition metals like La^{3+}, Th^{4+}, and UO_2^{2+}, with Pb^{2+} were well differentiated from each other. Similarly, if the tap water contained higher contents of inner transition metals, the simple array can recognize the different combinations of La^{3+}, Th^{4+}, and UO_2^{2+} in the water samples. Jackknife analysis also

showed that various metal mixtures can be assigned to the correct group with 100% accuracy (see Table S6.2).

The second set of samples was created by spiking La^{3+} and Th^{4+} at various molar ratios (La^{3+}:Th^{4+} = 0:21, 3:18, 6:15, 9:12, 12:9, 15:6, 18:3, 21:0, all in µM), to lake water obtained from Lake Evans, Riverside, CA. Three analytic samples were prepared for comparison: **A** – (16.5 µM La^{3+} + 4.5 µM Th^{4+}); **B** (10.8 µM La^{3+} + 10.2 µM Th^{4+}) and **C** (4.7 µM La^{3+} + 16.3 µM Th^{4+}). LDA was applied to the data collected from the test samples and the standard mixtures. We can see on the resultant scores plot that the test samples locate in the correct location, corresponding to their metal ratios. For example, sample A located in between the two standards with La^{3+}:Th^{4+} molar ratios at 15:6 and 18:3 respectively. This location indicates that it contains 15-18 µM La^{3+} and 3-6 µM Th^{3+}. This range agrees with what was detected by ICP-AES. Table 6.3 shows the full detection data, and illustrates the ability of the array to semi-quantitatively detect the presence of heavy metals in complex environmental samples. The simple optical array is an effective, quick survey method comparable to ICP-AES analysis without the expense.

Table 6.3 Metal Mixture Analysis in Environmental Sample[a]

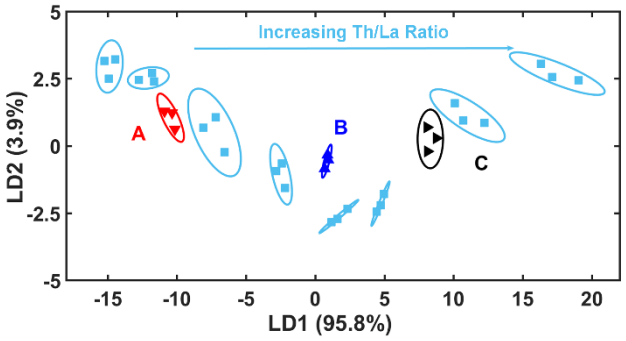

Entry	$[Th^{4+}]$, μM			$[La^{3+}]$, μM		
	Actual	ICP-AES	Array	Actual	ICP-AES	Array
A	4.5	4.3	3-6	16.5	16.6	15-18
B	10.2	10.3	9-12	10.8	11.1	9-12
C	16.3	16.3	15-18	4.7	4.7	3-6

[a] Quantifying the binary mixture of La^{3+}/Th^{4+} with the ratio of these two ions changing from 0:21 to 21:0 in 3 μM increments, with the three factor sensor array in natural lake water, containing **4•1** ([**1**] = 4 μM, [**4**] = 3 μM) in pH 7.4 or pH 5.5 buffer, and sensor **5•1** ([**1**] = 20 μM, [**5**] = 1.5 μM, pH 7.4). pH 7.4 = 20 mM Tris, pH 5.5 = 20 mM Bis-Tris. A, B, and C are the test samples. Performance of quantification compared with ICP-AES.

Conclusion

Here, we have shown that a simple three component host:fluorophore sensor array is capable of sensing and discriminating aqueous solutions of metal salts. Excellent sensitivity is possible, and highly similar metals such as lanthanides and actinides can be easily distinguished at low micromolar concentrations in complex salt mixtures. Multiple coordination and fluorescence quenching/enhancement mechanisms occur in the system, which contributes to the sensitivity of the discrimination. This flexible, yet simple sensor array represents a powerful tool for monitoring heavy or RE metal pollution in the

environment in a quick, low-cost, and high-throughput manner, which is essential for prompt pollution control and treatment implementation.

Experimental Section

General. Cavitands **1**,[36] **2**,[50] **3**[51] and guest **4**[43] were synthesized according to literature procedures. DSMI **5** (trans-4-[4-(Dimethylamino)styryl]-1-methylpyridinium iodide) was purchased from Sigma-Aldrich (St. Louis, MO) and used without further purification.All the metal salts were purchased from Sigma-Aldrich (St. Louis, MO) and Alfa Aesar (Tewksbury, MA), and they were directly used without further purification. The heavy metal ions were produced from their respective chloride salts as following with several exceptions: $MgCl_2$, $CaCl_2$, $MnCl_2$, $FeCl_2$, $CoCl_2$, $NiCl_2$, $CuCl_2$, $ZnCl_2$, $CdCl_2$, $Hg(OAc)_2$, $Pb(NO_3)_2$, $LaCl_3$, $CeCl_3$, $ErCl_3$, $ThCl_4$ and $UO_2(OAc)_2$. Molecular modeling (semi-empirical calculations) was performed using the AM1 force field using SPARTAN.

Experimental Procedures

Fluorescence sensor array with metals. In general, the fluorescence assay was carried out by mixing 10 μL of guest **4** (30 μM) or guest **5** (15 μM), 10 μL of the cavitand (40 μM for **1•4** or 200 μM for **1•5**, 50 μM for **2•4** or **3•4**), 70 μL of the incubation buffer (Tris pH 7.4 or Bis-Tris pH 5.5) in a 96-well plate, adding 10 μL of different metal salt solution to bring the total volume up to 100 μL, and incubating with mild shaking for 15 mins at room temperature. The fluorescence signal (F) was recorded in a Perkin Elmer Wallac 1420 Victor 2 Microplate Reader (PerkinElmer) with the Ex/Em wavelengths at 530/605 nm for guest **4** or 485/605 for guest **5**.

SELDI TOF-MS. Graphene oxide stock solution in water was first diluted to 1 mg/mL in either Tris buffer (pH 7.4, 20 mM) or Bis-Tris buffer (pH 5.5, 20 mM). Metal (100 μM) and cavitand **1** (10 μM) were mixed and incubated for 15 minutes in the same buffer condition. After incubation, 1 μL of above metal and cavitand mixture was mixed with graphene oxide and spotted on a stainless steel Opti-TOF™ 96 targets plate, and allowed to dry completely before introducing into the mass spectrometer. Analysis was carried out on an AB Sciex 5800 TOF/TOF proteomics analyzer with a laser irradiation at a repetition frequency of 1,000 Hz. A laser intensity index of 2900 was used for sample ionization and the MS spectra were acquired in the negative reflector mode within the mass range from 100 to 2,000 Da. The SELDI analysis of cavitand **1**, fluorescent guest (either **4** or **5**) and metal was also performed via this method. The final concentration of cavitand **1**, guest and metal was 10 μM, 7.5 μM and 100 μM respectively.

K_d calculations. The calibration curves of fluorescence response vs. metal concentration were obtained by adding 0 – 100 μM of metal into the sensor solution that contained either **4•1** ([**1**] = 4 μM, [**4**] = 3 μM) in pH 7.4 or pH 5.5 buffer, and **5•1** ([**1**] = 20 μM, [**5**] = 1.5 μM, pH 7.4). The fluorescence was recorded after 15 mins of mixing in the plate reader as described above.

In the metal-cavitand-guest complex formation model,[52] the curves were fitted with the Hill equation using Origin Pro 8.0 shown below:

$$\frac{F}{F_{max}} = \frac{F_{start}}{F_{max}} + \left(\frac{F_{end}}{F_{max}} - \frac{F_{start}}{F_{max}}\right)\frac{[metal]^n}{k^n + [metal]^n}$$

$$K_d^{MC} = k^n$$

where F is the fluorescence reading, F_{start} is starting fluorescence, F_{end} is the ending plateau fluorescence, $[metal]$ is the metal concentration, k is the microscopic dissociation constant, and n is the binding cooperativity. K_d^{MC} is the apparent dissociation constant, representing the stability of metal binding to the cavitand-guest sensor complex.

In the displacement model, K_d^D, the dissociation constant for the metal-cavitand complex were calculated following the typical approach for determination of inhibitor binding constant in protein-ligand-inhibitor binding assays.[20] The titration curves were fitted to the exponential decay equation and obtain the constant t1:

$$F/F_{max} = A\, e^{-[metal]/t_1}$$

Then IC50 was calculated from t_1 using the equation of $IC_{50} = \ln(1/2)\, t_1$. Followed, K_d^D was obtained by the following equation:

$$K_d^D = IC_{50}/(\frac{[L]_{50}}{K_d} + \frac{[cavitand]_0}{K_d} + 1)$$

where $[L]_{50}$ is the concentration of the free metal ions at 50% inhibition (approximated to be the starting small molecule concentration), $[cavitand]_0$ is the cavitand concentration at 0% inhibition, and K_d is the dissociation constant for the cavitand **1•4** or **1•5** complex.[43]

Data analysis. Linear Discriminant Analysis (LDA), Jackknife validation and Hierarchical clustering analysis (HCA) were completed with RStudio (Version 1.0.136), an integrated development environment (IDE) for R (version 3.3.2). Fluorescence data was first stored as an excel file, and then read into a matrix in RStudio. The internal function "princomp()" was used to perform PCA; the 'lda()' function was called for Jackknife Validation with the "CV" set as "true". One replicate was left out of the training set, and

the LDA classifier was fitted on the input data. The output was recorded in a two-dimensional table. HCA was performed with two steps: the Euclidean distance between any two objects within the dataset was first calculated and recorded into a two-dimensional matrix; then the matrix was used as the input for the built-in HCA function “hclust()”, and the result was drawn with the “plot()” function.

Confidence ellipses were drawn with the data obtained from PCA using Matlab (version R2016b) and a self-developed script. The full Matlab script is available upon request. The 3D scatter plot was performed with Plotly’s R package version 4.

Reference

(1) Weiss, D. J.; Rehkaemper, M.; Schoenberg, R.; McLaughlin, M.; Kirby, J.; Campbell, P. G. C.; Arnold, T.; Chapman, J.; Peel, K.; Gioia, S. *Environ. Sci. Technol.* **2008**, *42*, 655-663.

(2) Traudt, E. M.; Ranville, J. F.; Meyer, J. S., *Environ. Sci. Technol.* **2017**, *51*, 4471-4481.

(3) Nys, C.; Versieren, L.; Cordery, K. I.; Blust, R.; Smolders, E.; De Schamphelaere, K. A. C. *Environ. Sci. Technol.* **2017**, *51*, 4615-4623.

(4) Donohue, D. L. *Anal. Chem.* **2002**, *74*, 28A-35A.

(5) Steinhauser, G. *Environ. Sci. Technol.* **2014**, *48*, 4649-4663.

(6) Shen, Y.; Fang, Q.; Chen, B. *Environ. Sci. Technol.* **2015**, *49*, 67-84.

(7) Zhang, P.; Chen, Y.-P.; Wang, W.; Shen, Y.; Guo, J.-S. *Trends Anal. Chem.; TrAC* **2016**, *85*, 153-165.

(8) Zhou, W.; Saran, R.; Liu, J. *Chem. Rev.* **2017,** *117* , 8272-8325.

(9) Yuen, L. H.; Franzini, R. M.; Tan, S. S.; Kool, E. T. *J. Am. Chem. Soc.* **2014,** *136*, 14576-14582.

(10) Tan, S. S.; Kim, S. J.; Kool, E. T. *J. Am. Chem. Soc.* **2011,** *133*, 2664-2671.

(11) Yuen, L. H.; Franzini, R. M.; Wang, S.; Crisalli, P.; Singh, V.; Jiang, W.; Kool, E. T., *Angew. Chem. Int. Ed.* **2014,** *53*, 5361-5365.

(12) Huang, P.-J. J.; Vazin, M.; Lin, J. J.; Pautler, R.; Liu, J. *ACS Sensors* **2016,** *1*, 732-738.

(13) Gao, L.; Li, L.-L.; Wang, X.; Wu, P.; Cao, Y.; Liang, B.; Li, X.; Lin, Y.; Lu, Y.; Guo, X., *Chem. Sci.* **2015**, *6*, 2469-2473.

(14) Zhan, S.; Wu, Y.; Wang, L.; Zhan, X.; Zhou, P., *Biosens. Bioelectron.* **2016**, *86*, 353-368.

(15) Huang, P.-J. J.; Lin, J.; Cao, J.; Vazin, M.; Liu, J. *Anal. Chem.* **2014**, *86*, 1816-1821.

(16) Huang, P.-J. J.; Vazin, M.; Liu, J. *Anal. Chem.* **2014**, *86*, 9993−9999.

(17) Wu, C.-S.; Oo, M. K. K.; Fan, X. *ACS Nano* **2010**, *4*, 5897-5904.

(18) Cui, L.; Wu, J.; Ju, H., *Biosens. Bioelectron.* **2015**, *63*, 276-286.

(19) Saidur, M. R.; Aziz, A. R. A.; Basirun, W. J., *Biosens. Bioelectron.* **2017**, *90*, 125-139.

(20) Bakirci, H.; Koner, A. L.; Nau, W. M. *Chem. Commun.* **2005,** 43, 5411-5413.

(21) Aoki, S.; Kagata, D.; Shiro, M.; Takeda, K.; Kimura, E. *J. Am. Chem. Soc.* **2004,** *126*, 13377-13390.

(22) Gorden, A. E. V.; DeVore, II, M. A.; Maynard, B. A. *Inorg. Chem.* **2013**, *52*, 3445-3458.

(23) Panak, P. J.; Geist, A. *Chem. Rev.* **2013**, *113*, 1199-1236.

(24) Schwochau, K. *Top. Curr. Chem.* **1984**, *124*, 91-133.

(25) Balonov, M.; et al. *Radiological Conditions in the Dnieper River Basin*; Radiological Assessment Reports Series; International Atomic Energy Agency: Vienna, 2006.

(26) Sather, A.C.; Berryman, O. B.; Rebek, J., Jr. *J. Am. Chem. Soc.* **2010**, *132*, 13572–13574.

(27) Palacios, M. A.; Wang, Z.; Montes, V. A.; Zyryanov, G. V.; Anzenbacher, P. *J. Am. Chem. Soc.* **2008,** *130* , 10307-10314.

(28) Hewage, H. S.; Anslyn, E. V. *J. Am. Chem. Soc.* **2009,** *131*, 13099-13106.

(29) Kitamura, M.; Shabbir, S. H.; Anslyn, E. V. *J. Org. Chem.* **2009,** *74*, 4479-4489.

(30) Lee, J. W.; Lee, J.-S.; Kang, M.; Su, A. I.; Chang, Y.-T., *Chem. Eur. J.* **2006,** *12*, 5691-5696.

(31) Xu, W.; Ren, C.; Teoh, C. L.; Peng, J.; Gadre, S. H.; Rhee, H.-W.; Lee, C.-L. K.; Chang, Y.-T. *Anal. Chem.* **2014,** *86*, 8763-8769.

(32) Wang, Z.; Palacios, M. A.; Anzenbacher, P. *Anal. Chem.* **2008,** *80*, 7451-7459.

(33) Mayr, T.; Igel, C.; Liebsch, G.; Klimant, I.; Wolfbeis, O. S. *Anal. Chem.* **2003**, *75*, 4389-4396.

(34) Jurs, P.C.; Bakken, G.A.; McClelland, H.E. *Chem. Rev.* **2000**, *100*, 2649–2678.

(35) Stewart, S.; Ivy, M. A.; Anslyn, E. V. *Chem. Soc. Rev.* **2014,** *43*, 70-84.

(36) Biros, S. M.; Ullrich, E. C.; Hof, F.; Trembleau, L.; Rebek, J. *J. Am. Chem. Soc.* **2004**, *126*, 2870-2876.

(37) Liu, Y.; Liao, P.; Cheng, Q.; Hooley, R.J. *J. Am. Chem. Soc.* **2010**, *132*, 10383-10390.

(38) Liu, Y.; Young, M.C.; Moshe, O.; Cheng, Q.; Hooley, R.J. *Angew. Chem. Int. Ed.* **2012**, *51*, 7748-7751.

(39) Ghang, Y.-J.; Schramm, M.P.; Zhang, F.; Acey, R.A.; David, C.N.; Wilson, E.H.; Wang, Y.; Cheng, Q.; Hooley, R.J. *J. Am. Chem. Soc.* **2013**, *135*, 7090-7093.

(40) Li, V.; Ghang, Y.-J.; Hooley, R.J.; Williams T.J. *Chem. Commun.* **2014**, *50*, 1375 - 1377.

(41) Perez, L.; Mettry, M.; Hinman, S.S.; Byers, S. R.; McKeating, K.S.; Caulkins, B.G.; Cheng, Q.; Hooley, R.J. *Soft Matter* **2017**, *13*, 3966 - 3974.

(42) Liu, Y.; Perez, L.; Mettry, M.; Easley, C. J.; Hooley, R. J.; Zhong, W. *J. Am. Chem. Soc.* **2016**, *138*, 10746-10749.

(43) Liu, Y.; Perez, L.; Mettry, M.; Gill, A. D.; Byers, S. R.; Easley, C. J.; Bardeen, C. J.; Zhong, W.; Hooley, R. J. *Chem. Sci.* **2017**, *8*, 3960- 3970.

(44) You, L.; Zha, D.; Anslyn, E.V. *Chem. Rev.* **2015**, *115*, 7840−7892.

(45) Ghale, G.; Nau, W.M. *Acc. Chem. Res.* **2014**, *47*, 2150−2159.

(46) Umali, A. P.; Anslyn, E.V. *Curr. Opin. Chem. Biol.* **2010**, *14*, 685–692.

(47) Wright, A.T.; Anslyn, E.V.; McDevitt, J.T. *J. Am. Chem. Soc.* **2005**, *127*, 17405-17411.

(48) Minaker, S.A.; Daze, K.D.; Ma, M.C.F.; Hof, F. *J. Am. Chem. Soc.* **2012**, *134*, 11674−11680.

(49) Peacor, B. C.; Ramsay, C. M.; Waters, M. L. *Chem. Sci.* **2017**, 8, 1422-1428.

(50) Rafai Far, A.; Shivanyuk, A.; Rebek, J., Jr. *J. Am. Chem. Soc.* **2002**, *124*, 2854-2855.

(51) Soberats, B.; Sanna, E.; Martorell, G.; Rotger, C.; Costa, A. *Org Lett*. **2014**,*16*, 2480-2483.

(52) de la Peña, A. M.; Salanas, F.; Gómez, M. J.; Acedo, M. I.; Peña, M. S. *J. Inclus. Phenom. Mol. Rec. Chem*. **1993**, *15*, 131-143.

(53) Korbakov, N.; Timmerman, P.; Lidich, N.;Urbach, B.; Sa'ar, A.; Yitzchaik, S. *Langmuir* **2008**, *24*, 2580-2587.

(54) Fernández-Abad, S.; Pessêgo, M.; Basílio, N.; García-Río, L. *Chem. Eur. J.* **2016**, *22*, 6466 – 6470.

(55) Sun, S.; Yuan, Y.; Li, Z.; Zhang, S.; Zhang, H.; Peng, X. *New J. Chem.* **2014**, *38*, 3600-3605.

(56) Mettry, M.; Moehlig, M.P.; Hooley, R.J. *Org. Lett.* **2015**, *17*, 1497-1500.

(57) Shimizu, Y.; Azumi, A. *J. Phys. Chem.*, **1982**, *86*, 22–26.

(58) Hulme, E.C.; Birdsall, N.J.M. Strategy and Tactics in Receptor-Binding Studies. In *Receptor–Ligand Interactions: A Practical Approach*, Hulme, E.C. ed., Oxford University Press, 1992, pp 63–176.

(59) Cer, R. Z.; Mudunuri, U.; Stephens, R.; Lebeda, F. J. *Nucleic Acids Res.* **2009**, W441–W445.

Supporting Information

1. Calculation of the fraction of the bound guest in each sensor

Using the K_d of guest (G)-cavitand (Cav), we can solve the binding equilibrium and calculate the fraction of the bound fluorescent guest in the solution prior to mixing with different metal ions:

$$K_d = \frac{[Cav]\times[G]}{[Cav \cdot G]}$$

$$[Cav] = [Cav]_0 - [Cav \cdot G]$$

$$[G] = [G]_0 - [Cav \cdot G]$$

Then,

$$K_d = \frac{([Cav]_0 - [Cav \cdot G])\times([G]_0 - [Cav \cdot G])}{[Cav \cdot G]}$$

Solve for $[Cav \cdot G]$, which is the roots of above quadratic equation.

We found the following ratios:

For DSMI, the ratio of [complex]/[Total DSMI] = 45.6%

For RhB 7.4, the ratio of [complex]/[Total RhB] = 59.5%

For RhB 5.5, the ratio of [complex]/[Total RhB] = 80.0%.

Supporting Figures

1. Guest 5 (DSMI) Optical Properties

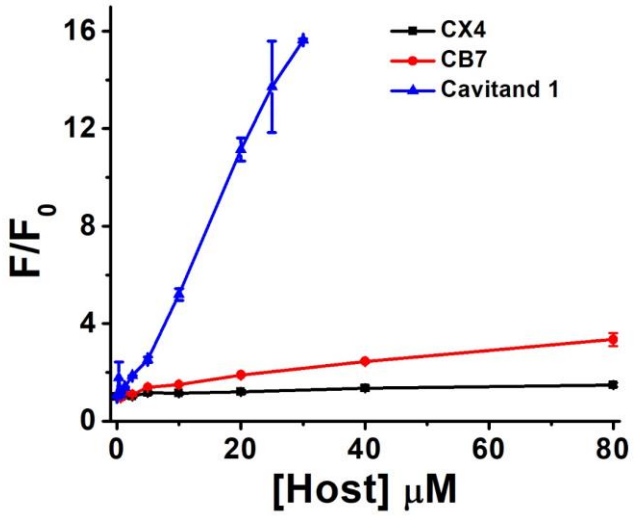

Figure S6.1 Increase of DSMI **5** fluorescence upon binding to three synthetic hosts, **CX4** (tetrasulfonatocalix[4]arene), **CB7** (cucurbit[7]uril) and cavitand **1**. [DSMI **5**] = 1.5 μM in 20 mM Tris, pH =7.4.

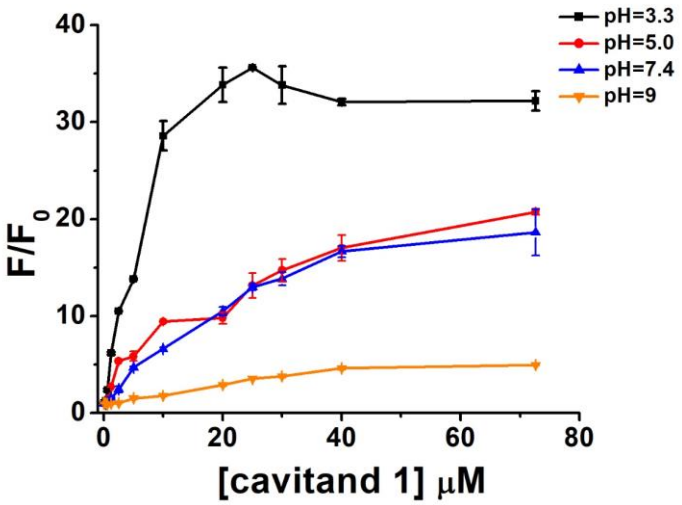

Figure S6.2 Increase of DSMI **5** fluorescence upon binding to cavitand **1** under various pH values. [DSMI **5**] = 1.5 μM in 50 mM citrate (pH 3.3), phosphate (pH 5.0 and pH 7.4), or carbonate (pH 9.0) buffer.

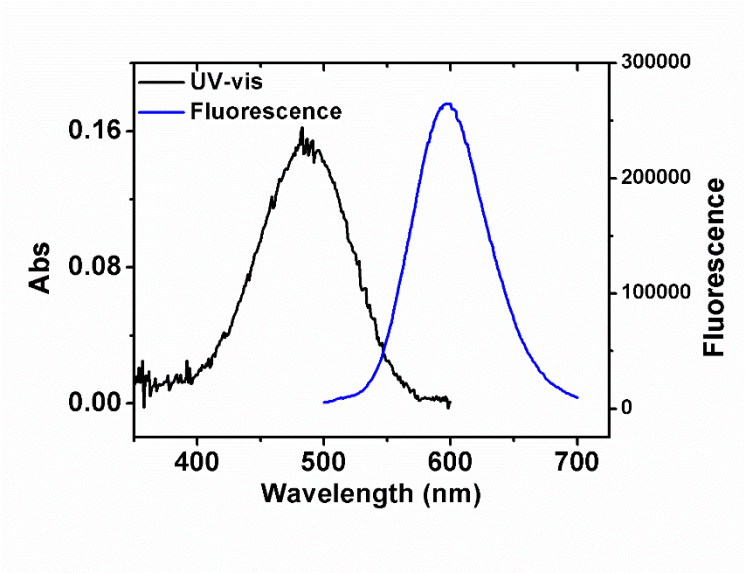

Figure S6.3 UV-Vis absorption and fluorescence emission (with λ_{ex} = 485 nm) spectra of the complex formed between cavitand **1** (20 µM) and DSMI **5** (5 µM) in 50 mM Tris, pH 7.4. The maximum λ_{abs} was found to be 485 nm which was used to excite the fluorescence of DSMI in the following experiments, and fluorescence emission was collected at λ = 605 nm, judged by the emission spectrum presented here.

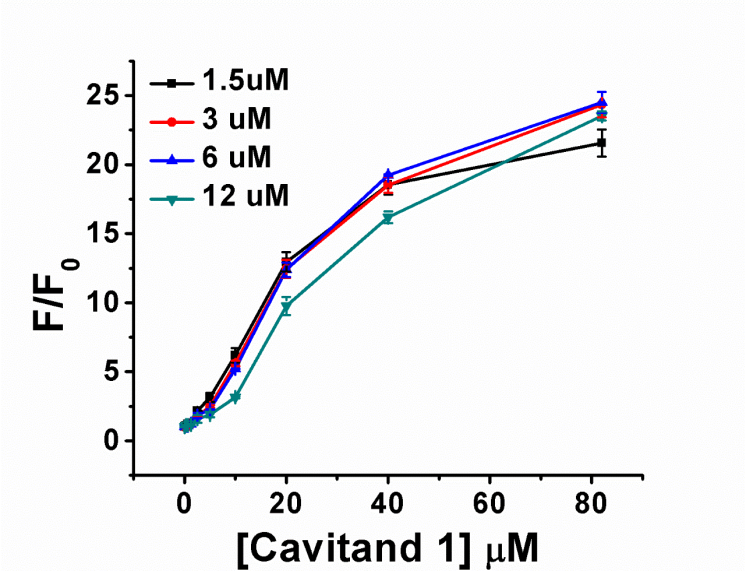

Figure S6.4 Fluorescence change ratio when mixing 1.5, 3, 6, and 12 μM of DSMI **5** with increasing concentrations of cavitand **1**. The combination of 1.5 μM DSMI **5** and 20 μM cavitand **1** was chosen to compose the metal sensing array.

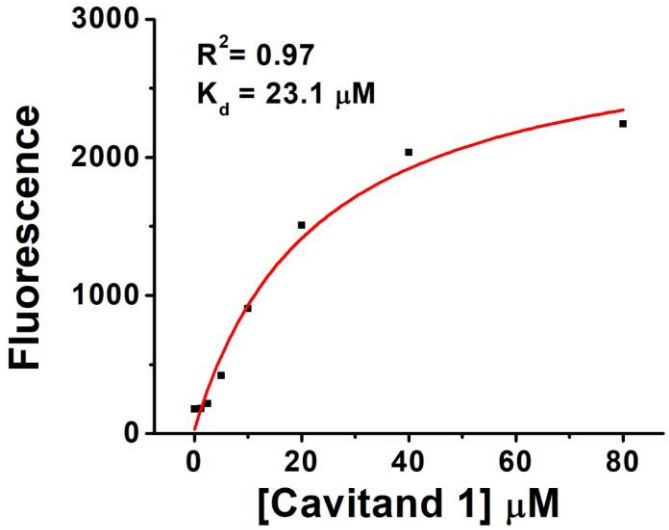

Figure S6.5 The binding curve of **1•5** fitted with the following equation to obtain the dissociation constant of **1•5**:

$$\frac{F}{F_0} = 1 + \left(\frac{F_{max}}{F_0} - 1 \right) \frac{1/K_d\ [host]}{1 + 1/K_d[host]}$$

where F = Fluorescence, F_0 = Fluorescence with cavitand, F_{max} = Fluorescence without cavitand, K_d = dissociation constant, [*host*] = cavitand concentration. [DSMI **5**] = 5 μM in 50 mM Tris at pH =7.4.

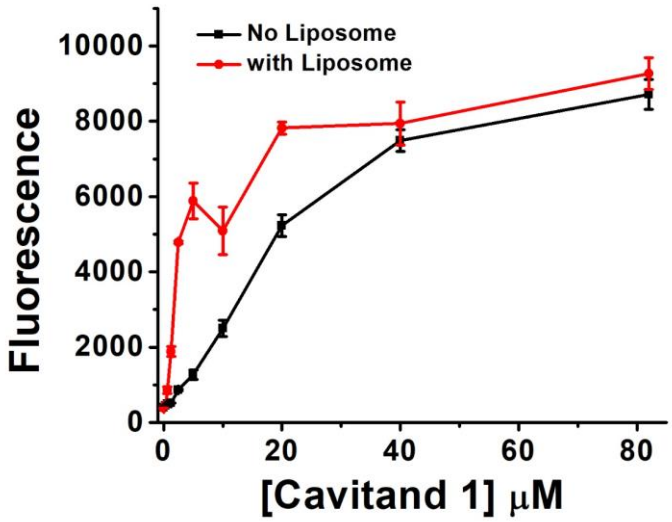

Figure S6.6 Effect of liposome on the fluorescence of the **1•5** complex. [DSMI **5**] = 1.5 μM, liposome = 1 mg/mL, in 20 mM Tris at pH =7.4.

2. Linear Discriminant Analysis and Metal Sensing Data

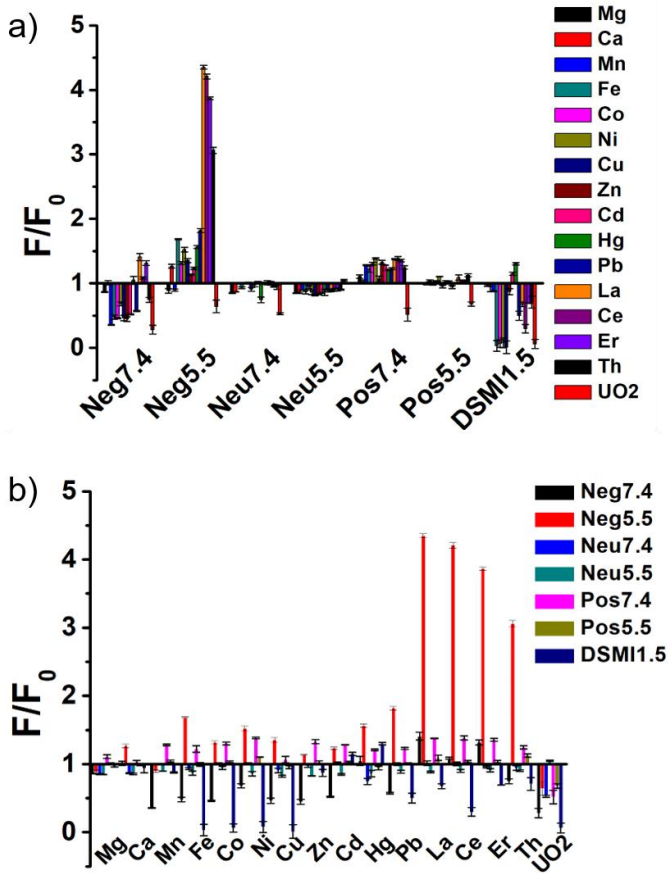

Figure S6.7 The fluorescence data used for LDA to obtain the score plot shown in Figure 6.5c. a) Fluorescence plotted by array elements. b) Fluorescence plotted by metals. [Metal] = 50 μM, 20 mM Tris at pH 7.4 or 20 mM Bis-Tris at pH 5.5, [cavitand] = 4 μM for **1•4**, 20 μM for **1•5**, or 5 μM for **2•4** and **3•4**, [guest **4**] = 3 μM and [DSMI **5**] = 1.5 μM.

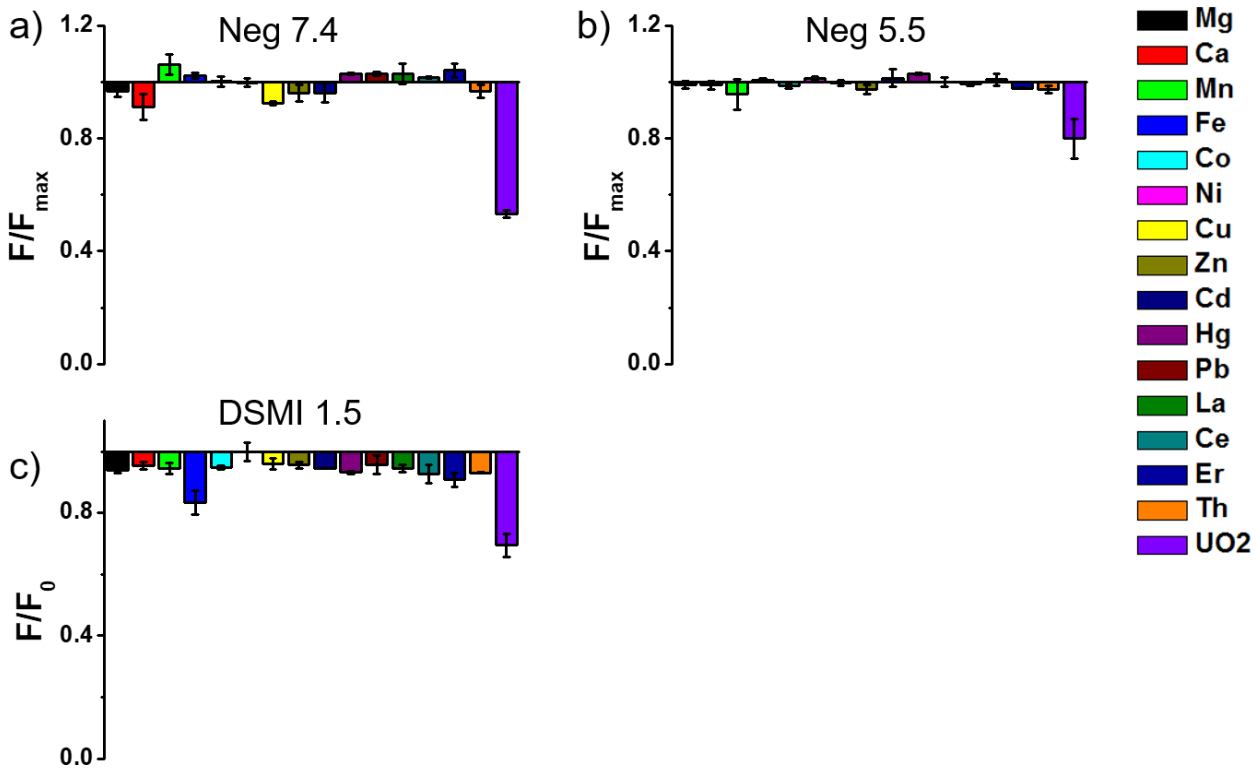

Figure S6.8 Effect of metal salts on the emission intensity of a) guest **4** in Tris buffer (pH =7.4, 20 mM); b) guest **4** in Bs-Tris buffer (pH = 5.5, 20 mM); and c) DSMI **5** in Tris buffer (pH =7.4, 20 mM). All metals other than UO_2^{2+} and Fe^{2+} show negligible effects on both guests. [Metal] = 50 µM.

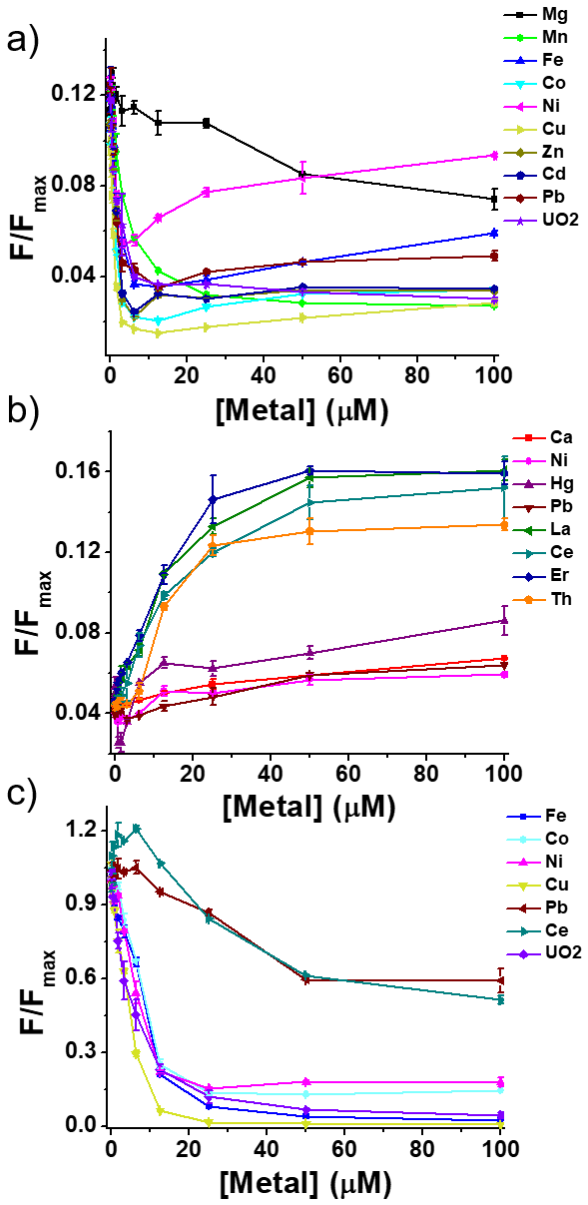

Figure S6.9 The calibration curves showing change in sensor fluorescence upon addition of increasing [Metal] for a) **1•4** at pH 7.4, b) **1•4** at pH 5.5 and c) **1•5** at pH 7.4. For **1•4**, [**1**] = 4 μM, [**4**] = 3 μM; for **1•5**, [**1**] = 20 μM, [**5**] = 1.5 μM.

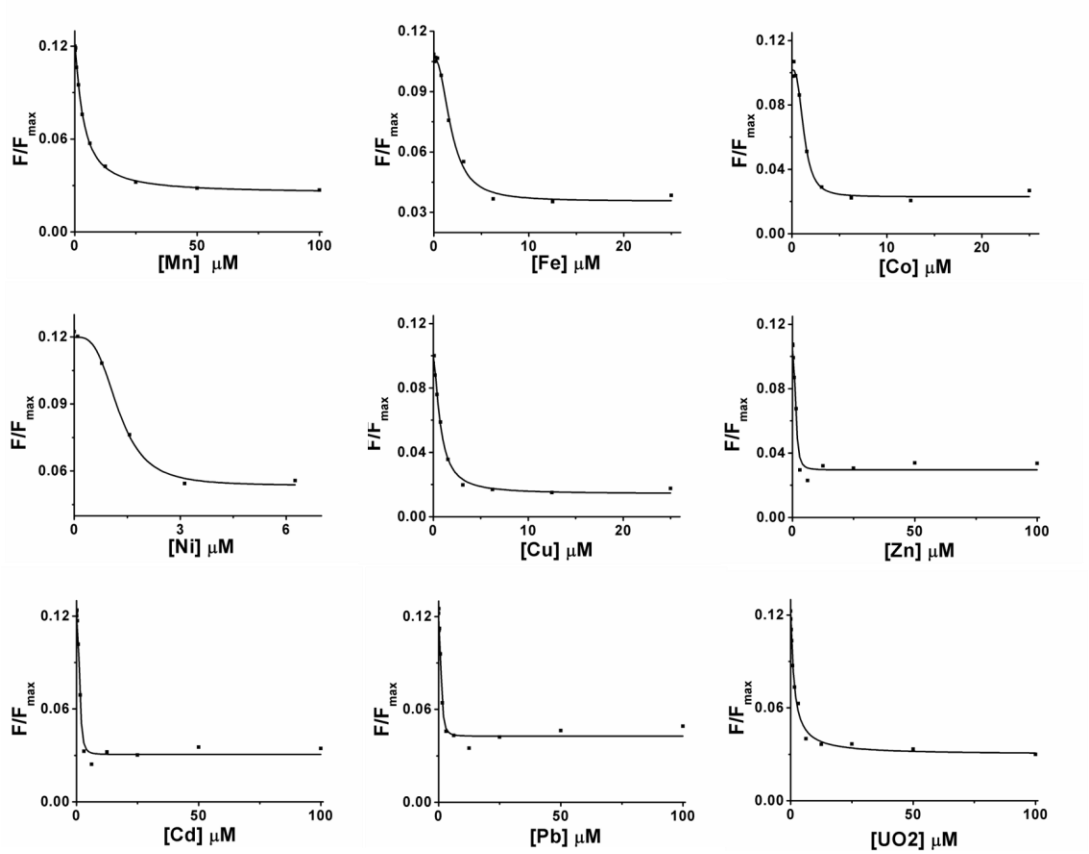

Figure S6.10 The Hill plots for metals with complex **1•4** at pH 7.4.

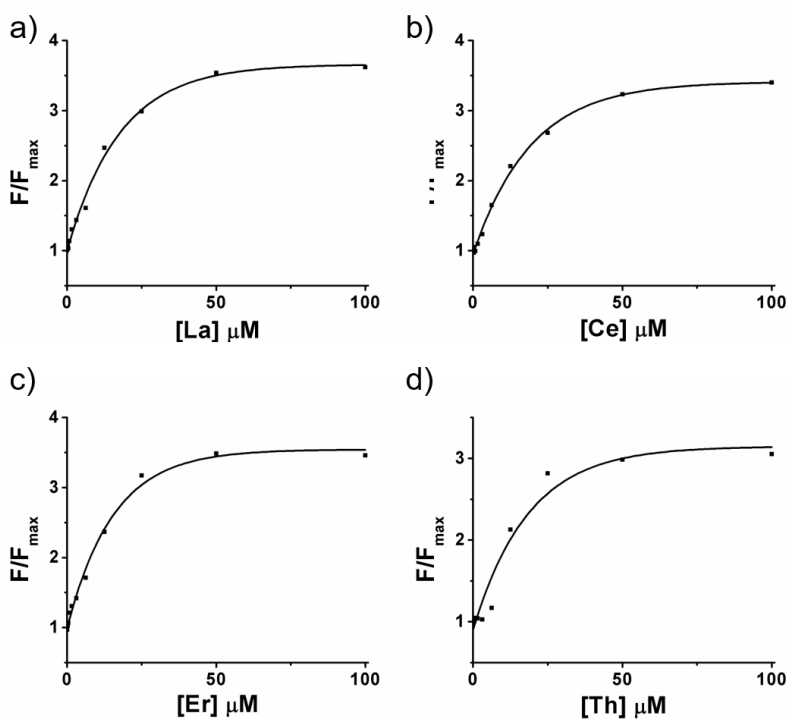

Figure S6.11 The exponential fitting curves for calculation of IC_{50} in the metal displacement model for sensor **1•4** at pH 5.5.

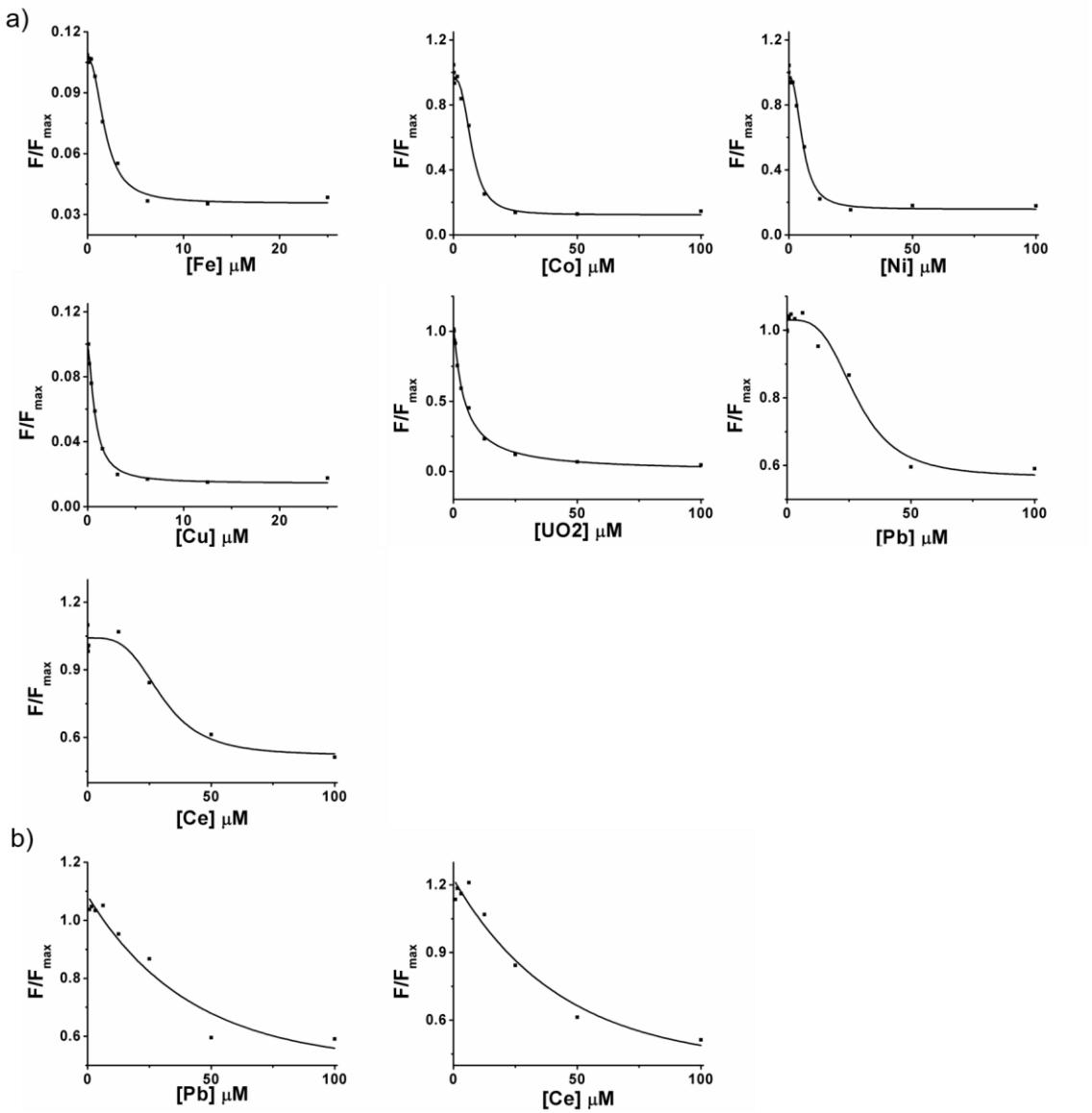

Figure S6.12 a) Hill plot for the binding of Fe^{2+}, Co^{2+}, Ni^{2+}, Cu^{2+}, UO_2^{2+}, Pb^{2+} and Ce^{3+} to sensor **1•5** at pH 7.4, and b) exponential fitting for Pb^{2+} and Ce^{3+} for displacing **5** off cavitand **1** at pH 7.4.

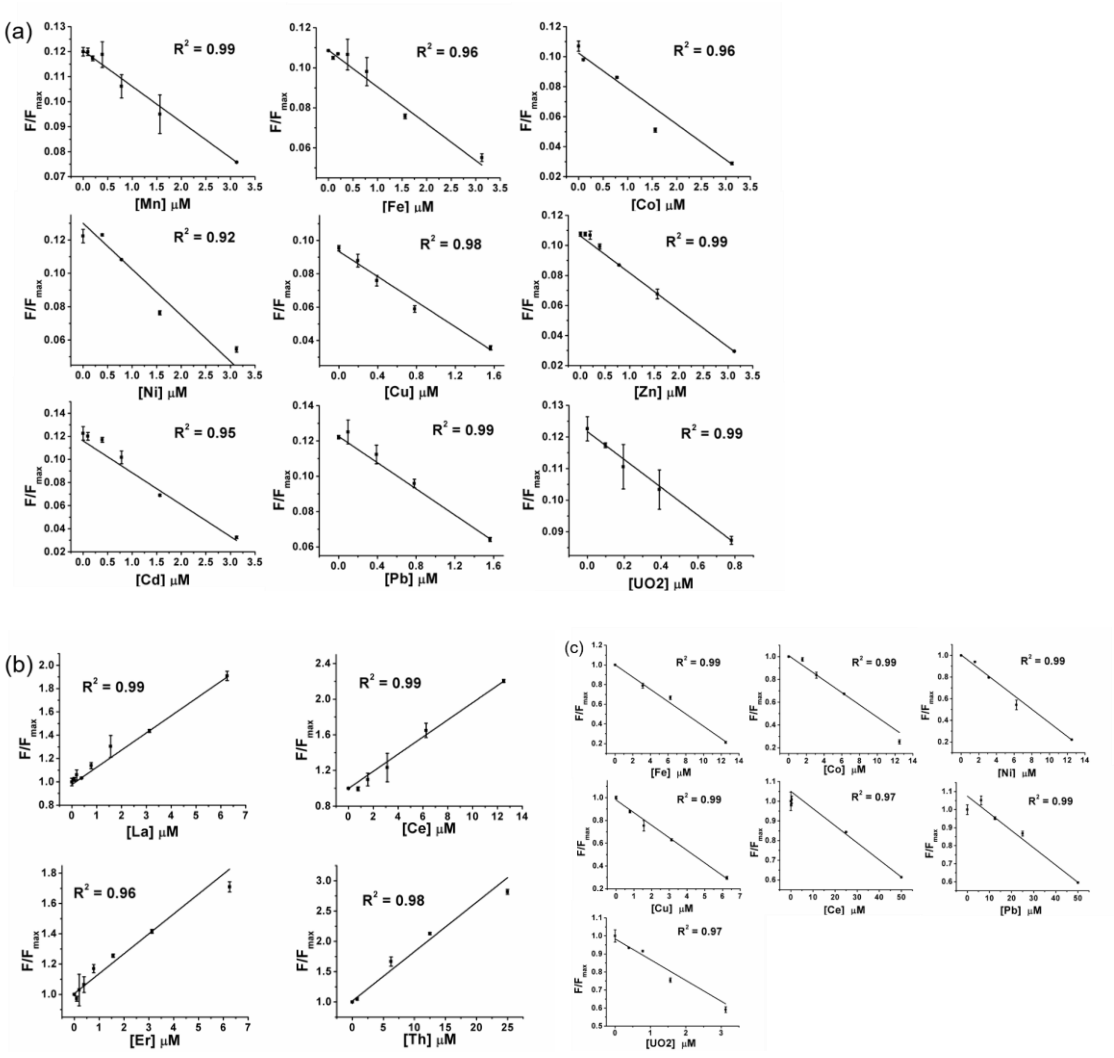

Figure S6.13 Linear range for metal detection and LOD calculation. a) **1•4** at pH 7.4; b) **1•4** at pH 5.5; c) **1•5** at pH 7.4.

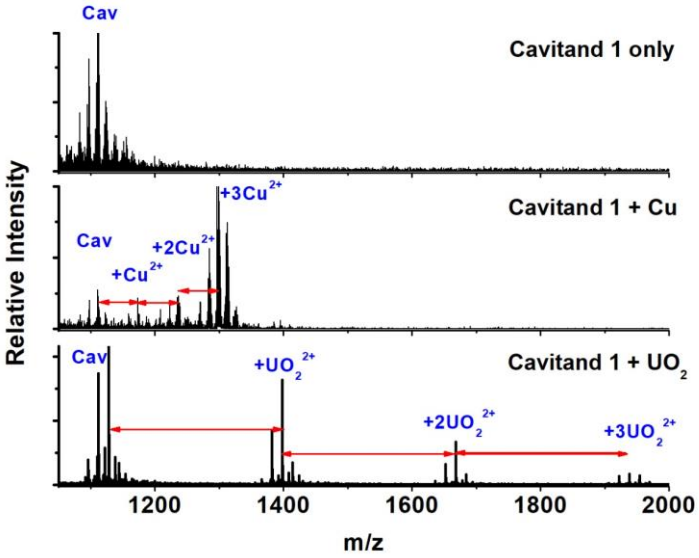

Figure S6.14 SELDI-TOF-MS data for cavitand **1** binding Cu^{2+} and UO_2^{2+}. Other metals were tested as well but no complex ion was detected in gas phase, neither the cavitand-guest complex was detected.

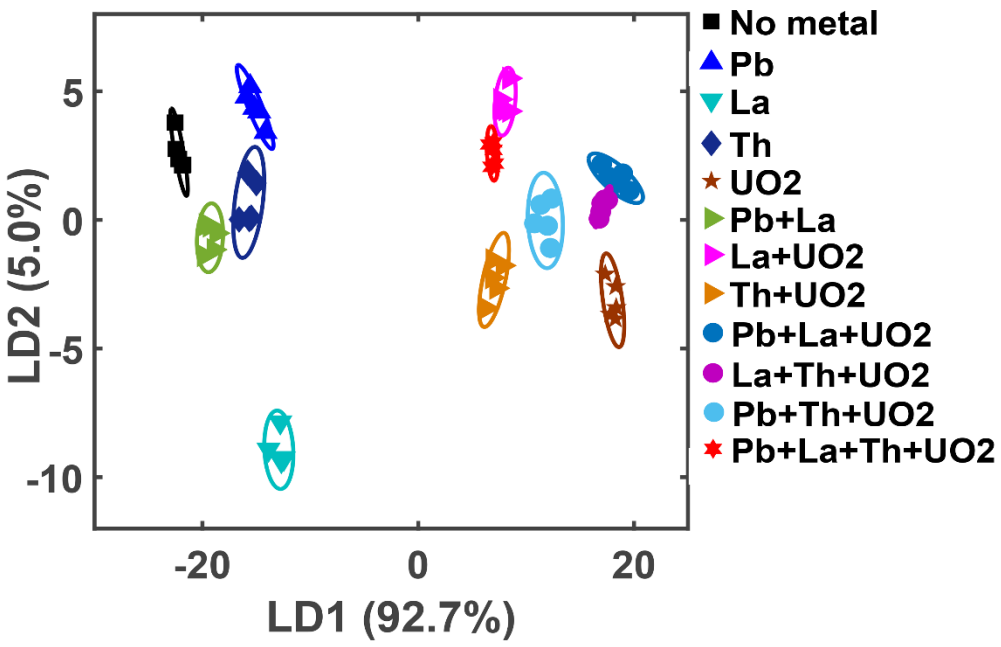

Figure S6.15 LDA score plot for metal mixtures spiked in tap water with the three-factor sensor array containing **1•4** ([**1**] = 4 µM, [**4**] = 3 µM) in pH 7.4 or pH 5.5 buffer, and sensor **1•5** ([**1**] = 20 µM, [**5**] = 1.5 µM, pH 7.4). [Metal] = 2 µM, pH 7.4 = 20 mM Tris, pH 5.5 = 20 mM Bis-Tris.

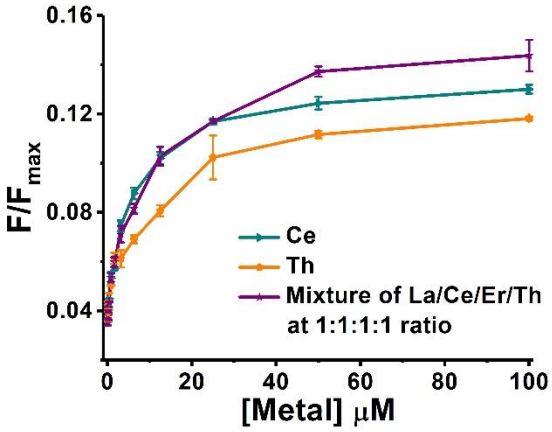

Metal	LOQ (μM)
Ce	1.26
Th	1.93
Metal Mixture (Ce,Th,La,Er)	2.12

Figure S6.16 Titration curves for detection of metals in lake water (collected from the Lake Evans, Riverside), using the **1•4** sensor ([**1**] = 4 μM, [**4**] = 3 μM) at pH 5.5. The limit of quantitation (LOQ) was calculated using the 10σ method, and the lanthanides and actinides showed similar LOQ. This indicates that a single sensor allows metal detection with low LOQ, but not metal identification. However, with the full sensor array, we can provide semi-quantitative identification (see Table 6.3, main text).

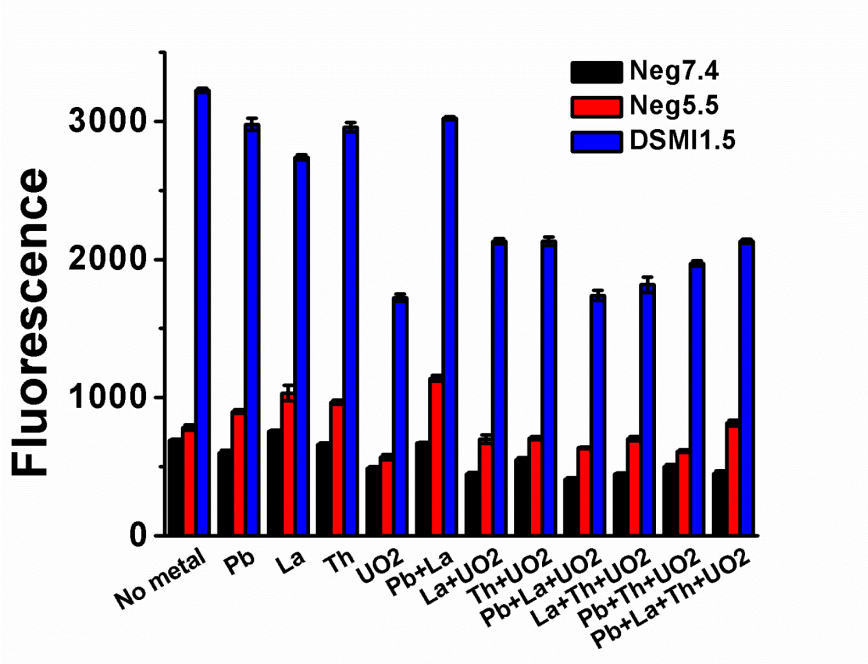

Figure S6.17 The fluorescence data used for LDA to obtain the score plot shown in Figure S6.15. [Metal] = 2 μM, 20 mM Tris at pH 7.4 or 20 mM Bis-Tris at pH 5.5, [cavitand **1**] = 4 μM and [guest **4**] = 3 μM for **1•4**, [cavitand **1**] = 20 μM and [DSMI **5**] = 1.5 μM for **1•5**.

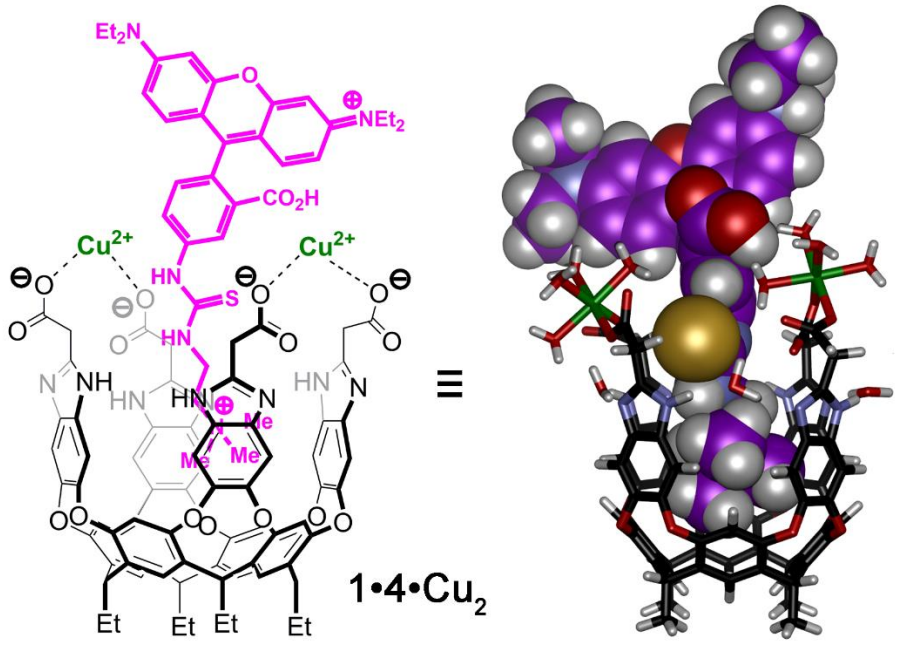

Figure S6.18 Minimized structure of a) **1•4•Cu2**, indicating the effect on metal orientation in the presence of a large guest (SPARTAN, AM1 forcefield).

Table S6.1 Jackknife analysis of the fluorescence data shown in Figure 6.6a.

	Cd	Pb	Ce	La	Er	Hg	Th	UO2	%Correct
Cd	16	0	0	0	0	0	0	0	100
Pb	0	16	0	0	0	0	0	0	100
Ce	0	0	16	0	0	0	0	0	100
La	0	0	0	16	0	0	0	0	100
Er	0	0	0	0	16	0	0	0	100
Hg	0	0	0	0	0	16	0	0	100
Th	0	0	0	0	0	0	16	0	100
UO2	0	0	0	0	0	0	0	16	100
Total	16	16	16	16	16	16	16	16	100

Table S6.2 Jackknife analysis of the fluorescence data shown in Figure S6.16, agreeing with the score plots shown in Figure 6.7.

	No metal	Pb	La	Th	UO2	La+UO2	Th+UO2	Pb+La+ UO2	La+Th +UO2	Pb+La+ Th+UO2	%Correct
No metal	5	0	0	0	0	0	0	0	0	0	100
Pb	0	5	0	0	0	0	0	0	0	0	100
La	0	0	5	0	0	0	0	0	0	0	100
Th	0	0	0	5	0	0	0	0	0	0	100
UO2	0	0	0	0	5	0	0	0	0	0	100
Pb+La	0	0	0	0	0	0	0	0	0	0	100
La+UO2	0	0	0	0	0	5	0	0	0	0	100
Th+UO2	0	0	0	0	0	0	5	0	0	0	100
Pb+La+UO2	0	0	0	0	0	0	0	5	0	0	100
La+Th+UO2	0	0	0	0	0	0	0	0	5	0	100
Pb+Th+UO2	0	0	0	0	0	0	0	0	0	0	100
Pb+La+Th+UO2	0	0	0	0	0	0	0	0	0	5	100
Total	5	5	5	5	5	5	5	5	5	5	100

Table S6.3 Dissociation constants obtained from curve fitting and limit of detection

Sensor	*Metal*	*K_d^{MC} (μM) by Hill plot*	*n by Hill plot*	*LOD (μM)*
1•4 At pH 7.4	Mn^{2+}	4.5±0.3	1.2	0.51
	Fe^{2+}	3.8±1.4	2.1	0.23
	Co^{2+}	2.0±0.4	2.7	0.22
	Ni^{2+}	1.8±0.4	3.1	0.48
	Cu^{2+}	0.7±0.1	1.4	0.07
	Zn^{2+}	2.7±0.8	2.0	0.22
	Cd^{2+}	2.5±0.3	2.3	0.52
	Pb^{2+}	1.3±0.3	2.0	0.13
	UO_2^{2+}	1.4±0.2	1.1	0.23

Sensor	*Metal*	*IC50 (μM) by Displacement Model*	*R^2*	*K_d^D (μM) by Displacement Model*	*LOD (μM)*
1•4 At pH 5.5	La^{3+}	12.27	0.99	1±0.1	0.58
	Ce^{3+}	13.43	0.99	1.1±0.1	1.21
	Er^{3+}	10.74	0.99	0.9±0.1	0.31
	Th^{3+}	12.75	0.95	1.1±0.1	1.29

(LOD) calculated for all metals tested in Figure S6.10.

Sensor	*Metal*	*K_d^{MC} (μM) by Hill plot*	*n by Hill plot*	*IC50 (μM) by Displacement Model*	*R^2*	*K_d^D (μM) by Displacement Model*	*LOD (μM)*
1•5 At pH 7.4	Fe^{2+}	58±14	2.0	7.07	0.98	NA	0.19
	Co^{2+}	200±40	2.6	6.71	0.97	NA	0.51
	Ni^{2+}	73±14	2.5	5.19	0.98	NA	0.33
	Cu^{2+}	8.7±1.7	1.6	3.71	0.99	NA	0.21
	Ce^{3+}	(1.9 ±0.6) x 10^3	2.3	17.92	0.99	2.7±0.1	4.60
	Pb^{2+}	(1.3±0.3) x 10^3	1.5	35.78	0.97	12.2±1.7	9.15
	UO_2^{2+}	4.9±0.5	1.1	4.35	0.99	NA	0.27

Chapter 7 Summary and Future Work

Summary

In this dissertation, we have demonstrated several useful analytical methods for analysis of toxicants including ROS and heavy metals. Furthermore, we also showed the successful built up of a sensor array based technique, which can be used to monitor histone modifications.

In Chapter 2, ZnS/CuS microgel was successfully adopted for detection of ROS, mainly H_2O_2. The detection is based on the hypothesis that H_2O_2 can oxidate ZnS and release Zn^{2+} cation, which will bind to Fluozin-3 (Zinc specific fluorescent dye) and show enhanced fluorescence. The addition of Copper into the microgel will give better sensitivity towards H_2O_2. This set-up could detect sub-micromolar of H_2O_2. And combining with two oxidases (glucose oxidase and cholesterol oxidase), this sensor was also able to be used for glucose and cholesterol quantification. This method was expected to be potentially applicable for any H_2O_2 involving assays.

Chapter 3 shows our first design using a synthetic host and guest system to analyze histone modifications. The fluorescein based trimethylammonium guest showed strong quenching after binding with negative cavitands. And when target molecule with trimethyl modification was introduced to the system, guest would be displaced from binding pocket of cavitand and show a strong fluorescence recovery. This fluorescence displacement assay was applied first for trimethyllysine detection and then further applied for JMJD2E

(demethylase) activity monitoring. In addition, we also demonstrated that this assay can be applied in complex environment like cell lysate digest.

In Chapter 4, we pushed the design in Chapter 4 further by adding another two hosts molecule and one guest molecule. The two newly added hosts are quite similar to negative cavitand, but different in their charge status: one is positive charged and the other is non-charged. A new Rhodamine B based guest was also synthesized and used here. A sensor array was successfully built up by using these hosts and guests' combination. The application of the sensor array was first demonstrated by a series of small molecules (different charge, chain length and methylation level) and a clear separation was demonstrated by PCA analysis. Then it is further applied to detect real histone peptides with different modifications. Our assay is very good at distinguish different methylation sites, length, methylation level and other modifications including acetylation and phosphorylation.

Chapter 5 demonstrated a more challenge work of using sensor arrays to do methylation enzyme monitoring. Thanks to our sensor array's strong ability to distinguish mono-, di-, tri-methylation targets and also different modification sites, we were able to distinguish very similar enzyme products. We first showed that we can clear separate different methylation sites and levels. And then one methyl transferase that specifically targeting lysine 4 and a demethylase that target lysine 9 were tested by our sensor array. Results showed that the products of these enzyme reactions were able to be monitored step by step. And more interestingly, we can use the same set up to do different enzymes without

the need to change our substrates. This could be very useful to screen unknown enzymes, because the patterns in PCA plot will be able to tell which site this enzyme is working on.

Chapter 6 is focusing on the other toxicants - heavy metals. Heavy metals were known to cause serious health problems in human beings. And a sensor array that can separate 16 metals were demonstrated in this chapter. Our assay is also based on cavitand-guest pair and for this time, heavy metal will be the quencher or enhancer. We were able to see very different signal change patterns (enhance or decrease) with different sensor elements. This is quite interesting and useful for distinguish and analysis of heavy metals. The detection was demonstrated in lake water and tap water for metal mixtures.

Future work

Based on above studies, we will continue to explore the application of cavitands and guest systems in other fields.

1. Immunoglobulin detection.

Immunoglobulins (Ig), also known as antibodies, are Y-shaped protein produced mainly by immune system to neutralize pathogens. There are mainly five sub categories of Ig protein, including IgA, IgD, IgE, IgG and IgM with quite similar structures but varying heavy chains. Ig proteins serve as important biomarkers for immune system. And it is shown that smoking,[1] alcohol consumption[2] and high working pressure[3] would cause a decrease in Ig proteins. The monitoring of Ig concentration was mostly based on immune assays. And antibody itself has problems like low stability and high cost. Thus, development of other new analytical methods was of great interests.

As shown in Scheme 7.1, serum samples were first mixed with Protein L (pan-specific to all Ig proteins) labelled beads to extract the Ig proteins. After washing to remove nonspecific proteins, the beads will be added to cavitands and guest mixtures. Protein will compete with guests for cavitands and possible fluorescence recovery could be induced. Since we have an arrayed system, we were able to detect different Ig proteins, mainly IgA, IgG and IgM, which are more abundant in serum comparing with IgE and IgD.

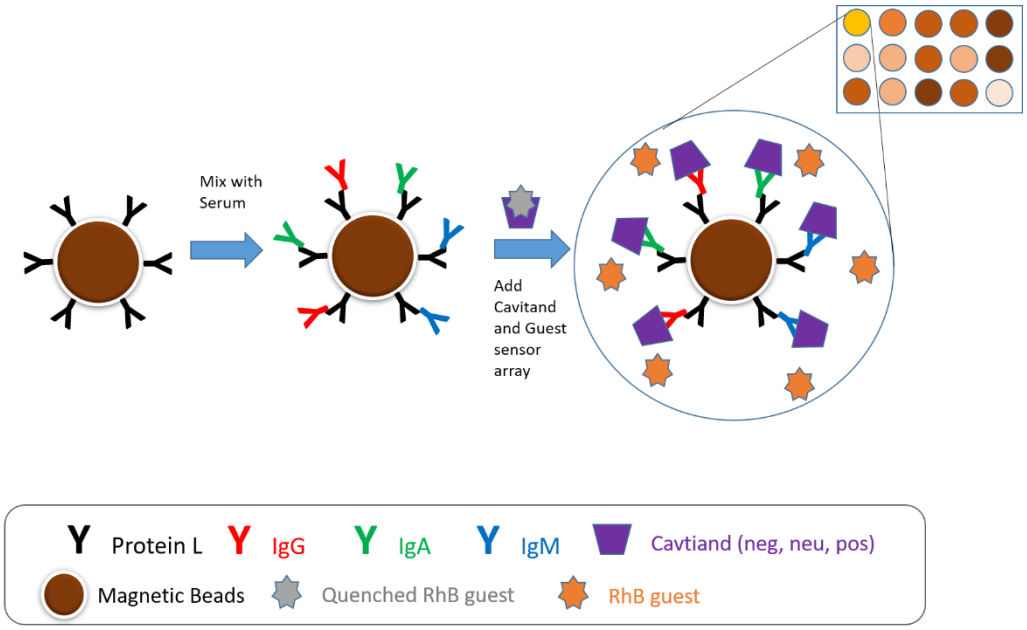

Scheme 7.1 Detection of Ig proteins with Protein L labelled beads and cavitands.

Preliminary data showed that we can achieve successful separation of these three Ig proteins in PBS buffer (Figure 7.1). A further test showed that with different ratios of IgA, IgG and IgM, we can also show clear separation (Figure 7.2). The next step is to test protein L beads based extraction and analysis.

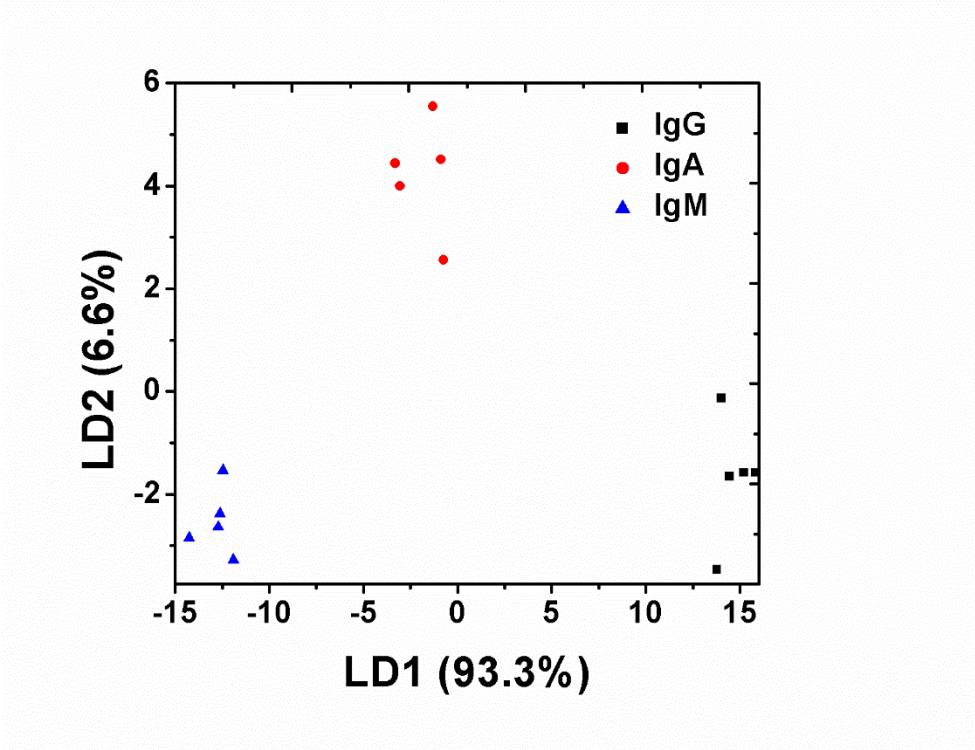

Figure 7.1 LDA plot for IgG proteins. Ig protein = 1.5 µg/mL, PBS buffer, pH =7.4.

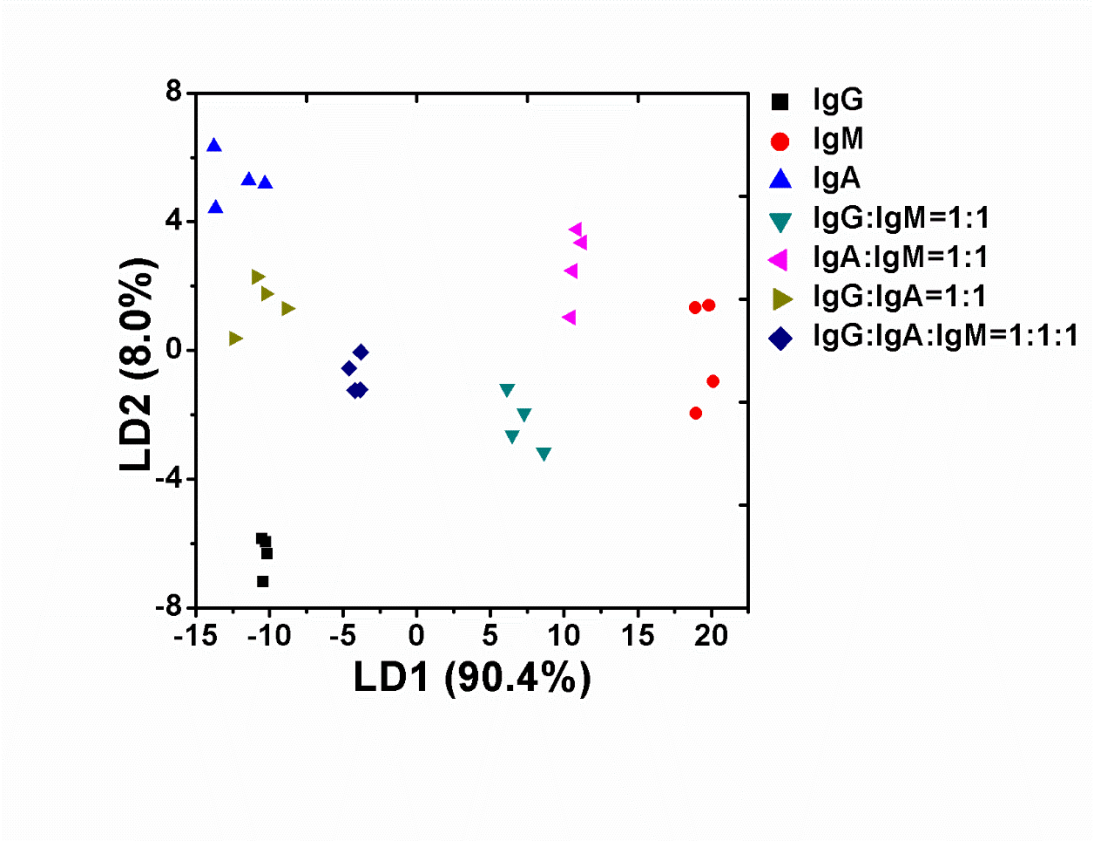

Figure 7.2 LDA plot of IgG proteins with different mixture ratio. Ig protein total = 1.5 μg/mL, PBS buffer, pH =7.4.

2. Protein Phosphorylation detection.

Protein phosphorylation plays a pivotal role in cellular regulation. It is reported that phosphorylation of protein is the major signal transduction pathway in cell and is controlled delicately by protein kinase and protein phosphatase. Phosphorylation are commonly happened to serine, threonine and tyrosine in eukaryotes and histidine in prokaryotes. And adding a phosphate group to protein will greatly influence its charge status. To monitor phosphorylation, different methods have been developed, such as biosensors, LC-MS/MS,

and electrochemistry. Among them, biosensors are good for quick test with cheap cost. And our approach was a fluorescent based bio sensing setup.

Our design is based on displacement of dye from cavitand. DSMI (Dye used Chapter 6) was chosen to achieve this purpose. We proved that DSMI is sensitive to charged molecules including peptides and surfactants. And based on this character, we hypothesize that phosphorylation could be detected due to the charge change of the peptide. As shown in Figure 7.3, a large change of fluorescence signal was seen for phosphorylated peptide (H3 peptide and a PKA substrate) comparing with peptide control. H3 is a histone peptide with 14 amino acids, and the serine 10 can be phosphorylated. PKA substrate is a shorter peptide with serine on it and was reported to be high efficient substrate for PKA. And based on this discovery, our future direction will be applying this method to monitor PKA activity as well as phosphatase activity.

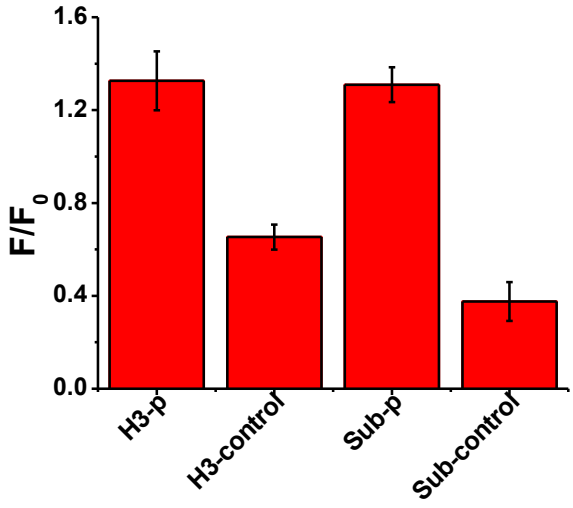

Figure 7.3 Phosphorylation caused signal change to cavitand and DSMI.

Reference

(1) Burrows, B.; Halonen, M.; Barbee, R.; Lebowitz, M. *Am. Rev. Respir. Dis.* **1981**, *124*, 523-525.

(2) Friedrich, N.; Husemoen, L. L. N.; Petersmann, A.; Nauck, M.; Völzke, H.; Linneberg, A. *Alcoholism: Clinical and Experimental Research* **2008**, *32*, 983-990.

(3) Henningsen, G.; Hurrell, J.; Baker, F.; Douglas, C.; MacKenzie, B.; Robertson, S.; Phipps, F. *Scand. J. Work. Environ. Health* **1992**, 133-136.